DTU Nanotech
Department of Micro- and Nanotechnology

Ph.D. Thesis

Electrokinetics and catalysis in microfluidic systems

Theory, topology optimization and experiments

Misha Marie Gregersen

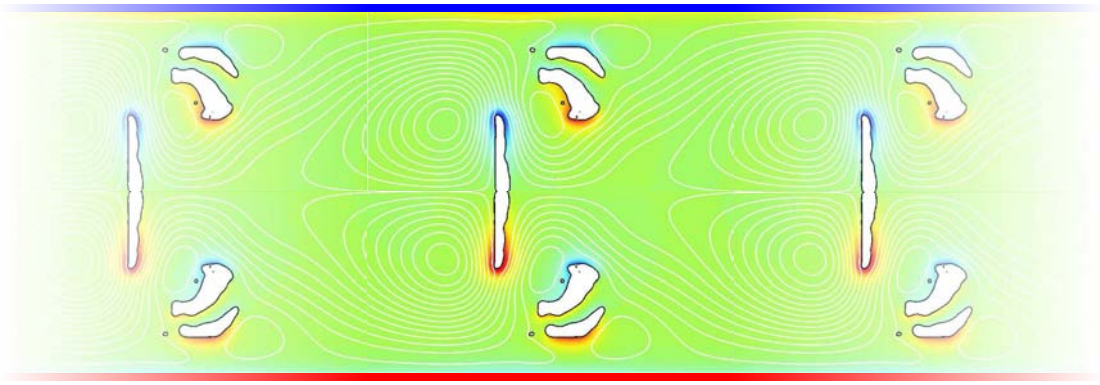

Supervisor: Henrik Bruus

Department of Micro- and Nanotechnology
Technical University of Denmark

28 February 2009

Abstract

The present PhD thesis is a contribution to the research field of induced-charge electro-osmotic (ICEO) flows, and to the field of applied topology optimization in microfluidic systems. The scientific efforts behind this contribution can be divided into four areas of research. These have been summarized below.

Within the topic of ICEO, experimental studies of AC electro-osmotic pumping in microchannels generated above an array of asymmetric electrodes have been carried out. In the regime of low frequencies and low voltages a hitherto unobserved reversal of the flow direction has been detected. No existing electrokinetic models published in the literature are able to account quantitatively for this observation. The impedance spectra of these pumps have additionally been thoroughly measured and investigated in terms of an equivalent circuit diagram. By fitting these spectra to a Bode plots, good agreement with our model was found using realistic parameter values.

Furthermore, a conventional full nonlinear model of DC-driven ICEO flows has been implemented and solved numerically for fully resolved electric double layers. The implemented model has subsequently been validated against analytical flow results. The generated flow calculated by this model has been compared to the same flow calculated using a linear ICEO model, which is based on the assumption of an infinitely thin Debye layer with an effective slip-velocity condition on the flow outside the electrical double layer. It turns out that the slip-velocity model overestimates the flow compared to the full model. When the Debye length increases relative to the size of the flow-generating electrode, the discrepancy between the models increases significantly. Even when the Debye length is one percent of the electrode size, deviations of at least 10% are to be expected. This deviation could provide a partial explanation of the quantitative discrepancy between observed and calculated ICEO velocities reported in the literature.

In extension of the numerical ICEO flow modeling, the third part of the thesis work concerns the application of topology optimization on ICEO systems. This numerical optimization method has been implemented for a linearized AC-driven ICEO system with fully resolved double layers. Contrary to previously optimized systems relying on bulk properties, the ICEO is purely a boundary dependent phenomenon relying on the dynamics taking place in a narrow region around the solid/fluid interface. This is of importance for the implementation of the topology optimization method, which depends on the introduction of an artificial design field describing the transition from liquid to solid in the governing equations. This extended model has successfully been established and validated against the conventional model without the design field. The model has subsequently been

utilized to optimize ICEO structures for their ability to generate pumping, i.e. maximize the net induced flow rate, perpendicular to the applied electrical field. Once found, the performance of the topology optimized geometries has been validated by transferring them to the conventional electrokinetic model without the artificial design field. Compared to simpler geometric structures previously utilized to generate pumping, the performance of the topology optimized geometries is superior.

Finally, the topology optimization method has also been applied to a chemical microreactor system. An existing implementation of this method in a simplified reaction model has been extended to include a realistic model for the reaction kinetics of a CO oxidation process supported by a platinum catalyst. The distribution of catalyst in a reactor chamber has subsequently been topology optimized with the goal of maximizing the overall reaction rate. An experimental setup for verifying these numerical optimization results has been prepared by incorporating the optimized catalyst structures in an existing microfabricated reactor. Reactor devices have been fabricated and the experimental testing of the system is progress at the time of writing.

Resumé

Den foreliggende ph.d.-afhandling er et bidrag til forskningen indenfor elektro-osmotiske strømninger via ladningsinduktion (ICEO) samt topologi-optimering anvendt på mikrofluide systemer. De videnskabelige bestræbelser der ligger til grund for denne afhandling kan inddeles i fire forskningsmæssige kategorier og er beskrevet således i det følgende.

Indenfor ICEO-området er der udført eksperimentelle undersøgelser af AC-elektro-osmotisk væskepumpning på mikroskala, som frembringes med en række asymmetriske elektroder placeret fortløbende i en mikrokanal. For lave frekvenser og spændinger er der i systemet konstateret væskestrømninger modsat rettet den teoretisk forudsagte strømningsretning, hvilket aldrig tidligere har været observeret. Til dato er der ikke blevet publiceret elektro-kinetiske modeller som kan redegøre for denne effekt. Herudover er der blevet foretaget udførlige målinger af impedansspektrummet for denne vekselspændings-elektro-osmotiske væskepumpe, og de herved fremkomne data er dernæst analyseret ved hjælp af et ækvivalenskreds-diagram. Anvendes realistiske parameter-værdier er der ved at tilpasse det resulterende spektrum til et Bode plot opnået god overensstemmelse med vores model.

Desuden er en konventionel ikke-lineær model af jævnstrøms-drevne ICEO væskestrømme blevet implementeret og løst numerisk for fuldt opløste elektriske dobbeltlag. Oftest antages det elektriske dobbeltlag at være uendelig tyndt i den fysiske modellering af ICEO-systemer, men ved at medtage de elektriske dobbeltlag i en mere realistisk form øges modellens nøjagtighed, idet elektrokinetiske effekter i systemets randområder inkluderes i de numeriske beregninger. Modellen er dernæst blevet valideret ved at sammenholde de numeriske løsninger med analytiske beregninger af samme modelsystem. Endvidere er modellens estimater af væskestrømmene blevet sammenholdt med tilsvarende estimater fra en lineær ICEO-model, som er baseret på antagelsen om et uendeligt tyndt Debye-lag med en effektiv slip-hastigheds-betingelse på væskestrømmen udenfor det elektriske dobbeltlag. Det har vist sig at den lineære model overestimerer styrken af væskestrømmene sammenlignet med den ikke-lineære model. Når forholdet mellem Debye-længden og dimensionerne for den væskestrøms-inducerende elektrode bliver større, forøges uoverensstemmelsen mellem modellerne markant. Selv når Debye-længden er en procent af elektrodens bredde kan der forventes en afvigelse på mindst 10 procent. Denne afvigelse kunne være en mulig forklaring på den kvantitative uoverensstemmelse mellem observerede og beregnede ICEO strømningshastigheder som er blevet rapporteret i litteraturen.

I forlængelse af den numeriske modellering af ICEO-systemer, og som den tredje del af arbejdsgrundlaget for denne Ph.d.-afhandling, er topologi-optimering blevet anvendt

på forskellige ICEO-modelsystemer. Den numeriske optimeringsmetode er blevet implementeret for et lineariseret vekselspændings-drevet ICEO-system med fuldt opløste dobbeltlag. I modsætning til tidligere optimerede systemer, hvor systemets materialeegenskaber var afgørende for optimeringsprocessen, afhænger optimeringen af ICEO-systemet udelukkende af dynamiske randeffekter, der optræder i en snæver region hvor væsken i systemet mødes med det faste stof der afgrænser systemet. Dette forhold er vigtigt for implementeringen af topologi-optimerings-metoden, idet implementering er baseret på indførelsen af et kunstigt design-felt som beskriver overgangen fra væske til fast stof i modellens grundlæggende ligninger. Denne udvidede model er med succes blevet etableret og dernæst valideret på grundlag af en konventionel model uden et design-felt. Modellen er efterfølgende blevet anvendt til at optimere ICEO-strukturers evne til at generere en effektiv væskestrøm i mikrokanalens længderetning og således vinkelret på det påtrykte elektriske felt. De fremkomne strukturers pumpeeffektivitet er, i lighed med selve modellen, blevet efterprøvet ved at indsætte strukturerne i en konventionel elektrokinetisk model uden det kunstige design-felt. Sammenlignet med mere simple geometriske strukturer tidligere anvendt til at generere væskestrømme i mikrokanaler, er de optimerede strukturers pumpeeffektivitet markant bedre.

Det sidste arbejdsområde i forbindelse med denne afhandling har været anvendelsen af topologi-optimerings-metoden på en kemisk mikroreaktor. En allerede implementeret optimeringsmetode anvendt på et simplificeret kemisk modelsystem er blevet udbygget således at modellen inkluderer en realistisk beskrivelse af reaktionskinetikken for en CO-oxidationsproces katalytisk understøttet af en platin-belagt overflade. Fordelingen af katalytisk materiale i reaktionskammeret er dernæst blevet optimeret med henblik på at maksimere den samlede reaktionsrate. For at kunne efterprøve de resulterende katalytiske strukturers evne til at fremme oxidationen af CO sammenlignet med et konventionelt struktureret reaktionskammer, er der blevet lavet en eksperimentel opstilling, som anvender den optimerede fordeling af katalytisk materiale i en eksisterende renrumsfabrikeret mikroreaktor. Fabrikationen af disse modificerede reaktor-enheder er blevet udført med succes og systemerne afprøves nu i skrivende stund.

Preface

This thesis is submitted in candidacy for the PhD degree at the Technical University of Denmark (DTU). The work has been carried out within the Theoretical Microfluidics group (TMF) at the Department of Micro- and Nanotechnology, DTU Nanotech, from January 2006 to February 2009. During the winter 2007/2008 I visited Laboratoire de Physico-Chimie Théorique at Ecole Supérieure de Physique et de Chimie Industrielles (ESPCI ParisTech), in Paris for five months. The project has been supervised by Prof. Henrik Bruus, and while abroad by Prof. Martin Z. Bazant.

First of all I would like to thank Henrik Bruus for his dedicated effort as supervisor and catching enthusiasm for the field of microfluidics. I have benefitted tremendously from Henrik's great knowledge about physics, and from his supervision in article writing and guidance during talk preparations. I thank Martin Bazant for motivating and enlightening conversations about electrokinetic phenomena and for providing great inspiration to my work during my stay at ESPCI. I also thank Elie Raphaël and Patrick Tabeling at ESPCI for welcoming and supporting me during my stay. I would like to thank Adam Monkowski for his interest and engagement in the part of my work concerning the chemical reactor. I also thank Ole Hansen for supervising this part of the project, and Jacob L. Olsen for his help on the device testing.

The people in the theoretical microfluidics group have contributed to an inspiring and exceptional good atmosphere. In particular, I thank my fellow PhD student and office-mate Martin Heller for always being very helpful and ready for clarifying discussions about both physical and non-physical topics. I thank Laurits Højgård Olesen for patiently sharing his knowledge about electrokinetics, and Fridolin Okkels for introducing me to topology optimization. I also thank Mathias Bækbo Andersen for the good collaboration on electrokinetics. I thank all former and present employees of DTU Nanotech and DANCHIP for creating a pleasant and good working atmosphere. Finally, I thank my family and friends for their encouragement during the project, and especially my boyfriend Thorbjørn for his invaluable support.

Misha Marie Gregersen
Department of Micro- and Nanotechnology
Technical University of Denmark
28 February 2009

Contents

List of figures **xiv**

List of tables **xv**

List of symbols **xvii**

1 Introduction **1**
1.1 Background and motivation 1
1.2 Thesis work 2
1.3 Outline of the thesis 3
1.4 Publications during the PhD studies 4

2 Basic concepts **7**
2.1 Conventional electro-hydrodynamic model 7
2.1.1 The electrical double layer 7
2.1.2 Electro-hydrodynamic transport 10
2.1.3 electro-osmosis 11
2.2 AC electro-osmosis 12
2.3 Induced-charge electro-osmosis 13
2.3.1 Finite Debye length for metalic cylinder 15
2.4 Numerical implementation of governing equations 16
2.5 Topology optimization 18
2.5.1 Topology optimization example: Reverse flow in a straight channel . 20

3 Experiments on ACEO system **23**
3.1 Experimental 24
3.1.1 System design 24
3.1.2 Chip fabrication 26
3.1.3 Measurement setup and procedures 27
3.1.4 AC biasing and impedance measurements 28
3.1.5 Flow velocity measurements 28
3.2 Results 30
3.2.1 Reproducibility of measurements 30
3.2.2 Flow reversal at low voltage and low frequency 31

3.2.3 Electrical characterization . . . 32
3.3 Discussion . . . 32
3.3.1 Equivalent circuit impedance analysis . . . 33
3.3.2 Flow analysis . . . 35
3.4 Summary . . . 37

4 DC-driven ICEO **39**
4.1 Model system . . . 39
4.2 Nonlinear governing equations . . . 40
4.2.1 Dimensionless form . . . 40
4.2.2 Boundary conditions . . . 41
4.2.3 The osmotic body force . . . 42
4.3 Validation of the numerical solutions . . . 44
4.4 Validation of perturbed cylinder in finite domain . . . 48
4.4.1 Zeroth order solution potential . . . 49
4.4.2 First order solution potential . . . 49
4.4.3 Resulting slip velocity . . . 51
4.5 Numerical analysis of finite Debye-length effects in ICEO . . . 52
4.5.1 Model system: flat center electrode at a wall . . . 53
4.5.2 Full nonlinear model (FN) . . . 53
4.5.3 Slip-velocity models . . . 55
4.5.4 Numerical issues . . . 56
4.5.5 Results of the finite Debye length effects . . . 57
4.5.6 Final remarks . . . 60

5 AC-driven ICEO **61**
5.1 Governing equations for time-averaged AC biased flow . . . 61
5.1.1 Linearized equation system . . . 62
5.1.2 Boundary conditions . . . 63
5.2 Validation . . . 64
5.2.1 Induced dipole strength and zeta potential . . . 65
5.2.2 Electric field . . . 66
5.2.3 Resulting slip velocity . . . 66
5.2.4 Frequency dependence of analytical and numerical solutions . . . 67

6 Topology optimization of ICEO system **69**
6.1 Model system . . . 70
6.2 Governing equations . . . 70
6.2.1 The artificial design field γ used in the topology optimization model of ICEO . . . 71
6.2.2 Dimensionless form . . . 73
6.2.3 Linearized and reformulated equations . . . 74
6.2.4 Boundary conditions . . . 74
6.3 Implementation and validation of numerical code . . . 75

6.3.1 Implementation and parameter values . . . 75
6.3.2 Validation of the γ-dependent ICEO model . . . 76
6.3.3 Validation of the self-consistency of the topology optimization . . . 77
6.4 Results . . . 79
6.4.1 Topology optimization . . . 79
6.4.2 Comparison to simple shapes . . . 81
6.4.3 Shape optimization . . . 82
6.4.4 Comparing topology optimization and shape optimization . . . 84
6.5 Concluding remarks . . . 85

7 Topology optimized chemical microreactors 89
7.1 Mathematical model . . . 90
7.1.1 Reaction kinetics . . . 90
7.1.2 Governing equations . . . 92
7.1.3 Dimensionless form . . . 93
7.2 Topology optimization . . . 94
7.2.1 Physical parameters . . . 94
7.2.2 Geometry and boundary conditions . . . 98
7.2.3 Results . . . 99
7.3 Experimental testing . . . 103

8 Conclusion and outlook 107

A Comsol code 111
A.1 Optmization of ICEO system . . . 111
A.2 Optmization of chemical microreactor . . . 119

B Paper published in Phys. Rev. E 125

C Paper in press in New J. Phys. 131

D Paper submitted to Phys. Rev. E 143

List of Figures

2.1 Schematic overview of the electric double layer 8
2.2 ACEO pumping by asymmetric electrodes 12
2.3 ICEO flow generation 14
2.4 Iterations during topology optimization 21

3.1 Fabricated ACEO electrokinetic micropump 25
3.2 Chip holder used for experimental testing of ACEO micropump 27
3.3 Reproducibility of flow-velocity measurements 30
3.4 Experimentally observed flow reversal 31
3.5 Bode plot of impedance measurements 32
3.6 Equivalent circuit diagram of ACEO micropump 33

4.1 Confined cylinder geometry for DC ICEO system 40
4.2 The dynamic pressure 43
4.3 Overview of integration areas 46
4.4 Finite Debye layer effects for cylinder geometry 47
4.5 Perturbed cylinders 48
4.6 Validation of perturbed cylinder in finite domain 52
4.7 Confined flat electrode geometry for DC ICEO system 54
4.8 Finite Debye layer effects for flat electrode geometry 58
4.9 Finite Debye layer effects for flat electrode geometry 59

5.1 Validation of AC biased averaged flow around cylinder 68

6.1 Model system for topology optimization of ICEO system 71
6.2 Examples of meshing for the topology optimization 76
6.3 Validation of the design-field model 77
6.4 Validation of the self-consistency of the topology optimized solution structures 78
6.5 Topology optimized ICEO system 79
6.6 ICEO pumping for simple symmetry breaking structures 81
6.7 Shape optimized simple polygon structures 82
6.8 Illustration of parametrization used in shape optimization 83
6.9 Shape optimized geometries with optimized topology 85

7.1 Schematics of reaction chamber etch 90
7.2 Post geometry representing porous medium 95
7.3 Reactor geometry 98
7.4 Topology optimized microreactors 99
7.5 Optimality check for optimized microreactors 100
7.6 Fabricated topology optimized microreactors 101
7.7 Fabricated topology optimized microreactors 102
7.8 SEM picture of etched reactor post test structures 104
7.9 SEM picture of etched topology optimized reactor 105

List of Tables

3.1 Dimensions and parameters of the fabricated microfluidic system 26
3.2 Comparison of measured and modeled values of equivalent circuit components 34

4.1 Parameters used in ICEO model of confined DC cylinder geometry 47

6.1 Parameters used in topology optimization of ICEO system 75
6.2 Characteristic physical quantities for topology optimized ICEO geometry . 80
6.3 Resulting flow rates for various ICEO geometries 86

7.1 Gas mixture 95
7.2 Parameter input for reactor model 96
7.3 Gain in reaction rate through optimization 103

List of symbols

Symbol	Description	Unit
$\boldsymbol{r}$	Position vector	m
$\boldsymbol{v}$	Velocity vector	m s^{-1}
v	Velocity	m s^{-1}
u_0	Characteristic velocity	m s^{-1}
l_0	Geometric length scale	m
a	Cylinder radius	m
$\boldsymbol{f}$	Force density	N m^{-3}
$\boldsymbol{\sigma}$	Stress tensor	Pa
p	Pressure	N m^{-2}
η	Viscosity	Pa s
T	Temperature	K
Q	Volume flow rate	m^3 s^{-1}
D	Diffusivity	m^2 s^{-1}
η	Viscosity	Pa s
ρ_m	Mass density	kg m^{-3}
$\boldsymbol{J}$	Flux density	(mol) s^{-1} m^{-1}
k_B	Boltzmann constant	J K^{-1}
$\hat{\boldsymbol{n}}$	Normal vector	-
$\hat{\boldsymbol{t}}$	Tangential vector	-
t	time	s

Symbol	Description	Unit
σ	Conductivity	S m^{-1}
ϕ	Electric potential	V
ϕ	Porosity	-
ζ	Zeta potential	V
λ_D	Debye length	m
ϵ	Dimensionless Debye length	-
β	Dimensionless electrode height	-
α	Dimensionless zeta potential	-
α	Inverse local permeability	Pa s m^{-2}
ε	Permittivity	F m^{-1}
ε_0	Permittivity of vacuum	F m^{-1}
Z	Ionic valence	-
Z	Impedance	Ω
μ	Chemical potential	J
e	Elementary charge	C
c	Ionic concentration	(mol) m^{-3}
q	Charge	C
ρ_{el}	Charge density	C m^{-3}
ρ	Half the charge density	C m^{-3}
ρ	Resistivity	Ω m
$\boldsymbol{E}$	Electric field	V m^{-1}
f	Frequency	Hz
ω	Angular frequency	rad s^{-1}
τ_0, τ_c	RC time	s
V	Voltage	V
C	Capacitance	F
R	Resistance	Ω
γ	Artificial design field	-
Φ	Objective function	-
Ω	Computational domain	

Chapter 1

Introduction

1.1 Background and motivation

Through technological developments in microfabrication, research within the field of lab-on-a-chip technology has flourished and consequently brought about the need for theoretical and experimental investigations of microfluidic systems. The usual liquid manipulation techniques, exploiting turbulent mixing and pressure driven flow, are often inefficient or even not viable for the low-Reynolds-number laminar flows realized in microfluidic devices. Yet, for micro-device length scales, i.e. 10 µm-100 µm, purely diffusive mixing is in most cases very time-consuming and thus impractical. Thus, it is desirable to introduce alternative fluid manipulation methods that preferably can be integrated directly with the microfluidic devices.

Demonstrated in several experiments [1–7], electrokinetic phenomena in microfluidics offer interesting alternatives to the common fluid manipulation techniques as they can be utilized in a range of different non-mechanical tools, which are particularly efficient on the micro-scale. For this reason, the utilization of electrokinetic phenomena for manipulation of minute amounts of liquid has been extensively investigated both theoretically and experimentally.

Although AC-driven elecro-osmotic flow has been utilized as the preferred method of fluid propulsion in the present work, electro-osmotic flows can also be achieved using a DC-source. However, the drawbacks of the latter technique, such as bubble-formation and alterations of pH, makes it is less suitable for lab-on-a-chip applications [6, 8]. Naturally, fluid motion in microchannels can also be realized by means of pressure driven flow or by employing capillary forces, but they collectively lack the degree of flow control and flow profile homogeneity seen for electro-osmotic flows [9, 10].

Prior research of electro-hydrodynamic effects has primarily been carried out in the context of colloids, where experimental and theoretical studies have focused on the electric double layer and induced dipole moments around spheres in electric fields, as reviewed by Dukhin [11] and Murtsovkin [12]. Around the turn of the millennium, experimental and theoretical investigations of AC-driven steady electroosmotic flow were initiated by observations of fluid motion induced by AC electroosmosis over pairs of microelectrodes

[13–16]. A theoretical prediction by Ajdari that the same mechanism would generate flow above an electrode array [17] closely followed by an experimental verification of the pumping mechanism by Brown *et al.* [1], suggested the use of the mechanism for pumping in microfluidic devices. From a microfabrication perspective planar electrodes are easy to fabricate and relatively easy to integrate in existing systems, and for this reason pumping and mixing devices based on the AC electro-osmotic effect has seen great interest. Since 2000, further investigations and theoretical extensions of the models have been published by numerous groups [2–5, 18–25].

Recently, induced-charge electro-osmotic (ICEO) flows around inert, polarizable objects have been observed and investigated theoretically [7, 26–30]. ICEO flow is generated when an external electric field polarizes a solid object placed in an electrolytic solution. The ICEO effect has been reported for both AC and DC forcing, and may be utilized in microfluidic devices for fluid manipulation, as proposed in 2004 by Bazant and Squires [26]. Various simple dielectric shapes have been analyzed analytically for their ability to pump and mix liquids [27]. Experimentally ICEO was observed and the basic model validated against particle image velocimetry in 2005 [28], and later it has been used in a microfluidic mixer, where a number of triangular shapes act as passive mixers [7].

In spite of the growing interest in the literature not all aspects of the flow-generating mechanisms in ICEO have been explained so far. While qualitative agreement is seen between theory and experiment, quantitative agreement is often lacking [7, 25, 31]. The present work seeks to illuminate some of the possible reasons underlying these observed discrepancies.

A numerical tool, topology optimization, has recently become available for the optimization of channel networks in microfluidic systems. The application of the method to microfluidics was suggested by Borrvall and Petterson [32], but topology optimization has been used since the late eighties for improving the stiffness-to-weight ratio of mechanical structures [33]. Since the initial introduction of the method, it has been extended to various physical fields, such as photonic band gap structures in optical waveguides [34], acoustic noise reduction [35], and as mentioned microfluidics. Topology optimization of fluidic channel networks has in particular led to promising results within the field of microreactors. A simplified model of a catalytic reaction has indicated a 20-fold improvement for the total reaction rate in a reactor chamber [36]. However, no experimental verification exists for the application of topology optimization in microreactors or in microfluidics in general.

1.2 Thesis work

Based on the observations in the previous section, the scientific efforts described in this thesis have been focused on three individual, yet closely related, topics within the field of microfluidics, and guided by three main objectives: Characterizing an ACEO microfluidic pumping system, applying advanced numerical simulations to optimize the reaction rate and throughput of a chemical microreactor as well as an ICEO microfluidic system, and furthermore applying these tools to investigate complex ICEO phenomena. A further elab-

oration on the experimental and theoretical work done in order to achieve these objectives is given below.

To gain better understanding of ICEO effects, experimental investigations of an ACEO flow generating device have been carried out; both by actual measurements of the generated pumping, but also by a basic impedance analysis of the electrical circuit. This analysis makes it possible to establish an equivalent circuit model for the device, whereby the purely electrical properties of the ACEO system may be understood independently of the flow generating mechanisms. To achieve a high degree of reproducibility of the measurements it has been chosen to use cleanroom fabricated devices for the experiments.

Furthermore, by design of a topology optimized chemical microreactor and preparation of the experimental fabrication and testing, it has been the goal to establish a basis for the experimental exploitation of topology optimization in microfluidics in general and in chemical microreactors in particular. Optimization of microreactors would especially be advantageous for chemical reactions taking place in the liquid phase, where the diffusive mixing is slow, and in reactors where a higher degree of flow control could increase the production safety.

It has finally been the aim to establish the method of topology optimization for ICEO systems, and use the method to optimize the flow rate, i.e. the pumping efficiency, in a model system. No studies have previously been carried out concerning the impact of topology changes on the mixing or pumping efficiency in these systems, and there is a great potential for optimization of device geometries in existing microfabricated systems. In order to implement the topology optimization method, the electrical double layers in the ICEO model system have been fully resolved, and thereby also provided a more precise understanding of complex ICEO phenomena.

Central to the theoretical part of the work outlined above are the governing equations of convection and diffusion. In addition, kinetics of chemical surface reactions are employed in the optimization of a microreactor, whereas kinetics of surface charge distributions in an electro-hydrodynamic system are essential in optimizing an induced-charge electro-osmotic flow system. Hence, the optimization process for both systems is based on the intricate balance between the coupled effects of surface kinetics and bulk-flows, representing a trade-off between the efficacy and the throughput of the system.

The scientific approach to accomplishing the objectives presented at the beginning of this section can conceptually be described as a circular work process, where experimental data is produced and structured to form a basis for advanced numerical models subsequently utilized in the explanation of other physical phenomena or the prediction of unknown effects, which can then be verified experimentally.

1.3 Outline of the thesis

- **Chap. 2: Basic concepts**
  Concepts known from the literature are presented here to provide a basis for the subjects treated in the subsequent chapters. Especially, the electric double layer is introduced along with the physics of induced-charge electro-osmosis. Additionally,

the numerical tools Comsol and the topology optimization routine are presented.

- **Chap. 3: Experiments on ACEO system**
  The experiments on a microfabricated AC electro-osmotic pump are described. The main part of the chapter has been published in our paper [25]. The focus is on a new observation of flow-reversal at low frequencies and low voltages, and a thorough investigation of the impedance response of the system is also included.

- **Chap. 4: DC-driven ICEO**
  A full nonlinear numerical model of a DC-driven ICEO flow is established and validated against analytical results. The effect of introducing a fully resolved and finite Debye layer in the model is compared to the widely used analytical models based on an assumption of an infinitely thin electrical double layer.

- **Chap. 5: AC-driven ICEO**
  A linearized numerical model of an AC-driven ICEO flow is established and validated against analytical results. This model constitutes the basis for the topology optimization of the system.

- **Chap. 6: Topology optimization of ICEO system**
  Topology optimization is implemented in the governing equations for an AC-driven ICEO system, and the resulting equations are validated against the conventional numerical model. Shapes optimized for liquid pumping with ICEO are presented. The efficiency of the resulting structures is finally compared to the that of simpler ICEO structures and shape optimized ICEO structures.

- **Chap. 7: Topology optimized chemical microreactors**
  A reaction kinetics model for CO oxidation on a platinum catalyst is implemented in the governing convection-diffusion-reaction equations prepared for topology optimization. The platinum distribution is subsequently topology optimized in the reactor chamber of an existing catalytic microreactor. The design of the optimized reactors is presented and the preliminary fabrication is briefly outlined.

1.4 Publications during the PhD studies

Papers in peer reviewed journals

1. *Flow reversal at low voltage and low frequency in a microfabricated ac electrokinetic pump*,
   M. M. Gregersen, L. H. Olesen, A. Brask, M. F. Hansen, and H. Bruus,
   Phys. Rev. E **76**, 056305 (2007)

2. *Topology and shape optimization of induced-charge electro-osmotic micropumps*,
   M. M. Gregersen, F. Okkels, M. Z. Bazant, and H. Bruus,
   New J. Phys. (in press, 2009)

3. *A numerical analysis of finite Debye-length effects in induced-charge electro-osmosis*, M. M. Gregersen, M. B. Andersen, G. Soni, C. Meinhart, T. Squires, and H. Bruus, Submitted to Phys Rev. E (2009)

Conference proceedings

1. *Characterization of flowreversal in anodically boded glass-based AC electrokinetic micropumps*,
   M. M. Gregersen, L. H. Olesen, A. Brask, M. F. Hansen, and H. Bruus,
   MicroTAS 2007, Paris, France, October 2007, proc. vol. 1, pp. 35-37.

2. *Numerical studies of nonlinear kinetics in induced-charge electro-osmosis*,
   M. M. Gregersen, M. Z. Bazant, and H. Bruus,
   ICTAM 2008, Adelaide, Australia, August 2008.

3. *Topology optimization of induced-charge electro-osmotic flows*,
   M. M. Gregersen, F. Okkels, M. Z. Bazant, and H. Bruus,
   APS-DFD08 Meeting, San Antonio, Texas, USA, November 2008.

4. *Microchannel electrokinetics of charged analytes in buffered solutions near floating electrodes*,
   M. B. Andersen, T. Wolfcale, M. M. Gregersen, S. Pannathur, and H. Bruus
   GAMM-2009, Gdansk, Poland, February 2009.

Chapter 2

Basic concepts

The basics of electro-hydrodynamics, our numerical solution method and topology optimization is briefly summarized in the present chapter. The introduced concepts are thoroughly described in the literature [9, 10, 37, 38] and constitute the basis for the work presented in the subsequent chapters.

2.1 Conventional electro-hydrodynamic model

2.1.1 The electrical double layer

In general most materials will acquire a surface charge when brought into contact with an electrolyte. The charge transfer between the material surface and the liquid occur through various mechanisms depending on the chemical composition of the solid and the electrolyte. In microfluidic systems this intrinsic charging of a solid surface is often modified by the application of external electric circuits. Metallic surfaces may be directly biased or external electric fields in the vicinity of the solid may induce an additional polarization of the solid.

Regardless of the specific charging mechanisms, an electrolyte in contact with a charged surface will influence the distribution of nearby ions in the solution. A thin layer with a large excess of counterions is formed near the surface to screen out the potential difference between the surface and the bulk electrolyte. A monolayer of hydrated ions are immobilized at the surface due to the strong electric forces. This layer is termed the compact layer or the Stern layer, and has a typical width λ_S of two solvent molecules, see Fig. 2.1. The remaining, mobile ions of the screening layer are subjected to thermal motions and this part of the layer is therefore called the diffusive layer or the Debye layer. It has a typical length of $\lambda_D \sim 10\,\text{nm}$, depending on the composition of the electrolyte. As one, the compact and diffusive layers are referred to as the electrical double layer. In conventional models of the double layer, the Stern layer is often neglected. This assumption may be applied for low surface-potentials, when the charged surface is bare and in direct contact with the electrolyte. Naturally, the assumption may also be applied when the exact potential of the surface behind the Stern layer is not important. The potential ϕ at the plane between the diffusive layer and the compact layer is called the zeta-potential $\phi = \zeta$ and may then be associated with the surface-potential when the Stern layer is neglected.

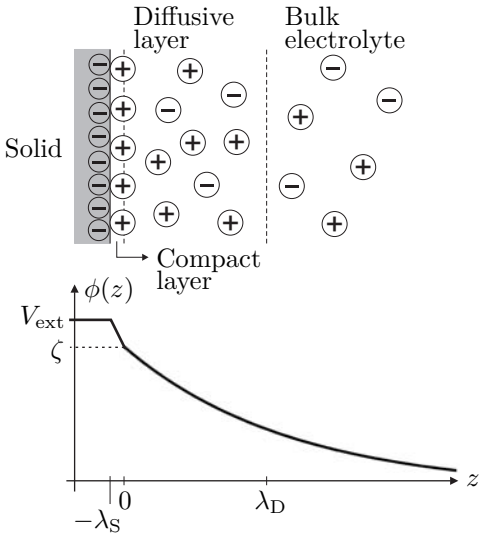

Figure 2.1: Schematic overview of the electric double layer established in an electrolyte near a charged surface. Positive counterions are attracted to the negatively charged solid surface, where they form an electric double layer consisting of a compact layer of width λ_{S} and a diffusive layer of width λ_{D}, which screens out the potential difference between the solid and the charge neutral bulk electrolyte. The graph shows the potential decrease as a function of distance from the charged surface.

Following the usual continuum description of the electro-hydrodynamic system, and assuming and ideal, dilute electrolytic solution, the governing equation for the ionic concentrations c_i is derived from the thermodynamic expression of the chemical potential for the ith species,

$$\mu_i = \mu_0 + Z_i e\phi + k_{\text{B}}T \ln\left(\frac{c_i}{c_0}\right). \tag{2.1}$$

Here e is the elementary charge, Z_i is the valence number, k_{B} is Boltzmanns constant, T is the absolute temperature, c_0 is the bulk ionic concentration for the charge-neutral electrolyte, and μ_0 is the chemical potential in the absence of the electrical potential. For simplicity we consider a symmetrical, binary electrolyte, where the positive and negative ions with concentrations c_+ and c_-, respectively, have the same charge number Z. In equilibrium, where the electrical and thermal forces balance, the gradient of the chemical potential is zero, and Eq. (2.1) leads to a Boltzmann distribution of the ions,

$$c_\pm(\boldsymbol{r}) = c_0 \exp\left[\mp \frac{Ze}{k_{\text{B}}T}\phi(\boldsymbol{r})\right]. \tag{2.2}$$

The electrostatic potential is determined by the charge density $\rho_{\text{el}} = Ze(c_+ - c_-)$ through the Poisson equation

$$\boldsymbol{\nabla} \cdot (\varepsilon \boldsymbol{\nabla}\phi) = -\rho_{\text{el}}. \tag{2.3}$$

For a constant electrolyte permittivity ε, Eqs. (2.2) and (2.3) combines into the nonlinear

Poisson–Boltzmann equation for the potential,

$$\nabla^2\phi(\boldsymbol{r}) = \frac{1}{\lambda_{\mathrm{D}}^2}\frac{k_{\mathrm{B}}T}{Ze}\sinh\left(\frac{Ze\phi}{k_{\mathrm{B}}T}\right). \tag{2.4}$$

In the Debye–Hückel limit the electrical energy is small compared to the thermal energy $Ze\zeta \ll k_{\mathrm{B}}T$, and the Poisson–Boltzmann equation may be linearized to facilitate further analytical studies of the fields,

$$\nabla^2\phi(\boldsymbol{r}) = \frac{2(Ze)^2c_0}{\varepsilon k_{\mathrm{B}}T}\phi(\boldsymbol{r}) \equiv \frac{1}{\lambda_{\mathrm{D}}^2}\phi(\boldsymbol{r}). \tag{2.5}$$

From this linearization a typical screening length for the diffusive layer has been defined and termed the Debye-length

$$\lambda_{\mathrm{D}} = \sqrt{\frac{\varepsilon k_{\mathrm{B}}T}{2(Ze)^2c_0}}. \tag{2.6}$$

It is noted, that the nonlinear Poisson–Boltzmann equation has an analytical solution for one-dimensional systems, the Gouy–Chapmann solution,

$$\phi(z) = \frac{4k_{\mathrm{B}}T}{Ze}\operatorname{artanh}\left[\tanh\left(\frac{Ze\zeta}{4k_{\mathrm{B}}T}\right)e^{-z/\lambda_{\mathrm{D}}}\right]. \tag{2.7}$$

The electrical double layer acts as a capacitor accumulating charge in response to the potential difference between the charged surface and the charge neutral bulk electrolyte. The total amount of charge accumulated in the Debye layer per unit area is from Eq. (2.7),

$$q_{\mathrm{D}} = \int_0^\infty \rho_{\mathrm{el}}\,\mathrm{d}z = \varepsilon\partial_z\phi|_{z=0} = -\frac{\varepsilon}{\lambda_{\mathrm{D}}}\frac{2k_{\mathrm{B}}T}{Ze}\sinh\left(\frac{Ze\zeta}{2k_{\mathrm{B}}T}\right). \tag{2.8}$$

The total potential drop across the Debye layer is $\Delta\phi = \zeta$, thus, the differential Debye layer capacitance becomes,

$$C_{\mathrm{D}} = \frac{\mathrm{d}q_{\mathrm{D}}}{\mathrm{d}\zeta} = -\frac{\varepsilon}{\lambda_{\mathrm{D}}}\cosh\left(\frac{Ze\zeta}{2k_{\mathrm{B}}T}\right). \tag{2.9}$$

On basis of the assumption of a charge free Stern layer, the Stern layer capacitance is assumed to be linear, $C_{\mathrm{S}} = \varepsilon_{\mathrm{S}}/\lambda_{\mathrm{S}}$, where ε_{S} is the permittivity of the Stern layer. The double layer can be treated as two parallel capacitors in series, thus, the total differential capacitance per unit area for the double layer becomes,

$$C_{\mathrm{dl}} = \left\{\frac{1}{C_{\mathrm{S}}} + \frac{\lambda_{\mathrm{D}}}{\varepsilon\cosh[Ze\zeta/(2k_{\mathrm{B}}T)]}\right\}^{-1}. \tag{2.10}$$

In the Debye–Hückel limit the double layer capacitance reduces to

$$C_{\mathrm{dl}} = \left\{\frac{1}{C_{\mathrm{S}}} + \frac{\lambda_{\mathrm{D}}}{\varepsilon}\right\}^{-1}. \tag{2.11}$$

The ratio between the two capacitances depends on the characteristics of the specific system and the variable parameters, such as the electrolyte concentration and the surface potential. For low potentials and a bare electrode in direct contact with the electrolyte, the Debye capacitance dominates the system. Conversely, if the electrode is for instance covered with a thin oxide layer or the voltage exceeds the Debye–Hückel limit, the ratio between the capacitances changes and the contribution from the Stern capacitance may become significant.

The interpretation of the electric double layer as a capacitor can be exploited to analyze electro-hydrodynamic systems in terms of an equivalent circuit diagram. The bulk electrolyte acts as a linear resistor with a resistivity of $1/\sigma$, where σ is the conductivity of the electrolyte. Thus, the basic unit of such a system is the series coupling between the double layer capacitance C_{dl} and the bulk electrolyte resistor R_{b}. This model of the electro-hydrodynamic system especially becomes important when the electrode is biased with an alternating voltage. Then the characteristic time for charging of the double layer through the bulk electrolyte is given as the RC-time of the equivalent circuit $\tau_0 = R_{\mathrm{b}} C_{\mathrm{dl}}$.

2.1.2 Electro-hydrodynamic transport

If the equilibrium balance of the double layer is disturbed, e.g. by gradients in the external potential or by time variations in the potential, the gradient of the chemical potential is no longer zero. The ionic transport is then governed by particle conservation through the continuity equation,

$$\partial_t c_\pm = -\boldsymbol{\nabla} \cdot \boldsymbol{J}_\pm, \tag{2.12}$$

where $\boldsymbol{J}_\pm$ is the flux density of the two ionic species, respectively. The flux densities $\boldsymbol{J}_\pm$ are functions of the chemical potential gradients,

$$\boldsymbol{J}_\pm = -\frac{D}{k_{\mathrm{B}}T}\, c_\pm \boldsymbol{\nabla}\mu_\pm + \boldsymbol{v} c_\pm, \tag{2.13}$$

where it is assumed that the two ionic species $c_\pm$ have the same diffusivity D. For dilute solutions Eq. (2.13) reduces to the Nernst–Planck equation

$$\boldsymbol{J}_\pm = -D\left(\boldsymbol{\nabla} c_\pm + \frac{\pm Ze}{k_{\mathrm{B}}T} c_\pm \boldsymbol{\nabla}\phi\right) + c_\pm \boldsymbol{v}, \tag{2.14}$$

where the first term expresses ionic diffusion and the second term ionic electromigration due to the electrostatic potential ϕ. The last term expresses the convective transport of ions by the fluid velocity field $\boldsymbol{v}$. The fluid velocity field $\boldsymbol{v}$ and pressure p are governed by the continuity equation and the Navier–Stokes equation for incompressible fluids with a body force density $\boldsymbol{f}_{\mathrm{el}} = -\rho_{\mathrm{el}}\boldsymbol{\nabla}\phi$ from the electrical forces acting on the ions in the elctrolyte,

$$\boldsymbol{\nabla} \cdot \boldsymbol{v} = 0, \tag{2.15a}$$

$$\rho_{\mathrm{m}}\Big[\partial_t \boldsymbol{v} + (\boldsymbol{v} \cdot \boldsymbol{\nabla})\boldsymbol{v}\Big] = -\boldsymbol{\nabla} p + \eta \nabla^2 \boldsymbol{v} - \rho_{\mathrm{el}} \boldsymbol{\nabla}\phi, \tag{2.15b}$$

where ρ_m and η are the fluid mass density and viscosity, respectively, both assumed constant. It is noted that the pressure p comprises contributions from both the hydrodynamic pressure and the osmotic pressure, see Sec. 4.2.3.

For a given flow solution, the dimensionless Reynolds number Re characterizes the flow,

$$Re = \frac{\rho_\mathrm{m} u_0 l_0}{\eta}, \tag{2.16}$$

where u_0 and l_0 are the characteristic velocity and length scale of the system, respectively. Due to the small length-scales involved in our microfluidic systems Re is generally much less than unity, and consequently we may neglect the nonlinear inertia term in the Navier–Stokes equation and simply solve the Stokes equation.

For simplicity and due to computational limitations we only consider two-dimensional problems throughout the present thesis, i.e. we assume translational invariance in the third dimension. This implies an infinite channel height in the third dimension, but for aspect ratios of 1:100 or even smaller it remains a good approximation. However, for systems with a stronger limitation in the third dimension, e.g. a shallow channel, we instead apply the Heley–Shaw approximation to account for the resistance exserted by the channel substrate and lid on the fluid flow. This additional shear is calculated by averaging the fluid velocity over the shallow channel height h, and modeling the lowered average velocity with an effective friction force density $\boldsymbol{f} = -\boldsymbol{v} 12\eta/h^2$ added to the Navier–Stokes equation.

2.1.3 electro-osmosis

When an electric field is applied parallel to the charged surface, the ions in the Debye layer electromigrate in the external electric field and drag the entire liquid along by viscous forces. At the outer surface of the double layer a resulting effective slip velocity v_slip is thus established. For a uniformly charged flat surface at $z = 0$ in contact with an electrolyte and with a tangential electric field E_x acting on the charges in the Debye layer, the steady-state Navier–Stokes equation reduces to

$$0 = \eta \partial_z^2 v_x(z) - \varepsilon \partial_z^2 \phi(z)\, E_x. \tag{2.17}$$

Integrating twice and exploiting that $v_x(0) = 0$ and $\phi(0) = \zeta$ at the surface, and $\partial_z v_x = 0$ and $\partial_z \phi = 0$ in the bulk electrolyte, we get

$$v_x(z) = -\frac{\varepsilon E_x}{\eta}\big[\zeta - \phi(z)\big] \tag{2.18}$$

So, the slip velocity at the outer surface of the double layer becomes

$$v_\mathrm{slip} = -\frac{\varepsilon \zeta}{\eta} E_x, \tag{2.19}$$

know as the Helmholtz–Smoluchowski formula. In a generalized formulation, the Helmholtz–Smoluchowski formula becomes

$$\boldsymbol{v}_\mathrm{HS} = -\frac{\varepsilon \zeta}{\eta}\, \boldsymbol{E}_\parallel. \tag{2.20}$$

where $\boldsymbol{E}_{\parallel}$ is the electric field parallel to the surface. In numerical models of electro-osmotic systems it is customary to exploit that the Debye-layer is much thinner than the remaining geometric length scales of the system, by applying this velocity v_{slip} as an effective boundary condition on the fluid velocity field at the electrode surface. In general the slip-condition based model remains valid as long as

$$\frac{\lambda_{\text{D}}}{a} \exp\left(\frac{Ze\zeta}{2k_{\text{B}}T}\right) \ll 1, \tag{2.21}$$

where a denotes the radius of curvature of the surface [37].

2.2 AC electro-osmosis

When the geometric dimensions of a device become small, e.g. in micro and nanofluidic systems, the electro-osmotic effect may be exploited to manipulate minute amounts of liquid. The DC electro-osmosis described above, where an electric field is applied across the channel to drag the ions in the mobile layer along the channel wall, may be directly applied in microfluidic systems, but requires a rather complex setup. The required voltage is relatively high, so electrode reactions will take place and create bubbles, affect the pH-value of the electrolyte etc. Ion exchange membranes may be used, however, the setup will not be very compact [39]. Alternatively, AC electro-osmosis has been proposed and investigated as an alternative flow generation method, during the last decade. In Chap. 3 experimental investigations in an AC electro-osmotic system is described, and below, the

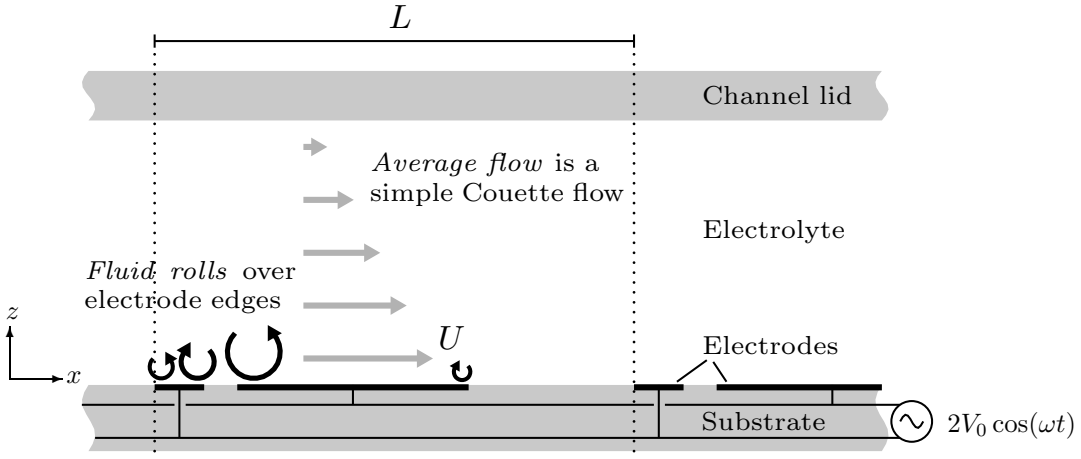

Figure 2.2: Schematic picture of ACEO pumping by asymmetric electrodes, shown in a side-view of the electrolyte filled channel. The widths and spacings for each electrode pair in the electrode array are breaking the left-right symmetry within the translation period L. The electrode array is externally biased with a harmonic oscillating voltage difference $\Delta\phi = 2V_0\cos(\omega t)$, which on average drives a net Couette flow in the horizontal x-direction. However, the actual flow pattern is very complex with flowrolls above the electrode edges. Courtesy of Laurits H. Olesen, DTU Nanotech 2006.

underlying mechanism for the generated flow is briefly outlined. Further discussions of the effect can for instance be found in Refs. [17, 19, 40, 41].

An electrode array on the bottom of an electrolyte filled channel is externally biased with an alternating voltage of $V_{\text{ext}} = \pm V_0 \cos(\omega t)$ on every second electrode, respectively. The double layers formed above the electrode surface partially screen out the electric field, depending on the applied frequency ω. For low frequencies the electric field is completely screened out by the equilibrium double layer, while the double layer is absent for very high frequencies due to the limited ionic mobility. However, for intermediate frequencies, the screening is partial, and the ions in the diffusive layer is affected by the remaining potential field gradients tangential to the electrode surface. Thus, an effective position dependent slip velocity $v_{\text{slip}}(x)$ is established at the electrode surface giving rise to a complex flow pattern with flowrolls above the electrode corners, as indicated at fig. 2.2.

If the left-right symmetry is broken within the electrode translation period, e.g. by introducing asymmetric electrode widths and spacings, the resulting flow pattern, with asymmetric flowrolls established above the electrode edges, gives rise to a net horizontal fluid motion. This resulting flow can be modeled as a simple Couette flow, driven by a constant fluid velocity U above the electrodes determined by time-averaging the slip velocity established at the electrode surfaces.

It is noted, that the AC electro-osmosis and the pumping by asymmetric electrodes may be categorized under the overall effect termed induced-charge electro-osmosis. Squires *et al.* [27] suggest that ICEO should include all electrokinetic phenomena involving a nonlinear flow component in which double-layer charge induced by the applied field is driven by that same field.

2.3 Induced-charge electro-osmosis

Induced-charge electro-osmotic (ICEO) flow is generated when an external electric field polarizes an object in an electrolytic solution. Counter ions in the electrolyte screen out the induced dipole, by forming an electric double layer at the surface of the object. The ions in the Debye layer then electromigrate in the external electric field, and an electro-osmotic flow with a resulting effective slip velocity $\boldsymbol{v}_{\text{slip}}$ is established around the object.

Squires and Bazant [27] have presented an analytical solution to the ICEO flow problem around a metallic cylinder with radius a using a linear slip-velocity model in the two dimensional plane perpendicular to the cylinder axis. The external electric field is assumed to be infinite and parallel to the cartesian, vertical z-axis $\boldsymbol{E} = E_0 \hat{\boldsymbol{z}}$, where $\hat{\boldsymbol{z}}$ is the unit vector in the z-direction. If the electric field is turned on at time $t = 0$, there is at first no screening of the induced dipole field. Solving the Laplace equation $\boldsymbol{\nabla}^2 \phi = 0$ in spherical polar coordinates (r, θ) with the boundary conditions $\phi(r = a) = 0$ and $\phi(r, \theta) \to -E_0 r \sin\theta$ for $r \to \infty$, leads to the well-known potential field

$$\phi_i(r, \theta) = -E_0 z \left[1 - \frac{a^2}{r^2}\right]. \tag{2.22}$$

As time progress, ions are driven into a charge cloud near the conductor surface, and steady-state is reached when the electric field ceases to exist within the evolved electric

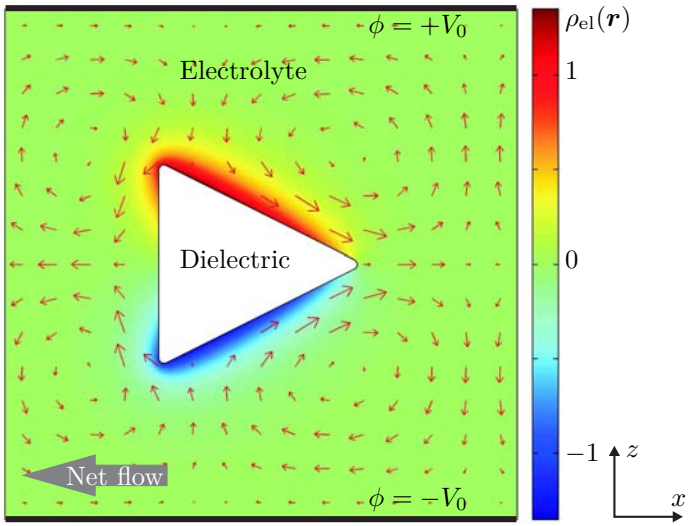

Figure 2.3: Illustration of the ICEO flow generated around an asymmetric dielectric object in an electrolyte subjected to a potential difference $\Delta\phi = 2V_0$ in the vertical z-direction. Electrical double layers are induced at the dielectric surface, shown with the color-plot of the electrical charge density $\rho_{\mathrm{el}}(\boldsymbol{r})$. The induced velocity field (small red arrows) results in a net horizontal flow rate due to the broken left-right symmetry in the system. The fields has been solved numerically by application of the model described in Secs. 4.1 and 4.2, but with periodic boundary conditions on the vertical side walls.

double layer. The slip-velocity model implies an infinitely thin double layer, and thus the effective boundary condition on the potential at the conductor surface becomes $\hat{\boldsymbol{r}} \cdot \boldsymbol{\nabla}\phi|_{r=a} = 0$, where $\hat{\boldsymbol{r}}$ is the radial unit vector. Solving the Laplace equation with this boundary condition and still assuming that the electric field becomes parallel to the z-axis when r approaches infinity, leads to the steady-state potential

$$\phi_s(r,\theta) = -E_0 z\left[1 + \frac{a^2}{r^2}\right]. \tag{2.23}$$

Defining the ζ-potential as the potential difference between the conductor potential $\phi_0 \equiv 0$ and the potential at the outer surface of the Debye layer $\phi_s(r = a)$ results in

$$\zeta(\theta) = -\phi_s(a,\theta) = 2E_0 a \sin\theta. \tag{2.24}$$

The radial component of the electric field is zero at the cylinder surface, while the tangential component $\hat{\boldsymbol{\theta}} \cdot \boldsymbol{E}$ drives the ions in the Debye layer tangentially to the surface. The total electric field is from Eq. (2.23) given as

$$\boldsymbol{E} = -\boldsymbol{\nabla}\phi_s = E_0 \sin\theta\left(1 - \frac{a^2}{r^2}\right)\hat{\boldsymbol{r}} + E_0 \cos\theta\left(1 + \frac{a^2}{r^2}\right)\hat{\boldsymbol{\theta}}. \tag{2.25}$$

The Helholtz–Smoluchowski formula Eq. (2.20) finally leads to the slip velocity at the

cylinder surface $r = a$,

$$\begin{aligned} \boldsymbol{v}_{\text{slip}} &= -\frac{\varepsilon\zeta}{\eta}(\hat{\boldsymbol{\theta}} \cdot \boldsymbol{E})\hat{\boldsymbol{\theta}}, \\ &= -2U_0 \sin(2\theta)\hat{\boldsymbol{\theta}}, \end{aligned} \tag{2.26}$$

where $U_0 = \varepsilon E_0^2 a/\eta$ is the characteristic velocity for the ICEO flow.

The symmetry in the problem of the conducting cylinder in an infinite electric field, results in a spatially symmetric flow field. In the second paper on the same subject by Squires and Bazant [29], it is shown analytically how the introduction of antisymmetry in the system can lead to net motion. Thus, breaking the left-right symmetry of the conducting cylinder problem by introducing a geometrical perturbation of the surface, results in a net fluid motion parallel to the horizontal x-direction, i.e. perpendicular to the externally applied electric field. In this way the cylinder effectively acts as a pump that moves liquid in the horizontal direction. A numerical solution of the generated ICEO flow around a dielectric asymmetric object is shown in Fig. 2.3 to illustrate the effect. For illustrative purposes, the chosen Debye length is very large compared to the rest of the geometrical length scales. The solution is calculated using the model system and equations introduced in Secs. 4.1 and 4.2, but with periodic boundary conditions on the vertical side walls. The top and bottom boundaries are equipotential surfaces with $\phi = \pm V_0$ driving the ICEO flow, which is shown with small arrows. The surface plot displays the electric charge density ρ_{el} scaled according to a characteristic charge density.

Finally, it is noted that an AC field drives an identical flow, since an oppositely directed field induces an oppositely charged screening cloud, resulting in the same net flow.

2.3.1 Finite Debye length for metalic cylinder

For a Debye layer of finite width at the cylinder surface it is possible to write down the potential and ionic concentration fields. Assuming the Debye–Hückel approximation to be valid, the ionic concentration may be linearized as

$$c_\pm = c_0 \mp c_1, \tag{2.27}$$

where the deviation c_1 from the background concentration is minute. Furthermore, assuming the effect from convection to be vanishing the last term of Eq. (2.14) may be neglected and the Nernst–Planck equation becomes

$$J_\pm = \pm D\boldsymbol{\nabla} c_1 \mp D\frac{Zec_0}{k_{\text{B}}T}\boldsymbol{\nabla}\phi. \tag{2.28}$$

The conservation of ions is given by Eq. (2.12), which in steady-state becomes $\boldsymbol{\nabla} \cdot \boldsymbol{J}_\pm = 0$. Combined with the poisson equation (2.3) and the Debye-length Eq. (2.6) we get

$$\boldsymbol{\nabla}^2 c_1 = \frac{1}{\lambda_{\text{D}}^2} c_1. \tag{2.29}$$

Using that the potential approaches $\phi(r, \theta) \to -E_0 r \sin\theta$ and that the concentration deviation c_1 vanishes for $r \to \infty$, the solution of Eq. (2.29) can be expressed by the

decaying modified Bessel function of order 1 K_1. Knowing the concentration c_1, the potential is given by the Poisson equation and the ionic current densities are found by the Nernst–Planck equation. At the conducting cylinder surface $r = a$ the potential is zero $\phi(a, \theta) = 0$, and the ionic current densities vanish in the radial direction $\boldsymbol{J} \cdot \hat{\boldsymbol{r}} = 0$. Given these boundary conditions, the final expressions for the concentration and potential fields becomes

$$c_1(r,\theta) = c_0 \frac{2ZeE_0 a}{k_{\mathrm{B}}T} \frac{K_1\left(\frac{r}{\lambda_{\mathrm{D}}}\right)}{K_1\left(\frac{a}{\lambda_{\mathrm{D}}}\right)} \sin\theta, \tag{2.30a}$$

$$\phi(r,\theta) = -E_0 a \left[\frac{r}{a} + \frac{a}{r} - 2\frac{K_1\left(\frac{r}{\lambda_{\mathrm{D}}}\right)}{K_1\left(\frac{a}{\lambda_{\mathrm{D}}}\right)}\right] \sin\theta. \tag{2.30b}$$

The tangential component of the electric field is then given as $E_{\parallel} = -\hat{\boldsymbol{\theta}} \cdot \boldsymbol{\nabla}\phi$, and the charge density is found from $\rho_{\mathrm{el}} = Ze(c_+ - c_-) = -2Zec_1$,

$$E_{\parallel}(r,\theta) = E_0 \left[1 + \frac{a^2}{r^2} - 2\frac{a}{r} \frac{K_1\left(\frac{r}{\lambda_{\mathrm{D}}}\right)}{K_1\left(\frac{a}{\lambda_{\mathrm{D}}}\right)}\right] \cos\theta, \tag{2.31a}$$

$$\rho_{\mathrm{el}}(r,\theta) = -2\,\frac{\epsilon E_0 a}{\lambda_{\mathrm{D}}^2} \frac{K_1\left(\frac{r}{\lambda_{\mathrm{D}}}\right)}{K_1\left(\frac{a}{\lambda_{\mathrm{D}}}\right)} \sin\theta, \tag{2.31b}$$

2.4 Numerical implementation of governing equations

For our numerical analysis we use the commercial numerical finite-element modeling tool COMSOL [42] controlled by scripts written in MATLAB [43]. We use second-order Lagrange elements for all the fields except the pressure, for which first-order elements suffices. In the following, the basic implementation method for the governing equations is briefly described. Within our research group, several thesis on both M.Sc. and Ph.d. level have been published, and further information about COMSOL implementation aspects may be found in for instance Refs. [40, 42, 44].

In general the partial differential equations must be formulated on divergence form to be used as input in COMSOL. The governing equations of a time independent system must be stated in the form

$$\boldsymbol{\nabla} \cdot \Gamma_l = F_l, \quad \text{in } \Omega, \quad \text{(Governing eq.)} \tag{2.32}$$

being valid in the domain Ω. Here U_l is a vector containing the l dependent variables, while Γ_l and F_l are coefficients, which may be functions of both the dependent and the independent variables as well as their derivatives.

The boundary conditions of the problem in general form are formulated as

$$R_l = 0, \quad \text{on } \partial\Omega, \quad \text{(Dirichlet bc.)} \tag{2.33a}$$

$$-\boldsymbol{n} \cdot \Gamma_l = G_l + \sum_{k=1}^{l} \mu_k \frac{\partial R_k}{\partial U_l}, \quad \text{on } \partial\Omega, \quad \text{(Neumann bc.)} \tag{2.33b}$$

where $\boldsymbol{n}$ is a normal vector to the boundary $\partial\Omega$ of the computational domain Ω, and μ_k is a lagrange multiplier computed internally in COMSOL to fulfill Eq. (2.33b). By specifying the coefficients R_k and G_l either a Dirichlet or a Neumann condition, may be applied at the boundary. If R_k is assigned a value, i.e. a Dirichlet condition is specified for one of the dependent variables, COMSOL determines a value of μ_k that fulfills Eq. (2.33b) and thereby effectively eliminates the equation. On the other hand, if $R_k \equiv 0$, Eq. (2.33a) is trivially fulfilled and the last term of Eq. (2.33b) vanishes. Thus, by specifying G_l a Neumann condition is applied at the boundary. When applying the general formulation it is therefore not possible to enforce both a Dirichlet and a Neumann boundary condition for the same variable simultaneously.

As a concrete example of the implementation method for the governing equations we use Eqs. (2.15), but omit the electric force density for simplicity. Neglecting the left-hand-side of Eq. (2.15b) and applying the general stress tensor formulation, we obtain

$$\boldsymbol{\nabla} \cdot \boldsymbol{v} = 0 \tag{2.34a}$$

$$0 = \boldsymbol{\nabla} \cdot \boldsymbol{\sigma}, \tag{2.34b}$$

where the components of the stress tensor are $\sigma_{lj} = -\delta_{lj}p + \eta(\partial_j u_l + \partial_l u_j)$. This is implemented in general form by defining the vectors

$$\boldsymbol{U} = [u,\ v,\ p], \qquad \boldsymbol{F} = [0,\ 0,\ \partial_x u + \partial_y v], \tag{2.35a}$$

$$\boldsymbol{\Gamma}_u = [\sigma_{xx},\ \sigma_{xy}], \qquad \boldsymbol{\Gamma}_u = [\sigma_{yx},\ \sigma_{yy}], \qquad \boldsymbol{\Gamma}_u = [0,\ 0]. \tag{2.35b}$$

Implemented in the underlying MATLAB controlled script, the equations take the form:

```
fem.form = 'general';
fem.dim = {'u' 'v' 'p'};
fem.expr = {'sigmaxx' '-p+2*ux' 'sigmayx' 'vx+uy' ...
           'sigmaxy' 'uy+vx' 'sigmayy' '-p+2*vy'};
fem.equ.ga = {{{'sigmaxx' 'sigmaxy'} ...
             {'sigmayx' 'sigmayy'} ...
             {'0' '0'}}};
fem.equ.f = {{'0'} {'0'} {'ux+vy'}};
```

In the numerical solutions presented in the following chapters, the strong formulation has been used for the COMSOL implementation. This implementation form is very convenient and has been possible to apply, since it is only necessary to use standard boundary conditions.[1]

[1] The strong formulation with the ideal constraints fails for many common physical systems, e.g. if more than one dependent variable were included in the Dirichlet condition. In that case the more flexible 'weak' implementation form is applied, where a higher degree of control is obtained through the explicitly defined lagrange multipliers.

2.5 Topology optimization

The mathematical method of topology optimization in microfluidic systems is based on the seminal paper by Borrvall and Petersson [32], while the implementation containing the method of moving asymptotes by Svanberg [45, 46] is taken from Olesen, Okkels and Bruus [41]. The topology optimization method is briefly outlined in the following based on the paper by Olesen *et al.* [41], where further details can be found.

Originally, the method of topology optimization for material distribution was developed for improving the stiffness-to-weight ratio of mechanical structures. Later is has been extended to various other fields, including optics, acoustics and fluidics in the Stokes flow regime. The general goal of topology optimization in microfluidic systems, is to determine the most optimal channel network for a given purpose, within a fixed design domain Ω with specified boundary condition on the domain boundary $\partial\Omega$. This is achieved by transforming the discrete problem into a continuous problem through the introduction of a material with spatially varying permeability in the entire design domain. Areas with low permeability then corresponds to the solid channel walls, while areas with high permeability mimic the open channels. During the optimization process the permeability may vary continuously between the two limits, while a discrete solution is preferable as the final result.

In a purely hydrodynamic system, the porous medium is modeled as a spatially varying Darcy friction force on the fluid, given as $\boldsymbol{f} = -\alpha\boldsymbol{v}$, where $\alpha(\boldsymbol{r})$ is the inverse of the local permeability. Thus, the governing steady-state equations becomes

$$\boldsymbol{\nabla}\cdot\boldsymbol{v} = 0, \tag{2.36a}$$

$$\rho_{\mathrm{m}}(\boldsymbol{v}\cdot\boldsymbol{\nabla})\boldsymbol{v} = -\boldsymbol{\nabla}p + \eta\nabla^2\boldsymbol{v} - \alpha\boldsymbol{v}, \tag{2.36b}$$

An artificial design field variable $\gamma(\boldsymbol{r})$ is introduced to model the local permeability. It varies continuously between zero (solid material) and unity (open channels), and is related to the local inverse permeability as

$$\alpha(\gamma) \equiv \alpha_{\min} + \left[\alpha_{\max} - \alpha_{\min}\right]\frac{q(1-\gamma)}{q+\gamma}. \tag{2.37}$$

Here q is a positive penalty parameter employed to control the convex shape of $\alpha(\gamma)$. $\alpha_{\max}$ and $\alpha_{\min}$ are the inverse permeability of the solid walls and open channels, respectively, and it is noted that $\alpha_{\min}$ can be exploited to model the friction force from the Heley–Shaw approximation, as explained above.

The goal or objective of the optimization is stated as the minimization of an objective function

$$\Phi(\boldsymbol{v},\gamma) = \int_\Omega A(\boldsymbol{v},\gamma)\mathrm{d}\boldsymbol{r} + \int_{\partial\Omega} B(\boldsymbol{v},\gamma)\mathrm{d}s, \tag{2.38}$$

where objectives assigned to A and B are minimized inside the fluidic domain Ω and on the domain boundary $\partial\Omega$, respectively. Objectives related to specific points are assigned to A and multiplied with Dirac delta functions.

It is possible to impose an additional volume constraint on the problem, which limits the amount of material to be distributed in the design domain. However, for the systems

treated in the following, it has not been necessary to enforce such a constraint. The problems have been formulated, so the optimal solution structure must contain the right balance between solid and void areas.

To summarize, the optimal design problem can be written as

$$\min_\gamma \ \Phi(\boldsymbol{U}, \gamma) \tag{2.39a}$$

$$\text{subject to :} \ \int_\Omega \gamma(\boldsymbol{r}) \mathrm{d}\boldsymbol{r} - \beta|\Omega| \leq 0, \quad \text{Volume constraint} \tag{2.39b}$$

$$: \ 0 \leq \gamma(\boldsymbol{r}) \leq 1, \quad \text{Design variable bounds} \tag{2.39c}$$

$$: \ \text{Governing equations (incl. bc.)} \tag{2.39d}$$

Here, the volume constraint requires that at least a fraction of $1 - \beta$ of the total volume $|\Omega|$ is covered with porous material.

The formulation of the optimization problem as a continuous design problem, makes it possible to apply efficient mathematical programming routines. In the applied implementation, the Method of Moving Asymptotes (MMA) is exploited. MMA is designed to find minima for large problems with many degrees of freedom. It is a gradient-based algorithm, which require that the gradient of the objective function Φ is calculated with respect to γ. Since the dependent variables $\boldsymbol{U}$ are calculated on basis of the γ-field, $\boldsymbol{U}(\gamma)$ is treated as an implicit function, so using the chain-rule the gradient becomes

$$\frac{\mathrm{d}}{\mathrm{d}\gamma}\{\Phi[\boldsymbol{U}(\gamma), \gamma]\} = \frac{\partial \Phi}{\partial \gamma} + \int_\Omega \frac{\partial \Phi}{\partial \boldsymbol{U}} \cdot \frac{\partial \boldsymbol{U}}{\partial \gamma} \mathrm{d}\boldsymbol{r}. \tag{2.40}$$

The derivative $\partial \boldsymbol{U}/\partial\gamma$ is eliminated from Eq. (2.40) by application of the adjoint method. For a detailed derivation of the calculation scheme and the implementation in Comsol, see Ref. [41] and references therein.

The iteration procedure for the topology optimization can be summarized as follows:

1. An initial guess $\gamma^{(k)}$ for the material distribution is inserted in the governing equations Eqs. (2.36), and they are solved using Comsol.

2. Sensitivity analysis is performed calculating the gradient of the objective and constraints with respect to γ, and the adjoint problem is solved using Comsol.

3. MMA is employed to obtain a new guess $\gamma^{(k+1)}$ for the material distribution.

This iteration routine is continued until convergence, which is typically obtained when $|\Phi^{(k+1)} - \Phi^{(k)}| < 10^{-5}$.

In the original problem formulation by Borrvall and Petersson [32] the existence of a unique optimal solution was proven in the case of minimizing the total power-dissipation inside a fluidic device. Furthermore, it was shown that in the case of a linear function $\alpha(\gamma)$, the optimal material distribution is discrete. However, applying a linear relation of $\alpha(\gamma)$, the severe penalty on the design often result in solutions caught in local minima. Therefore, the convex interpolation of $\alpha(\gamma)$ in Eq. (2.37) is introduced to soften the discrete boundaries of the optimal solution structure, and ease the transition between different topologies, though, it is noted that this method may fail. When objective functions

different from the power-dissipation are applied, there are no proofs for the existence of a unique solution. Thus, for applications involving several coupled fields and other objective functions, there are no guarantee for the existence of a unique optimal solution.

2.5.1 Topology optimization example: Reverse flow in a straight channel

To provide an example of the topology optimization process, we consider a classic and purely hydrodynamic problem, which is simple but serves the purpose of illustration. An elaborated treatment of this example is found in Ref. [41].

The computational domain consists of a long straight channel, where the design area is restricted to the central section of the channel, see Fig. 2.4. A pressure difference applied across the channel in the horizontal x-direction drives a flow along the x-axis, and a no-slip condition is applied at the channel walls. The objective is to minimize the horizontal flow in the point $\boldsymbol{r}^*$ in the center of the channel. This is implemented in Eq. (2.38) by choosing $B = 0$ and $A = v_x(\boldsymbol{r})\delta(\boldsymbol{r} - \boldsymbol{r}^*)$. The problem is optimized in the Stokes limit $Re = 0$, with the Darcy number set to $Da = 10^{-4}$. The value of q is gradually increased during the optimization process, from a low initial value of $q = 0.03$ to a final value of $q = 1$, where $\alpha(\gamma)$ is nearly linear.

Fig. 2.4 shows a number of iterations from the optimization process. Iteration 0 at the top of the figure corresponds to the initial guess of the material distribution, which in this case is $\gamma = 0.99$ in the entire design domain, corresponding to a completely empty channel. The thin gray lines show equidistant contours of the flowrate Q through the channel. Following the optimization process, it is observed how the fluid is first directed around the center point $\boldsymbol{r}^*$ in order to lower the velocity to zero. Subsequently, around iteration 4 a spontaneous symmetry break results in a change of topology towards an inverted S-shaped channel, that reverses the flow in point $\boldsymbol{r}^*$. During the remaining iterations no further large topology changes take place. The inverted S-shape may also come out in a regular S-shape version, depending on minor numerical changes in the system, e.g. a slightly different mesh or numerical noise. It is noted that the solution topology also depends on the chosen Da number, since the optimal barrier thicknesses depend strongly on the resistance exerted by the material on the fluid.

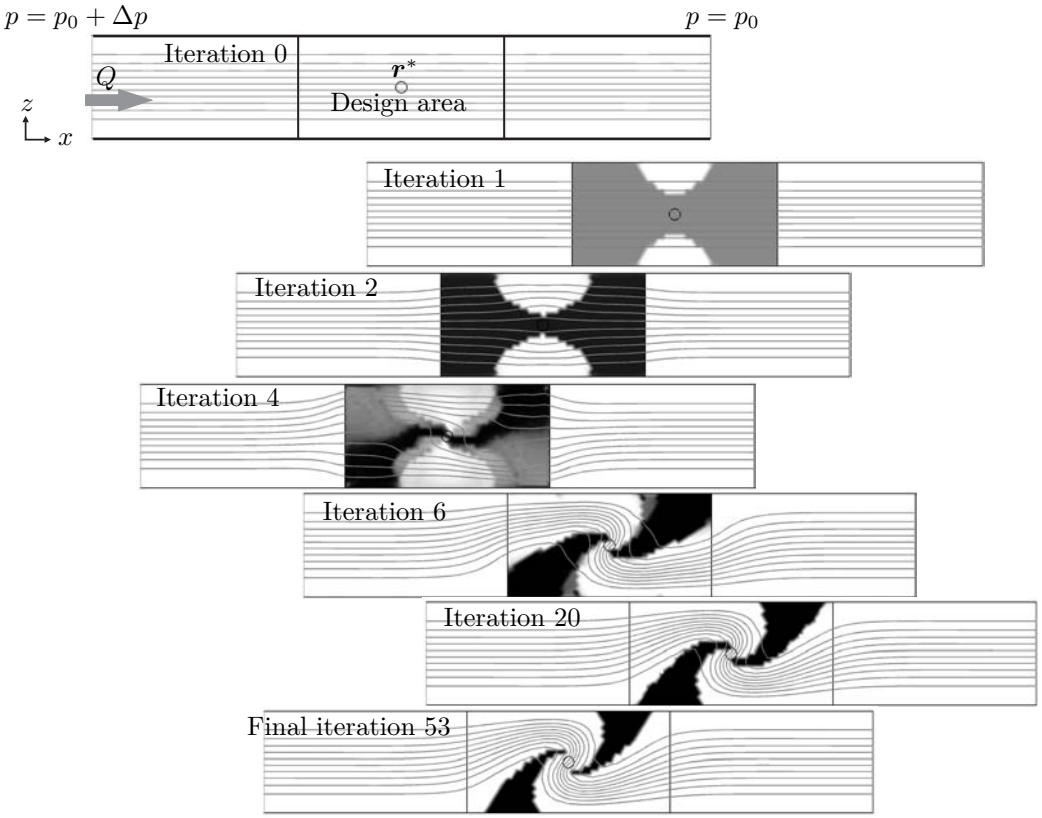

Figure 2.4: A series of iterations from the topology optimization of the reverse flow problem. The top panel shows the starting point of the iteration process. A pressure drop of Δp is applied across the channel driving a Poiseuille flow in the x-direction. The center section of the channel is the design area, where the material distribution $\gamma(\boldsymbol{r})$ is optimized, in order to minimize the horizontal flow in the center point $\boldsymbol{r}^*$. The thin gray lines are equidistant contours of the flow rate. The material porosity is shown as a gray-scale plot, where white corresponds to the limit of open areas with $\gamma = 1$, and black corresponds to the limit of nearly solid material with $\gamma = 0$. As starting point, the design area is nearly empty, corresponding to a constant design field value of $\gamma = 0.99$ (white). The panels below show iterations 1,2,4,6,20 and the final converged iteration 53, of the topology optimization routine, where the optimal S-shaped channel is formed to reverse the flow in the point $\boldsymbol{r}^*$.

Chapter 3

Experiments on ACEO system

During the M.Sc. project by same author [47] an integrated electrokinetic AC driven micropump (Sec. 2.2) was fabricated and initial tests of the system were performed. As part of the present Ph.D work the electrical characterization of the micropump and the measurements of the resulting pump effects were substantially extended and thoroughly analyzed. The work was published in our paper Ref. [25], which broadly comprises this chapter.

Studer *et al.* [3] made a thorough investigation of flow dependence on electrolyte concentration, driving voltage and frequency for a characteristic system. In that work a reversal of the pumping direction for frequencies above 10 kHz and rms voltages above 2 V was reported. For a travelling wave device Ramos *et al.* [5] observed reversal of the pumping direction at 1 kHz and voltages above 2 V. The reason for this reversal is not yet fully understood and the goal of this work is to contribute with further experimental observations of reversing flow for other parameters than those reported previously.

The micropump design follows Studer *et al.* [3], where an effective electrokinetic slip velocity is generated just above an asymmetric array of electrodes that covers the channel bottom in one section of a closed pumping loop. Pumping velocities are measured in another section of the channel without electrodes. In this way electrophoretic interaction between the beads used as flow markers and the electrodes is avoided. In contrast to the soft lithography utilized by Studer *et al.*, we use more well-defined MEMS fabrication techniques in Pyrex glass. This results in a very robust system, which exhibits stable properties and remains functional over time periods extending up to a year. Furthermore, we have a larger electrode coverage of the total channel length allowing for the detection of a given pumping velocity generated by a smaller electrokinetic slip velocity at a lower voltage. Our improved design has led to the observation of a new phenomenon, namely reversal of the flow at at low voltages ($V_{\mathrm{rms}} < 1.5$ V) and low frequencies ($f < 20$ kHz). The electrical properties of the fabricated microfluidic chip have been investigated to clarify whether these reflect the reversal of the flow direction. We propose an equivalent circuit diagram, evaluate it based on the electrical measurements, and conclude that we can rule out trivial circuit explanations of our findings. Supplementary details related to the present work can be found in Ref. [47].

3.1 Experimental

3.1.1 System design

The microchip was fabricated for studies of the basic electrokinetic properties of the system. Hence, a simple microfluidic circuit was designed to eliminate potential side-effects due to complex device issues. The microfluidic chip has a size of approximately 16 mm $\times$ 28 mm and is shown in Fig. 3.1, while the device parameters are listed in Table 3.1. It consists of two 500 μm thick Pyrex glass wafers anodically bonded together. Metal electrodes are defined on the bottom wafer and channels are contained in the top wafer, as illustrated schematically in Fig. 3.1(a). This construction ensures an electrical insulated chip with fully transparent channels.

An electrode geometry akin to the one utilized by Brown *et al.* [1] and Studer *et al.* [3] was chosen. The translation period of the electrode array is 50 μm with electrode widths of $W_1 = 4.2$ μm and $W_2 = 25.7$ μm, and corresponding electrode spacings of $G_1 = 4.5$ μm and $G_2 = 15.6$ μm, see Fig. 3.1(d). Further theoretical investigations have shown that this geometry results in a nearly optimal flow velocity [24]. The total electrode array consists of eight sub-arrays each having their own connection to the shared contact pad, Fig. 3.1(b). This construction makes it possible to disconnect a malfunctioning sub-array. The entire electrode array has a width of 1.3 mm ensuring that the alignment of the electrodes and the 1.0 mm wide fluidic channels is not critical.

A narrow side channel, Fig. 3.1(b), allows beads to be introduced into the part of the channel without electrodes, where a number of ruler lines with a spacing of 200 μm enable flow measurements by particle tracing, Fig. 3.1(c).

An outer circuit of valves and tubes is utilized to control and direct electrolytes and bead solutions through the channels. During flow-velocity measurements, the inlet to the narrow side channel is blocked and to eliminate hydrostatic pressure differences the two ends of the main channel are connected by an outer teflon tube with an inner diameter of 0.5 mm. The hydraulic resistance of this outer part of the pump loop is three orders of magnitude smaller than the on-chip channel resistance and is thus negligible.

In our design the channel has a rectangular cross-section of width $w = 967$ μm and height $H = 33.6$ μm, while the total length is $L_{\mathrm{tot}} = 40.8$ mm. The subsection containing electrodes has the length $L_{\mathrm{el}} = 16.0$ mm and the hydraulic resistance R_1, and here an average slip velocity v_{slip} is generated by electroosmosis just above the electrodes. The subsection containing the measurement channel section has length $L_{\mathrm{tot}} - L_{\mathrm{el}} = 24.2$ mm and hydraulic resistance R_2, and there a Poiseuille flow profile is established with a maximal center-point velocity denoted v_{pois}. In the electrode subsection of the channel the flow rate Q is the sum of a forward Couette flow [19] and a backward Poiseuille flow, $Q = \frac{1}{2}wHv_{\mathrm{slip}} - \Delta p/R_1$, while in the measurement subsection it is a forward Poiseuille flow, $Q = \Delta p/R_2$. By combining these two expressions, the unknown overpressure Δp can be eliminated, and we find $(1 + R_2/R_1)Q = \frac{1}{2}wHv_{\mathrm{slip}}$ or

$$v_{\mathrm{pois}} = \frac{3}{4}\,\frac{1}{(1 - 0.63\frac{H}{w})}\,\frac{L_{\mathrm{el}}}{L_{\mathrm{tot}}}\;v_{\mathrm{slip}} \approx 0.30\,v_{\mathrm{slip}}, \tag{3.1}$$

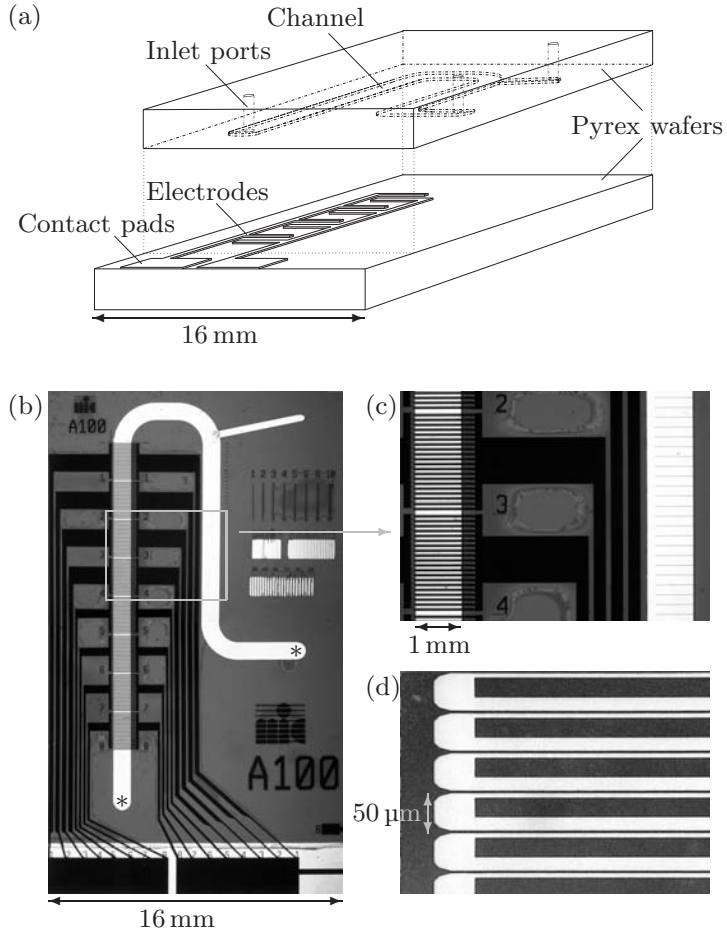

Figure 3.1: (a) Sketch of the fabricated chip consisting of two Pyrex glass wafers bonded together. The channels are etched into the top wafer, which also contains the fluid access ports. Flow-generating electrodes are defined on the bottom wafer. (b) Micrograph of the full chip containing a channel (white) with flow-generating electrodes (black) and a narrow side channel for bead injection (upper right corner). During flow measurements the channel ends, marked with asterisks, are connected by an outer tube. The electrode array is divided into eight sub arrays, each having its own connection to the electrical contact pad. (c) Magnification of the framed area in panel (b) showing the flow-generating electrodes to the left and the measurement channel with ruler lines to the right. (d) Close-up of an electrode array section with electrode translation period of 50 μm.

Table 3.1: Dimensions and parameters of the fabricated microfluidic system.

Channel height	H	33.6 μm
Channel width	w	967 μm
Channel length, total	L_{tot}	40.8 mm
Channel length with electrodes	L_{el}	16.0 mm
Width of electrode array	w_{el}	1300 μm
Narrow electrode gap	G_1	4.5 μm
Wide electrode gap	G_2	15.6 μm
Narrow electrode width	W_1	4.2 μm
Wide electrode width	W_2	25.7 μm
Electrode thickness	h	0.40 μm
Electrode surface area $([W_1 + 2h]w)$	A_1	4.84×10^{-9} m^2
Electrode surface area $([W_2 + 2h]w)$	A_2	25.63×10^{-9} m^2
Number of electrode pairs	p	312
Electrode resistivity (Pt)	ρ	10.6×10^{-8} Ωm
Electrolyte conductivity (0.1 mM)	σ	1.43 mS/m
Electrolyte conductivity (1.0 mM)	σ	13.5 mS/m
Electrolyte permittivity	ε	$80\,\varepsilon_0$
Pyrex permittivity	ε_{p}	$4.6\,\varepsilon_0$

where we have used that for Poiseuille flow in a rectangular channel $Q \approx \frac{2}{3}(1-0.63\frac{H}{w})wHv_{\text{pois}}$ and $1+R_2/R_1 = (R_1+R_2)/R_1 = L_{\text{tot}}/L_{\text{el}}$. So to obtain a given pumping velocity v_{pois} for as low an electrokinetic slip velocity v_{slip} as possible, the electrode coverage ratio $L_{\text{el}}/L_{\text{tot}}$ should be as large as possible. In our system $L_{\text{el}}/L_{\text{tot}} = 0.39$, which almost doubles the sensitivity compared to Studer *et al.* [3], where $L_{\text{el}}/L_{\text{tot}} = 0.21$.

3.1.2 Chip fabrication

The flow-generating electrodes of e-beam evaporated Ti(10 nm)/Pt(400 nm) were defined by lift-off in 1.5 μm thick photoresist AZ 5214-E (Hoechst) using a negative process. Platinum is electrochemically stable and has a low resistivity, which makes it suitable for the application. The thin Ti layer ensures good adhesion of the Pt layer to the Pyrex substrate. By choosing an electrode thickness of $h = 400$ nm, the metallic resistance between the contact pads and the channel electrolyte is at least one order of magnitude smaller than the resistance of the bulk electrolyte covering the electrode array.

In the top Pyrex wafer the channel of width $w = 967$ μm and height $H = 33.6$ μm was etched into the surface using a solution of 40% hydrofluoric acid. A 100 nm thick amorphous silicon layer was sputtered onto the wafer surface and used as etch mask in combination with a 2.2 μm thick photoresist layer. The channel pattern was defined by a photolithography process akin to the process used for electrode definition, and the wafer backside and edges were protected with a 70 μm thick etch resistant PVC foil. The silicon layer was then etched away in the channel pattern using a mixture of nitric acid and

buffered hydrofluoric acid, HNO_3:BHF:H_2O = 20:1:20. The wafer was subsequently baked at 120°C to harden the photoresist prior to the HF etching of the channels. Since the glass etching is isotropic, the channel edges were left with a rounded shape. However, this has only a minor impact on the flow profile, given that the channel aspect ratio is $w/H \approx 30$. The finished wafer was first cleaned in acetone, which removes both the photoresist and the PVC foil, and then in a piranha solution.

After alignment of the channel and the electrode array, the two chip layers were anodically bonded together by heating the ensemble to 400°C and applying a voltage difference of 700 V across the two wafers for 10 min. During this bonding process, the previously deposited amorphous Si layer served as diffusion barrier against the sodium ions in the Pyrex glass. Finally, immersing the chip in DI-water holes were drilled for the in- and outlet ports using a cylindrical diamond drill with a diameter of 0.8 mm.

3.1.3 Measurement setup and procedures

Liquid injection and electrical contact to the microchip was established through a specially constructed PMMA chip holder, shown in Fig. 3.2. Teflon tubing was fitted into the holder in which drilled channels provided a connection to the on-chip channel inlets. The interface from the chip holder to the chip inlets was sealed by O-rings. Electrical contact was obtained with spring loaded contact pins fastened in the chip holder and pressed against the electrode pads. The inner wires of thin coax cables were soldered onto the pins and likewise fastened to the holder.

The pumping was induced by electrolytic solutions of KCl in concentrations ranging from $c = 0.1$ mM to 1.0 mM. The chip was prepared for an experiment by careful injection of this electrolyte into the channel and tubing system, after which the three valves to in- and outlets were closed. The electrical impedance spectrum of the microchip was measured before and after each series of flow measurements to verify that no electrode damaging had occurred during the experiments. If the impedance spectrum had changed, the chip and the series of performed measurements were discarded. Velocity measurements were

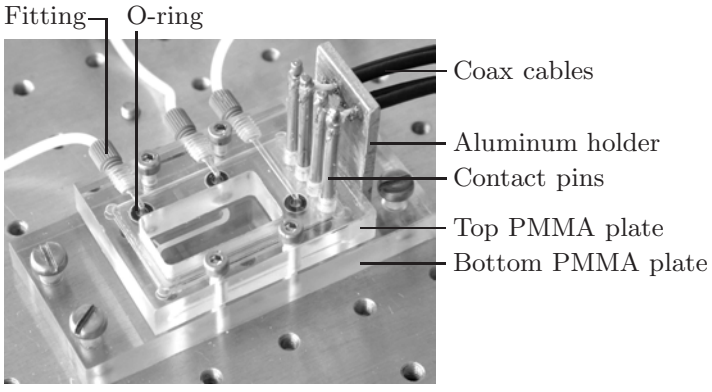

Figure 3.2: Chip holder constructed to connect external tubing and electrical wiring with the microfluidic chip.

only carried out when the tracer beads were completely at rest before biasing the chip, and it was always verified that the beads stopped moving immediately after switching off the bias. The steady flow was measured for 10 s to 60 s depending on the velocity, see Sec. 3.1.5. After a series of measurements was completed, the system was flushed thoroughly with milli-Q water. When stored in milli-Q water between experiments the chips remained functional for at least one year.

3.1.4 AC biasing and impedance measurements

Using an impedance analyzer (HP 4194 A), electrical impedance spectra of the microfluidic chip were obtained by four-point measurements, where each contact pad was probed with two contact pins. Data was acquired from 100 Hz to 15 MHz. To avoid electrode damaging by application of a too high voltage at low frequencies, all impedance spectra were measured at $V_{\mathrm{rms}} = 10$ mV.

The internal sinusoidal output signal of a lock-in amplifier (Stanford Research Systems SR830) was used for AC biasing of the electrode array during flow-velocity measurements. The applied rms voltages were in the range from 0.3 V to 1.5 V and the frequencies between 1.0 kHz and 100 kHz. A current amplification was necessary to maintain the correct potential difference across the electrode array, since the overall chip resistance could be small ($\sim$ 0.1 kΩ to 1 kΩ) when frequencies in the given interval were applied. The current through the microfluidic chip was measured by feeding the output signal across a small series resistor back into the lock-in amplifier.

The lock-in amplifier was also used for measuring impedance spectra for frequencies below 100 Hz, which were beyond the span of the impedance analyzer.

3.1.5 Flow velocity measurements

After filling the channel with an electrolyte and actuating the electrodes, the flow measurements were performed by optical tracing of fluorescent beads suspended in the electrolyte. Instead of the previously employed micro-PIV method [3, 48], we used a simpler, less accurate, but adequate optical particle tracing method for the velocity determination to be described below. We have demonstrated that our method is accurate within 10% for velocities between 10 μm/s and 100 μm/s by the following calibration measurements. A reservoir containing beads suspended in milli-Q water was placed at an adjustable height and connected by teflon tubing to the measurement channel through a partially closed valve. For each setting of the height the resulting hydrostatic pressure generated a Poiseuille flow in the microchannel. After waiting for half an hour to allow for compliant relaxation of the system, the flow velocity v_{pois} was measured using our optical tracing method and compared to the velocity $v_{\mathrm{nfs}} = \frac{3}{2}\, Q/\left[(1 - 0.63\frac{H}{w})wH\right]$ for a rectangular channel deduced from the flow rate Q measured directly by an Upchurch Scientific N-565 Nano Flow Sensor connected to the outlet. The two sets of velocity determinations agree within 10%, see the inset of Fig. 3.3.

For our optical tracing method we introduced fluorescent tracer beads (Molecular Probes, FluoSpheres F-8765) with a diameter $d = 1$ μm into the measurement section

of the channel. The diffusivity of the beads are estimated by using the Stokes–Einstein relation, $D = k_{\mathrm{B}}T/(3\pi\eta\, d) = 4.4 \times 10^{-13}$ m^2/s. The concentration of beads was kept low enough to allow the individual beads to be distinguished, when our Leica MZFLIII Fluorescence Microscope was focused on a section of length 700 μm of the measurement channel using a focal depth in the vertical z-direction slightly larger than the channel depth of 34 μm. With an attached Sony DFW-X710 Digital Camera, we recorded series of pictures of the beads at preset time intervals. We utilize the fact that for a Poiseuille flow in a wide, flat channel all particles in the middle third of the channel, $H/3 < z < 2H/3$, (except those within a distance H of the side walls) move with nearly the same horizontal velocity, namely between 0.9 and 1.0 times the maximal center-point velocity v_{pois}. Due to the size and density of the beads their vertical sedimentation speed and Brownian motion is negligible; it takes 420 s for a bead to fall from $z = 2H/3$ to $z = H/3$ under the influence of gravity and 275 s to diffuse out of that region; no single bead was followed for more than 20 s during our measurements.

The preset time intervals for acquiring pictures of the bead flows were adjusted to the velocity determined by the voltage setting on the electrode array. It ranged from 1.00 s for very low velocities below 15 μm/s to 0.125 s for high velocities around 100 μm/s. The measurement series for a given voltage setting contained between 80 and 600 frames, and for each series the displacements of the fastest moving particles in the 700 μm long field of view were traced over at least 20 frames. The displacement distances Δx we traced, using the in-channel ruler lines, were between 50 μm for the slowest and 200 μm for the fastest beads, while the corresponding measurement times Δt were between 20 s and 2 s. The diffusion length for these times is 1 μm and 3 μm, respectively, leading to relative uncertainties in displacement of 3 μm/50 μm = 6% and 1 μm/200 μm = 0.5% for slowest and fastest particles, respectively. By averaging over ensembles of 10 particles these uncertainties are lowered to 2% and 0.2%, respectively. For a given series it was checked that the selected fastest moving particles (typically 10) all moved with (nearly) the same, constant velocity, and the velocity v_{pois} was determined as the average over the individually determined velocities $\Delta x/\Delta t$. The total statistical uncertainty, mainly due to the vertical bead position and the horizontal Brownian motion, was estimated to be on the order of 10%. This estimate is in good agreement with the calibration measurements described above.

Flow reversal appearing as a result of a change in the bias voltage setting between two measurements, see Sec. 3.2, was thoroughly verified. It was checked that the beads were completely at rest before biasing the chip, and then the forward flow was measured. Subsequently, it was again controlled that the beads were completely at rest when turning off the bias. The bias value was then changed and turned on, and the reverse flow was measured. Finally, the bias was turned off and the beads were once more confirmed to be completely at rest.

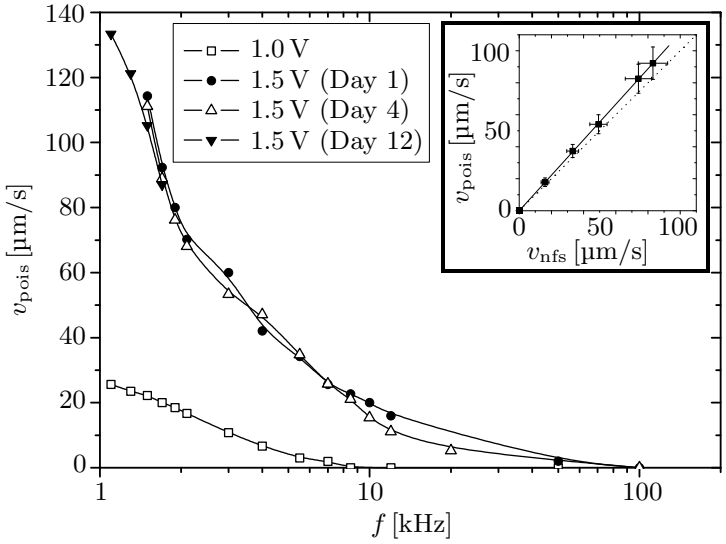

Figure 3.3: Reproducible flow-velocities induced in a 0.1 mM KCl solution and observed at different days as a function of frequency at a fixed rms voltage of 1.5 V. A corresponding series was measured at $V_{\mathrm{rms}} = 1.0$ V. The frequencies are distributed on a $\log_{10}$ scale, and lines have been added to guide the eye. The inset shows the flow velocity v_{pois}, measured using our optical tracing method, versus v_{nfs}, deduced from flow rates measured directly with a nano flow sensor. The linear fit, $v_{\mathrm{pois}} = 1.1\, v_{\mathrm{nfs}}$ (full line), is within 10% of perfect agreement, $v_{\mathrm{pois}} = v_{\mathrm{nfs}}$ (dotted line).

3.2 Results

In the parameter ranges corresponding to those published in the literature, our flow velocity measurements are in agreement with previously reported results. Using a $c = 0.1$ mM KCl solution and driving voltages of $V_{\mathrm{rms}} = 1.0$ V to 1.5 V over a frequency range of $f = 1.1$ kHz to 100 kHz, we observed among other measurement series the pumping velocities shown in Fig. 3.3. The general tendencies were an increase of velocity towards lower frequencies and higher voltages, and absence of flow above $f \sim 100$ kHz. The measured velocities corresponded to slightly more than twice those measured by Studer *et al.* [3] due to our larger electrode coverage of the total channel. We observed damaging of the electrodes if more than 1 V was applied to the chip at a driving frequency below 1 kHz, for which reason there are no measurements at these frequencies. It is, however, plausible that the flow velocity for our chip peaked just below $f \sim 1$ kHz.

3.2.1 Reproducibility of measurements

Our measured flow velocities were very reproducible due to the employed MEMS chip fabrication techniques and the careful measurement procedures described in Sec. 3.1. This is illustrated in Fig. 3.3, which shows three velocity series recorded several days apart. The measurements were performed on the same chip and for the same parameter values. Between each series of measurements, the chip was dismounted and other experiments

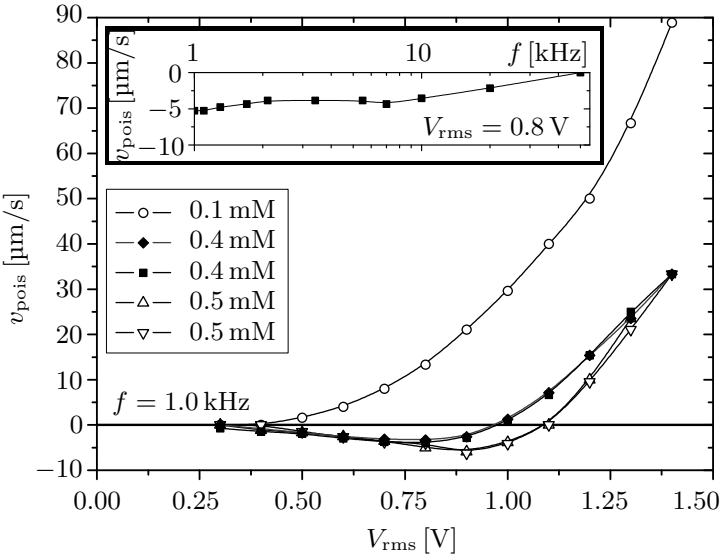

Figure 3.4: Experimentally observed flow reversal for repeated measurements of two concentrations of KCl at 1.0 kHz. The inset shows that for a 0.4 mM KCl solution at a fixed rms voltage of 0.8 V the flow direction remains negative, but slowly approaches zero on a $\log_{10}$ scale for frequencies up to 50 kHz.

performed. However, it should be noted that a very slow electrode degradation was observed when a dozen of measurement series were performed on the same chip over a couple of weeks.

3.2.2 Flow reversal at low voltage and low frequency

Devoting special attention to the low-voltage ($V_{\rm rms} < 1.5$ V), low-frequency ($f < 20$ kHz) regime, not studied in detail previously, we observed an unanticipated flow reversal for certain parameter combinations. This observation was made possible by the large electrode coverage ratio $L_{\rm el}/L_{\rm tot}$ appearing in the expression Eq. (3.1) for $v_{\rm pois}$ in terms of $v_{\rm slip}$.

Fig. 3.4 shows flow velocities measured for a frequency of 1.0 kHz as a function of applied voltage for various electrolyte concentrations. It is clearly seen that the velocity series of $c = 0.1$ mM exhibits the known exclusively forward and increasing pumping velocity as function of voltage, whereas for slightly increased electrolyte concentrations an unambiguous reversal of the flow direction is observed for rms voltages below approximately 1 V.

This reversed flow direction was observed for all frequencies in the investigated spectrum when the electrolyte concentration and the rms voltage were kept constant. This is shown in the inset of Fig. 3.4, where a velocity series was obtained over the frequency spectrum for an electrolyte concentration of 0.4 mM at a constant rms voltage of 0.8 V. It is noted that the velocity is nearly constant over the entire frequency range and tends to zero above $f \sim 20$ kHz.

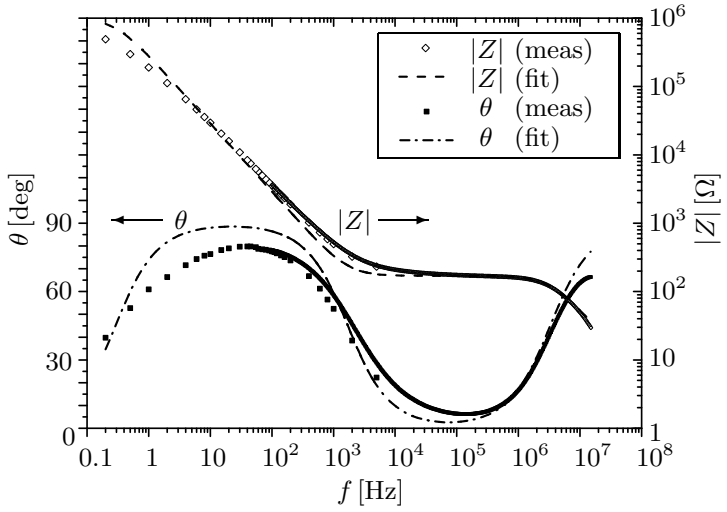

Figure 3.5: Bode plot showing the measured amplitude $|Z|$ on a $\log_{10}$ scale (right ordinate axis) and phase θ (left ordinate axis) of the impedance as a function of frequency over eight decades distributed on a $\log_{10}$ scale from 0.2 Hz to 15 MHz. The voltage was $V_{\mathrm{rms}} = 10$ mV and the electrolyte concentration $c = 1.0$ mM KCl. The measurements are shown with symbols while the curves of the fitted equivalent diagram, see Fig. 3.6, are represented by dashed lines. The measurement series obtained with the impedance analyzer consist of 400 very dense points while the series measured using the lock-in amplifier contains fewer points with a clear spacing.

3.2.3 Electrical characterization

To investigate whether the flow reversal was connected to unusual properties of the electrical circuit, we carefully measured the impedance spectrum $Z(f)$ of the microfluidic system. Spectra were obtained for the chip containing KCl electrolytes with the different concentrations $c = 0.1$ mM, 0.4 mM and 1.0 mM.

Fig. 3.5 shows the Bode plots of the impedance spectrum obtained for $c = 1.0$ mM. For frequencies between $f \sim 1$ Hz and $f \sim 10^3$ Hz the curve shape of the impedance amplitude $|Z|$ is linear with slope -1, after which a horizontal curve section follows, and finally the slope again becomes -1 for frequencies above $f \sim 10^6$ Hz. Correspondingly, the phase θ changes between 0° and 90°. From the decrease in phase towards low frequencies it is apparent that $|Z|$ must have another horizontal curve section below $f \sim 1$ Hz. When the curve is horizontal and the phase is 0°, the system behaves resistively, while it is capacitively dominated when the phase is 90° and the curve has a slope of -1.

3.3 Discussion

As we shall see in the following, our observation of a reproducible and stable flow reversal cannot be explained by the existing theories of induced-charge (AC) electroosmosis, even when faradaic current injection is taken into account as in the most developed theoretical model, the weakly nonlinear electro-hydrodynamic model presented in Ref. [24] and ex-

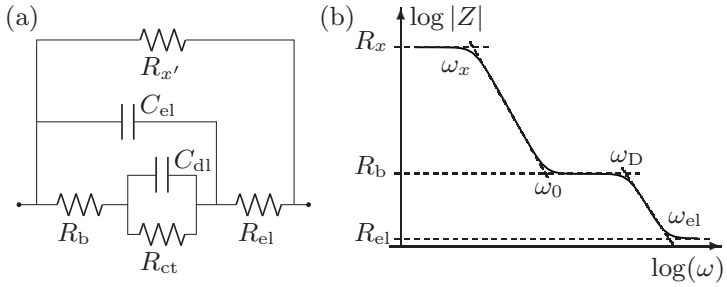

Figure 3.6: (a) Equivalent circuit diagram showing the total electrode resistance R_{el}, the total bulk electrolyte resistance R_{b}, the total faradaic (charge transfer) resistance R_{ct}, the internal resistance of the lock-in amplifier $R_{x'}$, the total electrode capacitance C_{el}, and the total double layer capacitance C_{dl}. (b) Sketch of the impedance amplitude response of the equivalent diagram. It consists of three plateaus, R_{el}, R_{b} and the DC-limit R_x of the total resistance. These are delimited by the four characteristic frequencies the inverse faradaic charge transfer time ω_x, the inverse ohmic relaxation time ω_0, the Debye frequency ω_{D} and the electrode circuit frequency ω_{el}.

tended in Ref. [40], see Sec. 3.3.2. This is not surprising, as this model and other similar models are limited to the weakly nonlinear regime $V \lesssim 0.2$ V. We nevertheless do find some qualitative agreement and discuss the experimentally observed trends of the flow velocities, in particular the flow reversal. The following discussion is included to relate our experimental results to a state-of-the-art theoretical model, and to indicate possible directions for future work in the field.

3.3.1 Equivalent circuit impedance analysis

In electrochemistry the standard way of analyzing impedance measurements is in terms of an equivalent circuit diagram [38]. Based on the Gouy–Chapman–Stern model for the electric double layer, the component values extracted from this analysis are used to estimate three important electrokinetic parameters: the Stern layer capacitance C_{s}, the intrinsic zeta potential ζ_{eq} on the electrodes and the charge transfer resistance R_{ct}.

Following [16,24,49] the basic unit in the diagram Fig. 3.6(a) is a double-layer electrode capacitor in series with a bulk electrolyte resistor and a double-layer counter electrode capacitor. The order of the series components is unimportant, so in the diagram the electrode pair can be placed next to each other. In our system all electrodes are identical except for their widths W_1 and W_2 and thus their respective surface areas A_1 and A_2. However, the important physical parameter, the RC-time due to the charge transfer resistance R and the capacitance C, is independent of the area since $R \propto 1/A$ and $C \propto A$. Consequently, only one RC-time is present in the system due to the electric double layers. As seen in Fig. 3.6(a) this can be represented by one single parallel coupling of C_{dl} (the total capacitance due to accumulation of charge in the double layers at all the electrodes) and R_{ct} (the total resistance due to faradaic current injection from electrochemical reactions at all the electrodes) in series with the bulk electrolyte resistor R_{b}. Moreover, we include the ohmic resistance of the metal electrodes R_{el}, a shunt resistance $R_{x'} = 10$ MΩ to represent the internal resistance of the lock-in amplifier, and the mutual capacitance between the narrow

Table 3.2: Comparison of measured (meas) and modeled (mod) values of the components in the equivalent diagram, Fig. 3.6. The measured values are given by curve fits of Bode plots, Fig. 3.5, obtained on two similar chips labelled A and B, respectively. Due to a minor error on the chip introduced during the bonding process, we were unable to measure R_{ct} for chip B. The modeled values are estimated on basis of Table 3.1 and a particular choice of the parameters ζ_{eq} and C_{s} as follows: The inverse of the total double layer capacitance is $1/C_{\mathrm{dl}} = (1/C_{\mathrm{s}}+1/C_{\mathrm{D}})(1/A_1+1/A_2)/p$, while the bulk electrolyte resistance is $R_{\mathrm{b}} = 0.85/(\sigma w p)$ and the mutual capacitance between the electrodes is $C_{\mathrm{el}} = \frac{p}{0.85}\big[\varepsilon w + \varepsilon_{\mathrm{p}}(2w_{\mathrm{el}} - w)\big]$, where 0.85 is a numerical factor computed for our particular electrode layout using the finite-element based program COMSOL MULTIPHYSICS.

Conc.	R_{b}	R_{b}	R_{el}	R_{el}	R_{ct}	C_{dl}	C_{dl}	C_{el}	C_{el}	ω_{D}	ω_{D}	ω_0	ω_0
	mod	meas	mod	meas	meas	mod	meas	mod	meas	mod	meas	mod	meas
[mM]	[kΩ]	[kΩ]	[Ω]	[Ω]	[MΩ]	[μF]	[μF]	[nF]	[nF]	[M rad s^{-1}]		[k rad s^{-1}]	
0.1 A	2.0	1.0	7.6	5	1.0	0.50	0.50	0.28	0.30	2.0	3.3	1.0	2.0
1.0 A	0.21	0.17	7.6	6	1.0	0.56	0.55	0.28	0.29	19.1	20.6	8.5	10.7
0.1 B	2.0	1.4	7.6	6	–	0.50	0.51	0.28	0.29	2.0	3.0	1.0	1.4
0.4 B	0.52	0.41	7.6	7	–	0.54	0.53	0.28	0.28	7.7	9.3	3.6	4.6
1.0 B	0.21	0.17	7.6	8	–	0.56	0.55	0.28	0.26	19.1	22.6	8.5	10.5

and wide electrodes C_{el}. The latter contains contributions from both the electrolyte and the surrounding glass. However, since it is three orders of magnitude smaller than C_{dl} its precise placement relative to C_{dl} is not important. Finally, since the separation between the electrodes is small and the charge transfer resistance is large, the diffusion-related Warburg impedance [38] can be neglected.

By fitting the circuit model Fig. 3.6(a) to the impedance measurements, see Figs. 3.5 and 3.6(b), we extract the component values listed in Table 3.2 including the four characteristic angular frequencies $\omega = 2\pi f$. The inverse frequency $\omega_x^{-1} = R_x\, C_{\mathrm{dl}}$ primarily expresses the characteristic time for the faradaic charge transfer into the Debye layer. The characteristic time for charging the Debye layer through the electrolyte is given by $\omega_0^{-1} = R_{\mathrm{b}}\, C_{\mathrm{dl}}$. The Debye frequency is $\omega_{\mathrm{D}} = 1/(R_{\mathrm{b}}\, C_{\mathrm{el}})$, and $\omega_{\mathrm{el}} = 1/(R_{\mathrm{el}}\, C_{\mathrm{el}})$ states the characteristic frequency for the on-chip electrode circuit in the absence of electrolyte.

These fitted values can be compared with the modeled values, which are found as explained in Table 3.2, with the following additional remarks regarding the parameters of the electric double layers. Although the impedance measurements were performed at a low voltage of $V_{\mathrm{rms}} = 10$ mV the presence of an intrinsic zeta potential ζ_{eq} of the order of typically 100 mV nevertheless forces us to use the nonlinear Gouy–Chapman–Stern theory, where C_{dl} can be expressed as a series coupling of the compact Stern layer capacitance C_{s} and the differential Debye-layer capacitance C_{D}, see Table 3.2. For simplicity C_{s} is often assumed constant and independent of potential and concentration, while C_{D} is given by $C_{\mathrm{D}} = (\varepsilon/\lambda_{\mathrm{D}})\cosh[\zeta_{\mathrm{eq}} z e/(2k_{\mathrm{B}}T)]$. Indeed, the measured C_{dl} is roughly 10 times larger than predicted by Debye–Hückel theory, which indicates that the intrinsic zeta potential is at least ± 125 mV. Unfortunately, it is not possible to estimate the exact values of both C_{s} and ζ_{eq} from a measurement of C_{dl}, because a range of parameters lead to the same

$C_{\rm dl}$. We can, nevertheless, state lower limits as $C_{\rm s} \geq 0.39$ F/m^2 and $|\zeta_{\rm eq}| \geq 175$ mV for $c = 0.1$ mM or $C_{\rm s} \geq 0.43$ F/m^2 and $|\zeta_{\rm eq}| \geq 125$ mV at $c = 1.0$ mM. For the model values in Table 3.2 we used $C_{\rm s} = 1.8$ F/m^2 and $\zeta_{\rm eq} = 190$ mV, 160 mV and 140 mV at 0.1 mM, 0.4 mM and 1.0 mM KCl, respectively, in accordance with the trend often observed that $\zeta_{\rm eq}$ decreases with increasing concentration [50].

At frequencies above 100 kHz the impedance is dominated by $R_{\rm b}$, $C_{\rm el}$ and $R_{\rm el}$, and the Bode plot closely resembles a circuit with ideal components, see Fig. 3.5. Around 1 kHz we observe some frequency dispersion, which could be due to the change in electric field line pattern around the inverse RC-time $\omega_0 = 1/(R_{\rm b}C_{\rm dl})$ [40]. Finally, below 1 kHz where the impedance is dominated by $C_{\rm dl}$, the phase never reaches 90° indicating that the double layer capacitance does not behave as an ideal capacitor but more like a constant phase element (CPE). This behavior is well known experimentally, but not fully understood theoretically [51].

Overall, we have a fair agreement between the measurements and the equivalent diagram analysis, so we conclude that the observation of flow reversal is not related to any unusual electrical properties of the chip, but must be due to the intrinsic electrokinetic properties of the electrolyte.

3.3.2 Flow analysis

The forward flow velocities measured at $c = 0.1$ mM as a function of frequency, Fig. 3.3, qualitatively exhibit the trends predicted by standard theory, namely, the pumping increases with voltage and falls off at high frequency [17, 19].

More specifically, the theory predicts that the pumping velocity should peak at a frequency around the inverse RC-time ω_0, corresponding to $f \approx 0.3$ kHz, and decay as the inverse of the frequency for our applied driving voltages, see Fig. 11 in Ref. [24]. Furthermore, the velocity is predicted to grow like the square of the driving voltage at low voltages, changing to $V \log V$ at large voltages [24, 40].

Experimentally, the velocity is indeed proportional to ω^{-1} and the peak is not observed within the range 1.1 kHz to 100 kHz, but it is likely to be just below 1 kHz. However, the increase in velocity between 1.0 V and 1.5 V displayed in Fig. 3.3 is much faster than V^2. That is also the result in Fig. 3.4 for $c = 0.1$ mM where no flow is observed below $V_{\rm rms} = 0.5$ V, while above that voltage the velocity increases rapidly. For $c = 0.4$ mM and $c = 0.5$ mM the velocity even becomes negative at voltages $V_{\rm rms} \leq 1$ V. This cannot be explained by the standard theory and is also rather different from the flow reversal that has been observed by other groups at larger voltages $V_{\rm rms} > 2$ V and at frequencies above the inverse RC-time [3, 5, 23].

The velocity shown in the inset of Fig. 3.4 is remarkable because it is almost constant between 1 kHz and 10 kHz. This is unlike the usual behavior for AC electroosmosis that always peaks around the inverse RC-time, because it depends on partial screening at the electrodes to simultaneously get charge and tangential field in the Debye layer. At lower frequency the screening is almost complete so there is no electric field in the electrolyte to drive the electroosmotic fluid motion, while at higher frequency the screening is negligible so there is no charge in the Debye layer and again no electroosmosis.

One possible explanation for the almost constant velocity as a function of frequency could be that the amount of charge in the Debye layer is controlled by a faradaic electrode reaction rather than by the ohmic current running through the bulk electrolyte. Our impedance measurement clearly shows that the electrode reaction is negligible at $f = 1$ kHz and $V_{\rm rms} = 10$ mV bias, but since the reaction rate grows exponentially with voltage in an Arrhenius type dependence, it may still play a role at $V_{\rm rms} = 0.8$ V. However, previous theoretical investigations have shown that faradaic electrode reactions do not lead to reversal of the AC electroosmotic flow or pumping direction [24].

Laurits Højgård Olesen, DTU Nanotech 2006, has been analyzing the flow reversal in terms of an extended theoretical model valid in the weakly nonlinear regime [40]. The model is based on classical approximations for the double layer dynamics and includes Butler–Volmer reaction kinetics for the faradaic electrode reaction, thus, the model is quite comprehensive compared to other published models. Detailed information about the model can be found in Refs. [24, 40]. For the comparison between the theoretical model predictions and the measured flow velocities (Fig. 3.4), the theoretical model parameters has been chosen in accordance with the impedance measurements. The conclusion on this comparison between model and measurements is as follows: The model is able to predict the trends of the experimentally observed velocity curves, but the quantitative agreement is lacking. In the model calculations, the flow reversal is predicted to take place for a frequency ten times higher than the experimentally applied frequency. Furthermore, the predicted reverse flow is weaker than observed experimentally and does not show the almost constant reverse flow profile below 10 kHz. Most important, the model is unable to account for the strong concentration dependence displayed in Fig. 3.4. It is noted though, that a lowering of the ambiguously determined Stern layer capacitance $C_{\rm s}$ in the theoretical model leads to a slight enhancement of the reverse flow. A detailed comparison between the theoretical model and the experimental results in Fig. 3.4 is reported in Ref. [25].

According to Ref. [52], steric effects give rise to a significantly lowered Debye layer capacitance and a potentially stronger concentration dependence when ζ exceeds $10\,k_{\rm B}T/e \sim 250$ mV, which roughly corresponds to a driving voltage of $V_{\rm rms} \sim 0.5$ V. Thus, by disregarding these effects we overestimate the double layer capacitance slightly in the calculations of the theoretical flow velocity for $V_{\rm rms} = 0.8$ V. This seems to fit with the observed tendencies, where theoretical velocity curves calculated on the basis of a lowered $C_{\rm dl}$ better resemble the measured curves.

It should be noted that several electrode reactions are possible for the present system. As an example we mention $2H_2O_{(l)} + O_{2(aq)} + 4e^- \rightleftharpoons 4OH^-_{(aq)}$. This reaction is limited by the amount of oxygen present in the solution, which in our experiment is not controlled. If this reaction were dominating the faradaic charge transfer, the value of $R_{\rm ct}$ could change from one measurement series to another.

In a recent Ph.D. work by García-Sánchez [53] it is suggested that differences in ionic mobilities could lead to the observed flow reversal. They observe a lowering in the pH value of the electrolyte near the positive electrode, which indicates that water reactions leads to a significant increase in the concentration of H^+ ions. For a KCl solution the mobility of the counterions Cl^- is 4.6 times lower than for the H^+ ions. In a linearized model they show how this ionic mobility difference leads to a negative velocity contribution for

frequencies below 10 kHz, and most important, how this negative contribution increases for increasing electrolyte concentration. Their calculation is based on parameter values corresponding to those applied in our system, thus, the effect of mobility difference may be part of the explanation of the flow reversal.

3.4 Summary

We have produced an integrated AC electrokinetic micropump using MEMS fabrication techniques. The resulting systems are very robust and may preserve their functionality over years. Due to careful measurement procedures it has been possible over weeks to reproduce flow velocities within the inherent uncertainties of the velocity determination.

An increased electrode coverage fraction of the channel has lead to an increased sensitivity as reflected in the velocity ratio $v_{\text{pois}}/v_{\text{slip}} = 0.30$. Based on this, a hitherto unobserved reversal of the pumping direction has been measured in a regime, where the frequency and the applied voltage are low ($f < 20$ kHz and $V_{\text{rms}} < 1.5$ V) compared to earlier investigated parameter ranges. This reversal depends on the exact electrolytic concentration and the applied voltage. The measured velocities are of the order -5 μm/s to -10 μm/s. Previously reported studies of flow measured at the same parameter combinations show zero velocity with the given resolution in this regime [3].

Finally, we have performed an impedance characterization of the pumping devices over eight frequency decades. By fitting Bode plots of the data, the measured impedance spectra compared favorably with our model using reasonable parameter values.

The trends of our flow velocity measurements are accounted for by a previously published theoretical model, but the quantitative agreement is lacking. Most of the theoretical models do not predict that the velocities should depend on electrolyte concentration, yet the concentration seems to be one of the causes of our measured low-voltage, low-frequency flow reversal, Fig. 3.4(a). Only recently a connection between electrolyte concentration and flow velocities has been proposed, and there are still need for further theoretical work on the electro-hydrodynamics of these systems.

Chapter 4

DC-driven ICEO

Regardless of the growing interest in the literature, not all aspects of the complex flow-generating mechanisms in ICEO systems have been explained by now. Qualitative agreement is often seen between theory and experiment, however, quantitative agreement is frequently lacking as reported by Gregersen *et al.* [25], Harnett *et al.* [7], and Soni *et al.* [31]. In the present chapter we seek through numerical simulations to illuminate some of the possible reasons underlying these observed discrepancies.

A numerical solution scheme is set up in COMSOL for solving the full nonlinear equation system for a DC-driven ICEO system. The code is validated against the well known analytical result of the ICEO flow around a cylinder in a weak infinite uniform electrical field [27], see Sec. 2.3. A validation is also performed using a corresponding analytical benchmark, where the domain is confined and the shape of the cylinder is slightly perturbed. Since the analytical results are only strictly valid for an infinitely thin Debye layer, i.e. for a Debye-length λ_D much shorter than the cylinder radius a, we investigate for which ratio λ_D/a the deviations between the models becomes negligible.

4.1 Model system

A model system corresponding to the geometry analyzed in the work of Squires *et al* [27] is chosen as starting point for the analysis. A single un-biased dielectric cylinder in a uniform, external electric field is considered. The cylinder of radius a is placed at the center, $(x, z) = (0, 0)$, of a square $2L \times 2L$ domain in the xz-plane filled with an electrolyte, see Fig. 4.1. The system is unbounded and translational invariant in the perpendicular y-direction. The uniform electric field, parallel to the z-axis, is provided by biasing the driving electrodes placed at the edges $z = \pm L$ with the DC voltages $\pm V_0$, respectively. This anti-symmetry in the bias voltage ensures that the potential along the x-axis is zero. A double layer, or a Debye screening layer, is induced around the center dielectric cylinder, and an ICEO flow is generated consisting of four flow rolls. Electric insulating walls at $x = \pm L$ confine the domain in the x-direction. The symmetries of the system around $x = 0$ and $z = 0$ are exploited in the numerical calculations.

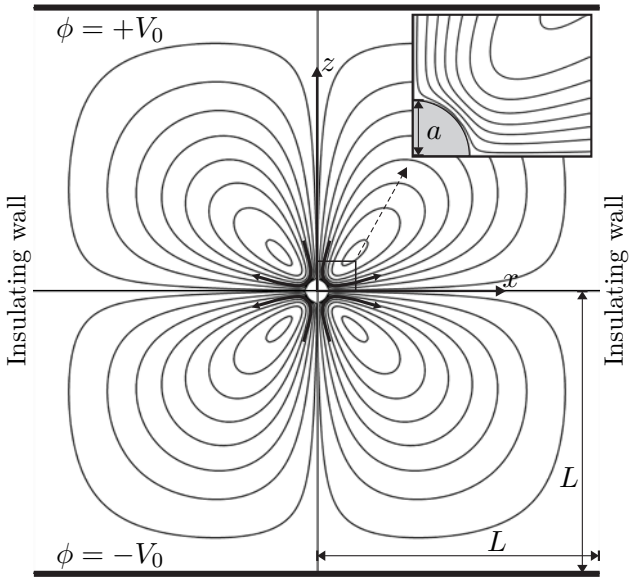

Figure 4.1: A sketch of the square $2L \times 2L$ electrolytic microchamber in the xz-plane. The external voltage is applied to the two electrodes (thick black lines) at $z = \pm L$. It induces a quadropolar flow pattern (curved black arrows) by electro-osmosis around the un-biased dielectric cylinder of radius a placed in the center $(x, z) = (0, 0)$. The spatial extent of the flow rolls is represented by the streamline plot (thin black curves) drawn as equidistant contours of the flow rate. The inset is a zoom-in on the upper right quadrant of the un-biased center electrode and the nearby streamlines.

4.2 Nonlinear governing equations

We follow the conventional continuum approach to the electrokinetic modeling of the electrolytic capacitor [27]. The full non-linear equation system, presented in Chap. 2, is applied to the electrolytic microchamber and only steady-state problems is treated. For simplicity a symmetric, binary electrolyte is considered, where the positive and negative ions with concentrations c_+ and c_-, respectively, have the same diffusivity D and charge number Z.

4.2.1 Dimensionless form

To simplify the numerical implementation, the governing equations are rewritten in dimensionless form, using the characteristic parameters of the system: The radius a of the cylinder, the ionic concentration c_0 of the bulk electrolyte, and the thermal voltage $\phi_0 = k_B T/(Ze)$. The characteristic velocity u_0 is chosen as the Helmholtz–Smoluchowski slip velocity induced by the local electric field $E = \zeta/a$, where the characteristic zeta-potential ζ of the dielectric cylinder is set to $\zeta = \phi_0$ above which value the Debye–Hückel approximation is violated. Finally, the pressure scale is set by the characteristic microflu-

idic pressure scale $p_0 = \eta u_0/a$. In summary,

$$\phi_0 = \frac{k_\mathrm{B}T}{Ze}, \quad u_0 = \frac{\varepsilon\zeta}{\eta}\frac{\zeta}{a} = \frac{\varepsilon\phi_0^2}{\eta a}, \quad p_0 = \frac{\eta u_0}{a}. \tag{4.1}$$

The new dimensionless variables (denoted by a tilde) thus become

$$\tilde{\boldsymbol{r}} = \frac{\boldsymbol{r}}{a}, \quad \tilde{c}_i = \frac{c_i}{c_0}, \quad \tilde{\phi} = \frac{\phi}{\phi_0}, \quad \tilde{\boldsymbol{v}} = \frac{\boldsymbol{v}}{u_0}, \quad \tilde{p} = \frac{p}{p_0}. \tag{4.2}$$

To exploit the symmetry of the system, the governing equations are reformulated in terms of the average ion concentration $c \equiv (c_+ + c_-)/2$ and half the charge density $\rho \equiv (c_+ - c_-)/2$. Correspondingly, the average ion flux density $\boldsymbol{J}_c = (\boldsymbol{J}_+ + \boldsymbol{J}_-)/2$ and half the current density $\boldsymbol{J}_\rho = (\boldsymbol{J}_+ - \boldsymbol{J}_-)/2$ are introduced. Thus, the resulting full system of coupled nonlinear equations takes the following form for the ionic fields

$$\tilde{\boldsymbol{\nabla}} \cdot \tilde{\boldsymbol{J}}_c = \tilde{\boldsymbol{\nabla}} \cdot \tilde{\boldsymbol{J}}_\rho = 0, \tag{4.3a}$$

$$\tilde{\boldsymbol{J}}_c = -\tilde{\rho}\tilde{\boldsymbol{\nabla}}\tilde{\phi} - \tilde{\boldsymbol{\nabla}}\tilde{c} + P\acute{e}\,\tilde{c}\tilde{\boldsymbol{v}}, \tag{4.3b}$$

$$\tilde{\boldsymbol{J}}_\rho = -\tilde{c}\tilde{\boldsymbol{\nabla}}\tilde{\phi} - \tilde{\boldsymbol{\nabla}}\tilde{\rho} + P\acute{e}\,\tilde{\rho}\tilde{\boldsymbol{v}}, \tag{4.3c}$$

$$P\acute{e} = \frac{u_0 a}{D}, \tag{4.3d}$$

while the electric potential obeys

$$\tilde{\boldsymbol{\nabla}}^2\tilde{\phi} = -\frac{1}{\epsilon^2}\tilde{\rho}, \tag{4.4}$$

and finally the fluid fields satisfy

$$\tilde{\boldsymbol{\nabla}} \cdot \tilde{\boldsymbol{v}} = 0, \tag{4.5a}$$

$$Re(\tilde{\boldsymbol{v}} \cdot \tilde{\boldsymbol{\nabla}})\tilde{\boldsymbol{v}} = -\tilde{\boldsymbol{\nabla}}\tilde{p} + \tilde{\boldsymbol{\nabla}}^2\tilde{\boldsymbol{v}} - \frac{\tilde{\rho}}{\epsilon^2}\tilde{\boldsymbol{\nabla}}\tilde{\phi}, \tag{4.5b}$$

$$Re = \frac{\rho u_0 a}{\eta}. \tag{4.5c}$$

Here the small dimensionless parameter $\epsilon = \lambda_\mathrm{D}/a$ has been introduced, where λ_D is the Debye length,

$$\epsilon = \frac{\lambda_\mathrm{D}}{a} = \frac{1}{a}\sqrt{\frac{\varepsilon k_\mathrm{B}T}{2(Ze)^2 c_0}}. \tag{4.6}$$

4.2.2 Boundary conditions

The symmetries around $x = 0$ and $z = 0$ are exploited, and only the upper, right quadrant ($0 < (x, z) < L$) of the domain is considered, see Fig. 4.1. As boundary conditions on the driving electrode we take both ion concentrations to be constant and equal to the bulk charge neutral concentration. Correspondingly, the charge density is set to zero. Consequently, we ignore all dynamics taking place on the driving electrode and simply

treat it as an equipotential surface with the value V_0. We set a no-slip condition for the fluid velocity, and thus at $z = L$ we have

$$\tilde{c} = 1, \quad \tilde{\rho} = 0, \quad \tilde{\phi} = \frac{V_0}{\phi_0}, \quad \tilde{\boldsymbol{v}} = \boldsymbol{0}. \tag{4.7}$$

On the top-down symmetry axis ($z = 0$) the potential and the charge density must be zero due to the anti-symmetry of the applied potential. Moreover, there is neither a fluid flux nor a net ion flux in the normal direction and the shear stresses vanish. So at $z = 0$ the conditions are

$$\tilde{\phi} = 0, \quad \hat{\boldsymbol{n}} \cdot \tilde{\boldsymbol{J}}_c = 0, \quad \tilde{\rho} = 0, \tag{4.8a}$$

$$\hat{\boldsymbol{t}} \cdot \tilde{\boldsymbol{\sigma}} \cdot \hat{\boldsymbol{n}} = 0, \quad \hat{\boldsymbol{n}} \cdot \tilde{\boldsymbol{v}} = 0, \tag{4.8b}$$

where the stress tensor is $(\boldsymbol{\sigma})_{ik} = -p\delta_{ik} + \eta(\partial_i u_k + \partial_k u_i)$, and $\hat{\boldsymbol{n}}$ and $\hat{\boldsymbol{t}}$ are the normal and tangential unit vectors, respectively, which in 2D, contrary to 3D, are uniquely defined. On the left-right symmetry axis ($x = 0$) the same conditions apply for for the fluid velocity and there are no net ion flux in the normal direction. Additionally, the potential field gradient vanishes in the normal direction, thus, at $x = 0$ we have

$$\hat{\boldsymbol{n}} \cdot \tilde{\boldsymbol{\nabla}}\tilde{\phi} = 0, \quad \hat{\boldsymbol{n}} \cdot \tilde{\boldsymbol{J}}_c = 0, \quad \hat{\boldsymbol{n}} \cdot \tilde{\boldsymbol{J}}_\rho = 0, \tag{4.9a}$$

$$\hat{\boldsymbol{t}} \cdot \tilde{\boldsymbol{\sigma}} \cdot \hat{\boldsymbol{n}} = 0, \quad \hat{\boldsymbol{n}} \cdot \tilde{\boldsymbol{v}} = 0, \tag{4.9b}$$

On the dielectric cylinder surface a no-slip condition is applied on the fluid velocity and a no-current condition in the normal direction. For the potential the usual electrostatic boundary conditions apply, so the conditions on the dielectric surface are

$$\hat{\boldsymbol{n}} \cdot \tilde{\boldsymbol{J}}_c = 0, \quad \hat{\boldsymbol{n}} \cdot \tilde{\boldsymbol{J}}_\rho = 0, \qquad \tilde{\boldsymbol{v}} = \boldsymbol{0}, \tag{4.10a}$$

$$\tilde{\phi}_{\text{diel}} = \tilde{\phi}_{\text{fluid}}, \qquad \varepsilon_{\text{diel}}\, \hat{\boldsymbol{n}} \cdot \tilde{\boldsymbol{\nabla}}\tilde{\phi}_{\text{diel}} = \varepsilon_{\text{fluid}}\, \hat{\boldsymbol{n}} \cdot \tilde{\boldsymbol{\nabla}}\tilde{\phi}_{\text{fluid}}. \tag{4.10b}$$

On the solid, insulating walls there are no fluxes in the normal direction, the normal component of the electric field vanishes and there are no-slip on the fluid velocity.

$$\hat{\boldsymbol{n}} \cdot \tilde{\boldsymbol{J}}_c = 0, \quad \hat{\boldsymbol{n}} \cdot \tilde{\boldsymbol{J}}_\rho = 0, \quad \hat{\boldsymbol{n}} \cdot \tilde{\boldsymbol{\nabla}}\tilde{\phi} = 0, \quad \tilde{\boldsymbol{v}} = \boldsymbol{0}. \tag{4.11}$$

4.2.3 The osmotic body force

The osmotic pressure is much larger than the pure hydrodynamic pressure within the double layer, and in this section we analyze how these pressures enters the Navier–Stokes equation. The force $\boldsymbol{F}_\pm$ on a given ion can be expressed as minus the gradient $\boldsymbol{\nabla}\mu$ of the chemical potential Eq. (2.1),

$$\boldsymbol{F}_\pm = -\boldsymbol{\nabla}\mu_\pm = \mp Ze\boldsymbol{\nabla}\phi - \frac{k_{\text{B}}T}{c_\pm}\boldsymbol{\nabla}c_\pm. \tag{4.12}$$

Assuming a complete force balance between each ion and the surrounding electrolyte, the body force density $\boldsymbol{f}_{\text{ion}}$ appearing in the Navier–Stokes equation for the electrolyte due to

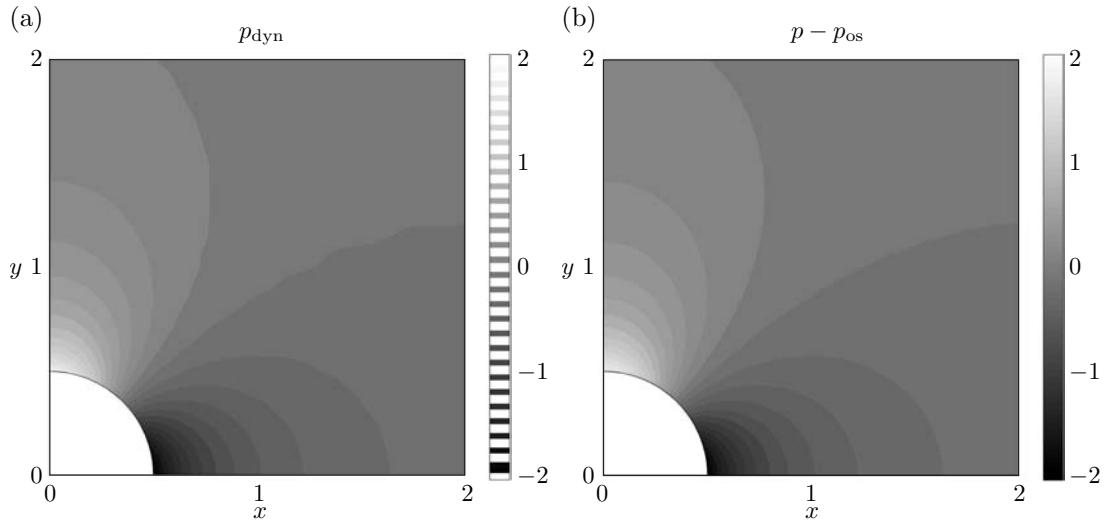

Figure 4.2: The purely hydrodynamic pressure calculated by solving the full nonlinear governing equation system for the geometry shown in Fig. 4.1. (a) The explicitly calculated hydrodynamic pressure $\tilde{p}_{\mathrm{dyn}}$ entering Eq. (4.14). (b) The hydrodynamic pressure contribution calculated as $\tilde{p} - \tilde{p}_{\mathrm{os}} = \tilde{p} - (\tilde{c} - 1)/\epsilon^2$ on basis of the equation set including Eq. (4.5b).

the forces acting on the ions, can be written as the sum of the electric and the osmotic body force density,

$$\boldsymbol{f}_{\mathrm{ion}} = \sum_{i=\pm} c_i \boldsymbol{F}_i = -Ze(c_+ - c_-)\boldsymbol{\nabla}\phi - k_{\mathrm{B}}T\boldsymbol{\nabla}(c_+ - c_-). \tag{4.13}$$

In terms of the average ion concentration c and half the charge density ρ, the dimensionless Navier–Stokes equation then becomes

$$Re(\tilde{\boldsymbol{v}} \cdot \tilde{\boldsymbol{\nabla}})\tilde{\boldsymbol{v}} = -\tilde{\boldsymbol{\nabla}}\tilde{p}_{\mathrm{dyn}} + \tilde{\boldsymbol{\nabla}}^2\tilde{\boldsymbol{v}} - \frac{1}{\epsilon^2}(\tilde{\rho}\tilde{\boldsymbol{\nabla}}\tilde{\phi} + \tilde{\boldsymbol{\nabla}}\tilde{c}), \tag{4.14}$$

where $\tilde{p}_{\mathrm{dyn}}$ is a purely hydrodynamic pressure. For the undisturbed salt concentration $\tilde{c} = 1$ the osmotic pressure p_{os} is absent, thus, it is natural to define $\tilde{p}_{\mathrm{os}}$ as the scalar field

$$\tilde{p}_{\mathrm{os}} \equiv \frac{1}{\epsilon^2}(\tilde{c} - 1). \tag{4.15}$$

Hence, the Navier–Stokes equation becomes

$$Re(\tilde{\boldsymbol{v}} \cdot \tilde{\boldsymbol{\nabla}})\tilde{\boldsymbol{v}} = -\tilde{\boldsymbol{\nabla}}(\tilde{p}_{\mathrm{dyn}} + \tilde{p}_{\mathrm{os}}) + \tilde{\boldsymbol{\nabla}}^2\tilde{\boldsymbol{v}} - \frac{1}{\epsilon^2}\tilde{\rho}\tilde{\boldsymbol{\nabla}}\tilde{\phi}, \tag{4.16}$$

where the total pressure is $\tilde{p} = \tilde{p}_{\mathrm{dyn}} + \tilde{p}_{\mathrm{os}}$.

Consequently, in analogy with the gravitational potential energy density and the hydrostatic pressure, the osmotic effect can either appear explicitly as a body force $\boldsymbol{f}_{\mathrm{os}} = -\boldsymbol{\nabla}\tilde{c}/\epsilon^2$ or it can be absorbed into the pressure gradient term,

$$\tilde{\boldsymbol{\nabla}}\tilde{p} = \tilde{\boldsymbol{\nabla}}\tilde{p}_{\mathrm{dyn}} + \tilde{\boldsymbol{\nabla}}\tilde{p}_{\mathrm{os}}. \tag{4.17}$$

To check the result numerically, we use the model system described in Sec. 4.1, and solve the full nonlinear governing equations including either Eq. (4.5b) or Eq. (4.14) for the Navier–Stokes equation. The ratio between the domain half-height L and the cylinder diameter a is set to $L/a = 10$, while the dimensionless Debye length is set to $\epsilon = 0.01$. The potential difference across the cylinder diameter is $0.1\phi_0$, where ϕ_0 is the thermal voltage, ensuring that the calculation is performed in the Debye–Hückel regime. In Fig. 4.2 the purely hydrodynamic pressure contribution has been plotted for each of the numerical solutions in the area close to the cylinder. Panel (a) shows the explicitly calculated $\tilde{p}_{\mathrm{dyn}}$ entering Eq. (4.14), while panel (b) is a plot of $\tilde{p} - \tilde{p}_{\mathrm{os}} = \tilde{p} - (\tilde{c} - 1)/\epsilon^2$ calculated on basis of the equation set including Eq. (4.5b). It is clearly seen, that there is full agreement between the two solutions. Consequently, the explicit body force density arising from the osmotic pressure of the ions, may be treated implicitly through the total pressure in the electrolyte. In the following, we only calculate the total pressure $\tilde{p}$.

4.3 Validation of the numerical solutions

To validate the numerical solutions of the model system presented above, the analytical flow solution presented by Squires and Bazant in Ref. [27] is used as benchmark. In their analytical work the geometry corresponds to the one defined above, but the electrical background field extends to infinity and the double layer is assumed to be infinitely thin. These limits are not directly realizable in the numerical solution scheme, so instead the convergence of the numerical solutions toward the limiting analytical solution is checked. The comparison between the analytical and numerical flow solutions can be carried out in different ways. At least three parameters can be employed for the comparison; the generated slip velocity immediately outside the Debye-layer, the generated kinetic energy around the cylinder, or the total kinetic energy dissipation from the resulting velocity field in the bulk electrolyte. In Fig. 4.4 these three different methods have been employed to compare the numerical results with corresponding the analytical values as functions of both the relative double layer width $\epsilon = \lambda_{\mathrm{D}}/a$ and the total domain size $2L$.

The slip velocity is uniquely defined for the analytical solution as the Helmholtz-Smoluchowski slip-velocity at the cylinder surface $v_{\mathrm{slip}} = 2u_0 \sin\theta$, where $u_0 = \varepsilon E_0^2 a/\eta$, see Sec. 2.3. For the numerical solution, however, the double layer is fully resolved, and it is not obvious to decide where the slip velocity should be measured. In this case, the magnitude of the fluid velocity grows up from zero at the cylinder boundary $r = a$ to a maximum at approximately $r = a + 3\lambda_{\mathrm{D}}$, whereafter it decays into the bulk electrolyte. Since the slip velocity is maximal at angles $\theta = n_{\mathrm{odd}}\pi/4$, where n_{odd} are odd integers, we choose to define the numerical slip velocity as the maximal velocity tangential to the cylinder surface along the radial direction $(r, \theta) = (r, \pi/4)$, i.e.

$$\boldsymbol{v}_{\mathrm{slip}} = \max\big[\, \boldsymbol{v}(r, \pi/4) \cdot \hat{\boldsymbol{t}} \,\big], \tag{4.18}$$

where $\hat{\boldsymbol{t}}$ is the tangential vector to the cylinder surface.

Alternative to the direct slip velocity comparison, the total kinetic energy of the in-

duced flow field $\boldsymbol{v}$ is independent of the local velocity profile in the double layer.

$$E_{\text{kin}} = \tfrac{1}{2}\rho_{\text{m}} \int_{\Omega} v^2 \,\mathrm{d}x\,\mathrm{d}z, \tag{4.19}$$

Numerically, this parameter is beneficial, since it depends directly on the velocity field and not its gradients, and furthermore it is a bulk integral of good numerical stability. Nevertheless, the total kinetic energy is not well defined for the analytical flow solution, since the integral of the squared velocity field across the infinite plane diverges. The comparison between the two models can still be performed, though, by introducing a cut-off radius $r = R_0$ for the calculation of the kinetic energies in both models. The analytical expression for the kinetic energy then becomes

$$E_{\text{kin}} = -\tfrac{1}{2}\rho_{\text{m}} \left[\frac{2a^2\pi u_0^2 \{(a^2 - R_0^2)^2 - 2R_0^4 \ln(\frac{R_0}{a})\}}{R_0^4} \right] \tag{4.20}$$

The energy dissipation in the bulk electrolyte can also be used as a comparable parameter for the two models. In the analytical model with its infinitely thin double layer, the surrounding electrolyte is charge neutral, and hence the strength of the ICEO flow can be defined solely in terms of the hydrodynamic stress tensor $\boldsymbol{\sigma}$, as the mechanical power P_{mech} exerted on the electrolyte by the tangential slip-velocity $v_{\text{slip}}\hat{\boldsymbol{t}}$

$$P_{\text{mech}} = \oint_{|\boldsymbol{r}|=a} \hat{\boldsymbol{n}} \cdot \boldsymbol{\sigma} \cdot \hat{\boldsymbol{t}}\, v_{\text{slip}} \mathrm{d}a, \tag{4.21}$$

where $\hat{\boldsymbol{n}}$ and $\hat{\boldsymbol{t}}$ is the normal and tangential vector to the cylinder surface, respectively. In steady flow, this power is equal to the total kinetic energy dissipation P_{kin} of the resulting quadrupolar velocity field in the electrolyte. In cartesian coordinates P_{kin} for an incompressible fluid is given as

$$P_{\text{kin}} = \tfrac{1}{2}\eta \int_{a<|\boldsymbol{r}|} (\partial_i v_j + \partial_j v_i)^2 \mathrm{d}\boldsymbol{r}. \tag{4.22a}$$

Exploiting that the trace of a tensor is invariant under coordinate transformation, we get the following expression for P_{kin} in polar coordinates [54],

$$P_{\text{kin}} = \frac{1}{2\eta} \int_{a<|\boldsymbol{r}|} \mathrm{Tr}(\boldsymbol{\sigma}^2) \mathrm{d}\boldsymbol{r} = \frac{1}{2\eta} \int_{a<|\boldsymbol{r}|} (\sigma_{rr}^2 + 2\sigma_{r\theta}^2 + \sigma_{\theta\theta}^2) r \mathrm{d}r \mathrm{d}\theta = 16\pi\eta u_0^2. \tag{4.22b}$$

The analytical expression for the flow field in cylindrical coordinates leads to the following value of the mechanical power per unit length in the y-direction,

$$P_{\text{mech}} = \oint_{|\boldsymbol{r}|=a} \hat{\boldsymbol{r}} \cdot \boldsymbol{\sigma} \cdot \boldsymbol{v}_{\text{slip}} r \mathrm{d}\theta = a \int_0^{2\pi} \sigma_{r\theta} v_\theta \mathrm{d}\theta = -16\pi\eta u_0^2. \tag{4.23}$$

Here $\hat{\boldsymbol{r}}$ is the unit vector in the radial direction. Indeed, the expression for the kinetic energy dissipation leads to the same absolute value.

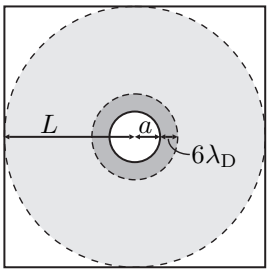

P_{kin}: $a + 6\lambda_{\text{D}} < r < L$
$E_{\text{kin}}(a + 6\lambda_{\text{D}})$: $a < r < a + 6\lambda_{\text{D}}$
$E_{\text{kin}}(L)$: $a < r < L$

Figure 4.3: Overview of the integration areas used in the calculations of the graphs shown in Fig. 4.4.

First, in the full double-layer resolving simulation we determined the value $P^*_{\text{mech}}(R_0) = \oint_{|\boldsymbol{r}|=R_0} \hat{\boldsymbol{n}}\cdot\boldsymbol{\sigma}\cdot\boldsymbol{v}\,\mathrm{d}a$ of the mechanical input power, where R_0 is the radius of a cylinder surface placed co-axially with the metallic cylinder. Then, as expected due to the electrical forces acting on the net charge in the double layer, we found that $P^*_{\text{mech}}(R_0)$ varied substantially as long as the integration cylinder surface was inside the double layer. For $R_0 \approx a+6\lambda_{\text{D}}$ the mechanical input power stabilized at a certain value. However, since surface integrals are generally more numerical stable, the corresponding kinetic energy dissipation $P^*_{\text{kin}}(R_0) = \frac{1}{2}\eta\int_{R_0<|\boldsymbol{r}|}(\partial_i v_j + \partial_j v_i)^2\mathrm{d}\boldsymbol{r}$ is employed for the comparison with the analytical result.

Fig. 4.4 (a) shows how the confinement of the domain influences the numerical solutions. The full nonlinear equation system has been solved for increasing values of the domain width L, and each of the above outlined comparable parameters P_{kin}, E_{kin} and v_{slip} has been calculated. For the kinetic energy dissipation P_{kin} the integral has been evaluated on the entire domain outside the co-axially placed cylinder surface of radius $R_0 = a + 6\lambda_{\text{D}}$. The generated kinetic energy has been calculated for two different cut-off radii of $R_0 = a + 6\lambda_{\text{D}}$ and $R_0 = L$, respectively. An overview of the different integration areas is given in Fig. 4.3. The physical parameter values and corresponding dimensionless values used as input in the model are displayed in Table 4.1.

It is noted that the problem is formulated well below the Debye–Hückel limit with a voltage drop of $0.05\phi_0$ across the cylinder to meet the approximations of the analytical model. The curves in Fig. 4.4 (a) are the relative differences of the parameter values $[E_{\text{kin}}(L_i) - E_{\text{kin}}(L_{i+1})]/E_{\text{kin}}(L_i)$ plotted as function of L_i, where i is an index indicating the numerical solution for increasing values of L, and the numerical parameter values E_{kin} have been divided by the corresponding analytical parameter value. From this plot the confinement effects seams vanishing when the domain exceeds a size of $L = 25a$, where all relative differences are below 0.5%. A domain of $L = 15a$ is enough if we use v_{slip}, P_{kin} or the generated kinetic energy inside the double layer $E_{\text{kin}}(r < a + 6\lambda_{\text{D}})$.

In Fig. 4.4 (b) the analytical and numerical results are compared for a domain of half-width $L = 25a$. The full non-linear equation system with fully resolved double layer has been solved for a series of ϵ values. Each of the parameters P_{kin}, E_{kin} and v_{slip} have been calculated for the numerical solution and normalized by the corresponding analytical value, i.e. full agreement between the two models would give the value unity. The cut-off radii and integration limits are the same as for Fig. 4.4 (a) and the input parameters of

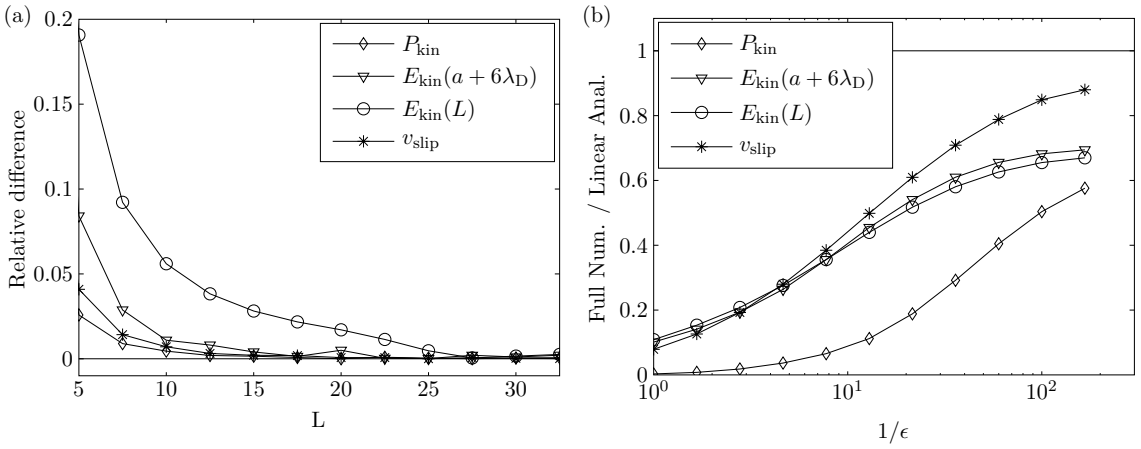

Figure 4.4: Plots of the kinetic energy dissipation P_{kin}, the generated kinetic energy for two different cut-off radii, $E_{\text{kin}}(r < a + 6\lambda_{\text{D}})$ and $E_{\text{kin}}(r < L)$, and the slip velocity v_{slip}. (a) Plot of the relative differences calculated as $[E_{\text{kin}}(L_i) - E_{\text{kin}}(L_{i+1})]/E_{\text{kin}}(L_i)$ as function of an increasing domain size L_i. (b) Plots of the four parameters divided by their corresponding analytical values as function of the inverse dimensionless Debye length $1/\epsilon$. The value of ϵ decreases from 1 to 3×10^{-3} going from left to right.

Table 4.1 has been used. The numerical values are significantly lower than the analytical values, but the discrepancies decrease for decreasing values of $\epsilon = \lambda_{\text{D}}/a$. Remarkably, even for a quite thin Debye layer, $\lambda_{\text{D}} = 0.01\,a$, the values of the full numerical simulation are at least about 20% lower than the analytical value, depending on the compared parameter. Clearly, the analytical model overestimates the ICEO effect, and the double-layer width must be extremely thin before the simple analytical model agrees well with the full model.

Table 4.1: Parameters used in the simulations of the conventional ICEO model of the generated flow around a dielectric cylinder in an electrolyte between by two DC biased capacitor plates in a confined square domain.

Parameter	Symbol	Dimensionless value	Physical value
Cylinder radius	a	1.0	125 nm
Domain half-length and half-height	L	50.0	6.25 µm
Linear Debye length	λ_{D}	0.01	1.25 nm
Characteristic velocity	u_0	1.0	3.5×10^{-3} m/s
Characteristic potential	ϕ_0	1.0	25 mV
External potential amplitude	V_0	1.25	32 mV
Bulk fluid permittivity	$\varepsilon_{\text{fluid}}$	1.0	$78\,\varepsilon_0$
Dielectric permittivity	$\varepsilon_{\text{diel}}$	1.3×10^4	$10^6\,\varepsilon_0$
Bulk ionic concentration	c_0	1.0	58 mM
Fluid viscosity	η	1.0	10^{-3} Pas
Ionic diffusion constant	D	1.0	$2 \times 10^{-9}\,\text{m}^2/\text{s}$

The discovered discrepancies presented above have become the primary motivation for the study presented in our paper Ref. [30], where a much more extensive numerical investigation of these discrepancies have been carried out. In Sec. 4.5 the main results from this paper is presented.

4.4 Validation of perturbed cylinder in finite domain

To further validate our numerical simulations, we solve the potential and slip velocity around a perturbed cylinder in a square domain confined by two capacitor plates, corresponding to the geometry shown in Fig. 4.1. Assuming an infinitely thin Debye layer at the cylinder surface leaves the bulk electrolyte charge neutral and the Laplace equation valid for the potential in the entire domain. The Laplace equation is solved using perturbation theory and the solution potential then leads to the slip-velocity at the cylinder surface by insertion in the Helmholtz–Smoluchowski formula Eq. (2.20). The corresponding problem is subsequently solved using the conventional ICEO model with fully resolved double layer and compared to the analytical solution.

The radius of the perturbed cylinder, see Fig. 4.5, is chosen as

$$R = a\big[1 + \alpha\cos(3\theta)\big]. \tag{4.24}$$

The plates at $z = \pm L_y$ are symmetrically biased $\phi = \pm V_0$, and on the vertical side walls $x = \pm L_x$ a linear potential $\phi = V_0 z/L$ is assumed. We exploit the symmetry around $z = 0$, and use the boundary condition $\phi = 0$ at the symmetry line. The general solution to the Laplace equation in cylindrical coordinates is given by

$$\phi(r,\theta) = A_0 + B_0 \ln r + \sum_{n=1}^{\infty} \big[A_n r^n + B_n r^{-n}\big]\big[C_n\cos(n\theta) + D_n\sin(n\theta)\big]. \tag{4.25}$$

Due to the symmetry of the problem the constants A_0, B_0 and C_n equals zero, and the general solution becomes

$$\phi(r,\theta) = \sum_{n=1}^{\infty} \big[A_n r^n + B_n r^{-n}\big]\sin(n\theta). \tag{4.26}$$

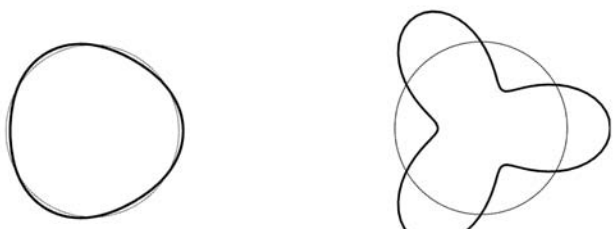

$\alpha = 0.05$ $\alpha = 0.5$

Figure 4.5: The perturbed cylinders given by Eq. (4.24). The small perturbation with $\alpha = 0.05$ is used in the perturbation analysis of the cylinder in a finite domain. The strongly perturbed cylinder with $\alpha = 0.5$ is used in the calculation of the ICEO flow result in Fig. 6.6.

4.4.1 Zeroth order solution potential

First, the potential ϕ_0 around the unperturbed cylinder in the confined domain is determined. In steady state the induced dipole field is completely screened and the boundary condition at the cylinder surface becomes

$$\partial_r \phi(r,\theta)|_{r=a} = 0, \tag{4.27}$$

leading to the potential

$$\phi_0 = \sum_{l=1}^{\infty} A_l a^l \left[\left(\frac{r}{a}\right)^l + \left(\frac{r}{a}\right)^{-l} \right] \sin(l\theta). \tag{4.28}$$

The condition along the domain boundary $(r,\theta) = (r^*,\theta)$ is divided into three parts corresponding to the confining edges,

$$\phi_0(L_x/\cos\theta,\theta) = V\frac{L_x}{L_y}\tan\theta, \qquad \text{for} \quad 0 < \theta < \theta_0, \tag{4.29a}$$

$$\phi_0(L_y/\sin\theta,\theta) = V, \qquad \text{for} \quad \theta_0 < \theta < \pi - \theta_0, \tag{4.29b}$$

$$\phi_0(-L_x/\cos\theta,\theta) = -V\frac{L_x}{L_y}\tan\theta, \qquad \text{for} \quad \pi - \theta_0 < \theta < \pi, \tag{4.29c}$$

where $\theta_0 = \arctan(L_y/L_x)$. Denoting the left- and right-handside of Eq. (4.29) $\phi_{0,1}(r^*,\theta)$ and $\phi_{0,2}(\theta)$, respectively, a fouriertranformation of the equation yields

$$\int_0^{\pi} \phi_{0,1}(r^*,\theta)\sin(m\theta)\mathrm{d}\theta = \int_0^{\pi} \phi_{0,2}(\theta)\sin(m\theta)\mathrm{d}\theta. \tag{4.30a}$$

Switching summation and integration gives

$$\sum_{l=1}^{\infty} A_l a^l \int_0^{\pi} \left[\left(\frac{r^*(\theta)}{a}\right)^l + \left(\frac{r^*(\theta)}{a}\right)^{-l} \right] \sin(l\theta)\sin(m\theta)\mathrm{d}\theta = \int_0^{\pi} \phi_{0,2}(\theta)\sin(m\theta)\mathrm{d}\theta, \tag{4.30b}$$

or with a simplified notation

$$\sum_{l=1}^{\infty} M_{ml}(A_l a^l) = B_m, \tag{4.30c}$$

leading to the matrix equation

$$\boldsymbol{M}\cdot\boldsymbol{A} = \boldsymbol{B} \quad \Rightarrow \quad \boldsymbol{A} = \boldsymbol{M}^{-1}\boldsymbol{B}. \tag{4.30d}$$

4.4.2 First order solution potential

On basis of the known solution potential ϕ_0 around the unperturbed cylinder, the first order perturbation term ϕ_1 can be found, assuming that the potential can be written as

$$\phi = \phi_0 + \alpha\phi_1. \tag{4.31}$$

ϕ_1 has the general form given in Eq. (4.26),

$$\phi_1(r,\theta) = \sum_{k=1}^{\infty} \left[C_k r^k + D_k r^{-k}\right] \sin(k\theta). \tag{4.32}$$

On the domain boundary ϕ_0 fulfills the boundary condition, thus, $\phi_1(r^*(\theta),\theta) = 0$. Fourier transforming the equation and rearranging the terms yields

$$\sum_{k=1}^{\infty} C_k \int_0^{\pi} \left[r^*(\theta)^k \sin(k\theta)\sin(m\theta)\right] \mathrm{d}\theta = -\sum_{k=1}^{\infty} D_k \int_0^{\pi} \left[r^*(\theta)^{-k} \sin(k\theta)\sin(m\theta)\right] \mathrm{d}\theta, \tag{4.33}$$

which results in a second matrix equation

$$\boldsymbol{L}\cdot\boldsymbol{C} = -\boldsymbol{N}\cdot\boldsymbol{D} \quad \Rightarrow \quad \boldsymbol{C} = -\boldsymbol{L}^{-1}\boldsymbol{N}\boldsymbol{D}. \tag{4.34}$$

The resulting expression for the perturbation term is

$$\phi_1(r,\theta) = \sum_{k=1}^{\infty} \left[-L_{km}^{-1} N_{km} r^k + \delta_{km} r^{-k}\right] D_k \sin(k\theta). \tag{4.35}$$

On the cylinder boundary the condition is

$$\hat{\boldsymbol{n}} \cdot \boldsymbol{\nabla}\phi|_{r=R} = 0, \tag{4.36}$$

where the normal vector for the perturbed cylinder is given by

$$\hat{\boldsymbol{n}} = \hat{\boldsymbol{r}} - \alpha\partial_\theta \cos(3\theta)\hat{\boldsymbol{\theta}} = \hat{\boldsymbol{r}} + \alpha 3\sin(3\theta)\hat{\boldsymbol{\theta}}. \tag{4.37}$$

Taylor expanding the condition Eq. (4.36) to first order yields

$$\hat{\boldsymbol{n}} \cdot \boldsymbol{\nabla}\phi|_{r=R} \simeq \hat{\boldsymbol{n}} \cdot \boldsymbol{\nabla}\phi|_{r=a} + (r-a)\partial_r \hat{\boldsymbol{n}} \cdot \boldsymbol{\nabla}\phi|_{r=a} = 0. \tag{4.38}$$

Inserting and rearranging leads to the following known boundary condition on ϕ_1,

$$\partial_r \phi_1|_{r=a} = -\frac{3}{r}\sin(3\theta)\partial_\theta\phi_0|_{r=a} - a\cos(3\theta)\partial_r^2\phi_0|_{r=a}, \tag{4.39}$$

which after manipulation of the involved infinite sums gives the final expression for the boundary condition on the cylinder,

$$\begin{aligned}\partial_r \phi_1|_{r=a} = &-2a(A_2 + 2a^2 A_4)\sin\theta - 2(A_1 + 5a^4 A_5)\sin(2\theta) - 18a^5 A_6 \sin(3\theta) \\ &- \sum_{n=4}^{\infty} \left[n(n-3)a^{n-4}A_{n-3} + n(n+3)a^{n+2}A_{n+3}\right]\sin(n\theta).\end{aligned} \tag{4.40}$$

Simplified this expression can be written

$$\partial_r \phi_1|_{r=a} = \sum_{n=1}^{\infty} H_n \sin(n\theta). \tag{4.41}$$

From Eq. (4.35) the general expression for the derivative in the radial direction of ϕ_1 is given as

$$\partial_r \phi_1(r,\theta)|_{r=a} = \sum_{k=1}^{\infty} \frac{k}{a}\big[- L^{-1}_{km} N_{km} a^k + \delta_{km} a^{-k}\big] D_k \sin(k\theta), \tag{4.42}$$

which can be denoted

$$\partial_r \phi_1|_{r=a} = \sum_{k=1}^{\infty} J_{kn} D_k \sin(k\theta). \tag{4.43}$$

By combination of Eqs. (4.41) and (4.43) the final vector $\boldsymbol{D}$ is determined,

$$\boldsymbol{H} = \boldsymbol{J}\boldsymbol{D} \Rightarrow \boldsymbol{D} = \boldsymbol{J}^{-1}\boldsymbol{H}. \tag{4.44}$$

It is now possible to calculate the perturbed potential around the cylinder in the confined domain as

$$\begin{aligned} \phi(r,\theta) &= \phi_0(r,\theta) + \alpha\phi_1(r,\theta) \\ &= \sum_{l=1}^{\infty} \left\{ A_l\, a^l \left[\left(\frac{r}{a}\right)^l + \left(\frac{r}{a}\right)^{-l} \right] + \alpha\big[C_l\, r^l + D_l\, r^{-l}\big] \right\} \sin(l\theta) \end{aligned} \tag{4.45}$$

4.4.3 Resulting slip velocity

Knowing the potential field around the perturbed cylinder, the ζ potential and the tangential electrical field $E_{\parallel}$ is easily determined and inserted in the Helmholtz–Smoluchowski formula for the slip-velocity. The zeta potential is found by direct insertion of the perturbed cylinder boundary Eq. (4.24) in the potential,

$$\zeta = -\phi(R(\theta),\theta). \tag{4.46}$$

Using the tangential unit vector $\hat{\boldsymbol{t}} = \hat{\boldsymbol{\theta}} + \alpha\partial_\theta \cos(3\theta)\hat{\boldsymbol{r}} = \hat{\boldsymbol{\theta}} - \alpha 3\sin(3\theta)\hat{\boldsymbol{r}}$, the tangential E-field to the first order of α is given as

$$E_{\parallel} = \hat{\boldsymbol{t}} \cdot \boldsymbol{\nabla}\phi = \frac{1}{r}\partial\phi - \alpha 3\sin(3\theta)\partial_r\phi_0. \tag{4.47}$$

By insertion the, final expression is found

$$\begin{aligned} E_{\parallel} = \sum_{l=1}^{\infty} \Bigg[& \left\{ A_l\, a^l \left[\left(\frac{r}{a}\right)^l + \left(\frac{r}{a}\right)^{-l} \right] + \alpha\big[C_l\, r^l + D_l\, r^{-l}\big] \right\} \frac{l}{r}\cos(l\theta) \\ & - \alpha 3\sin(3\theta) A_l \frac{l a^l}{r} \left[\left(\frac{r}{a}\right)^l - \left(\frac{r}{a}\right)^{-l} \right] \sin(l\theta) \Bigg] \end{aligned} \tag{4.48}$$

Thus, the slip-velocity can now be determined from the Helmholtz–Smoluchowski formula

$$v_{\text{slip}} = -\frac{\varepsilon}{\eta}\zeta(R(\theta),\theta) E_{\parallel}(R(\theta),\theta). \tag{4.49}$$

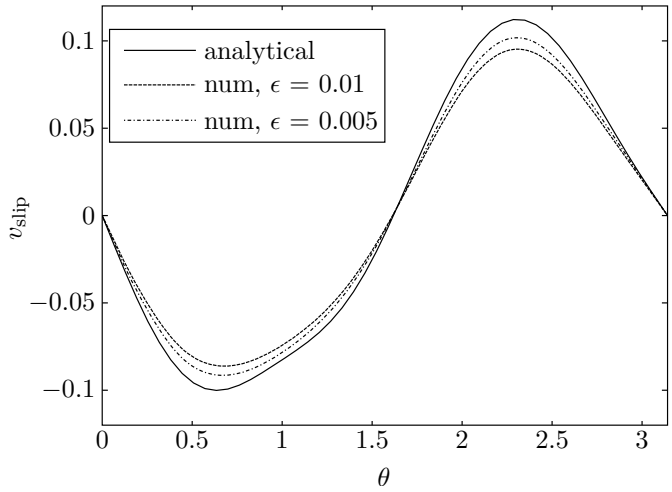

Figure 4.6: Slip-velocity v_{slip} as function of angle θ at the surface of a cosine-perturbed cylinder in a confined domain with ratio $L/a = 6$. An analytical solution obtained by perturbation theory (solid line) is compared to two corresponding numerical solutions calculated by the conventional full Debye layer resolving ICEO model (dashed lines) for two different values of $\epsilon = \lambda_{\text{D}}/a$.

Choosing a ratio of $L/a = 6$, a potential $V_0 = 1$ and a perturbation of $\alpha = 0.05$, the coefficients entering Eq. (4.49) can be calculated using Matlab for the matrix inversions and multiplications. The analytical slip-velocity calculated using the first ten terms of the infinite sums is shown in Fig. 4.6 as function of the angle θ. Two corresponding numerically calculated slip-velocity graphs are also shown in the figure. They have been calculated for a corresponding system using the conventional full Debye-layer resolving model for two values of $\epsilon = \lambda_{\text{D}}/a$, $\epsilon = 0.01$ and $\epsilon = 0.005$. The numerical slip-velocity is determined by calculating the velocity tangential to the perturbed cylinder surface at $r = (a + \delta_a)[1 + \alpha\cos(3\theta)]$, where δ_a is calculated using Eq. (4.18) on the corresponding unperturbed cylinder. It is seen how the numerical slip-velocities agrees well with the analytical perturbation result. There is a small discrepancy between the absolute values of the two solution methods, but the difference decreases with decreasing ϵ as expected from the discussions in the previous sections of this chapter. Furthermore, the difference between the values falls within the range expected on basis of Fig. 4.4.

Based on the validations presented in this and the previous section, we have gained confidence in our numerical approach for treating DC-ICEO systems.

4.5 Numerical analysis of finite Debye-length effects in ICEO

This section presents the results published in our paper Ref. [30]. The primary motivation for the studies presented in the paper and summarized in the following, were the discovered discrepancies presented in the previous section. From the preliminary investigations, shown in the convergence graph Fig. 4.4 (b), we were surprised to find such a rapidly

increasing difference between the analytical slip-velocity model and the full Debye-layer resolving numerical model for small increments in the double-layer width ($\epsilon = \lambda_D/a$). It was surprising since the simple slip-velocity model often is applied as reference for work reported in the literature, without the very sharp restrictions on system length scales that our findings suggests.

MSc. student Mathias Bækbo Andersen, DTU Nanotech, carried out the more thorough investigation of the discrepancies, where a stricter numerical mesh convergence scheme was applied and the dimensionless ratio ϵ was decreased to a value of $\epsilon \sim 10^{-4}$. A more advanced slip-velocity model, briefly mentioned in the following, was additionally set up through a collaboration with Gaurav Soni and Carl Meinhart, UCSB and compared to the full nonlinear model.

We analyze quantitatively the impact of a finite Debye length on the kinetic energy of the flow rolls generated by ICEO for three different models: (*i*) The full nonlinear electrokinetic model (FN) with a fully resolved double layer, (*ii*) the linear slip-velocity model (LS), where electrostatics and hydrodynamics are completely decoupled, and (*iii*) a nonlinear slip-velocity model (NSL) including the double layer charging through ohmic currents from the bulk electrolyte and the surface conduction in the Debye layer. The latter two models are only strictly valid for infinitely thin double layers, and we emphasize that the aim of our analysis is to determine the errors introduced by these models neglecting the finite width of the double layers compared to the full nonlinear model resolving the double layer. We do not seek to provide a more accurate description of the physics in terms of extending the modeling by adding, say, the Stern layer (not present in the model) or the steric effects of finite-sized ions (not taken into account).

4.5.1 Model system: flat center electrode at a wall

To keep our analysis simple, we consider a single un-biased metallic electrode in a uniform, external electric field. The electrode of width $2a$ and height h is placed at the bottom center, $-a < x < a$ and $z = 0$, of a square $2L \times 2L$ domain in the xz-plane filled with an electrolyte, see Fig. 6.1. The system is unbounded and translational invariant in the perpendicular y-direction. The uniform electric field, parallel to the surface of the center electrode, is provided by biasing the driving electrodes placed at the edges $x = \pm L$ with the DC voltages $\pm V_0$, respectively. This anti-symmetry in the bias voltage ensures that the constant potential of the center electrode is zero. A double layer, or a Debye screening layer, is induced above the center electrode, and an ICEO flow is generated consisting of two counter-rotating flow rolls. Electric insulating walls at $z = 0$ (for $|x| > a$) and at $z = 2L$ confine the domain in the z-direction. The symmetry of the system around $x = 0$ is exploited in the numerical calculations.

4.5.2 Full nonlinear model (FN)

The full nonlinear electrokinetic model is governed by the equations presented in Sec. 4.2.1. The same characteristic parameters applies to the present system, where a becomes the half-width of the electrode in this geometry. Additionally, we introduce the dimensionless

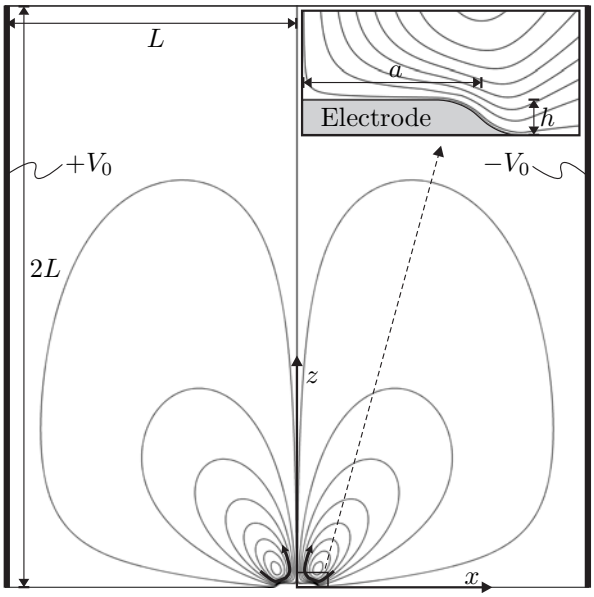

Figure 4.7: A sketch of the square $2L \times 2L$ electrolytic microchamber in the xz-plane. The external voltage $\pm V_0$ is applied to the two electrodes (thick black lines) at $x = \pm L$, respectively. It induces two counter-rotating flow rolls (curved black arrows) by electro-osmosis over the un-biased metallic center electrode of length $2a$ and height h placed at the bottom wall around $(x, z) = (0, 0)$. The spatial extent of the flow rolls is represented by the streamline plot (thin black curves) drawn as equidistant contours of the flow rate. The inset is a zoom-in on the right half, $0 < x < a$, of the un-biased center electrode and the nearby streamlines.

zeta-potential α. The characteristic zeta-potential ζ of the center electrode, i.e. its induced voltage, is given as the voltage drop along half of the electrode, $\zeta = (a/L)V$, thus, $\zeta \equiv \alpha\phi_0$, or $\alpha = (aV)/(L\phi_0)$. Consequently, the characteristic velocity can be expressed through α as

$$u_0 = \frac{\varepsilon\zeta}{\eta}\frac{\zeta}{a} = \frac{\varepsilon\phi_0^2}{\eta a}\alpha^2. \tag{4.50}$$

Furthermore, the electric body force term in the Navier–Stokes equation (last term of Eq. (4.5b)) can then explicitly be expressed by α as $\boldsymbol{f}_{\mathrm{el}} = -[\tilde{\rho}/(\epsilon^2\alpha^2)]\tilde{\boldsymbol{\nabla}}\tilde{\phi}$, while the osmotic body force term (last term of Eq. (4.14)) becomes $\boldsymbol{f}_{\mathrm{os}} = -\boldsymbol{\nabla}\tilde{c}/(\epsilon^2\alpha^2)$.

We exploit the symmetry around $x = 0$ and consider only the right half $(0 < x < L)$ of the domain. The boundary conditions on the driving electrode $(x = L)$ is given by Eq. (4.7), where the condition on the potential ϕ can be expressed by α as $\tilde{\phi} = \alpha L/a$. On the symmetry axis $(x = 0)$ the boundary conditions are given by Eq. (4.8). On the floating electrode the potential is zero $\tilde{\phi} = 0$ and the boundary conditions for the remaining fields are given in Eq. (4.10a). Finally, the boundary conditions on the solid insulating wall $(z = 2L)$ are given by Eq. (4.11).

At high values of the induced ζ-potential, the concentrations of counter- and co-ions acquire very large and very small values, respectively, near the center electrode. Numerically this is problematic. The concentration ratio becomes extremely large and the vanishingly

small concentration of co-ions is comparable to the round-off error and may even become negative. However, this numerical problem can be circumvented by working with the logarithms (marked by a breve accent) of the concentration fields, $\breve{c}_\pm = \log(c_\pm/c_0)$. By inserting

$$c_\pm = c_0 \, \exp\left(\breve{c}_\pm\right) \tag{4.51}$$

in the governing equations (2.3), (2.14), and (2.15b), a new equivalent set of governing equations is derived. This transformation serves to help linearize solutions of the dependent variables, $\breve{c}$ and $\breve{\rho}$, at the expense of introducing more nonlinearity into the governing equations. More details about the resulting equations is found in our paper [30].

4.5.3 Slip-velocity models

The numerical calculation of ICEO flows in microfluidic systems is generally connected with computational limitations due to the large difference of the inherent length scales. Typically, the Debye length is much smaller than the geometric length scale, $\lambda_\mathrm{D} \ll a$, making it difficult to resolve both the dynamics of the Debye layer and the entire microscale geometry with the available computer capacity. Therefore, it is customary to use slip-velocity models, where it is assumed that the electrodes are screened completely by the Debye layer leaving the bulk electrolyte charge neutral. The dynamics of the Debye layer is modeled separately and applied to the bulk fluid velocity through an effective, Helmholtz–Smoluchowski slip velocity condition, Eq. (2.20), at the electrode surface. Regardless of the modeled dynamics in the double layer, the slip-velocity models are only strictly valid in the limit of infinitely thin double layers $\lambda_\mathrm{D} \ll a$, as mentioned in Sec. 2.1.3

The linear slip-velocity model (LS)

The double-layer screening of the electrodes leaves the bulk electrolyte charge neutral, and hence the governing equations only include the potential ϕ, the pressure field p and the flow velocity field $\boldsymbol{v}$. In dimensionless form they become,

$$\tilde{\boldsymbol{\nabla}}^2 \tilde{\phi} = 0, \tag{4.52a}$$

$$Re(\tilde{\boldsymbol{v}} \cdot \tilde{\boldsymbol{\nabla}})\tilde{\boldsymbol{v}} = -\tilde{\boldsymbol{\nabla}}\tilde{p} + \tilde{\boldsymbol{\nabla}}^2 \tilde{\boldsymbol{v}}, \tag{4.52b}$$

$$\tilde{\boldsymbol{\nabla}} \cdot \tilde{\boldsymbol{v}} = 0. \tag{4.52c}$$

The electrostatic problem is solved independently of the hydrodynamics, and the potential is used to calculate the effective slip velocity applied to the fluid at the un-biased electrode surface. The boundary conditions of the potential and fluid velocity are equivalent to the conditions applied to the full non-linear system, except at the surface of the un-biased electrode. Here, the normal component of the electric field vanishes, and the effective slip velocity of the fluid is calculated from the electrostatic potential using $\zeta = -\phi$ and $\boldsymbol{E}_\parallel = -\left[(\hat{\boldsymbol{t}} \cdot \tilde{\boldsymbol{\nabla}})\tilde{\phi}\right] \hat{\boldsymbol{t}}$,

$$\hat{\boldsymbol{n}} \cdot \boldsymbol{\nabla}\tilde{\phi} = 0, \tag{4.53a}$$

$$\tilde{\boldsymbol{v}}_\mathrm{HS} = \frac{1}{\alpha^2}\, \tilde{\phi} \left[(\hat{\boldsymbol{t}} \cdot \tilde{\boldsymbol{\nabla}})\tilde{\phi}\right] \hat{\boldsymbol{t}}. \tag{4.53b}$$

This represents the simplest possible, so-called linear slip-velocity model; a model which is widely applied as a starting point for numerical simulations of actual microfluidic systems [9, 10]. In this simple model all the dynamics of the double layer has been neglected, an assumption known to be problematic when the voltage across the electrode exceeds the thermal voltage.

The nonlinear slip-velocity model (NLS)

The linear slip-velocity model can be improved by taking into account the nonlinear charge dynamics of the double layer. This is done in the so-called nonlinear slip-velocity model, where, although still treated as being infinitely thin, the double layer has a non-trivial charge dynamics with currents from the bulk in the normal direction and currents flowing tangential to the electrode inside the double layer. For details on the non-linear slip-velocity model, the reader is referred to references [30] and [55], and in the following the model is roughly outlined.

For simplicity we assume in the present nonlinear model that the neutral salt concentration c_0 is uniform. This assumption breaks down at high zeta potentials, where surface transport of ionic species can set up gradients in the salt concentrations leading to chemi-osmotic flow.

The charging of the double layer by the ohmic bulk current is assumed to happen in quasi-equilibrium characterized by a nonlinear differential capacitance C_{dl} given by the Gouy–Chapmann model (Sec. 2.1.1), $C_{\mathrm{dl}} = \varepsilon \cosh[ze\zeta/(2k_{\mathrm{B}}T)]/\lambda_{\mathrm{D}}$, where the Stern layer is ignored. The zeta-potential is then directly proportional to the bulk potential right outside the double layer, $\zeta = -\phi$. The current along the electrode inside the Debye layer is described by a 2D surface conductance σ_s[1], and in steady state the conservation of charge then yields

$$0 = \hat{\boldsymbol{n}} \cdot (\sigma \boldsymbol{\nabla} \phi) + \boldsymbol{\nabla}_s \cdot \left[\sigma_s \boldsymbol{\nabla}_s \phi\right], \tag{4.54}$$

where the operator $\boldsymbol{\nabla}_s = \hat{\boldsymbol{t}}(\hat{\boldsymbol{t}} \cdot \boldsymbol{\nabla})$ is the gradient in the tangential direction of the surface. Eq. (4.54) is then applied as an effective boundary condition for the potential on the floating unbiased electrode.

4.5.4 Numerical issues

We have applied the so-called weak formulation mainly to be able to control the coupling between the bulk equations and the boundary constraints, such as Eqs. (4.53b) and (4.54), in the implementation of the slip-velocity models in script form. Details on the weak implementation of the boundary conditions can be found in Ref. [30].

The accuracy and the mesh dependence of the simulation has been investigated as follows. The comparison between the three models quantifies relative differences of orders down to 10^{-3}, and the convergence of the numerical results is ensured in the following way. COMSOL has a build-in adaptive mesh generation technique that is able to refine a given mesh so as to minimize the error in the solution. The adaptive mesh generator increases

[1] Following Dukhin [56] the surface conductance is given as $\sigma_s = 4\lambda_{\mathrm{D}}\sigma(1+m)\sinh^2[Ze\zeta/(4k_{\mathrm{B}}T)]$, where $m = 2[k_{\mathrm{B}}T/(Ze)]^2\varepsilon/(\eta D)$ indicates the relative contribution of electroosmosis to surface conduction.

the mesh density in the immediate region around the electrode to capture the dynamics of the ICEO in the most optimal way under the constraint of a maximum number of degrees of freedom (DOFs). For a given set of physical parameters, the problem is solved each time increasing the number of DOFs and comparing consecutive solutions. As a convergence criterium we demand that the standard deviation of the kinetic energy relative to the mean value should be less than a given threshold value typically chosen to be around 10^{-5}. All of the simulations ended with more than 10^6 DOFs, and the ICEO flow is therefore sufficiently resolved even for the thinnest double layers in our study for which $\epsilon = 10^{-4}$.

4.5.5 Results of the finite Debye length effects

Our comparison of the three numerical models is primarily focused on variations of the three dimensionless parameters ϵ, α, and β relating to the Debye length λ_D, the applied voltage V_0, and the height h of the electrode, respectively,

$$\epsilon = \frac{\lambda_\mathrm{D}}{a}, \quad \alpha = \frac{aV_0}{L\phi_0}, \quad \beta = \frac{h}{a}. \tag{4.55}$$

As mentioned in Sec. 4.3, the strength of the generated ICEO flow can be measured in several ways. We could use either the mechanical power input P_mech exerted on the electrolyte by the slip-velocity just outside the Debye layer or equivalently the kinetic energy dissipation P_kin in the bulk of the electrolyte. However, both these methods suffers from numerical inaccuracies due to the dependence of both the position of the integration path and of the less accurately determined velocity gradients in the stress tensor $\boldsymbol{\sigma}$. To obtain a numerically more stable and accurate measure, we have chosen in the following analysis to characterize the strength of the ICEO flow by the kinetic energy E_kin of the induced flow field $\boldsymbol{v}$,

$$E_\mathrm{kin} = \tfrac{1}{2}\rho_\mathrm{m} \int_\Omega v^2 \,\mathrm{d}x\,\mathrm{d}z, \tag{4.56}$$

which depends on the velocity field and not its gradients, and which furthermore is a bulk integral of good numerical stability.

Zero height of the un-biased center electrode

We assume the height h of the un-biased center electrode to be zero, i.e. $\beta = 0$, while varying the Debye length and the applied voltage through the parameters ϵ and α. We note that the linear slip-velocity model Eqs. (4.52) and (4.53) is independent of the dimensionless Debye length ϵ. It is therefore natural to use the kinetic energy $E_\mathrm{kin}^\mathrm{LS}$ of this model as a normalization factor.

In the lin-log plot of Fig. 4.8 (a) we show the kinetic energy $E_\mathrm{kin}^\mathrm{NLS}$ and $E_\mathrm{kin}^\mathrm{FN}$ normalized by $E_\mathrm{kin}^\mathrm{LS}$ as a function of the inverse Debye length $1/\epsilon$ for three different values of the applied voltage, $\alpha = 0.05, 0.5$ and 5, ranging from the linear to the strongly nonlinear voltage regime.

We first note that in the limit of vanishing Debye length (to the right in the graph) all models converge towards the same value for all values of the applied voltage α. For small

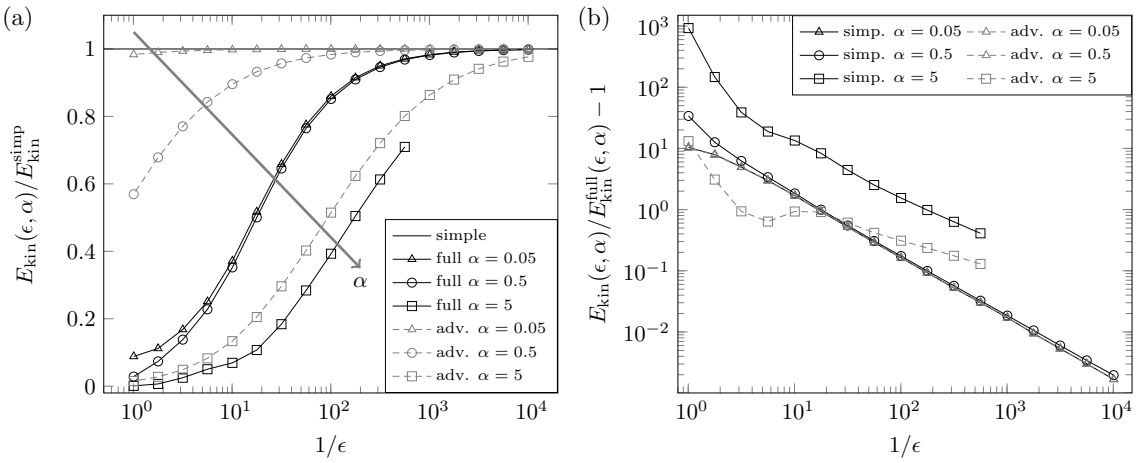

Figure 4.8: (a) The total induced kinetic energy $E_{\mathrm{kin}}^{\mathrm{NLS}}$ (gray dashed) and $E_{\mathrm{kin}}^{\mathrm{FN}}$ (black) for the nonlinear slip-velocity model and the full model, respectively, relative to $E_{\mathrm{kin}}^{\mathrm{LS}}$ (horizontal black line) of the linear slip-velocity model as a function of dimensionless inverse Debye length $1/\epsilon$. Each are shown for three values of the dimensionless applied voltage $\alpha = 0.05, 0.5$ and 5. The value of ϵ decreases from 1 to 10^{-4} going from left to right. (b) The difference between the induced kinetic energies $E_{\mathrm{kin}}^{\mathrm{LS}}$ and $E_{\mathrm{kin}}^{\mathrm{NLS}}$ of the linear and nonlinear slip-velocity models, respectively, relative to the full model $E_{\mathrm{kin}}^{\mathrm{FN}}$ as a function of the inverse Debye length $1/\epsilon$. for three different applied voltages $\alpha = 0.05, 0.5, 5$.

values of α the advanced slip-velocity model $E_{\mathrm{kin}}^{\mathrm{NLS}}$ is fairly close to the linear slip-velocity model $E_{\mathrm{kin}}^{\mathrm{LS}}$, but as α increases, it requires smaller and smaller values of ϵ to obtain the same results in the two models. In the linear regime $\alpha = 0.05$ a deviation less than 5% is obtained already for $\epsilon < 1$. In the nonlinear regime $\alpha = 0.5$ the same deviation requires $\epsilon < 10^{-2}$, while in the strongly nonlinear regime $\epsilon < 10^{-4}$ is needed to obtain a deviation lower than 5%.

In contrast, it is noted how the more realistic full model $E_{\mathrm{kin}}^{\mathrm{FN}}$ deviates strongly from $E_{\mathrm{kin}}^{\mathrm{LS}}$ for most of the displayed values of ϵ and α. To obtain a relative deviation less than 5% in the linear ($\alpha = 0.05$) and nonlinear ($\alpha = 0.5$) regimes, a minute Debye length of $\epsilon < 10^{-3}$ is required, and in the strongly nonlinear regime the 5% level it not reached at all.

The deviations are surprisingly large. The Debye length in typical electrokinetic experiments is $\lambda_{\mathrm{D}} = 30$ nm. For a value of $\epsilon = 0.01$ this corresponds to an electrode of width $2 \times 3\,\mu\mathrm{m} = 6\,\mu\mathrm{m}$, comparable to those used in Refs. [3, 21, 25]. In Fig. 4.8 (a) we see that for $\alpha = 5$, corresponding to a moderate voltage drop of 0.26 V across the electrode, the linear slip-velocity model overestimates the ICEO strength by a factor $1/0.4 = 2.5$. The nonlinear slip-model does a better job. For the same parameters it only overestimates the ICEO strength by a factor $0.5/0.4 = 1.2$.

For more detailed comparisons between the three models the data of Fig. 4.8 (a) are plotted in a different way in Fig. 4.8 (b). Here the overestimates $(E_{\mathrm{kin}}^{\mathrm{LS}}/E_{\mathrm{kin}}^{\mathrm{FN}}) - 1$ and $(E_{\mathrm{kin}}^{\mathrm{NLS}}/E_{\mathrm{kin}}^{\mathrm{FN}}) - 1$ of the two slip-velocity models relative to the more correct full model are plotted in a log-log plot as a function of the inverse Debye length $1/\epsilon$ for three

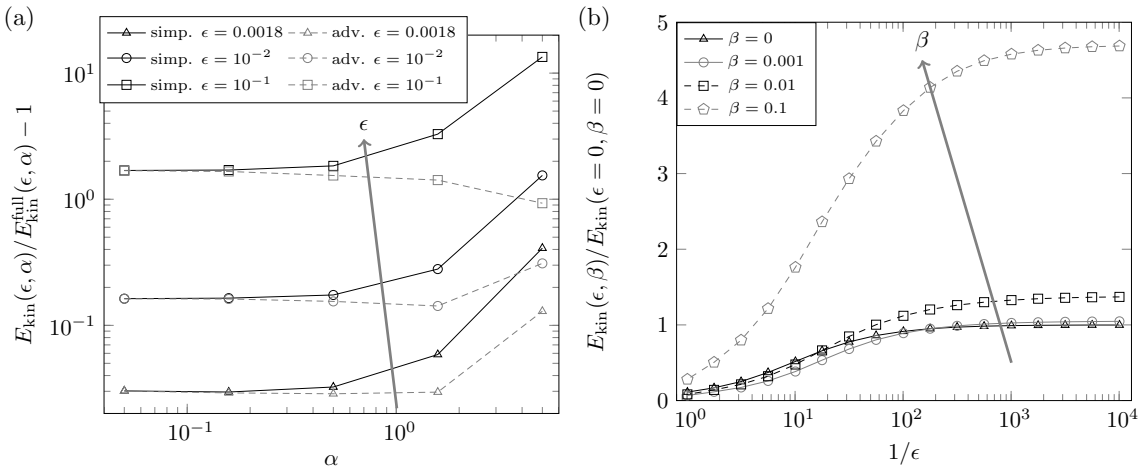

Figure 4.9: (a) The difference between the induced kinetic energies $E_{\mathrm{kin}}^{\mathrm{LS}}$ and $E_{\mathrm{kin}}^{\mathrm{NLS}}$ of the linear and nonlinear slip-velocity models, respectively, relative to the full model $E_{\mathrm{kin}}^{\mathrm{FN}}$ as a function of the voltage bias α for three different Debye layer thicknesses $\epsilon = 1.8 \times 10^{-3}, 10^{-2}, 10^{-1}$. (b) The difference between the induced kinetic energies $E_{\mathrm{kin}}^{\mathrm{FN}}(\epsilon,\beta)$ of the full model at finite Debye length and electrode height relative to the full model $E_{\mathrm{kin}}^{\mathrm{FN}}(0,0)$ at zero Debye length and zero electrode height as a function of the inverse Debye length $1/\epsilon$ for four electrode heights $\beta = 0, 10^{-3}, 10^{-2}, 10^{-1}$.

different values of the applied voltage. It is clearly seen how the relative deviation decreases proportional to ϵ as ϵ approaches zero.

Finally, in Fig. 4.9 (a) the relative deviations $(E_{\mathrm{kin}}^{\mathrm{LS}}/E_{\mathrm{kin}}^{\mathrm{FN}}) - 1$ and $(E_{\mathrm{kin}}^{\mathrm{NLS}}/E_{\mathrm{kin}}^{\mathrm{FN}}) - 1$ are plotted versus the voltage α in a log-log plot. For any value of the applied voltage α, both slip-velocity models overestimates by more than 100% for large Debye lengths $\epsilon = 10^{-1}$ and by more than 10% for $\epsilon = 10^{-2}$. For the minute Debye length $\lambda_{\mathrm{D}} = 1.8 \times 10^{-3}$ the overestimates are about 3% in the linear and weakly nonlinear regime $\alpha < 1$, however, as we enter the strongly nonlinear regime with $\alpha = 5$ the overestimation increases to a level above 10%.

Finite height of the un-biased electrode

Compared to the full numerical model, the slip-velocity models are convenient to use, but even for small Debye lengths, say $\lambda_{\mathrm{D}} = 0.01a$, they are prone to significant quantitative errors as shown above. Similarly, it is of relevance to study how the height of the un-biased electrode influences the strength of the ICEO flow rolls. In experiments the thinnest electrodes are made by evaporation techniques. The resulting electrode heights are of the order 50 nm − 200 nm, which relative to the typical electrode widths $a \approx 5\,\mu\mathrm{m}$ results in dimensionless heights $10^{-3} < \beta < 10^{-1}$.

In Fig. 4.9 (b) is shown the results for the numerical calculation of the kinetic energy $E_{\mathrm{kin}}^{\mathrm{FN}}(\epsilon,\beta)$ using the full numerical model. The dependence on the kinetic energy of the dimensionless Debye length $\epsilon = \lambda_{\mathrm{D}}/a$ and the dimensionless electrode height $\beta = h/a$ is measured relative to the value $E_{\mathrm{kin}}^{\mathrm{FN}}(\epsilon,\beta)$ of the infinitely small Debye length for an

electrode of zero height.

For small values of the height no major deviations are seen. The curve for $\beta = 0$ and $\beta = 0.001$ are close. As the height is increased to $\beta = 10^{-2}$ we note that the strength of the ICEO is increased by 20%−25% as $\beta > \epsilon$. This tendency is even stronger pronounced for the higher electrode $\beta = 10^{-1}$. Here the ICEO strength is increased by approximately 400% for a large range of Debye lengths.

4.5.6 Final remarks

Our calculations show that the simple zero-width models significantly overestimates the ICEO flow velocities compared to more realistic models taking the finite size of the Debye screening length into account. This may provide a partial explanation of the observed quantitative discrepancy between observed and calculated ICEO velocities. The discrepancy increases substantially for increasing ϵ, i.e. in nanofluidic systems.

Even larger deviations of the ICEO strength is calculated in the full numerical model when a small, but finite height of the un-biased electrode is taken into account.

A partial explanation of the quantitative failure of the analytical slip velocity model is the radial dependence of the tangential field $E_{\|}$ combined with the spatial extent of the charge density ρ_{el} of the double layer. In the Debye–Hückel approximation $E_{\|}$ and ρ_{el} around the metallic cylinder of radius a are given by Eq. (2.31). The slowly varying part of $E_{\|}$ is given by $E_0\left[1 + (a/r)^2\right] \sin\theta$. For very thin double layers it is well approximated by the r-independent expression $2E_0 \sin\theta$, while for wider double layers, the screening charges sample the decrease of $E_{\|}$ as a function of the distance from the cylinder. Also tangential pressure gradients developing in the double layer may contribute to the lower ICEO strength when taking the finite width of the double layer into account.

Our work shows that for systems with a small, but non-zero Debye length of 0.001 to 0.01 times the size of the electrode, and even when the Debye-Hückel approximation is valid, a poor quantitative agreement between experiments and model calculations must be expected when applying the linear slip-velocity model based on a zero Debye-length. For a typically applied electrolyte concentration of 0.1 mM the Debye length becomes $\lambda_{\mathrm{D}} = 30\,\mathrm{nm}$. Hence, the electrodes of the systems have to be larger than 30 µm corresponding to $\epsilon = 10^{-3}$ to obtain deviations less than 5%. Thus, it is advised to employ the full numerical model of ICEO, when comparing simulations with experiments.

Chapter 5

AC-driven ICEO

In microsystems it is often more convenient to drive ICEO flows with AC biasing than DC biasing. AC-driving prevents the formation of completely screening double layers at the driving electrodes, and can therefore generate steady liquid motion without any additional requirements. In contrast, DC systems require a rather complex setup with ion-exchange membranes and buffers in the solution to drive a steady flow. Thus, for AC-systems it is possible to implement the driving electrodes directly in a micro-channel in contact with the electrolyte to be manipulated. Given that the frequency is sufficiently high and the voltage sufficiently low, no additional chemistry or membranes are necessary to stabilize the ICEO effect. Furthermore, the AC-system provides us with an additional tunable parameter, the frequency, which may be utilized to change the resulting motion of the electrolyte. One could imagine a system which for instance is tuned to pump liquid in one frequency regime and to mix liquid in another regime. To prepare the optimization of AC-driven ICEO systems, which is the subject of the following Chap. 6, the governing equations are rewritten and the numerical solutions are validated by comparison with an analytical model.

5.1 Governing equations for time-averaged AC biased flow

The model system is identical to the DC biased system shown in Fig. 4.1, with the exception that the capacitor plates are biased with a harmonic oscillating voltage $\phi = \pm V_0 \cos(\omega t)$. We take a starting point in the full non-linear equation system Eqs. (2.3), (2.12), (2.14) and (2.15b), and rewrite the equations in dimensionless form. For simplicity we consider a symmetric, binary electrolyte, where the positive and negative ions with concentrations c_+ and c_-, respectively, have the same diffusivity D and valence charge number Z. The characteristic numbers of the DC system also applies for the AC system, see Eqs. (4.1) and (4.2), and additionally, the RC time for the ICEO system is introduced as the characteristic time scale,

$$\tau_c = \frac{a\lambda_\mathrm{D}}{D}, \quad \tilde{t} = \frac{t}{\tau_c}. \tag{5.1}$$

To prepare a linearization of the equation system, the governing equations are reformulated in terms of the average ion concentration $c \equiv (c_+ + c_-)/2$ and half the charge density $\rho \equiv (c_+ - c_-)/2$, in the same way as for the DC system. The resulting full nonlinear dimensionless equation system takes the following form for the ionic transport,

$$\frac{\partial \tilde{c}}{\partial \tilde{t}} = \epsilon \boldsymbol{\nabla} \cdot (\tilde{\rho} \tilde{\boldsymbol{\nabla}} \tilde{\phi} + \tilde{\boldsymbol{\nabla}} \tilde{c} - P\acute{e}\, \tilde{c} \tilde{\boldsymbol{v}}), \tag{5.2a}$$

$$\frac{\partial \tilde{\rho}}{\partial \tilde{t}} = \epsilon \boldsymbol{\nabla} \cdot (\tilde{c} \tilde{\boldsymbol{\nabla}} \tilde{\phi} + \tilde{\boldsymbol{\nabla}} \tilde{\rho} - P\acute{e}\, \tilde{\rho} \tilde{\boldsymbol{v}}), \tag{5.2b}$$

$$P\acute{e} = \frac{u_0 a}{D}, \tag{5.2c}$$

while the electric potential obeys

$$\tilde{\boldsymbol{\nabla}}^2 \tilde{\phi} = -\frac{1}{\epsilon^2} \tilde{\rho}, \tag{5.3}$$

and finally the fluid fields satisfy

$$\tilde{\boldsymbol{\nabla}} \cdot \tilde{\boldsymbol{v}} = 0, \tag{5.4a}$$

$$Re\left[\frac{1}{\epsilon P\acute{e}} \frac{\partial \tilde{\boldsymbol{v}}}{\partial \tilde{t}} + (\tilde{\boldsymbol{v}} \cdot \tilde{\boldsymbol{\nabla}}) \tilde{\boldsymbol{v}}\right] = -\tilde{\boldsymbol{\nabla}} \tilde{p} + \tilde{\boldsymbol{\nabla}}^2 \tilde{\boldsymbol{v}} - \frac{\tilde{\rho}}{\epsilon^2} \tilde{\boldsymbol{\nabla}} \tilde{\phi}, \tag{5.4b}$$

$$Re = \frac{\rho u_0 a}{\eta}. \tag{5.4c}$$

Again, the small dimensionless parameter $\epsilon = \lambda_\mathrm{D}/a$ is used. In the following, the tilde is omitted for convenience.

5.1.1 Linearized equation system

The topology optimization routine is very time and memory consuming, so to ease the numerical simulations we choose to linearize the equations. There are several nonlinearities to consider.

By virtue of a low Reynolds number $Re = \rho_\mathrm{m} v_\mathrm{slip} a/\eta = 10^{-6}$, the nonlinear Navier–Stokes equation is replaced by the linear Stokes equation. Likewise, the low Péclet number $P\acute{e} = v_\mathrm{slip} a/D = 5 \times 10^{-4}$ allows us to neglect the nonlinear ionic convection flux density $c_\pm \boldsymbol{v}$. This approximation implies the additional simplification that the electrodynamic problem is independent of the hydrodynamics.

Finally, since $Ze\zeta/k_\mathrm{B}T = 0.05 \ll 1$ the linear Debye–Hückel approximation is valid, and we can utilize that the ionic concentrations only deviate slightly from the bulk equilibrium ionic concentration. Thus, by expanding the fields to first order as $c = 1 + \delta c$ and $\rho = 0 + \delta\rho$, the resulting differential equation for ρ is decoupled from that of c. Introducing complex field notation, the applied external bias voltage is $\Delta\phi(t) = 2V_0 \cos(\omega t) = \mathrm{Re}[2V_0 \exp(\mathrm{i}\omega t)]$, yielding a corresponding response for the potential ϕ and charge density ρ, with the complex amplitudes $\Phi(\boldsymbol{r}) = \Phi_R(\boldsymbol{r}) + \mathrm{i}\Phi_I(\boldsymbol{r})$ and $P(\boldsymbol{r}) = P_R(\boldsymbol{r}) + \mathrm{i}P_I(\boldsymbol{r})$,

respectively.

$$\phi(\pm L, t) = \pm V_0 \cos(\omega t) = \mathrm{Re}\big[\pm V_0 \exp(i\omega t)\big], \tag{5.5a}$$
$$\phi(\mathbf{r}, t) = \mathrm{Re}\big[\Phi(\mathbf{r}) \exp(i\omega t)\big], \tag{5.5b}$$
$$\rho(\mathbf{r}, t) = \mathrm{Re}\big[P(\mathbf{r}) \exp(i\omega t)\big]. \tag{5.5c}$$

The resulting governing equations for the electrodynamic problem is then

$$\boldsymbol{\nabla}^2 \Phi_R = -\frac{1}{\epsilon^2} P_R, \tag{5.6a}$$
$$\boldsymbol{\nabla}^2 \Phi_I = -\frac{1}{\epsilon^2} P_I, \tag{5.6b}$$
$$\boldsymbol{\nabla} \cdot \big[\boldsymbol{\nabla}\Phi_R + \boldsymbol{\nabla} P_R\big] = -\frac{\omega}{\epsilon} P_I, \tag{5.6c}$$
$$\boldsymbol{\nabla} \cdot \big[\boldsymbol{\nabla}\Phi_I + \boldsymbol{\nabla} P_I\big] = +\frac{\omega}{\epsilon} P_R, \tag{5.6d}$$

Given the electric potential Φ and the charge density P, we solve for the time-averaged hydrodynamic fields $\langle \boldsymbol{v} \rangle$ and $\langle p \rangle$,

$$\boldsymbol{\nabla} \cdot \langle \boldsymbol{v} \rangle = 0, \tag{5.7a}$$
$$0 = -\boldsymbol{\nabla}\langle p \rangle + \nabla^2 \langle \boldsymbol{v} \rangle + \langle \boldsymbol{f}_{\mathrm{el}} \rangle, \tag{5.7b}$$

where the time-averaged electric body force density $\langle \boldsymbol{f}_{\mathrm{el}} \rangle$ is given by

$$\langle \boldsymbol{f}_{\mathrm{el}} \rangle = -\frac{1}{2\epsilon^2} \big[P_R \boldsymbol{\nabla}\Phi_R + P_I \boldsymbol{\nabla}\Phi_I\big]. \tag{5.7c}$$

5.1.2 Boundary conditions

In contrast to the DC system, where both the left-right and top-down symmetries of the system were exploited, we only make use of the top-down symmetry in the AC system, for reasons that become clear in the following chapter about optimization. We exploit the symmetry around $z = 0$ and consider only the upper half ($0 < z < L/a$) of the domain. As boundary condition on the driving electrode we set the amplitude V_0 of the applied potential. Neglecting any electrode reactions taking place at the surface there is no net ion flux in the normal direction to the boundary with unit vector $\hat{\boldsymbol{n}}$. For the fluid velocity we set a no-slip condition, and thus at $z = L/a$ we have

$$\Phi_R = \pm V_0, \quad \Phi_I = 0, \tag{5.8a}$$
$$\mathbf{n} \cdot \big[\boldsymbol{\nabla}\Phi_R + \boldsymbol{\nabla} P_R\big] = 0, \tag{5.8b}$$
$$\mathbf{n} \cdot \big[\boldsymbol{\nabla}\Phi_I + \boldsymbol{\nabla} P_I\big] = 0, \tag{5.8c}$$
$$\langle \boldsymbol{v} \rangle = 0. \tag{5.8d}$$

On the symmetry axis ($z = 0$) the potential and the charge density must be zero due to the anti-symmetry of the applied potential. Furthermore, there is no fluid flux in the normal direction and the shear stresses vanish. So at $z = 0$ we have

$$\Phi_R = \Phi_I = 0, \quad P_R = P_I = 0, \tag{5.9a}$$

$$\hat{\boldsymbol{n}} \cdot \langle \boldsymbol{v} \rangle = 0, \quad \hat{\boldsymbol{t}} \cdot \langle \boldsymbol{\sigma} \rangle \cdot \hat{\boldsymbol{n}} = 0, \tag{5.9b}$$

where the dimensionless stress tensor is $\langle \sigma_{ik} \rangle = -\langle p \rangle \delta_{ik} + \big(\partial_i \langle v_k \rangle + \partial_k \langle v_i \rangle\big)$, and $\hat{\boldsymbol{n}}$ and $\hat{\boldsymbol{t}}$ are the normal and tangential unit vectors, respectively. On the dielectric cylinder surface a no-slip condition is applied on the fluid velocity and a no-current condition in the normal direction. For the potential the usual electrostatic boundary conditions apply, so the conditions on the dielectric surface are

$$\Phi_{diel} = \Phi_{\text{fluid}}, \quad \varepsilon_{\text{diel}}\, \hat{\boldsymbol{n}} \cdot \boldsymbol{\nabla} \tilde{\Phi}_{\text{diel}} = \varepsilon_{\text{fluid}}\, \hat{\boldsymbol{n}} \cdot \boldsymbol{\nabla} \tilde{\Phi}_{\text{fluid}}, \tag{5.10a}$$

$$\mathbf{n} \cdot \big[\boldsymbol{\nabla} \Phi_R + \boldsymbol{\nabla} P_R\big] = 0, \tag{5.10b}$$

$$\mathbf{n} \cdot \big[\boldsymbol{\nabla} \Phi_I + \boldsymbol{\nabla} P_I\big] = 0, \tag{5.10c}$$

$$\langle \boldsymbol{v} \rangle = 0. \tag{5.10d}$$

On the remaining vertical insulating walls ($x = \pm L/a$) there are no fluxes in the normal direction, the normal component of the electric field vanishes and there are no-slip on the fluid velocity.

$$\hat{\boldsymbol{n}} \cdot \boldsymbol{\nabla} \Phi_R = \hat{\boldsymbol{n}} \cdot \boldsymbol{\nabla} \Phi_I = 0, \tag{5.11a}$$

$$\mathbf{n} \cdot \big[\boldsymbol{\nabla} \Phi_R + \boldsymbol{\nabla} P_R\big] = 0, \tag{5.11b}$$

$$\mathbf{n} \cdot \big[\boldsymbol{\nabla} \Phi_I + \boldsymbol{\nabla} P_I\big] = 0, \tag{5.11c}$$

$$\langle \boldsymbol{v} \rangle = 0. \tag{5.11d}$$

5.2 Validation

To validate the numerical solution of the linearized governing equations, the analytical model presented by Squires and Bazant [27] is once more used as benchmark. On basis of the method and expressions presented in the paper, an analytical solution is written down for a conducting cylinder confined by an AC biased parallel plate capacitor. The analytical model is valid for an infinitely thin double layer $\lambda_{\text{D}} \ll a$ and for a plate distance $2L$ much larger than the cylinder diameter $2a$, i.e. $a \ll L$.

5.2.1 Induced dipole strength and zeta potential

For a cylindrical conductor with radius a in an infinite DC electric field $\boldsymbol{E} = E_0\boldsymbol{e}_z$, the general time dependent potential can be expressed by the dipole strength $g(t)$ as

$$\phi = -E_0 z\left[1 + g(t)\frac{a^2}{r^2}\right], \tag{5.12}$$

such that $g(t = 0) = -1$ and $g(t \to \infty) = 1$, in order to reconstruct the solutions Eqs. (2.22) and (2.23).

Using the same formulation in the case of an applied AC electric field, where the infinite electric background field varies as $\boldsymbol{E} = E_0 e^{i\omega t}\boldsymbol{e}_z$ and the background potential correspondingly is $\phi_0 = -E_0 z e^{i\omega t}$, the overall potential can be written as

$$\phi = -E_0 z\left[1 + g(t)\frac{a^2}{r^2}\right]e^{i\omega t} = -E_0 r\sin(\theta)\left[1 + g(t)\frac{a^2}{r^2}\right]e^{i\omega t}. \tag{5.13}$$

In the Debye–Hückel limit the potential drop across the double layer can be approximated by the linear relation

$$\phi(r = a, \theta, t) - \phi_0 = -\zeta(\theta) = -q(\theta)\lambda_\mathrm{D}/\epsilon. \tag{5.14}$$

Here $c_\mathrm{D} = \lambda_\mathrm{D}/\epsilon$ is the linear Debye capacitance, $\phi_0 \equiv 0$ is the conductor potential, and q is the induced surface charge. The time change of q is governed by the ionic current $J_\perp$ into the charge cloud perpendicular to the conductor surface at $r = a$, i.e.

$$J_\perp = -\dot{q}(\theta) = -\sigma\boldsymbol{E}\cdot\boldsymbol{e}_r = -\sigma E_0\sin(\theta)e^{i\omega t}(1 - g(t)), \tag{5.15}$$

where σ is the conductivity of the bulk electrolyte. Inserting Eq. (5.13) in Eq. (5.14) and differentiating leads to

$$\dot{q}(\theta) = \frac{E_0 a\epsilon}{\lambda_\mathrm{D}}\sin(\theta)e^{i\omega t}\big[i\omega(1 + g(t)) + \dot{g}(t)\big]. \tag{5.16}$$

Equalizing these two expressions for $\dot{q}(\theta)$ results in an ordinary differential equation for g,

$$\dot{g}(t) = \frac{\sigma\lambda_\mathrm{D}}{a\epsilon} - i\omega - g(t)\left[\frac{\sigma\lambda_\mathrm{D}}{a\epsilon} + i\omega\right], \tag{5.17}$$

where the initial condition $g(0) = -1$ leads to the solution

$$g(t) = \frac{1 - i\omega\tau_c - 2e^{-t(1/\tau_c + i\omega)}}{1 + i\omega\tau_c}. \tag{5.18}$$

Here the characteristic charging time, or the RC time, for the Debye layer has been introduced,

$$\tau_c = R_c C_\mathrm{D} = \frac{a\varepsilon}{\sigma\lambda_\mathrm{D}} = \frac{\lambda_\mathrm{D} a}{D}. \tag{5.19}$$

Thus, the zeta-potential is then given by

$$\zeta(\theta) = \frac{\lambda_{\mathrm{D}}}{\epsilon}\, q(\theta) = E_0 a \sin(\theta) e^{i\omega t}[1 + g(t)] = 2E_0 a \sin(\theta) \frac{e^{i\omega t} - e^{-t/\tau_c}}{1 + i\omega\tau_c}. \tag{5.20}$$

When the transient has passed and the steady state situation is reached, the induced dipole strength becomes

$$g = \frac{1 - i\omega\tau_c}{1 + i\omega\tau_c}, \tag{5.21}$$

and the zeta-potential is correspondingly

$$\zeta = \frac{\lambda_{\mathrm{D}}}{\epsilon}\, q(\theta) = 2E_0 a \sin(\theta) \frac{e^{i\omega t}}{1 + i\omega\tau_c} = E_0 a \sin(\theta) e^{i\omega t}[1 + g]. \tag{5.22}$$

5.2.2 Electric field

The electric field between two capacitor plates with distance $2L$ biased with an AC voltage $\Delta\phi(t) = \mathrm{Re}[2V_0 \exp(\mathrm{i}\omega t)]$ and filled with electrolyte is calculated using the standard electric circuit theory on the RC circuit presented in Chap. 2. The equivalent circuit for the parallel plate capacitor consists of two double layer capacitances and a bulk electrolytic resistance coupled in series, so the total capacitance is $C_{\mathrm{D}} = \varepsilon/(2\lambda_{\mathrm{D}})$ and the resistance is $R_e = 2L/\sigma$, where σ is the bulk electrolytic conductivity.

$$E_0(t) = \frac{V_0}{L}\, \mathrm{Re}\left[\frac{i\omega\tau_e}{1 + i\omega\tau_e}\, e^{i\omega t}\right]. \tag{5.23}$$

Given that $\sigma = 2Zec_0\mu$ for a binary, symmetric electrolyte, and that the ionic mobility μ is related to the ionic diffusivity D through the Einstein relation as $\mu = DZe/(k_{\mathrm{B}}T)$, we have the following expression for the characteristic electrode charging time

$$\tau_e = R_e C_{\mathrm{D}} = \frac{L\varepsilon}{\sigma\lambda_{\mathrm{D}}} = \frac{\lambda_{\mathrm{D}} L}{D}. \tag{5.24}$$

Two time scales dominates the system, the cylinder charging time τ_c and the electrode charging time τ_e, corresponding to the characteristic driving frequencies ω_c and ω_e, respectively. The bulk flow around the cylinder is generated when the ions have time to partially screen the induced dipole field at the cylinder surface, i.e. for frequencies around $\omega \leq \omega_c$. If the frequency becomes higher $\omega \gg \omega_c$, the screening of the induced dipole is negligible, and no flow can be generated. For very low frequencies $\omega \ll \omega_e$ Debye layers have time to form and fully screen the electrode surfaces such that no electric fields are left in the bulk electrolyte to induce and drive a flow. Consequently, the induced flow only has a maximum within a small band of driving frequencies $\omega_e \leq \omega \leq \omega_c$.

5.2.3 Resulting slip velocity

If $L \gg a$ it may be assumed that Eq. (5.23) acts as the applied electric field "at infinity" in the calculation of the slip velocity just outside the infinitely thin Debye layer around at

the cylindrical conductor surface. Thus, from Eq. (5.13) the steady state potential field is given by

$$\phi = -E_0(t) r \sin(\theta)\left[1 + g\frac{a^2}{r^2}\right], \tag{5.25}$$

and thereby the electric field becomes

$$E = -\boldsymbol{\nabla}\phi = E_0(t)\sin(\theta)\left[1 - g\frac{a^2}{r^2}\right]\boldsymbol{e}_r + E_0(t)\cos(\theta)\left[1 + g\frac{a^2}{r^2}\right]\boldsymbol{e}_\theta. \tag{5.26}$$

Correspondingly, from Eq. (5.22) the ζ potential can be written as

$$\zeta = E_0(t) a \sin(\theta)[1 + g] = E_0(t) a \sin(\theta)\frac{2}{1 + i\omega\tau_c}. \tag{5.27}$$

The resulting slip velocity is then determined by the Helmholtz–Smoluchowski formula $\boldsymbol{v}_{\text{slip}} = -(\zeta\,\varepsilon/\eta)\,(-\boldsymbol{e}_\theta \cdot \boldsymbol{\nabla}\phi)\,\boldsymbol{e}_\theta$ by insertion of Eqs. (5.26) and (5.27) at $r = a$. Rearranging and time averaging lead to the final expression

$$\langle \boldsymbol{v}_{\text{slip}} \rangle = -\frac{\varepsilon E_0^2 a}{\eta}\sin(2\theta)\frac{\tau_e^2\omega^2}{(1 + \tau_c^2\omega^2)(1 + \tau_e^2\omega^2)}\,\boldsymbol{e}_\theta, \tag{5.28}$$

where $E_0 = V_0/L$. It is noted that the pre-factor $\varepsilon E_0^2 a/\eta$ represents the characteristic velocity for the average flow.

5.2.4 Frequency dependence of analytical and numerical solutions

The parameters of Table 4.1 is used for the calculation of the analytical and numerical solutions. The characteristic time scale of the system is chosen as the cylinder charging time $\tau_c = \lambda_{\text{D}} a/D = 7.8 \times 10^{-8}\,\text{s}$, and the electrode charging time then becomes $\tau_e = \tau_c L/a$.

In Fig. 5.1 the analytically and numerically calculated slip velocities v_{slip} have been plotted as functions of angular frequency ω for three different ratios $L/a = 5$, $L/a = 15$ and $L/a = 25$. The numerical slip velocities are determined in the same way as in the case of the DC driven flow, see Sec. 4.3. Additionally, the analytical average slip velocity for the unconfined cylinder has been plotted using the expression given explicitly in the paper of Squires and Bazant [27] as

$$\langle \boldsymbol{v}_{\text{slip}} \rangle = -\frac{\varepsilon E_0^2 a}{\eta}\sin(2\theta)\frac{1}{(1 + \tau_c^2\omega^2)}\,\boldsymbol{e}_\theta. \tag{5.29}$$

The frequency dependence of the slip velocities follows the expected curve with maximum in the frequency band $a/L \leq \omega \leq 1$. Furthermore, the numerical solutions (dashed lines) have the exact frequency dependence expected from the analytical solutions (solid lines). For all three ratios of L/a the maximal numerical slip velocity is approximately 20 % lower than the analytically expected velocity. This corresponds to the deviation seen in the DC driven flow for the same ratio $\epsilon = \lambda_{\text{D}}/a = 0.01$. Conclusively, on basis of the discussion of Chap. 4, we obtain the expected correspondence between the analytical numerical calculations.

With this validation we have gained confidence in our numerical simulation scheme for AC-driven ICEO flows.

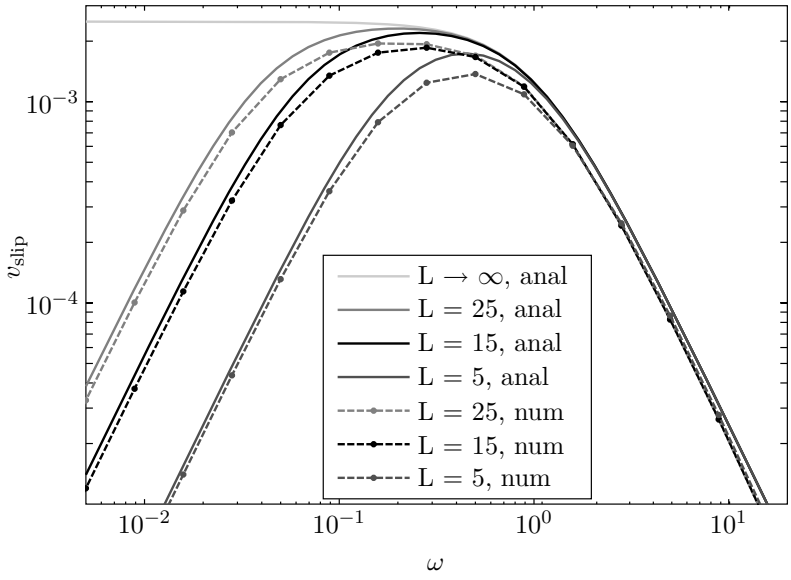

Figure 5.1: Comparison between numerical (dashed lines) and analytical (solid lines) slip velocities as function of frequency for three different dimensionless capacitor half lengths L, where the characteristic length scale is the cylinder radius a. The analytical slip velocity for the unconfined cylinder $L \to \infty$ is additionally plotted.

Chapter 6

Topology optimization of ICEO system

In this chapter we focus on the application of topology optimization to AC-driven ICEO systems. With this method it is possible to optimize the dielectric shapes for many purposes, such as mixing and pumping efficiency, where the latter is the main focus here. No studies have previously been carried out concerning the influence of topological changes on the efficiency of the systems.

Our model system consists of two externally biased, parallel capacitor plates confining an electrolyte. A dielectric solid is shaped and positioned in the electrolyte, and the external bias induces ICEO flow at the dielectric surfaces. In this work we focus on optimizing the topology and shape of the dielectric solid to generate the maximal flow perpendicular to the external applied electric field. This example of establishing an optimized ICEO micropump serves as demonstration of the implemented topology optimization method.

Following the method of Borrvall and Petersson [32] and the implementation by Olesen, Okkels and Bruus [41] of topology optimization in microfluidic systems we introduce an artificial design field $\gamma(\boldsymbol{r})$ in the governing equations. The design field varies continuously from zero to unity, and it defines to which degree a point in the design domain is occupied by dielectric solid or electrolytic fluid. Here, $\gamma = 0$ is the limit of pure solid and $\gamma = 1$ is the limit of pure fluid, while intermediate values of γ represent a mixture of solid and fluid. In this way, the discrete problem of placing and shaping the dielectric solid in the electrolytic fluid is converted into a continuous problem, where the sharp borders between solid and electrolyte are replaced by continuous transitions throughout the design domain. In some sense one can think of the solid/fluid mixture as a sort of ion-exchange membrane in the form of a sponge with varying permeability. This continuum formulation allows for an efficient gradient-based optimization of the problem.

In one important aspect our system differs from other systems previously studied by topology optimization: induced-charge electro-osmosis is a boundary effect relying on the polarization and screening charges in a nanometer-sized region around the solid/fluid interface. Previously studied systems have all been relying on bulk properties such as the distribution of solids in mechanical stress analysis [57], photonic band gap structures in

optical wave guides [34], and acoustic noise reduction [35], or on the distribution of solids and liquids in viscous channel networks [32, 41, 58] and chemical microreactors [36]. In our case, as for most other applications of topology optimization, no mathematical proof exists that the topology optimization routine indeed will result in an optimized structure. Moreover, since the boundary effects of our problem result in a numerical analysis which is very sensitive on the initial conditions, on the meshing, and on the specific form of the design field, we take the more pragmatic approach of finding non-trivial geometries by use of topology optimization, and then validate the optimality by transferring the geometries to conventional electrokinetic models not relying on the artificial design field.

6.1 Model system

We consider a parallel-plate capacitor externally biased with a harmonic oscillating voltage difference $\Delta\phi = 2V_0\cos(\omega t)$ and enclosing an electrolyte and a dielectric solid. The two capacitor plates are positioned at $z = \pm H$ and periodic boundary conditions are applied at the open ends at $x = \pm L/2$. The resulting bound domain of size $L \times 2H$ in the xz-plane is shown in Fig. 6.1. The system is assumed to be unbounded and translational invariant in the perpendicular y-direction. The topology and shape of the dielectric solid is determined by the numerical optimization routine acting only within a smaller rectangular, central design domain of size $l \times 2h$. The remaining domain outside this area is filled with pure electrolyte. Double layers, or Debye screening layers, are formed in the electrolyte around each piece of dielectric solid to screen out the induced polarization charges. The pull from the external electric field on these screening layers in the design domain drives an ICEO flow in the entire domain.

If the dielectric solid is symmetric around the x-axis, the anti-symmetry of the applied external bias voltage ensures that the resulting electric potential is anti-symmetric and the velocity and pressure fields symmetric around the center plane $z = 0$. This symmetry appears in most of the cases studied in this paper, and when present it is exploited to obtain a significant decrease in memory requirements of the numerical calculations.

The specific goal of our analysis is to determine the topology and shape of the dielectric solid such that a maximal flow rate Q is obtained parallel to the x-axis, i.e. perpendicular to the direction of external potential field gradient.

6.2 Governing equations

The governing equations for the conventional ICEO model have been presented in Sec. 5.1. As mentioned, we employ the linearized equation system, and introduce complex field notation. The decoupled electrical problem is then solved in one step, while the time averaged flow problem is subsequently solved. In the following, the corresponding governing equations used in the implementation of the topology optimization problem is presented.

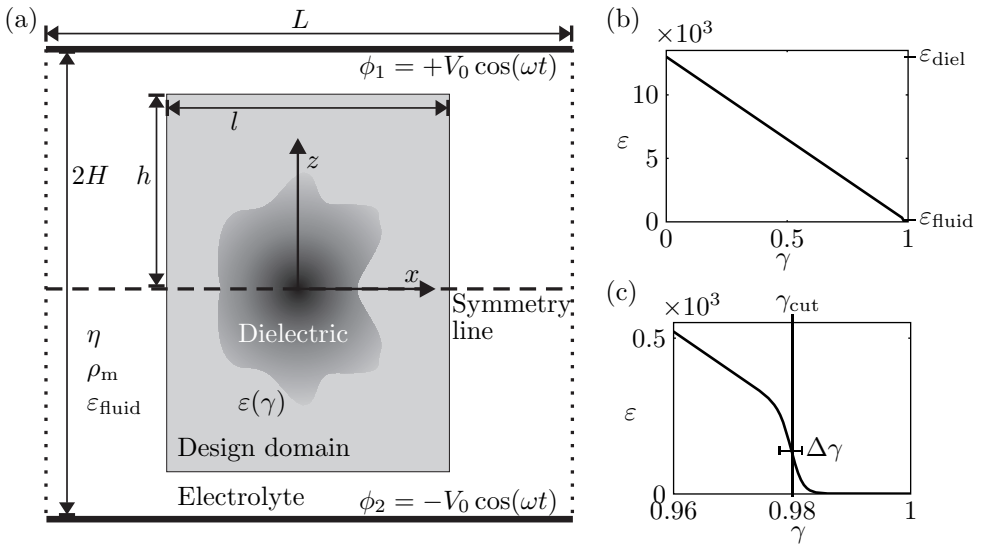

Figure 6.1: (a) A sketch of the rectangular $L \times 2H$ cross-section of the electrolytic capacitor in the xz-plane. The external voltage ϕ_1 and ϕ_2 is applied to the two infinite parallel-plate electrodes (thick black lines) at $z = \pm H$. The voltage difference $\phi_1 - \phi_2$ induces an ICEO flow around the un-biased dielectric solid (dark gray) shaped by the topology optimization routine limited to the rectangular $l \times 2h$ design domain (light gray). The dielectric solid is surrounded by pure electrolyte (light gray and white). Periodic boundary conditions are applied ar the vertical edges (dotted lines). (b) The dimensionless electric permittivity ε as a function of the design variable γ. (c) Zoom-in on the rapid convergence of $\varepsilon(\gamma)$ towards $\varepsilon_{\text{fluid}} = 1$ for γ approaching unity after passing the value $\gamma_{\text{cut}} - \Delta\gamma \simeq 0.98$.

6.2.1 The artificial design field γ used in the topology optimization model of ICEO

To be able to apply the method of topology optimization, it is necessary to extend the conventional ICEO model with three additional terms, all functions of a position-dependent artificial design field $\gamma(\boldsymbol{r})$. The design field varies continuously from zero to unity, where $\gamma = 0$ is the limit of a pure dielectric solid and $\gamma = 1$ is the limit of a pure electrolytic fluid. The intermediate values of γ represent a mixture of solid and fluid.

The first additional term concerns the purely fluid dynamic part of our problem. Here, we follow Borrvall and Petersson [32] and model the dielectric solid as a porous medium giving rise to a Darcy friction force density $-\alpha(\gamma)\boldsymbol{v}$, where $\alpha(\gamma)$ may be regarded as a local inverse permeability, which we denote the Darcy friction. We let $\alpha(\gamma)$ be a linear function of γ of the form $\alpha(\gamma) = \alpha_{\max}(1-\gamma)$, where $\alpha_{\max} = \eta/\ell_{\text{pore}}^2$ is the Darcy friction of the porous dielectric material assuming a characteristic pore size ℓ_{pore}. In the limit of a completely impenetrable solid the value of $\alpha_{\max}$ approaches infinity, which leads to a vanishing fluid velocity $\boldsymbol{v}$. The modified Navier–Stokes equation extending to the entire

domain, including the dielectric material, becomes

$$\rho_{\mathrm{m}}\left[\frac{\partial \boldsymbol{v}}{\partial t} + (\boldsymbol{v}\cdot\boldsymbol{\nabla})\boldsymbol{v}\right] = -\boldsymbol{\nabla}p + \eta\nabla^2\boldsymbol{v} - \rho_{\mathrm{el}}\boldsymbol{\nabla}\phi - \alpha(\gamma)\boldsymbol{v}. \tag{6.1}$$

The second additional term is specific to our problem. Since the Navier–Stokes equation is now extended to include also the porous dielectric medium, our model must prevent the unphysical penetration of the electrolytic ions into the solid. Following the approach of Kilic *et al.* [59], where current densities are expressed as gradients of chemical potentials, $\boldsymbol{J} \propto -\boldsymbol{\nabla}\mu$, we model the ion expulsion by adding an extra free energy term $\kappa(\gamma)$ to the chemical potential $\mu_\pm = \pm Ze\phi + k_{\mathrm{B}}T\ln(c_\pm/c_0) + \kappa(\gamma)$ of the ions, where c_0 is the bulk ionic concentration for both ionic species. As above we let $\kappa(\gamma)$ be a linear function of γ of the form $\kappa(\gamma) = \kappa_{\max}(1-\gamma)$, where $\kappa_{\max}$ is the extra energy cost for an ion to enter a point containing a pure dielectric solid as compared to a pure electrolytic fluid. The value of $\kappa_{\max}$ is set to an appropriately high value to expel the ions efficiently from the porous material while still ensuring a smooth transition from dielectric solid to electrolytic fluid. The modified ion flux density becomes

$$\boldsymbol{J}_\pm = -D\left(\boldsymbol{\nabla}c_\pm + \frac{\pm Ze}{k_{\mathrm{B}}T}c_\pm\boldsymbol{\nabla}\phi + \frac{1}{k_{\mathrm{B}}T}c_\pm\boldsymbol{\nabla}\kappa(\gamma)\right). \tag{6.2}$$

The third and final additional term is also specific to our problem. Electrostatically, the transition from the dielectric solid to the electrolytic fluid is described through the Poisson equation by a γ-dependent permittivity $\varepsilon(\gamma)$. This modified permittivity varies continuously between the value $\varepsilon_{\mathrm{diel}}$ of the dielectric solid and $\varepsilon_{\mathrm{fluid}}$ of the electrolytic fluid. As above, we would like to choose $\varepsilon(\gamma)$ to be a linear function of γ. However, during our analysis using a metallic dielectric with $\varepsilon_{\mathrm{diel}} = 10^6\varepsilon_0$ in an aqueous electrolyte with $\varepsilon_{\mathrm{fluid}} = 78\,\varepsilon_0$ we found unphysical polarization phenomena in the electrolyte due to numerical rounding-off errors for γ near, but not equal to, unity. To overcome this problem we ensured a more rapid convergence towards the value $\varepsilon_{\mathrm{fluid}}$ by introducing a cut-off value $\gamma_{\mathrm{cut}} \simeq 0.98$, a transition width $\Delta\gamma \simeq 0.002$, and the following expression for $\varepsilon(\gamma)$,

$$\varepsilon(\gamma) = \varepsilon_{\mathrm{diel}} + (\varepsilon_{\mathrm{fluid}} - \varepsilon_{\mathrm{diel}})\left\{1 - \frac{(1-\gamma)}{2}\left[\tanh\left(\frac{\gamma_{\mathrm{cut}}-\gamma}{\Delta\gamma}\right) + 1\right]\right\}. \tag{6.3}$$

For $\gamma \lesssim \gamma_{\mathrm{cut}}$ we obtain the linear relation $\varepsilon(\gamma) = \varepsilon_{\mathrm{diel}} + (\varepsilon_{\mathrm{fluid}} - \varepsilon_{\mathrm{diel}})\gamma$, while for $\gamma \gtrsim \gamma_{\mathrm{cut}}$ we have $\varepsilon(\gamma) = \varepsilon_{\mathrm{fluid}}$, see Fig. 6.1(b)-(c). For γ sufficiently close to unity (and not only when γ equals unity with numerical precision), this cut-off procedure ensures that the calculated topological break up of the dielectric solid indeed leads to several correctly polarized solids separated by pure electrolyte. The modified Poisson equation becomes

$$\boldsymbol{\nabla}\cdot\left[\varepsilon(\gamma)\boldsymbol{\nabla}\phi\right] = -\rho_{\mathrm{el}}. \tag{6.4}$$

Finally, we introduce the γ-dependent quantity, the so-called objective function $\Phi[\gamma]$, to be optimized by the topology optimization routine: the flow rate in the x-direction perpendicular to the applied potential gradient. Due to incompressibility, the flow rate

$Q(x)$ is the same through cross-sections parallel to the yz-plane at any position x. Hence we can use the numerically more stable integrated flow rate as the objective function,

$$\Phi[\gamma(\boldsymbol{r})] = \int_0^L Q(x)\,\mathrm{d}x = \int_\Omega \boldsymbol{v}\cdot\hat{\boldsymbol{n}}_x\,\mathrm{d}x\,\mathrm{d}z, \tag{6.5}$$

where Ω is the entire geometric domain (including the design domain), and $\hat{\boldsymbol{n}}_x$ the unit vector in the x direction.

6.2.2 Dimensionless form

To prepare the numerical implementation, the governing equations are rewritten in dimensionless form, using the characteristic parameters of the system. In conventional ICEO systems the size a of the dielectric solid is the natural choice for the characteristic length scale ℓ_0, since the generated slip velocity at the solid surface is proportional to a. However, when employing topology optimization we have no prior knowledge of this length scale, and thus we choose it to be the fixed geometric half-length $\ell_0 = H$ between the capacitor plates. Further characteristic parameters are the ionic concentration c_0 of the bulk electrolyte, and the thermal voltage $\phi_0 = k_\mathrm{B}T/(Ze)$. The characteristic velocity u_0 is chosen as the Helmholtz–Smoluchowski slip velocity, Eq. (2.20), induced by the local electric field $E = \phi_0/\ell_0$, and finally the pressure scale is set by the characteristic microfluidic pressure scale $p_0 = \eta u_0/\ell_0$.

Although strictly applicable only to parallel-plate capacitors, the characteristic time τ_0 of the general system in chosen as the RC time of the double layer in terms of the Debye length λ_D of the electrolyte [49],

$$\tau_0 = \frac{\ell_0}{D}\,\lambda_\mathrm{D} = \frac{\ell_0}{D}\sqrt{\frac{k_\mathrm{B}T\varepsilon_\mathrm{fluid}}{2(Ze)^2 c_0}}. \tag{6.6}$$

Moreover, three characteristic numbers are connected to the γ-dependent terms in the governing equations: The characteristic free energy κ_0, the characteristic permittivity chosen as the bulk permittivity $\varepsilon_\mathrm{fluid}$, and the characteristic Darcy friction coefficient α_0. In summary,

$$\ell_0 = H, \qquad \phi_0 = \frac{k_\mathrm{B}T}{Ze}, \quad u_0 = \frac{\varepsilon_\mathrm{fluid}\phi_0^2}{\eta\,\ell_0}, \quad p_0 = \frac{\eta\,u_0}{\ell_0}, \tag{6.7a}$$

$$\tau_0 = \frac{\ell_0\lambda_\mathrm{D}}{D}, \quad \omega = \frac{1}{\tau_0}, \qquad \kappa_0 = k_\mathrm{B}T, \qquad \alpha_0 = \frac{\eta}{\ell_0^2}. \tag{6.7b}$$

The new dimensionless variables (denoted by a tilde) thus become

$$\tilde{\boldsymbol{r}} = \frac{\boldsymbol{r}}{\ell_0}, \quad \tilde{\boldsymbol{v}} = \frac{\boldsymbol{v}}{u_0}, \quad \tilde{p} = \frac{p}{p_0}, \quad \tilde{\phi} = \frac{\phi}{\phi_0}, \quad \tilde{c}_\pm = \frac{c_\pm}{c_0}, \tag{6.8a}$$

$$\tilde{t} = \frac{t}{\tau_0}, \quad \tilde{\kappa} = \frac{\kappa}{\kappa_0}, \quad \tilde{\alpha} = \frac{\alpha}{\alpha_0}, \quad \tilde{\varepsilon} = \frac{\varepsilon}{\varepsilon_\mathrm{fluid}}. \tag{6.8b}$$

In the following all variables and parameters are made dimensionless using these characteristic numbers and for convenience the tilde is henceforth omitted.

6.2.3 Linearized and reformulated equations

The approximations and reformulations presented in Sec. 5.1 are applied to the governing equations, which are now extended by the artificial γ-field terms. The resulting electrodynamic equations for the electric potential Φ and the charge density P are then

$$\boldsymbol{\nabla}\cdot\big[\varepsilon(\gamma)\boldsymbol{\nabla}\Phi_R\big] = -\frac{1}{\epsilon^2}P_R, \tag{6.9a}$$

$$\boldsymbol{\nabla}\cdot\big[\varepsilon(\gamma)\boldsymbol{\nabla}\Phi_I\big] = -\frac{1}{\epsilon^2}P_I, \tag{6.9b}$$

$$\boldsymbol{\nabla}\cdot\big[\boldsymbol{\nabla}\Phi_R + \boldsymbol{\nabla}P_R + P_R\boldsymbol{\nabla}\kappa(\gamma)\big] = -\frac{\omega}{\epsilon}P_I, \tag{6.9c}$$

$$\boldsymbol{\nabla}\cdot\big[\boldsymbol{\nabla}\Phi_I + \boldsymbol{\nabla}P_I + P_I\boldsymbol{\nabla}\kappa(\gamma)\big] = +\frac{\omega}{\epsilon}P_R, \tag{6.9d}$$

where we have introduced the dimensionless thickness of the linear Debye layer $\epsilon = \lambda_{\mathrm{D}}/\ell_0$. Correspondingly, the time-averaged hydrodynamic fields $\langle\boldsymbol{v}\rangle$ and $\langle p\rangle$ are governed by,

$$\boldsymbol{\nabla}\cdot\langle\boldsymbol{v}\rangle = 0, \tag{6.10a}$$

$$0 = -\boldsymbol{\nabla}\langle p\rangle + \nabla^2\langle\boldsymbol{v}\rangle + \langle\boldsymbol{f}_{\mathrm{el}}\rangle - \alpha(\gamma)\langle\boldsymbol{v}\rangle, \tag{6.10b}$$

where the time-averaged electric body force density $\langle\boldsymbol{f}_{\mathrm{el}}\rangle$ is given by

$$\langle\boldsymbol{f}_{\mathrm{el}}\rangle = -\frac{1}{2\epsilon^2}\big[P_R\boldsymbol{\nabla}\Phi_R + P_I\boldsymbol{\nabla}\Phi_I\big]. \tag{6.10c}$$

6.2.4 Boundary conditions

In the search for left-right symmetry breaking topologies of the dielectric material, it is possible to exploit the top-down symmetry around $z = 0$ and only consider the upper half $(0 < z < 1)$ of the domain. The boundary conditions of this problem are much alike the conditions presented in Sec. 5.1. On the driving electrode we set the amplitude V_0 of the applied potential, and a no-slip condition for the fluid velocity. Any electrode reactions at the electrode surface is neglected, so there is no net ion flux in the normal direction to the boundary with unit vector $\hat{\boldsymbol{n}}$. Thus, at $z = 1$ we have

$$\Phi_R = V_0, \quad \Phi_I = 0, \tag{6.11a}$$

$$\hat{\boldsymbol{n}}\cdot\big[\boldsymbol{\nabla}\Phi_R + \boldsymbol{\nabla}P_R + P_R\boldsymbol{\nabla}\kappa(\gamma)\big] = 0, \tag{6.11b}$$

$$\hat{\boldsymbol{n}}\cdot\big[\boldsymbol{\nabla}\Phi_I + \boldsymbol{\nabla}P_I + P_I\boldsymbol{\nabla}\kappa(\gamma)\big] = 0, \tag{6.11c}$$

$$\langle\boldsymbol{v}\rangle = \boldsymbol{0}. \tag{6.11d}$$

Due to the anti-symmetry of the applied potential, the charge density and the potential must be zero on the symmetry axis $(z = 0)$. There is no fluid flux in the normal direction and the shear stresses vanish. So, at $x = 0$ we have

$$\Phi_R = \Phi_I = 0, \quad P_R = P_I = 0, \tag{6.12a}$$

$$\hat{\boldsymbol{n}} \cdot \langle \boldsymbol{v} \rangle = 0, \quad \hat{\boldsymbol{t}} \cdot \langle \boldsymbol{\sigma} \rangle \cdot \hat{\boldsymbol{n}} = 0, \tag{6.12b}$$

where the dimensionless stress tensor is $\langle \sigma_{ik} \rangle = -\langle p \rangle \delta_{ik} + \big(\partial_i \langle v_k \rangle + \partial_k \langle v_i \rangle\big)$, and $\hat{\boldsymbol{n}}$ and $\hat{\boldsymbol{t}}$ are the normal and tangential unit vectors, respectively. On the remaining vertical boundaries ($x = \pm L/2\ell_0$) periodic boundary conditions are applied to all the fields.

6.3 Implementation and validation of numerical code

6.3.1 Implementation and parameter values

For our numerical analysis we use the programs, methods and implementation presented in Sec. 2.5.

Due to the challenges discussed in Sec. 6.3.2 of resolving all length scales in the electrokinetic model, we have chosen to study small systems, $2H = 500$ nm, with a relatively large Debye length, $\lambda_{\mathrm{D}} = 20$ nm. Our main goal is to provide a proof of concept for the use of topology optimization in electro-hydrodynamic systems, so the difficulties in fabricating actual devices on this sub-micrometric scale is not a major concern for us in the present work. A list of the parameter values chosen for our simulations is given in Table 6.1.

For a typical topology optimization, as the one shown in Fig. 6.5(a), approximately 5400 FEM elements are involved. In each iteration loop of the topology optimization routine three problems are solved: the electric problem , the hydrodynamic problem, and

Table 6.1: Parameters used in the simulations of the topology optimization ICEO model and the conventional ICEO model.

Parameter	Symbol	Dimensionless value	Physical value
Characteristic length	ℓ_0	1.0	250 nm
Channel half-height	H	1.0	250 nm
Channel length	L	2.0	500 nm
Design domain half-height	h	0.8	200 nm
Design domain length	l	0.6	150 nm
Linear Debye length	λ_{D}	0.08	20 nm
Characteristic velocity	u_0	1.0	1.7×10^{-3} m/s
Characteristic potential	ϕ_0	1.0	25 mV
External potential amplitude	V_0	1.0	25 mV
External potential frequency	ω	6.25	4×10^5 rad/s
Bulk fluid permittivity	$\varepsilon_{\mathrm{fluid}}$	1.0	$78\,\varepsilon_0$
Dielectric permittivity	$\varepsilon_{\mathrm{diel}}$	1.3×10^4	$10^6\,\varepsilon_0$
Bulk ionic concentration	c_0	1.0	0.23 mM
Fluid viscosity	η	1.0	10^{-3} Pa s
Ionic diffusion constant	D	1.0	$2 \times 10^{-9}\mathrm{m}^2/\mathrm{s}$
Ionic free energy in solid	κ	3.0	75 mV
Maximum Darcy friction	$\alpha_{\max}$	10^5	2×10^{16} Pa s/m^2

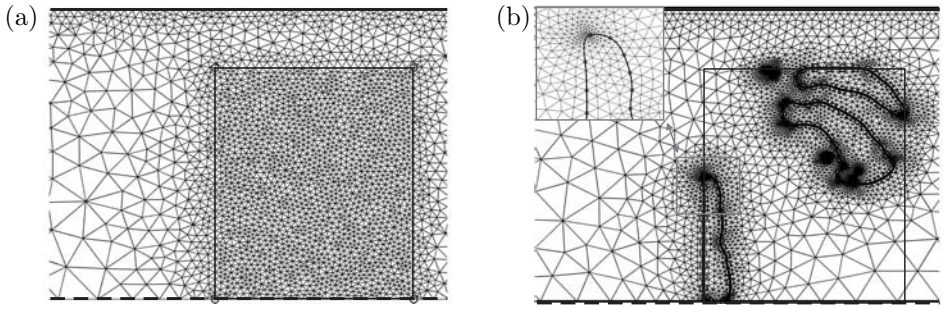

Figure 6.2: (a) Meshing for a design field model of Fig. 6.5(a) with a uniformly fine mesh inside the design domain and a coarser mesh outside. (b) Meshing for the hard-wall model of Fig. 6.5(b) with a mesh refinement in the double layer surrounding the dielectric solids.

the adjunct problem for the sensitivity analysis, involving 4×10^4 , 2×10^4 , and 7×10^4 degrees of freedom, respectively. On an Intel Core 2 Duo 2 GHz processer with 2 GB RAM the typical CPU time is several hours.

6.3.2 Validation of the γ-dependent ICEO model

We have validated our simulations in two steps. First, the conventional ICEO model not involving the design field $\gamma(\boldsymbol{r})$ is validated against the analytical result for the slip velocity at a simple dielectric cylinder in an infinite AC electric field given by Squires and Bazant [27]. Second, the design field model is compared to the conventional model. This two-step validation procedure is necessary because of the limited computer capacity. The involved length scales in the problem make a large number of mesh elements necessary for the numerical solution by the finite element method. Four different length scales appear in the gamma-dependent model for the problem of a cylinder placed mid between the parallel capacitor plates: The distance H from the center of the dielectric cylinder to the biased plates, the radius a of the cylinder, the Debye length λ_D, and the length d over which the design field γ changes from zero to unity. This last and smallest length-scale d in the problem is controlled directly be the numerical mesh size set up in the finite element method. It has to be significantly smaller than λ_D to model the double layer dynamics correctly, so here a maximum value of the numerical mesh size is defined. Examples of the meshing are shown in Fig. 6.2.

The analytical solution of Squires and Bazant [27] is only strictly valid in the case of an infinitely thin Debye layer in an infinite electric field. So, to compare this model with the bounded numerical model the plate distance must be increased to minimize the influence on the effective slip velocity. Furthermore, in the perspective of the results presented in Chap. 4 the Debye length λ_D should be about a factor of 10^3 smaller than the cylinder radius a to approximate the solution for the infinitely thin Debye layer model. Including the demand of d being significantly smaller than λ_D we end up with a length scale difference of at least 10^5, which is difficult to resolve by the finite element mesh, even when mesh adaption is used. Consequently, we have checked that the slip velocity for the conventional model converges towards the analytical value when the ratio λ_D/a decreases,

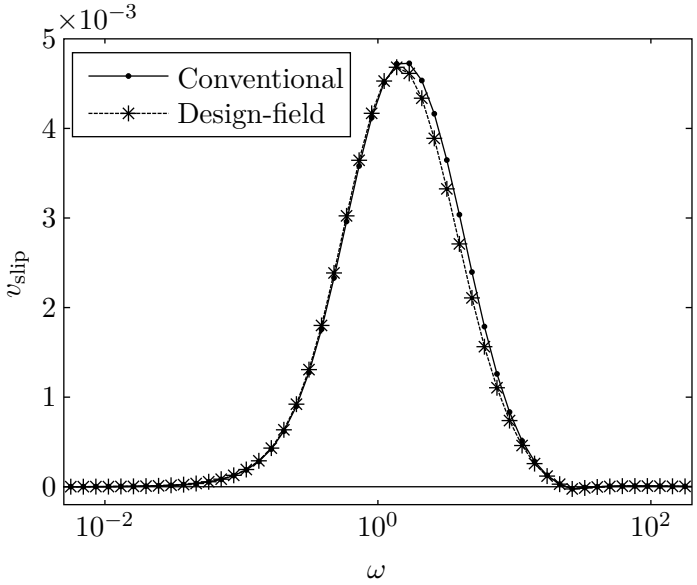

Figure 6.3: Comparison of the slip velocities v_{slip} calculated with conventional ICEO model (solid line) and with the design-field ICEO model (dashed line) as function of the frequency ω. The slip velocity is generated around a dielectric cylinder between two capacitor plates.

see Figs. 4.4 and 5.1.

Afterwards, we have compared the slip velocities for the conventional and design-field models in a smaller system, where a dielectric cylinder with radius $a = 0.25$ is placed centrally between the capacitor plates. The parameter values were the same as listed in Table 6.1, but with slightly changed lengths H and λ_{D}, resulting in the ratios $H/a = 6$, $a/\lambda_{\text{D}} = 10$ and $\lambda_{\text{D}}/d = 5$.

Fig. 6.3 shows the calculated slip-velocities v_{slip} as function of frequency ω for each of the models, where v_{slip} has been determined by Eq. (4.18). The plot is shown on a semi-logarithmic scale since a single negative velocity was calculated in the high frequency regime. We note that the resonance peak corresponds to the expected value of $\omega_c = 4$ for the cylinder diameter $a = 0.25$. The two models yield nearly the same result. The only difference between the two models is a slight shift in the resonance peak. In the gamma-dependent model the cylinder effectively has a slightly larger diameter corresponding to one mesh-element $d = 5 \times 10^{-3}$. This diameter difference between the two models theoretically results in a resonance frequency shift of $\Delta\omega_c \sim 0.1$ for the cylinder, which could be the origin of the minor discrepancy. The velocity decrease towards lower frequencies coincides for the two models, where the characteristic frequency is controlled by the capacitor plate distance, which is exactly the same in the two models.

6.3.3 Validation of the self-consistency of the topology optimization

As an example of our validation of the self-consistency of the topology optimization, we study the dependence of the objective function $Q = \Phi[\omega, \gamma(\omega, \boldsymbol{r})]$ on the external driving

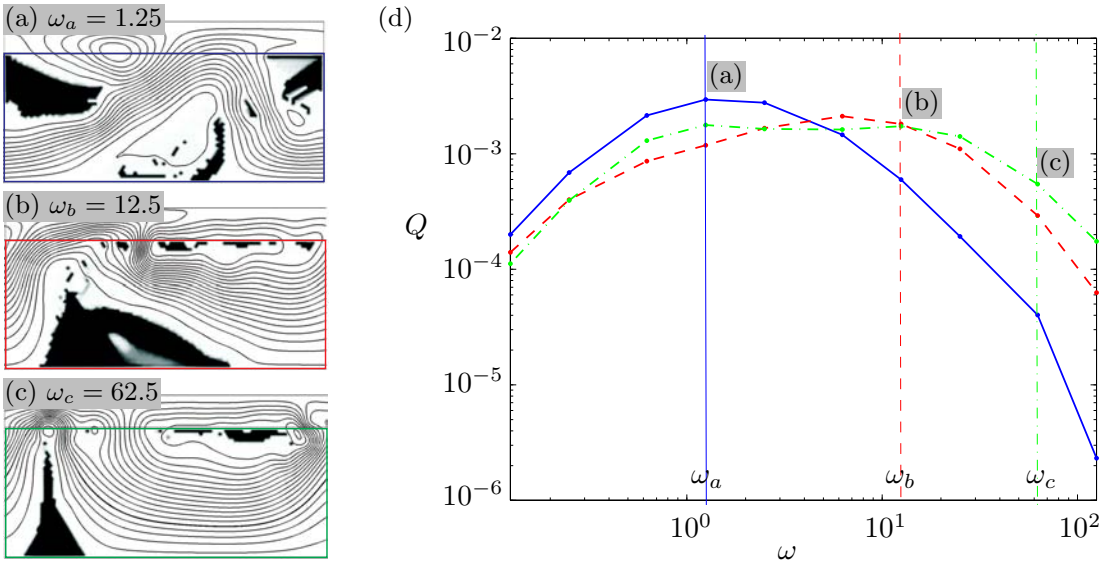

Figure 6.4: Validation of the self-consistency of the topology optimization for different driving frequencies ω. (a) The streamline pattern (thick lines) for $\omega = \omega_a = 1.25$ calculated using the design-field ICEO model with a porous dielectric medium (black and gray), the structure γ_a of which has been found by topology optimization within the indicated rectangular design domain (straight lines). The flow rate for this converged solution structure is $Q = 2.95 \times 10^{-3}$. (b) As panel (a) but with $\omega = \omega_b = 12.5$ and $Q = 1.82 \times 10^{-3}$. (c) As panel (a) but with $\omega = \omega_c = 62.5$ and $Q = 0.55 \times 10^{-3}$. (d) Flow rate Q versus frequency ω for each of the three structures in panel (a), (b), and (c). Note that structure γ_a indeed yields the highest flow rate Q for $\omega = \omega_a$, structure γ_b maximizes Q for $\omega = \omega_b$, and structure γ_c maximizes Q for $\omega = \omega_c$.

frequency ω. As shown in Fig. 6.4(a)-(c) we have calculated the topology optimized dielectric structures $\gamma_j = \gamma(\omega_j, \boldsymbol{r})$, $j = a, b, c$, for three increasing frequencies $\omega = \omega_a = 1.25$, $\omega = \omega_b = 12.5$, and $\omega = \omega_c = 62.5$. In the following we let $Q_j(\omega)$ denote the flow rate calculated at the frequency ω for a structure optimized at the frequency ω_j.

First, we note that $Q_j(\omega_j)$ decreases as the frequency increases above the characteristic frequency $\omega_0 = 1$; $Q_a(\omega_a) = 2.95 \times 10^{-3}$, $Q_b(\omega_b) = 1.82 \times 10^{-3}$, and $Q_c(\omega_c) = 0.55 \times 10^{-3}$. This phenomenon is a general aspect of ICEO systems, where the largest effect is expected to happen at $\omega \sim 1$.

Second, and most significant, we see in Fig. 6.4(d) that structure γ_a is indeed the optimal structure for $\omega = \omega_a$ since $Q_a(\omega_a) > Q_b(\omega_a), Q_c(\omega_a)$. Likewise, γ_b is optimal for $\omega = \omega_b$, and γ_c is optimal for $\omega = \omega_c$.

We have gained confidence in the self-consistency of our topology optimization routine by carrying out a number of tests like the one in the example above.

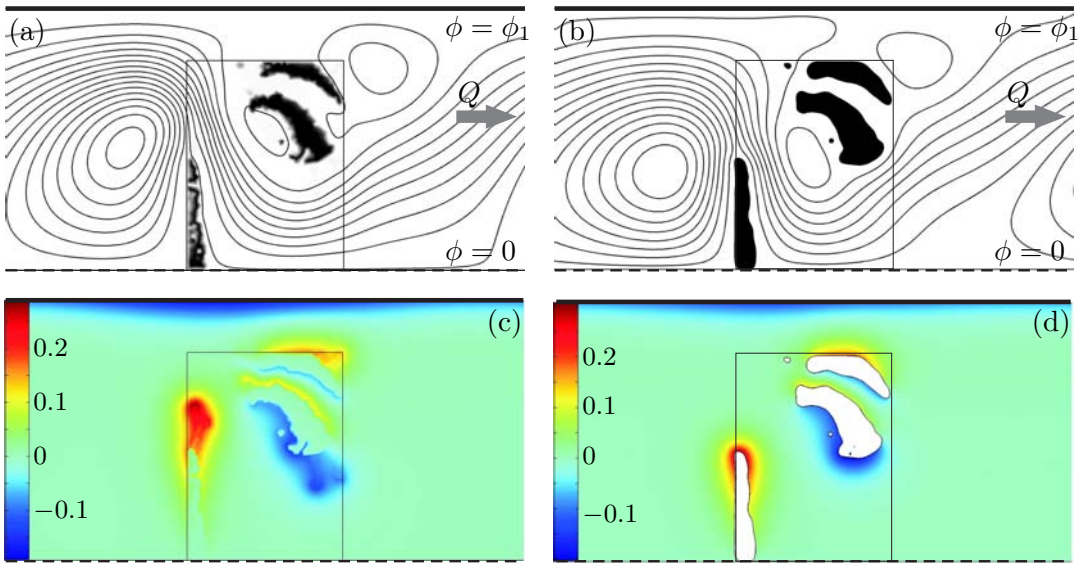

Figure 6.5: (a) The streamline pattern (thick lines) drawn as equidistant contours of the flowrate. The flow has been calculated for $\omega = 6.25$ using the design-field ICEO model with a porous dielectric medium (black and gray), the structure of which has been found by topology optimization within the indicated rectangular design domain (thin lines). The flow rate for this converged solution structure is $Q = 2.99 \times 10^{-3}$. (b) The streamline pattern (full lines) calculated using the conventional ICEO model with a hard-walled dielectric solid (black). The shape of the dielectric solid is the 0.95-contour of the γ-field taken from the topology-optimized structure shown in panel (a). The flow rate is $Q = Q^* = 1.88 \times 10^{-3}$. (c) and (d) Color plot of the charge density $\rho(\boldsymbol{r})$ corresponding to panel (a) and (b), respectively. See Table 6.1 for parameter values.

6.4 Results

6.4.1 Topology optimization

For each choice of parameters the topology optimization routine converges to a specific distribution of dielectric solid given by $\gamma(\boldsymbol{r})$. As a starting point for the investigation of the optimization results we used the parameters listed in Table 6.1. As discussed above, the geometric dimensions are chosen as large as possible within the computational limitations: the Debye length is set to $\lambda_D = 20$ nm and the distance between the capacitor plates to $2H = 500$ nm. The external bias voltage is of the order of the thermal voltage $V_0 = 25$ mV to ensure the validity of the linear Debye–Hückel approximation. We let the bulk fluid consist of water containing small ions, such as dissolved KCl, with a concentration $c_0 = 0.23$ mM set by the chosen Debye length. The dielectric material permittivity is set to $\varepsilon_{\text{diel}} = 10^6\, \varepsilon_0$ in order to mimic the characteristics of a metal. The artificial parameters κ and $\alpha_{\max}$ are chosen on a pure computational basis, where they have to mimic the real physics in the limits of fluid and solid, but also support the optimization routine when the

phases are mixed.

Throughout our simulations we have primarily varied the applied frequency ω and the size $l \times 2h$ of the design domain. In Fig. 6.4 we have shown examples of large design domains with $l \times h = 2.0 \times 0.8$ covering 80% of the entire domain and frequency sweeps over three orders of magnitude. However, in the following we fix the frequency to be $\omega = 6.25$, where the ICEO response is close to maximum. Moreover we focus on a smaller design domain $l \times h = 0.6 \times 0.8$ to obtain better spatial resolution for the given amount of computer memory and to avoid getting stuck in local optima. It should be stressed that the size of the design domain has a large effect on the specific form and size of the dielectric islands produced by the topology optimization. Also, it is important if the design domain is allowed to connect to the capacitor plates or not, see the remarks in Sec. 6.5.

The converged solution found by topology optimization under these conditions is shown in Fig. 6.5(a). The shape of the porous dielectric material is shown together with a streamline plot of equidistant contours of the flow rate. We notice that many stream lines extend all the way through the domain from left to right indicating that a horizontal flow parallel to the x-axis is indeed established. The resulting flow rate is $Q = 2.99 \times 10^{-3}$. The ICEO flow of this solution, based on the design-field model, is validated by transferring the geometrical shape of the porous dielectric medium into a conventional ICEO model with a hard-walled dielectric not depending on the design field. In the latter model the sharp interface between the dielectric solid and the electrolyte is defined by the 0.95-contour of the topology optimized design field $\gamma(\boldsymbol{r})$. The resulting geometry and streamline pattern of the conventional ICEO model is shown in Fig. 6.5(b). The flow rate is now found to be $Q = Q^* = 1.88 \times 10^{-3}$. There is a close resemblance between the results of two models both qualitatively and quantitatively. It is noticed how the number and positions of the induced flow rolls match well, and also the absolute values of the induced horizontal flow rates differs only by 37%.

Based on the simulation we can now justify the linearization of our model. The largest velocity u_{gap} is found in the gap of width ℓ_{gap} between the two satellite pieces and the central piece. As listed in Table 6.2 the resulting Reynolds number is $Re = 2.8 \times 10^{-7}$, the Péclet number is $Pé = 1.4 \times 10^{-3}$, while the Debye–Hückel number is $Hü = 0.13$.

Table 6.2: The value of characteristic physical quantities calculated in the topology optimization ICEO model corresponding to Fig. 6.5.

Quantity	Symbol	Dimensionless value	Physical value
Gap between dielectric pieces	ℓ_{gap}	0.4	100 nm
Velocity in the gap	u_{gap}	$0.016\, u_0$	28 μm/s
Largest zeta potential	$\zeta_{\max}$	$0.5\, \phi_0$	12.5 mV
Reynolds number Re	$\rho_{\mathrm{m}} u_{\mathrm{gap}} \ell_{\mathrm{gap}} / \eta$	2.8×10^{-6}	–
Péclet number $Pé$	$u_{\mathrm{gap}} \ell_{\mathrm{gap}} / D$	1.4×10^{-3}	–
Debye–Hückel number $Hü$	$e\zeta_{\max} / (4 k_{\mathrm{B}} T)$	0.13	–

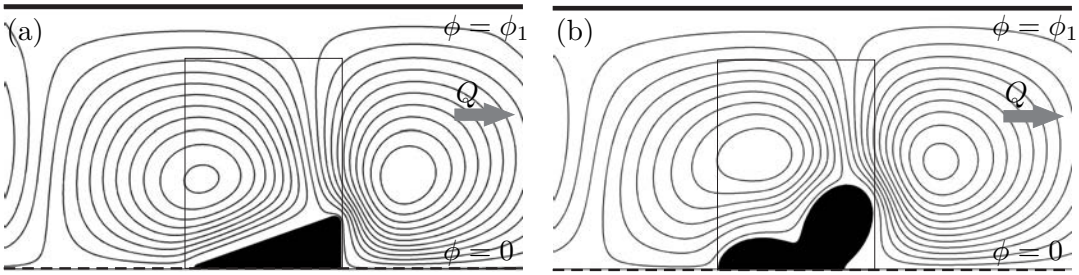

Figure 6.6: (a) The streamline pattern (thick lines) for the shape-optimized right-angled triangle fixed at the symmetry line $z = 0$ calculated for $\omega = 6.25$ using the conventional ICEO model with a hard-walled dielectric solid (black). In the full domain this is a triangle symmetric around $z = 0$. The flow rate is $Q = 0.32 \times 10^{-3}$. (b) As in panel (a) but without constraining the triangle to be right-angled. In the full domain the shape is foursided polygon symmetric around $z = 0$. The flow rate is $Q = 0.76 \times 10^{-3}$. Note that all sharp corners of the polygons have been rounded by circular arcs of radius 0.01.

6.4.2 Comparison to simple shapes

We evaluate our result for the optimized flow rate by comparing it to those obtained for more basic, simply connected, dielectric shapes, such as triangles and perturbed circles previously studied in the literature as flow inducing objects both analytically and experimentally [7,27]. For comparison, such simpler shapes have been fitted into the same design domain as used in the topology optimization Fig. 6.5(a), and the conventional ICEO model without the design field was solved for the same parameter set. In Fig. 6.7(a) the resulting flow for a triangle with straight faces and rounded corners is shown. The height b of the face perpendicular to the symmetry line was varied within the height of the design domain $0 < b < 0.8$, and the height $b = 0.32$ generating the largest flow in the x-direction results in a flow rate of $Q = 0.22 \times 10^{-3}$, which is eight times smaller than the topology optimized result. In Fig. 6.7(b) the induced flow around a perturbed cylinder with radius $r(\theta) = 0.24\big[1+0.5\cos(3\theta)\big]$ is depicted. Again the shape has been fitted within the allowed design domain. The resulting flow rate $Q = 0.46 \times 10^{-3}$ is higher than for the triangle but still a factor of four slower than the optimized result. It is clearly advantageous to change the topology of the dielectric solid from simply to multiply connected.

For the topology optimized shape in Fig. 6.5(a) it is noticed that only a small amount of flow is passing between the two closely placed dielectric islands in the upper left corner of the design domain. To investigate the importance of this separation, the gap between the islands was filled out with dielectric material and the flow calculated. It turns out that this topological change only lowered the flow rate slightly (15%) to a value of $Q = 1.59 \times 10^{-3}$. Thus, the important topology of the dielectric solid in the top-half domain is the appearance of one center island crossing the antisymmetry line and one satellite island near the tip of the center island.

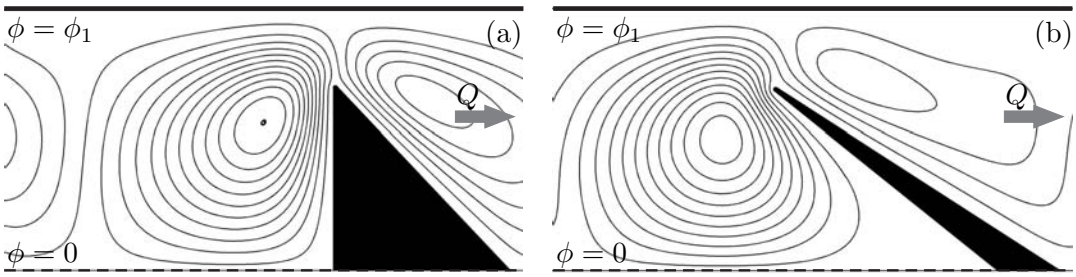

Figure 6.7: (a) The streamline pattern (thick lines) for a simple triangular reference structure calculated for $\omega = 6.25$ using the conventional ICEO model with a hard-walled dielectric solid (black). The height $b = 0.32$ of the triangle is chosen to give the largest flow rate for a fixed base line given by the rectangular design domain of Fig. 6.5(a). The flow rate is $Q = 0.22 \times 10^{-3}$. (b) The same as panel (a) except the geometry of the dielectric solid is given by the perturbed circle $r(\theta) = 0.24[1 + 0.5\cos(3\theta)]$. The flow rate is $Q = 0.46 \times 10^{-3}$.

6.4.3 Shape optimization

The topology optimized solutions are found based on the extended ICEO model involving the artificial design field $\gamma(\boldsymbol{r})$. To avoid the artificial design field it is desirable to validate and further investigate the obtained topology optimized results by the physically more correct conventional ICEO model involving hard-walled solid dielectrics. We therefore extend the reasoning behind the comparison of the two models shown in Fig. 6.5 and apply a more stringent shape optimization to the various topologies presented above. With this approach we are gaining further understanding of the specific shapes comprising the overall topology of the dielectric solid. Moremore, it is possible to point out simpler shapes, which are easier to fabricate, but still perform well. The shape optimization routine has been implemented by Fridolin Okkels, DTU Nanotech, on basis of the validated scripts solving the conventional ICEO model for solid, dielectric objects.

In shape optimization the goal is to optimize the objective function Φ, which depends on the position and shape of the boundary between the dielectric solid and the electrolytic fluid. This boundary is given by a line interpolation through a small number of points on the boundary. These control points are in turn given by N design variables $\boldsymbol{g} = (g_1, g_2, \ldots, g_N)$, so the objective function of Eq. (6.5) depending on the design field $\gamma(\boldsymbol{r})$ is now written as $\Phi[\boldsymbol{g}]$ depending on the design variables $\boldsymbol{g}$,

$$\Phi[\boldsymbol{g}] = \int_\Omega \boldsymbol{v} \cdot \hat{\boldsymbol{n}}_x \, \mathrm{d}x \, \mathrm{d}z. \tag{6.13}$$

To carry out the shape optimization we use a direct bounded Nelder-Mead simplex method [60] implemented in MATLAB [61,62]. This robust method finds the optimal point $\boldsymbol{g}_{\mathrm{opt}}$ in the N-dimensional design variable space by initially creating a simplex in this space, e.g. a N-dimensional polyhedron spanned by $N + 1$ points, one of which is the initial guess. The simplex then iteratively moves towards the optimal point by updating

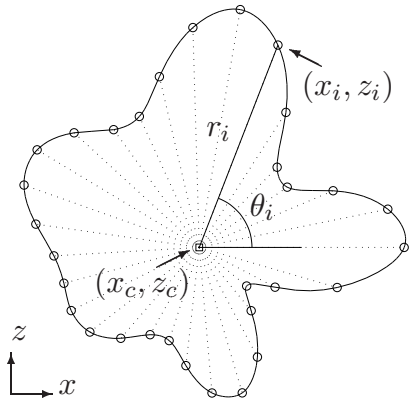

Figure 6.8: Illustration of the parametrization, Eq. (6.14), of the boundary of a dielectric solid with a complex shape. The polar representation is shown for point $i = 7$. The shape consist of five harmonic components represented by Eq. (6.15) with the design-variables $x_c = -0.1312$, $z_c = 0.7176$, $r_0 = 0.1403$, $A_i = \{0.2501, 0.0151, 0.0062, 0.2103, 0.2313\}$, $\varphi_i = \{-1.7508, -2.2526, 0.4173, 0.1172, -0.2419\}$.

one of the $N + 1$ points at the time. During the iteration, the simplex can expand along favorable directions, shrink towards the best point, or have its worst point replaced with the point obtained by reflecting the worst point through the centroid of the remaining N points. The iteration terminates once the extension of the simplex is below a given tolerance. We note that unlike topology optimization, the simplex method relies only on values of the objective function $\Phi[\boldsymbol{g}]$ and not on the sensitivity $\partial\Phi/\partial\boldsymbol{g}$ [63].

First, we perform shape optimization on a right-angled triangle corresponding to the one shown in Fig. 6.7(a). Due to the translation invariance in the x-direction, we fix the first basepoint of the triangle $(x_1, 0)$ to the right end of the simulation domain, while the second point $(x_2, 0)$ can move freely along the baseline, in contrast to the original rectangular design. To ensure a right-angled triangle only the z-coordinate of the top point (x_2, z_2) may move freely. In this case the design variable becomes the two-component vector $\boldsymbol{g} = (x_2, z_2)$. The optimal right-angled triangle is shown in Fig. 6.6(a). The flow rate is $Q = 0.32 \times 10^{-3}$ or 1.5 times larger than that of the original right-angled triangle confined to the design domain.

If we do not constrain the triangle to be right-angled, we instead optimize a polygon shape spanned by three corner points in the upper half of the electrolytic capacitor. So, due to the symmetry of the problem, we are in fact searching for the most optimal, symmetric foursided polygon. The three corner points are now given as $(x_1, 0)$, $(x_2, 0)$,and (x_3, z_3), and again due to translation invariance, it results in a three-component design variable $\boldsymbol{g} = (x_2, x_3, z_3)$. The resulting shape-optimized polygon is shown in Fig. 6.6(b). The flow rate is $Q = 0.76 \times 10^{-3}$, which is 3.5 times larger than that of the original right-angled triangle confined to the design domain and 2.4 times better than that of the best right-angled triangle. However, this flow rate is still a factor of 0.4 lower than the topology optimized results.

To be able to shape optimize the more complex shapes of Fig. 6.5 we have employed two methods to obtain a suitable set of design variables. The first method, the radial method, is illustrated in Fig. 6.8. The boundary of a given dielectric solid is defined through a cubic interpolation line through N control points $(x_i, z_i), i = 1, 2, \ldots, N$, which are parameterized in terms of two co-ordinates (x_c, z_c) of a center point, two global scale factors A and B, N lengths r_i, and N fixed angles θ_i distributed in the interval from 0 to 2π,

$$(x_i, z_i) = (x_c, z_c) + r_i\,(A\cos\theta_i,\ B\sin\theta_i). \tag{6.14}$$

In this case the design variable becomes $\boldsymbol{g} = (x_c, z_c, r_1, r_2, \ldots, r_N, A, B)$.

The second parametrization method involves a decomposition into harmonic components. As before we define a central point (x_c, z_c) surrounded by N control points. However now, the distances r_i are decomposed into M harmonic components given by

$$r_i = r_0\Big(1 + \sum_{n=1}^{M} A_n \cos(n\theta_i + \varphi_n)\Big), \tag{6.15}$$

where r_0 is an overall scale parameter and φ_n is a phase shift. In this case the design variable becomes $\boldsymbol{g} = (x_c, z_c, r_0, A_1, A_2, \ldots, A_M, \varphi_1, \varphi_2, \ldots, \varphi_M)$.

6.4.4 Comparing topology optimization and shape optimization

When shape-optimizing a geometry similar to the one found by topology optimization, we let the geometry consist of two pieces: (*i*) an elliptic island centered on the symmetry-axis and fixed to the right side of design domain, and (*ii*) an island with a complex shape to be placed anywhere inside the design domain, but not overlapping with the elliptic island. For the ellipse we only need to specify the major axis A and the minor axis B, so these two design parameters add to the design variable listed above for either the radial model or the harmonic decomposition model. To be able to compare with the topology optimized solution the dielectric solid is restricted to the design domain.

The result of this two-piece shape optimization is shown in Fig. 6.9. Compared to the simply connected topologies, the two-piece shape-optimized systems yields much improved flow rates. For the shape optimization involving the radial method with 16 directional angles and $A = B$ for the complex piece, the flow rate is $Q = 1.92 \times 10^{-3}$, Fig. 6.9(a), which is 2.5 times larger than that of the shape-optimized foursided symmetric polygon. The harmonic decomposition method, Fig. 6.9(b), yields a flow rate of $Q = 1.52 \times 10^{-3}$ or 2.0 times larger than that of the polygon.

All the results for the obtained flow rates are summarized in Table 6.3. It is seen that two-piece shape optimized systems performs as good as the topology optimized system, when analyzed using the conventional ICEO model without the artificial design field. We also note by comparing Figs. 6.5 and 6.9 that the resulting geometry found using either topology optimization or shape optimization is essentially the same. The central island of the dielectric solid is a thin structure perpendicular to the symmetry axis and covering approximately 60% of the channel width. The satellite island of complex shape is situated near the tip of the central island. It has two peaks pointing towards the central island

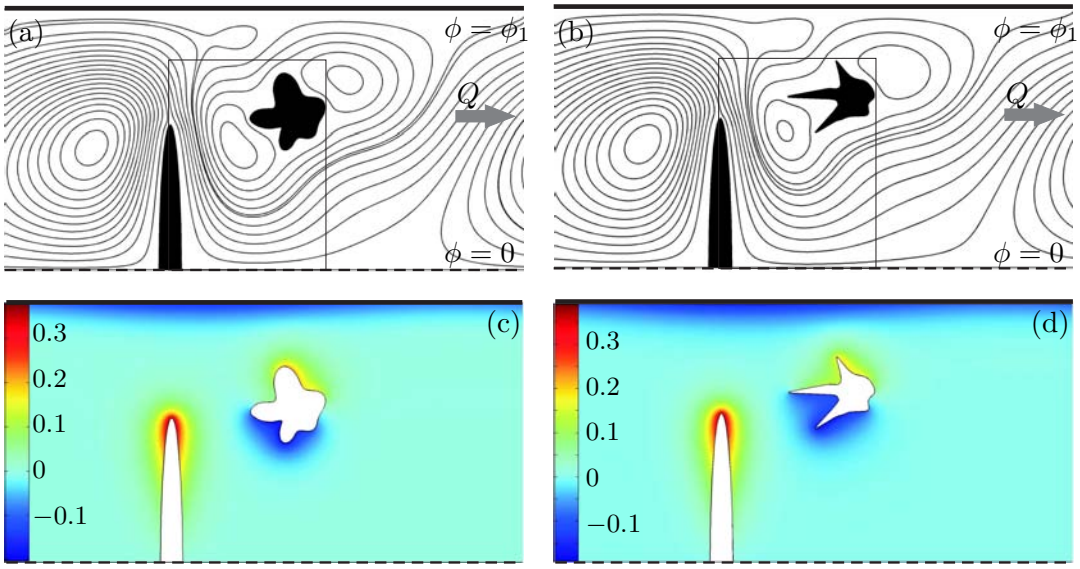

Figure 6.9: Shape-optimized dielectrics with a topology corresponding to the topology-optimized shapes of Fig. 6.5. (a) The streamline pattern (thick lines) for a two-piece geometry calculated using the conventional ICEO model. The shape of the hard-walled dielectric solid (black) is found by shape optimization using the radial method Eq. (6.14) with $N = 16$ directional angles. The flow rate is $Q = 1.92 \times 10^{-3}$. (b) The same as panel (a) except the geometry of the dielectric solid is by shape optimization using the harmonic decomposition method Eq. (6.15) with $M = 5$ modes. The flow rate is $Q = 1.52 \times 10^{-3}$. (c) and (d) Color plot of the charge density $\rho(\boldsymbol{r})$ corresponding to panel (a) and (b), respectively.

that seem to suspend a flow roll which guides the ICEO flow through the gap between the two islands.

6.5 Concluding remarks

The main result presented in this chapter is the establishment of the topology optimization method for ICEO models extended with the design field $\gamma(\boldsymbol{r})$. In contrast to the conventional ICEO model with its sharply defined, impenetrable dielectric solids, the design field ensures a continuous transition between the porous dielectric solid and the electrolytic fluid, which allows for an efficient gradient-based optimization of the problem. This extended model has been validated against the conventional ICEO model without the design field. In contrast to previous applications of the topology optimization method, which all have been relying on bulk properties of the system with a static, externally applied energy source, the ICEO effect is relying exclusively on a boundary layer effect, which at the same time induces the flow. In spite of the complexity level, the method has successfully been tested on a concrete example. We have shown how the use of topology optimization

has led to non-trivial system geometries with a flow rate increase of nearly one order of magnitude, from $Q = 0.22 \times 10^{-3}$ in Fig. 6.7(a) to $Q = 1.92 \times 10^{-3}$ in Fig. 6.9(a).

When applied to ICEO, the design field method is qualitative but not quantitative correct. We have found deviations of 37% when comparing design field simulations with hard-wall simulations. The magnitude of the ICEO effect is sensitive to the exact configuration of the charge density and the electric field within the only 20 nm thick double layer. From the results in Chap. 4, we know how the magnitude of the ICEO depends on the thickness of the double layer. The artificial γ-field changes the detailed properties of the double layer both through the permittivity $\varepsilon[\gamma(\boldsymbol{r})]$, and through the additional term in the chemical potential $\kappa[\gamma(\boldsymbol{r})]$. Quantitative agreement between the design field model and the hard-wall model is therefore only expected for an extremely fine resolution of the γ-field, which is difficult if not impossible to realize. In that perspective, we regard the deviation of 37% between the two models as relatively small.

The topology optimization algorithm of ICEO systems leads to many local optima, and we cannot be sure that the converged solution is the global optimum. The resulting shapes and the generated flow rates depend on the initial condition for the artificial γ-field. Generally, the initial condition used throughout this paper, $\gamma = 0.99$ in the entire design domain, leads to the most optimal results compared to other initial conditions. This initial value corresponds to a very weak change from the electrolytic capacitor completely void of dielectric solid. In contrast, if we let $\gamma = 0.01$ corresponding to almost pure dielectric material in the entire design region, the resulting shapes are less optimal, i.e. the topology optimization routine is more likely to be caught caught in a local optimum. Furthermore, the resulting shapes turns out to be mesh-dependent as well. So, we cannot conclude much about global optima. Instead, we can use the topology optimized shapes as inspiration to improve existing designs. For this purpose shape optimization turns out to be a powerful tool. We have shown in this work how shape optimization can be used efficiently to refine the shape of the individual pieces of the dielectric solid once its topology has been identified by topology optimization.

For all three additional γ-dependent fields $\alpha(\gamma)$, $\kappa(\gamma)$, and $\varepsilon(\gamma)$ we have used (nearly) linear functions. In many previous applications of topology optimization non-linear func-

Table 6.3: Overview of the resulting flow rates Q relative to the topology optimized value $Q^* = 1.88 \times 10^3$, see Fig. 6.5(b), for the various geometries analyzed in the conventional ICEO model. The methods by which the geometries have been determined are listed.

Shape	Method	Flow rate Q/Q^*
Triangle with optimal height, Fig. 6.7(a)	Shape optimization	0.12
Perturbed cylinder, Fig. 6.7(b)	Fixed shape	0.24
Optimized triangle, Fig. 6.6(a)	Shape optimization	0.17
Optimized foursided polygon, Fig. 6.6(b)	Shape optimization	0.40
Topology optimized result, Fig. 6.5(b)	Topology optimization	1.00
Harmonic decomposition and ellipse, Fig. 6.9(a)	Shape optimization	0.81
Radial varying points and ellipse, Fig. 6.9(b)	Shape optimization	1.02

tions have successfully been used to find global optima by gradually changing the non-linearity into strict linearity during the iterative procedure [32, 36, 41, 57]. However, we did not improve our search for a global optimum by employing such schemes, and simply applied the (nearly) linear functions during the entire iteration process.

The limited size of the design domain is in some cases restricting the free formation of the optimized structures. This may be avoided by enlarging the design domain. However, starting a topology optimization in a very large domain gives a huge amount of degrees of freedoms, and the routine is easily caught in local minima. These local minima often yield results not as optimal as those obtained for the smaller design boxes. A solution could be to increase the design domain during the optimization iteration procedure. It should be noted that increasing the box all the way up to the capacitor plates results in solution shapes, where some of the dielectric material is attached to the electrode in order to extend the electrode into the capacitor and thereby maximize the electric field locally. This may be a desirable feature for some purposes. In this work we have deliberately avoided such solutions by keeping the edges of the design domain from the capacitor plates.

Throughout the chapter we have only presented results obtained for dielectric solids shapes forced to be symmetric around the center plane $z = 0$. However, we have performed both topology optimization and shape optimization of systems not restricted to this symmetry. In general we find that the symmetric shapes always are good candidates for the optimal design. It cannot be excluded, though, that in some cases a spontaneous symmetry breaking occurs similar to the asymmetric S-turn channel presented in Sec. 2.5.

By studying the optimized shapes of the dielectric solids, we have noted that pointed features often occurs, such as those clearly seen on the dielectric satellite island in Fig. 6.9(b). The reason for these to appear seems to be that the pointed regions of the dielectric surfaces can support large gradients in the electric potential and associated with this also with large charge densities. As a result large electric body forces act on the electrolyte in these regions. At the same time the surface between the pointed features curve inward which lowers the viscous flow resistance due to the no-slip boundary condition. This effect is similar to that obtained by creating electrode arrays of different heights in AC electro-osmosis [64, 65].

Another noteworthy aspect of the topology optimized structures is that the appearance of dielectric satellite islands seem to break up flow rolls that would otherwise be present and not contribute to the flow rate. This leads to a larger net flow rate, as can be seen be comparing Figs. 6.7 and 6.9.

Throughout the chapter we have treated the design field γ as an artificial field. However, the design-field model could perhaps achieve physical applications to systems containing ion exchange membranes, as briefly mentioned in the beginning of this chapter. Such membranes are indeed porous structures permeated by an electrolyte.

In conclusion, our analysis points out the great potential for improving actual ICEO-based devices by changing simply connected topologies and simple shapes of the dielectric solids, into multiply connected topologies of complex shapes.

Chapter 7

Topology optimized chemical microreactors

In the theoretical work from 2007 on topology optimized microreactors by Fridolin Okkels *et al.* [36,66], promising results were obtained for a simplified reaction kinetics model. We extend this work and apply the topology optimization method to an existing experimentally tested microreactor system. At Center for Individual Nanoparticle Functionality (CINF), DTU, a CO oxidation process on a platinum catalyst is carried out in a microreactor system. The cleanroom fabricated microreactor is made of silicon with a Pyrex lid. The reactor chamber, the in- and outlet channels, and a mass spectrometer interface are etched in the silicon using deep reactive ion etching (DRIE). The mass spectrometer interface is a very narrow through-hole with a diameter of approximately 3 µm in the outlet channel leading away from the reactor chamber. Keeping the mass spectrometer at low pressure and the reactor at atmospheric pressure, the setup is scaled such that the flow resistance of the hole lets a sufficient flow rate through to the mass spectrometer. Further details about the fabrication and setup can be found in Ref. [67]. The CO oxidation is a gas phase reaction catalyzed by platinum deposited in the reaction chamber. The platinum is deposited in the reaction chamber using various techniques, which typically result in a rather homogenous distribution of the catalyst. In the present work we do not aim at such a homogenous distribution. Instead, we control the distribution of catalyst in order to optimize the overall reaction rate of the reactor chamber. We use topology optimization to calculate the most optimal catalyst distribution, and an experimental verification of the optimal solutions is initiated.

Experimentally, the distribution of catalyst in the reactor chamber is controlled by structuring the silicon surface via etching, and subsequently depositing the platinum catalyst in a thin layer on the silicon surface inside the chamber. In areas, where a high reaction rate is desirable, densely placed silicon pillars are etched out in order to create a large surface area to be covered with platinum. In areas, where a low or no reaction should take place, the silicon is completely etched away leaving a void space in the reactor chamber, see Fig. 7.1.

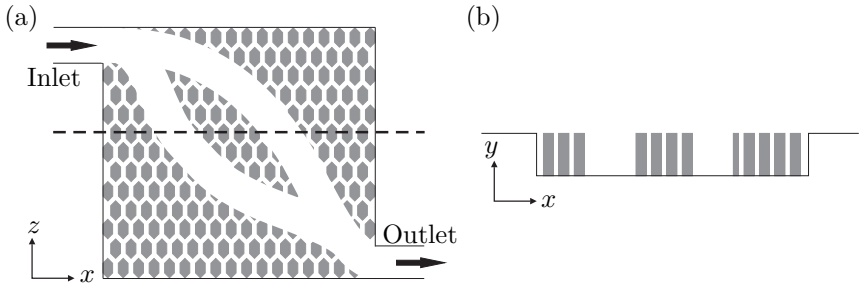

Figure 7.1: Schematic overview of the reactor chamber with silicon pillars placed with spatially varying density. The silicon is colored gray, while the areas etched away are shown with white. (a) Top-view of the reactor chamber, where open channels are created between the areas of densely packed silicon pillars. (b) Side-view of the reactor chamber along the dashed line in panel (a).

7.1 Mathematical model

Extending the mathematical model of Ref. [36], the reaction kinetics of the CO oxidation process is now included in the model system. The reactor still consists of an inlet feeding reactants into the chamber by a pressure driven flow and an outlet for the products and residual reactants. The chamber is filled with a porous medium of spatially varying porosity both offering resistance to the flow through a Darcy friction force and acting as catalytic material for the reaction. In accordance with the simple bulk flow problem in Sec. 2.5 the porosity γ may vary continuously between zero and unity. When $\gamma = 0$ the pores are dense corresponding to a high friction force on the fluid and a high concentration of catalytic material, and oppositely for $\gamma = 1$. In the right parameter range the reaction rate is proportional to the density of catalytic material, and this gives rise to two opposing situations. When the pores are dense the reaction rate is high but almost no fluid passes through. Oppositely, when the pores are very large the fluid flow unhindered, but the reaction rate is nearly zero. So, to obtain the maximal possible reaction rate in the chamber a balance between the two scenarios is needed, and this can be calculated with topology optimization as shown in Ref. [36].

7.1.1 Reaction kinetics

The CO oxidation process is catalyzed by metals such as platinum and palladium, and the overall reaction for carbon oxide and oxygen converting into carbon dioxide is

$$2\,\mathrm{CO} + \mathrm{O_2} \rightleftharpoons 2\,\mathrm{CO_2}. \tag{7.1}$$

The O_2 molecules adsorb and dissociate on the catalytic surface where the CO molecules also adsorb. On the surface CO combines with O to become CO_2 that desorps from the surface again. The overall reaction rate is controlled by several parameters of which temperature and the number of occupied and free surface sites are among the most important. In steady state the catalytic surface is under a constant bombardment of molecules that might adsorb or desorp from the surface, and the reaction rate is therefore dependent on

the actual coverage of molecules on the surface. The surface coverages are modeled by the statical possibilities for the molecules to be present on the surface, and these can be provided from experimental data or Monte-Carlo simulations [68, 69].

The reaction is typically described by a Langmuir–Hinshelwood mechanism [70], where it is assumed that all reacting species are adsorbed on the catalytic surface and in thermal equilibrium before they take part in reactions. It may also be assumed that the adsorbed species taking part in the CO oxidation, i.e. CO, O and CO_2, are equilibrated with the gas phase locally. Thus, the reaction mechanism can be described by a quasi-equilibrium approximation, where one elementary reaction step is assumed to be the rate determining one, while the rest occur sufficiently fast to be assumed in quasi-equilibrium. Consequently, the CO oxidation may be described by the following reaction mechanism with step (S3) being the rate-determining step:

$$\text{(S1)} \qquad \mathrm{CO} + {}^\star \overset{K_1}{\longleftrightarrow} \mathrm{CO}^\star, \tag{7.2a}$$

$$\text{(S2)} \qquad \mathrm{O_2} + 2\,{}^\star \overset{K_2}{\longleftrightarrow} 2\,\mathrm{O}^\star, \tag{7.2b}$$

$$\text{(S3)} \quad \mathrm{CO}^\star + \mathrm{O}^\star \underset{k_3^-}{\overset{k_3^+}{\rightleftharpoons}} \mathrm{CO_2^\star} + {}^\star, \tag{7.2c}$$

$$\text{(S4)} \qquad \mathrm{CO_2^\star} \overset{K_4^{-1}}{\longleftrightarrow} \mathrm{CO_2} + {}^\star. \tag{7.2d}$$

The * denotes a free surface site. K_x represents the equilibrium constant for the given reaction step and is defined as $K_x \equiv k_x^+/k_x^-$, where k_x^+ and k_x^- denote the forward and backward reaction rate constants, respectively. Note that the equilibrium constant for the last desorption step is given by K_4^{-1}.

The reaction rate per catalytic surface site, i.e. the turnover frequency, for each step is expressed by the partial pressures p_x (the reference pressure p_{tot} is omitted for convenience) just above the catalytic surface and the local fraction of sites θ_x occupied by species x. For instance is the rate for step 1 given by $r_1 = k_1^+ p_{\mathrm{CO}} \theta_\star - k_1^- \theta_{\mathrm{CO}}$, where $\theta_\star$ represents the fraction of free surface sites. Corresponding rate expressions can be written for step 2 and 4, and the rate determining step 3 has the rate $r_3 = k_3^+ \theta_{\mathrm{CO}} \theta_{\mathrm{O}} - k_3^- \theta_{\mathrm{CO_2}} \theta_\star$. Following the quasi equilibrium approach by [70] expressions for θ_x are found by setting $r_1 \simeq r_2 \simeq r_4 \simeq 0$. Utilizing that the fractions of occupied and free surface sites add up to unity $\theta_{\mathrm{CO}} + \theta_{\mathrm{O_2}} + \theta_{\mathrm{CO_2}} + \theta_\star = 1$, the probability of finding a free surface site can be expressed as

$$\theta_\star = \left(1 + K_1 p_{\mathrm{CO}} + \sqrt{K_2 p_{\mathrm{O_2}}} + K_4^{-1} p_{\mathrm{CO_2}}\right)^{-1}. \tag{7.3}$$

The overall reaction rate can then be written directly as the rate of the limiting third elementary step,

$$r = k_3^+ K_1 p_{\mathrm{CO}} \sqrt{K_2 p_{\mathrm{O_2}}} \left(1 - \frac{p_{\mathrm{CO_2}}}{p_{\mathrm{CO}} \sqrt{p_{\mathrm{O_2}}}\, K_{\mathrm{G}}}\right) \theta_\star^2, \tag{7.4}$$

where K_G is the equilibrium constant for the overall reaction rate $K_\mathrm{G} = K_1\sqrt{K_2}K_3K_4$.

Usually, the CO_2 molecules only interacts weakly with the surface and their presence locally may therefore be neglected. Consequently, the fourth elementary step is close to irreversible and the local partial pressure of CO_2 can be set to zero. This finally leads to the following overall reaction rate [70]

$$r = k_3^+ \frac{K_1 p_\mathrm{CO}\sqrt{K_2 p_{\mathrm{O}_2}}}{1 + K_1 p_\mathrm{CO} + \sqrt{K_2 p_{\mathrm{O}_2}}}. \tag{7.5}$$

If the gas is modeled as an ideal gas, the partial pressures p_x are interchangeable with the concentrations c_x.

7.1.2 Governing equations

The steady-state gas flow is treated as incompressible, since the typical fluid velocities in the system is of the order 1 m/s much less than the sound velocity. Due to the reduction of the overall number of molecules in the catalytic reaction there will be local compression of the fluid. However, since the reactant species only occupies 7.5 % of the entire gas mixture this compression may be neglected for convenience. Thus, the steady-state flow is governed by the Navier–Stokes equation and the continuity equation for incompressible fluids,

$$\rho(\boldsymbol{v}\cdot\boldsymbol{\nabla})\boldsymbol{v} = -\boldsymbol{\nabla}p + \eta\boldsymbol{\nabla}^2\boldsymbol{v} - \alpha(\gamma(\mathbf{r}))\,\boldsymbol{v}, \tag{7.6a}$$

$$\boldsymbol{\nabla}\cdot\boldsymbol{v} = 0. \tag{7.6b}$$

Applying the Heley–Shaw approximation by integration across the channel height make the equations valid in two dimensions.

The reactant concentrations are found from the Nernst equation and particle conservation for incompressible, dilute solutions for species i,

$$\partial_t c_i = -\boldsymbol{\nabla}\cdot\boldsymbol{J}_i + R_i, \tag{7.7a}$$

$$\boldsymbol{J}_i = -\frac{D_i}{k_\mathrm{B}T}\,c_i\boldsymbol{\nabla}\mu_i + \boldsymbol{v}c_i. \tag{7.7b}$$

The chemical potential μ_i for species i is given by

$$\mu_i = \mu_0 + k_\mathrm{B}T\ln\frac{c_i}{c_{i0}}. \tag{7.7c}$$

In steady state the latter three equations may be combined to

$$\boldsymbol{\nabla}\cdot\Big(D_i\boldsymbol{\nabla}c_i - \boldsymbol{v}\,c_i\Big) = -R_i. \tag{7.8}$$

Integrating over the channel height h_0 in the z direction and letting the concentrations denote the average number of molecules per area in the xy plane, $c^{2\mathrm{D}}(x,y) =$

$\int_0^{h_0} c^{3\mathrm{D}}(x,y,z)\mathrm{d}z \simeq h_0 c^{3\mathrm{D}}(x,y)$, leads to the following averaged 2D equation in the xy-plane:

$$\boldsymbol{\nabla}\cdot\Big(D_i\boldsymbol{\nabla}c_i - \boldsymbol{v}\,c_i\Big) = -R_{i,\mathrm{eff}}(\tilde{c}_i,\gamma(\mathbf{r})). \tag{7.9}$$

The effective reaction rate $R_{i,\mathrm{eff}}(\tilde{c}_i,\gamma) = k_{i,\mathrm{eff}}(\gamma)f(\tilde{c}_i)$ is then the average number of molecules reacting per time per unit area in the xy-plane depending on the catalytic material density through $\gamma(\mathbf{r})$. The dimensionless concentration dependence $f(\tilde{c}_i)$ is derived from Eq. (7.5), where the rate can be written as $r = k_3^+ F(\tilde{c}_i)$ with tilde denoting the dimensionless concentrations. The concentration dependence is then modeled by $f(\tilde{c}_i) = F(\tilde{c}_i)/|F(\tilde{c}_i)|$.

The performance of the reactor can be characterized by the average reaction rate in the chamber. So, the aim of the topology optimization is stated as an optimization of the reaction rate integrated over the chamber area Ω, i.e. the objective function Φ becomes

$$\Phi(\gamma) = \int_\Omega R_{i,\mathrm{eff}}(\tilde{c}_i,\gamma)\mathrm{d}x\mathrm{d}y. \tag{7.10}$$

7.1.3 Dimensionless form

The variables are scaled according to the characteristic numbers of the problem. The new dimensionless variables are denoted by a tilde.

$$\tilde{\mathbf{r}} = \frac{\boldsymbol{r}}{l_0},\quad \tilde{c}_\pm = \frac{c_\pm}{c_0},\quad \tilde{\boldsymbol{v}} = \frac{\boldsymbol{v}}{u_0},\quad \tilde{p} = \frac{p}{p_0},\quad \tilde{R} = \frac{\tau_r}{c_0}R,\quad \tilde{\alpha} = \frac{\alpha}{\alpha_0}. \tag{7.11}$$

The characteristic geometric length scale l_0 is chosen as the height h_0 of the reaction chamber. The reaction takes place at atmospheric pressure, and denoting the total molecular concentration in the chamber c_{atm} leads to $c_0 = c_{\mathrm{atm}}h_0$ applicable in the 2D Nernst–Planck equation. The characteristic pressure is calculated as p_0 for a Poiseuille flow along the chamber length L_0 and the characteristic Darcy friction coefficient is denoted α_0. The characteristic times in the system are the convection time τ_c expressed by the characteristic convection velocity u_0 arising from the Poiseuille flow, the diffusion time τ_d and the reaction time τ_r.

$$\tau_c = \frac{l_0}{u_0},\quad \tau_d = \frac{l_0^2}{D},\quad \tau_r = \frac{c_0}{k_{i,\mathrm{eff}}},\quad p_0 = \frac{\eta\,u_0\,L_0}{l_0^2},\quad \alpha_0 = \frac{\eta}{l_0^2}. \tag{7.12}$$

Here $k_{i,\mathrm{eff}}$ is the effective reaction rate constant for reactant i. The dimensionless numbers Péclet number *Pé*, Reynolds number *Re*, Damköhler number *Dm*, and Darcy number *Da* then appear in the dimensionless equations.

$$P\acute{e} = \frac{u_0 l_0}{D},\quad Re = \frac{\rho u_0 l_0}{\eta},\quad Dm = \frac{\tau_d}{\tau_r} = \frac{l_0^2/D}{c_0/k_{i,\mathrm{eff}}},\quad Da = \frac{\eta}{\alpha_{\max} l_0^2}. \tag{7.13}$$

Below, Eqs. (7.14a) - (7.14c) show the dimensionless form of the governing equations.

$$\tilde{\boldsymbol{\nabla}}\cdot\left(\tilde{\boldsymbol{\nabla}}\tilde{c}_i - P\acute{e}\,\tilde{\boldsymbol{v}}\,\tilde{c}_i\right) = -Dm\,\tilde{R}_{i,\mathrm{eff}}(\tilde{c}_i,\tilde{\gamma}(\tilde{\boldsymbol{r}})), \tag{7.14a}$$

$$Re(\tilde{\boldsymbol{v}}\cdot\tilde{\boldsymbol{\nabla}})\tilde{\boldsymbol{v}} = -\epsilon\tilde{\boldsymbol{\nabla}}\tilde{p} + \tilde{\boldsymbol{\nabla}}^2\tilde{\boldsymbol{v}} - \tilde{\alpha}(\tilde{\gamma}(\tilde{\boldsymbol{r}}))\,\tilde{\boldsymbol{v}}, \tag{7.14b}$$

$$\tilde{\boldsymbol{\nabla}}\cdot\tilde{\boldsymbol{v}} = 0. \tag{7.14c}$$

Here the small aspect ratio $\epsilon = l_0/L_0$ has been introduced. Omitting the $\mathbf{r}$ dependence of γ, the friction coefficient is given by

$$\tilde{\alpha}(\tilde{\gamma}) = \tilde{\alpha}_{\max} + (\tilde{\alpha}_{\min} - \tilde{\alpha}_{\max}) \frac{\tilde{\gamma}\,(1+q)}{q+\tilde{\gamma}}. \tag{7.15}$$

The maximum friction $\tilde{\alpha}_{\max} \equiv \mathrm{Da}^{-1}$ is applied inside the porous medium, and the minimum friction $\alpha_{\min} = 12\eta/h_{\max}^2$ is obtained in the open channels where the Heley–Shaw approximation applies, which in this case where the channel height is constant $h_0 = l_0$ leads to $\tilde{\alpha}_{\min} = 12$.

Correspondingly, the effective reaction rate constant is given by

$$\tilde{k}_{i,\mathrm{eff}}(\tilde{\gamma}) = \tilde{k}_{\phi,i} + (\tilde{k}_{\mathrm{ch},i} - \tilde{k}_{\phi,i}) \frac{\tilde{\gamma}\,(1+q)}{q+\tilde{\gamma}}, \tag{7.16}$$

where $\tilde{k}_\phi$ symbolizes the average reaction rate constant in the pillar area, while $\tilde{k}_{\mathrm{ch}}$ is the average rate constant in the areas with open channels.

It is noted from Eqs. (7.10) and (7.11) that the objective function scales as $\Phi = (l_0^2 c_0/\tau_r)\tilde{\Phi}$.

7.2 Topology optimization

It was decided to perform the experimental testing of the topology optimized microreactors on the previously mentioned setup running in the DTU-CINF laboratory [71–73]. This existing setup combined with the MEMS fabrication limitations naturally introduces a number of restrictions on the model. In addition to the restrictions on reaction chamber dimensions and post geometries mimicking the porous medium, also the dynamic parameters such as diffusion constants, flow rate and reaction rate are limited to certain values. The outcome of topology optimization on such a system strongly depends on the choice of parameters, i.e. how the different time scales entering the problem relate to each other. For the present purpose, where we want to prove the concept of topology optimization in a microfluidic system, it is important that the optimal catalytic structures in the chamber are possible to fabricate. In the case of a pressure driven catalytic reactor it means that a convection-diffusion-reaction time balance has to be achieved. In some parameter regimes structuring of the catalytic material is not necessary, and in other regimes structures become too fine for the fabrication. In the following the parameters entering the model are presented along with the numerical results of the optimization of the catalytic reactors.

7.2.1 Physical parameters

The gas mixture, which is let into the reaction chamber, consists of the reactants CO and O_2 mixed according to their stoichiometric reaction ratio, a carrier gas He and a calibration gas Ar, see Table 7.1. The characteristic parameters for this gas mixture is estimated on basis of table values in Ref. [74]. The viscosity of the individual gas compounds differs less than 20%, and since helium is the primary gas compound, the overall viscosity is

Table 7.1: The mixture of gasses let into the reaction chamber.

Compound	CO	O_2	He	Ar
Concentration [mol%]	5.0	2.5	90.0	2.5

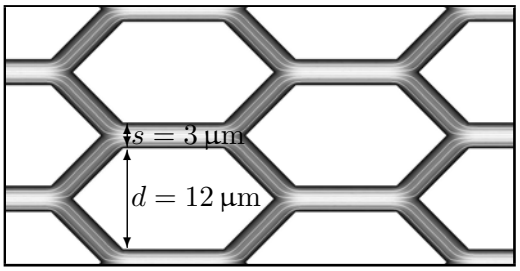

Figure 7.2: Topview of a segment of the post geometry used as representation of the porous catalytic medium in the reactor chamber. A pressure difference applied in the horizontal direction results in the flow shown with white streamlines and gray-scale surface plot of the speed $|\boldsymbol{v}|$ from dark (low) to white (high).

approximated by the viscosity of He. The density of the gas is estimated from a weighted average of the atomic masses[1]. The diffusion constant for the reactants in the gas mixture is approximated by the diffusivity of an equimolar mixture of helium and the reactant gas. The hereby introduced error is estimated to be less than 4%. Furthermore, since the diffusivities of CO and O_2 only differs by $\sim 4\%$, the diffusion constants are assumed to be equal for the two reactant gasses, and the value for CO is applied.

The physical representation of the porous medium is a dense collection of high aspect-ratio posts, where the flow velocity becomes significantly reduced and the catalytic reaction becomes strongly enhanced. To efficiently represent a porous medium a very high aspect-ratio is needed. However, fabrication issues limits the achievable aspect-ratio, and from the first fabrication tests, Sec. 7.3, the pillar geometry shown in Fig. 7.2 was chosen.

Generally, a pressure driven flow through a porous medium has experimentally been shown to obey Darcy's law [75],

$$0 = -\boldsymbol{\nabla} p - \frac{\eta}{k}\boldsymbol{v}_{\text{av}}, \tag{7.17}$$

where $\boldsymbol{v}_{\text{av}}$ is an average flow velocity (total flow rate divided by cross sectional area) and k is the permeability of the medium. Traditionally, k can be estimated from the empirical relation known as the Kozency–Carman equation, which relates k to the geometrical characteristics of the porous medium as well as the porosity ϕ of the medium, defined as $\phi \equiv$ (void vol)/(total vol) [75]. However, in this initial attempt to modeling this specific geometry as a continuous porous medium, we do not have any experimental values for the geometrical factors entering the Kozency–Carman equation. Instead of estimating parameters a numerical solution of flow through the pillar structure is found and the

[1]The average atomic weight w_{gas} of the gas atoms is estimated as $0.90 w_{\text{He}} + 0.025 w_{\text{O}_2} + 0.05 w_{\text{CO}} + 0.025 w_{\text{Ar}} = 6.80\,\text{g/mol}$, and the density of a gas at 600 K is 0.020 mol/L leading to $\rho_{\text{gas}} = 0.136\,\text{kg/m}^3$.

Table 7.2: Estimated and measured parameters used as input in the model of the chemical reactor.

Parameter	Symbol	Value
Temperature	T	$600\,^{\circ}\mathrm{C}$
Diffusivity	D	$2.4 \times 10^{-4}\,\mathrm{m}^2/\mathrm{s}$
Density	ρ	$0.14\,\mathrm{kg/m}^3$
Viscosity	η	$3.2 \times 10^{-5}\,\mathrm{Pa\,s}$
Chamber height	h_0	$100\,\mu\mathrm{m}$
Chamber length and width	L_0	$10.0\,\mathrm{mm}$
Characteristic length	l_0	h_0
Porosity of catalytic material	ϕ	0.30
Pillar width	d	$6.0\,\mu\mathrm{m}$
Pillar spacing	s	$3.0\,\mu\mathrm{m}$
Darcy number in pillar area	Da	1.7×10^{-5}
Total pressure in chamber	p_{tot}	$1 \times 10^{-5}\,\mathrm{Pa}$
Inlet partial pressure of CO	$p_{\mathrm{CO},0}$	$5\%\ p_{\mathrm{tot}}$
Inlet partial pressure of O_2	$p_{\mathrm{O}_2,0}$	$2.5\%\ p_{\mathrm{tot}}$
Total molecular concentration	c_{atm}	$44.6\,\mathrm{mol/m}^3$
Molecular concentration in 2D ($c_{\mathrm{atm}} h_0$)	c_0	$4.5 \times 10^{-3}\,\mathrm{mol/m}^2$
Measured reaction rate for CO_2	$r_{\max}$	$8.5 \times 10^{-9}\,\mathrm{mol/(s\,mm}^2)$
Reaction rate in open channels	k_{ch}	$8.5 \times 10^{-9}\,\mathrm{mol/(s\,mm}^2)$
Reaction rate in porous medium	k_ϕ	$1.7 \times 10^{-7}\,\mathrm{mol/(s\,mm}^2)$

result is applied. By comparison of Darcy's law with the low Reynolds number, inertia free Poiseuille solution in a capillary, it is seen that dimensionally $k \sim a^2$, where a is the characteristic radius of the capillary.

An estimate of the Darcy number based on numerical calculations can be found by solving Stokes equation in the two dimensional post geometry, shown in Fig. 7.2. Eq. (7.18a) is solved in a corresponding channel of height h_0 with a pressure difference applied in the x-direction across $\sim 400\,\mu\mathrm{m}$. In the y-direction a symmetry condition is applied to neglect possible wall effects. Assuming that Darcy's law is valid it is possible to calculate the average permeability k or Darcy number Da from equation Eq. (7.18b), where $\alpha_{\max} = \eta/k$ has been inserted in Eq. (7.17),

$$0 = -\epsilon\tilde{\boldsymbol{\nabla}}\tilde{p} + \tilde{\boldsymbol{\nabla}}^2\tilde{\boldsymbol{v}} - \tilde{\alpha}_{\min}\tilde{\boldsymbol{v}}, \tag{7.18a}$$

$$0 = -\epsilon\tilde{\boldsymbol{\nabla}}\tilde{p} - \frac{1}{Da}\tilde{\boldsymbol{v}}_{\mathrm{av}}. \tag{7.18b}$$

If the geometry of the post area simply consisted of straight channels of width $3\,\mu\mathrm{m}$, the Da number would be $\mathrm{Da} = k/l_0^2 \sim a^2/l_0^2 = 9.0 \times 10^{-4}$. Calculations of the Poiseuille flow in the x and y-directions of the actual geometry result in $\mathrm{Da} = 1.7 \times 10^{-5}$ and $\mathrm{Da} = 7.9 \times 10^{-4}$, respectively. A more thorough study of the lattice dependence of the Da number could be included in the model as a function of the direction of the flow velocity,

however, in this case we simply put in the number for the horizontal Darcy friction force.

The diffusion of the reactants is also affected by the geometry of the dense posts. Generally, the Nernst–Planck equations hold in the post area, since the mean-free path of the particles is much less than the pillar spacings, but the diffusion constant has to be replaced by an effective diffusion constant given as $D_\phi = (\phi/T)D_{\text{free}}$, where T is the tortuosity expressing the relative difference in path length due to the post geometry [77]. Again T would depend on the lattice direction and in all cases it would be close to unity, so we simply approximate D inside the post area by the free space D multiplied with the porosity,

$$D_{\text{eff}}(\gamma) = D\left[\phi + (1-\phi)\frac{\gamma(1+q)}{q+\gamma}\right]. \tag{7.19}$$

From previous experiments, performed with the same experimental setup letting the same gas-mixture into a chamber containing a well defined Pt surface, the reaction rate r is known as function of temperature [68,78]. At 600 K the highest value of r was measured to $r_{\max} = 8.5 \times 10^{-9}\,\text{mol}/(\text{s}\,\text{mm}^2)$. Since the modeled fields are averaged over the third dimension z, the reaction rate on the post walls is integrated and translated into an effective rate in xy-plane, this rate is denoted k_ϕ.[2] The equilibrium constants are assumed to be $K_1 = K_2 = 1$ corresponding to equally many molecules adsorbed on the surface and free just above the surface [70]. The reaction rate Eq. (7.5) is a monotonic function for inlet concentrations being less than 5% of the total molecule concentration. The final expression for the reaction rate is then found by normalizing Eq. (7.5) and multiplying with the effective reaction rate.

$$\tilde{R}_{\text{CO}} = \tilde{k}_{\text{CO,eff}}(\tilde{\gamma})\frac{\tilde{c}_{\text{CO}}\sqrt{\tilde{c}_{\text{O}_2}}}{1+\tilde{c}_{\text{CO}}+\sqrt{\tilde{c}_{\text{O}_2}}}\,\tilde{R}^{-1}_{\text{CO,max}}, \tag{7.20}$$

where $R_{\text{CO,max}} = R_{\text{CO}}(c_{\text{CO}} = 0.050, c_{\text{O}_2} = 0.025)$, and $R_{\text{O}_2} = R_{\text{CO}}/2$.

The microreactor chip design allows us to make the reaction chamber as big as $L_0^2 = 1\,\text{cm}^2$ and due to the fabrication of high aspect ratio posts a chamber height of $h_0 = 100\,\mu\text{m}$ was chosen. During testing of the microreactors the adjustable parameters are the temperature T, which mostly influences the effective reaction rate, and the pressure difference Δp applied across the reaction chamber controlling the convection time. In practice are the three parameters L_0, T and Δp the only parameters, which may be varied within certain limits when a suitable convection-diffusion-reaction time balance has to be achieved.

In this case, where the reaction takes place in the gas phase, diffusion time is very short compared to the convection time and reaction time. If the diffusion time is much shorter than the other times the most optimal solution to the problem will be a total uniform distribution of posts/catalytic material, since there is time enough to distribute the gas and exploit the reactivity of the catalytic sites. Decreasing of the convection time leads to a balance between convection and diffusion but if the reaction time is long, the optimal

[2] The surface area of a post with height H is $A_p = (2d + 4\sqrt{2}\,d/2)\,H$. Multiplying the number of posts per xy-surface area with A_p leads to the effective surface area in the xy-plane.

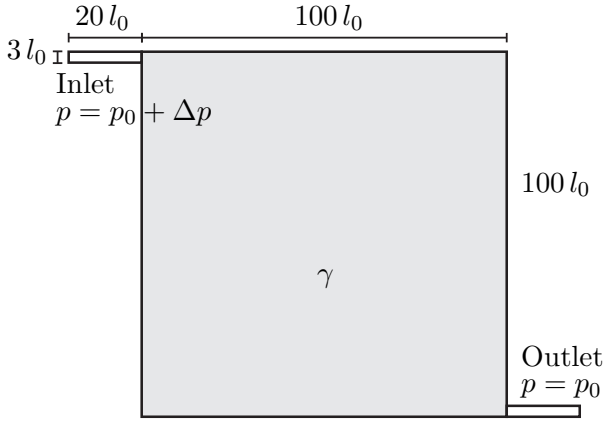

Figure 7.3: The geometry used for optimization of the catalytic material distribution in the chemical reactor. The porous catalytic material (gray) is distributed in the chamber while the inlet/outlet (white) are empty.

system does not consist of an advanced channel network, but a uniform distribution or a single channel.

Consequently, to maximize the diffusion time as much as possible, the size of the reaction chamber is maximized within the limited area of $1\,\mathrm{cm}^2$. To lower the reaction rate, the temperature is set to $T = 600\,\mathrm{K}$ with the corresponding measured reaction rate r, which is known to be in the upper range of the achievable rate. Finally, adjusting the pressure difference leads to different suitable topology optimized structures.

7.2.2 Geometry and boundary conditions

The final geometry used for the optimization is shown in Fig. 7.3. The inlet boundary condition on the flow is a normal stress, normal flow condition, where the tangential flow is zero and the normal stress is equal to the applied pressure difference. The pressure condition could also be applied as a Diriclet condition along with a no viscous stress condition, however, for numerical stability reasons the first formulation is chosen [42].

$$\boldsymbol{\sigma} \cdot \boldsymbol{n} = -\Delta p\, \boldsymbol{n}, \quad \boldsymbol{t} \cdot \boldsymbol{v} = 0, \tag{7.21a}$$

where $\boldsymbol{t}$ and $\boldsymbol{n}$ are unit vectors in the tangential and normal directions, respectively. Diriclet conditions set the inlet concentrations,

$$c_{\mathrm{CO}} = c_{\mathrm{CO},0}, \quad c_{\mathrm{O}_2} = c_{\mathrm{O}_2,0}. \tag{7.21b}$$

At the outlet a corresponding boundary condition is set for the flow, while a convective flux condition is specified for the concentration fields,

$$\boldsymbol{\sigma} \cdot \boldsymbol{n} = 0, \quad \boldsymbol{t} \cdot \boldsymbol{v} = 0, \tag{7.22a}$$

$$\boldsymbol{n} \cdot (-D \boldsymbol{\nabla} c_i) = 0. \tag{7.22b}$$

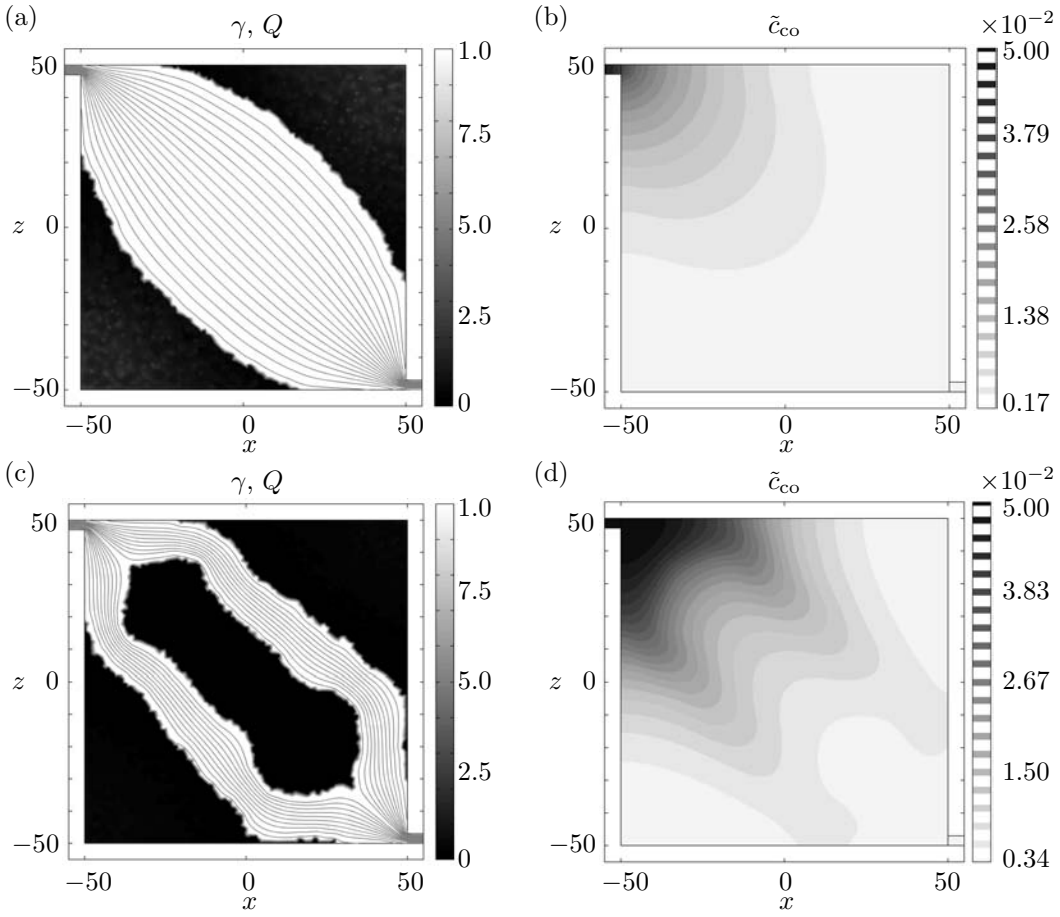

Figure 7.4: Topology optimized solutions for a chemical microreactor. (a) and (b) Solutions optimized for the pressure difference $\Delta p = 10^2$ and the reaction rate $r = r_{\max}/4$. (c) and (d) Solutions optimized for the pressure difference $\Delta p = 10^3$ and the reaction rate $r = r_{\max}/4$. (a) and (c) Grayscale plots of the γ-field (black and white areas) and streamline plots (thin gray lines) drawn as equidistant contours of the flow rate. (b) and (d) The concentration of the reactant species c_{co} (grayscale plot).

At the solid walls a no-slip condition is applied for the velocity field and the normal reactant current density is set to zero,

$$\boldsymbol{v} = \boldsymbol{0}, \quad \boldsymbol{n} \cdot \boldsymbol{J}_i = 0. \tag{7.23}$$

7.2.3 Results

The topology optimization of the chemical microreactors is performed using the parameters listed in Table 7.2, along with varying values of both the pressure difference Δp across the chamber and the reaction rate r on the platinum surface. These two parameters may be controlled experimentally through a flow-controller mounted on the inlet channel

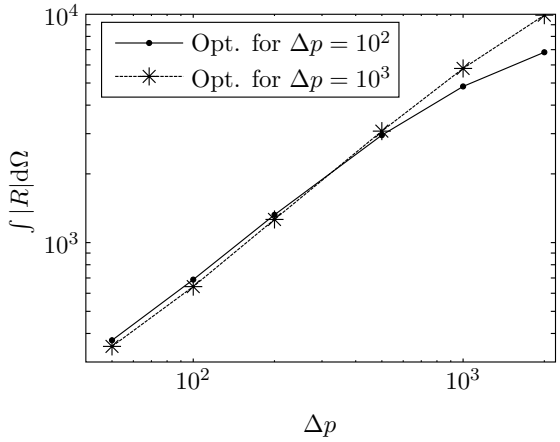

Figure 7.5: The integrated flow rate $\int |R| \mathrm{d}\Omega$ versus pressure difference Δp across the reaction chamber for each of the two structures shown in Fig. 7.4(a) (optimal for $\Delta p = 10^2$) and Fig. 7.4(c) (optimal for $\Delta p = 10^3$). The structure in panel (a) indeed yields the highest integrated reaction rate for the pressure $\Delta p = 10^2$ and the structure in panel (c) yields the highest rate for $\Delta p = 10^3$.

and a heating element integrated in the microchip [71–73]. The values of Δp and r are chosen within a range that promotes a discrete 0-1 solution of the γ-field. If the applied pressure difference is too low, the relative diffusion becomes very fast and consequently, a structuring of the catalytic material is not very beneficial. This causes a slow or absent convergence of the topology optimization routine and the obtained solutions consist of intermediate gamma values. On the other hand very high pressure differences lead to high Reynolds numbers that violate the laminar flow assumption of the gas. Regarding the reaction rate r, the value in Table 7.2 represents an upper limit for the rate and lower values may be applied. However, if the rate becomes too low, it is not necessary with more than one open channel through the reaction chamber, since the reactant transportation no longer is rate limiting. A valid but not very interesting solution. This discussion reflects how the topology optimized solution structures are determined by the interplay between the timescales of convection, diffusion and reaction.

In Fig. 7.4 two optimization results are shown. Fig. 7.4(a) and (b) are plots of the optimal solution for the parameter set $\Delta p = 10^2$ and $r = r_{\max}/4$, while Fig. 7.4(c) and (d) shows the solution corresponding to the parameter set $\Delta p = 10^3$ and $r = r_{\max}/4$. Panels (a) and (c) display gray scale plots of the γ-fields, where $\gamma = 0$ corresponds to the dense pillar structure and $\gamma = 1$ represents the open channels. It is noted that that the γ-fields have converged to pure 0-1 solutions, and that the slightly wavy channel boundaries are results of the underlying FEM mesh structures. The thin gray lines are streamline plots of the flow drawn as equidistant contours of the flow rate. Panels (b) and (d) show gray scale plots of the reactant concentration c_{co} with inlet concentration $c_{\mathrm{co}} = 0.05$. In Fig. 7.5 the optimality of the two solution structures shown in Fig. 7.4(a) and (c) is checked. The response is calculated for a series of pressure differences Δp applied to each of the solution structures. It is seen how each of the structures indeed is optimal for the

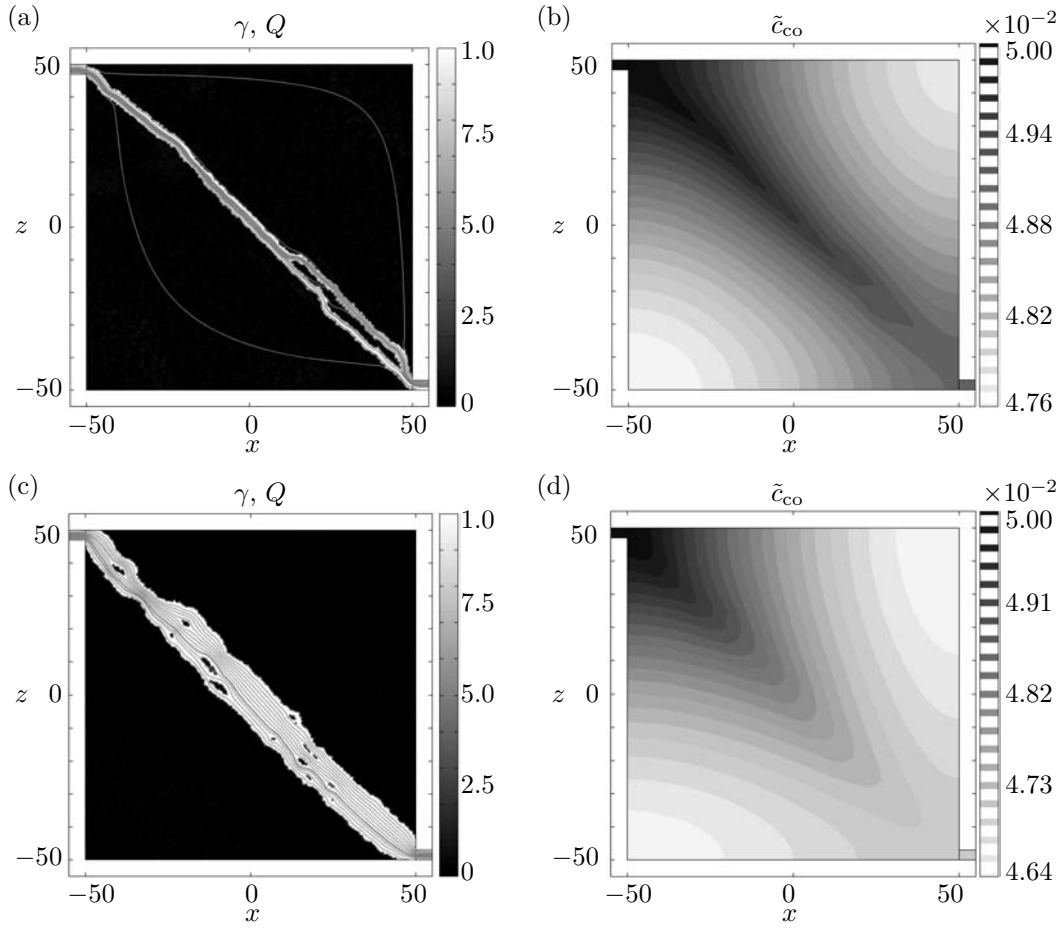

Figure 7.6: Topology optimized solutions for chemical microreactors. The reaction rate is $r = r_{\max}/10^3$ for both solution structures. The fields displayed in panel (a) and (b) are calculated for a pressure difference of $\Delta p = 10^4$. In panel (c) and (d) the fields are calculated for a pressure difference of $\Delta p = 10^3$. (a) and (c) Grayscale plots of the γ-field (black and white areas), and streamline plots (thin gray lines) drawn as equidistant contours of the flow rate. (b) and (d) The concentration of the reactant species c_{co} (grayscale plot).

pressure Δp applied during the topology optimization, though, it is also noted that the difference between the solutions can be very small.

Analogously, we calculate the optimized structures used in the fabricated microreactors. After initiating the manufacturing process, the mathematical model was slightly improved into the version presented above, and in the following, the solutions are shown using this modified version. Figs. 7.6 and 7.7 present the four fabricated reactor types. Each individual reactor is displayed with the solution fields calculated for a specific parameter set Δp, r. When this specific set of parameters is applied to all four reactor types, the displayed reactor yields the highest integrated reaction rate $\int R \mathrm{d}\Omega$, i.e. it is more optimal than the remaining three reactors. The solutions are presented as described

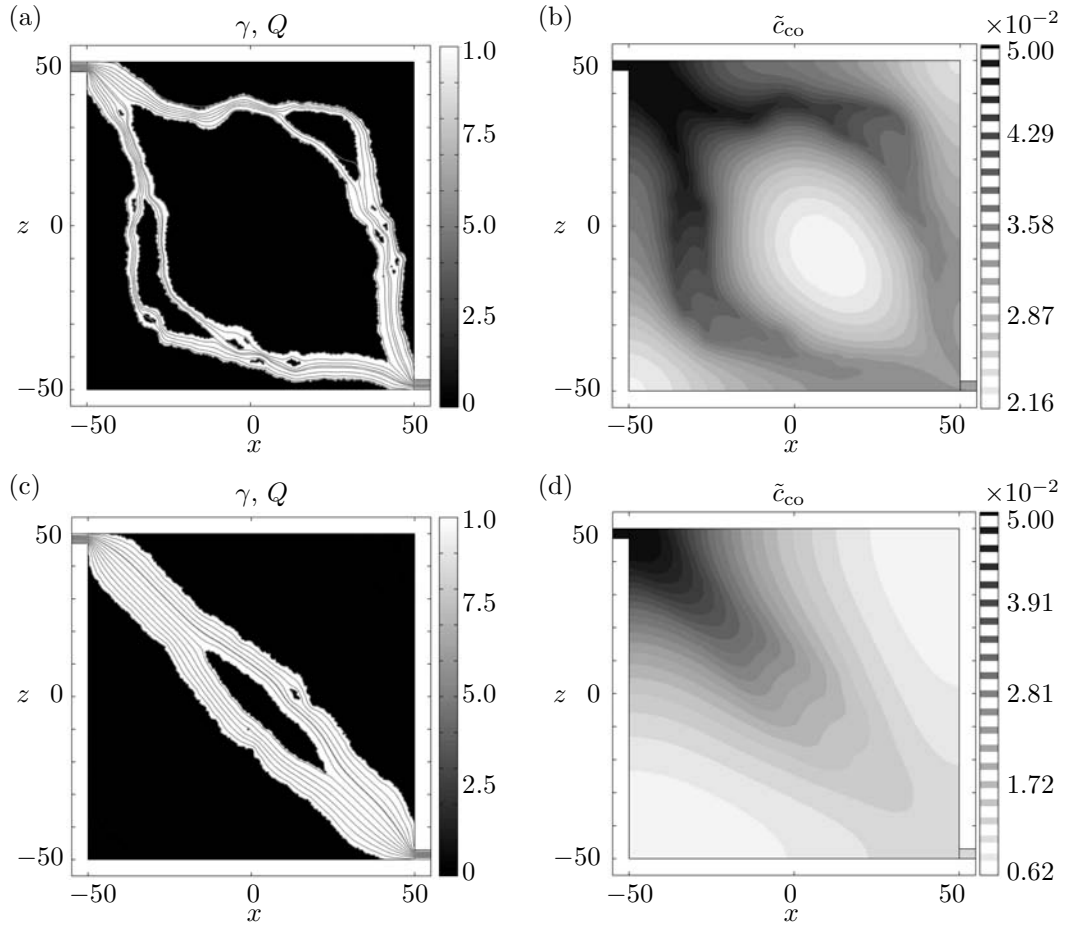

Figure 7.7: Topology optimized solutions for chemical microreactors. The reaction rate is $r = r_{\max}/10$ for both solution structures. The fields displayed in panel (a) and (b) are calculated for a pressure difference of $\Delta p = 10^4$. In panel (c) and (d) the fields are calculated for a pressure difference of $\Delta p = 10^3$. (a) and (c) Grayscale plots of the γ-field (black and white areas), and streamline plots (thin gray lines) drawn as equidistant contours of the flow rate. (b) and (d) The concentration of the reactant species c_{co} (grayscale plot).

for Fig. 7.4, with a combined γ-field and streamline plot next to a plot of the reactant concentration c_{co}. In Fig. 7.6 the fields of the reactors are displayed for a very low reaction rate $r = r_{\max}/10^3$. The pressure difference in Fig. 7.6(a) and (b) is $\Delta p = 10^4$, while it for Fig. 7.6(c) and (d) is $\Delta p = 10^3$. In Fig. 7.7 the reaction rate is much higher $r = r_{\max}/10$, and again the pressure difference for the structure in Fig. 7.7(a) and (b) is $\Delta p = 10^4$, while it for Fig. 7.7(c) and (d) is $\Delta p = 10^3$.

The FEM mesh applied in the numerical solution of the fabricated reactors was chosen as fine as possible within the computational limitations in order to minimize the mesh effect on the channel boundaries. However, even with 4×10^5 degrees of freedom and a solution time for the topology optimization routine of several days, the resolution is still

Table 7.3: Comparison between the performance R_{opt} of reactors with topology optimized catalytic material distribution, and the performance R_{uni} of the corresponding reactors with homogenous catalytic material distribution.

Reactor geometry	7.6(a)	7.6(c)	7.7(a)	7.7(c)
R_{opt}	3.0×10^2	2.7×10^2	1.5×10^4	4.6×10^3
R_{uni}	1.4×10^2	90	6.8×10^2	1.7×10^2
$R_{\text{opt}}/R_{\text{uni}}$	2.1	2.9	22.0	27.0

very coarse and on the order of approximately ten pillar translation periods in the reaction chamber. Thus, the channel boundaries are not completely smooth for the manufactured reactors.

Comparing the performance $\int R\mathrm{d}\Omega$ of the individual reactors for different parameter sets Δp, r indicates that the largest difference between the reactors is found for the high values of the reaction rate, i.e. the fields shown in Fig. 7.7. So, the experimental confirmation of the optimization method may be easiest to obtain in that range. Another reference is a reactor with a uniform distribution of catalytic material. Often the catalytic material is the most costly part of the reaction process and traditionally it is uniformly distributed in the reaction chamber. A valid reference is therefore a reaction chamber containing the same amount of catalytic material as the optimized reactor, but with the material homogenously distributed throughout the chamber. Thus, a reference is established by calculating the spatial averaged porosity ϕ for an optimized reactor, the corresponding Darcy number Da and the average reaction rate r. The problem is then solved using these new parameters in a reaction chamber with a uniform gamma field $\gamma = 1$, and the integrated reaction rate $\int R\mathrm{d}\Omega$ is determined. Experimentally, this reference reactor is realized by keeping the dimension of the individual pillar fixed and distribute them homogenously in the reaction chamber in accordance with the calculated average spatial porosity. Such a reference reactor is fabricated for each of the four optimized reactor types. The expected improvement from a homogenous pillar distribution to a structured distribution is significant. In Table 7.3 the performance $R_{\text{opt}} = \int |R|\mathrm{d}\Omega$ of the four different reactor types is compared to the performance $R_{\text{uni}} = \int |R|\mathrm{d}\Omega$ of their corresponding homogenous reference reactors. Again it is noted that the largest differences and improvements are found for the higher reaction rate.

7.3 Experimental testing

The experimental testing of the microreactors is being carried out in collaboration with Ole Hansen, Adam Monkowski and Jacob L. Olsen CINF, DTU. This is an on-going project, not concluded at the time of writing. But in the following, the initial progress is briefly presented.

The details of the fabrication process for the entire microreactor chip are described in Ref. [67] for an empty reaction chamber. The chamber, inlet and outlet channels are etched in a single fabrication step using deep reactive ion etching (DRIE). The etching

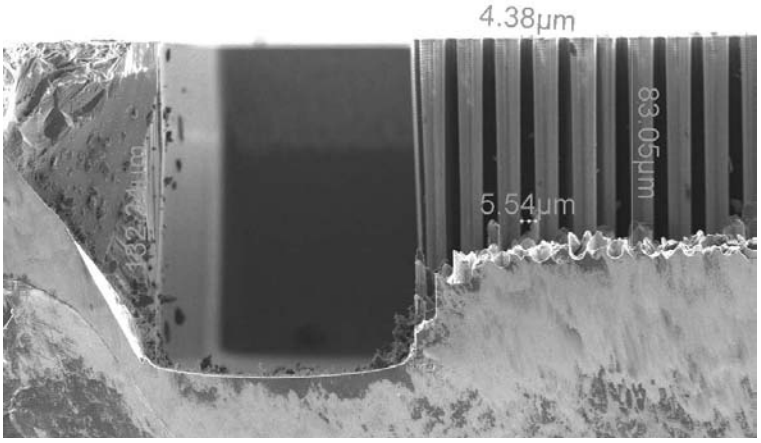

Figure 7.8: SEM picture of a preliminary etch (DRIE) test of the silicon pillar structure later applied as the porous material in the topology optimized microreactors. The picture is a side view of a cleaved surface, where the etch has taken place from the top and downwards. The densely packed pillars are located to the right, and to the left of the pillars there is a wider channel, which has been etched slightly deeper due to the nonuniformity of the DRIE. Courtesy of Adam Monkowski, DTU Nanotech 2008.

of the topology optimized pattern, consisting of mixed areas with dense pillars and open channels within the chamber, is included in this single etching step. It is well known that the etching depth for a DRIE process is strongly dependent on the etched structure size, the expected aspect ratio and the surrounding etch-patterns [79]. Thus, an initial etch test was performed to determine the most suitable pillar diameter and spacing, and the obtainable aspect ratio. It is crucial for the topology optimization that a rather high aspect-ratio of the pillars can be obtained, since we want to mimic an actual porous material.

For the testing purpose a photolithography mask for the etch step was prepared having 152 different combinations of pillar spacings and radii (ranging from 2 µm to 50 µm), and testing two different pillar shapes, the circular and the hexagonal shown in Fig. 7.2. The etching of the test structures and the subsequent cleanroom manufacturing of the complete topology optimized microreactors was carried out by Adam Monkowski. The scanning electron microscope (SEM) picture in Fig. 7.8 shows a side view of a cleaved silicon wafer with an etch test of the hexagonal pillar shape (top right) with pillar-diameters of 6 µm and pillar-spacings of 3 µm. To the left of the etched pillars, a larger area has been etched to mimic the situation for the topology optimized structures, where wide channels are etched next to the densely packed pillars. The result is very satisfying. We obtain a high aspect-ratio pillar structure next to a very wide channel with only 30% height difference. The pillars have an aspect ratio of approximately 16 and a total height of 83 µm. We decided to use the pillar structure of Fig. 7.8 for the actual optimized reactors, since these represented the pillars with highest aspect ratio, which were still robust in the etching process. Thus, from this decision it is clear that the average chamber height becomes

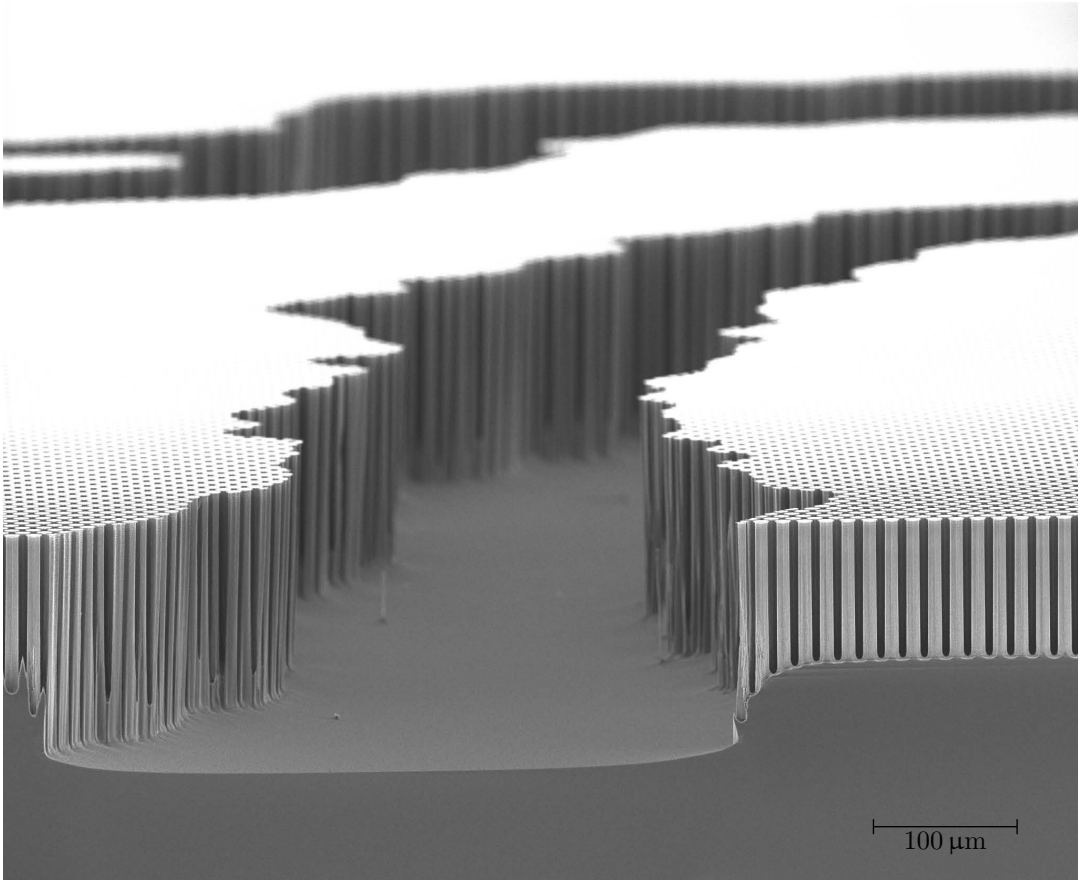

Figure 7.9: SEM picture of the raw, etched silicon surface in a topology optimized reactor chamber. The picture is a top/side view of a cleaved surface through the reactor chamber. The uniform gray area in the bottom of the picture is the bulk silicon wafer, while the edged, topology optimized channel is running through the densely packed pillars from the cleaved edge and into the picture. A second channel is out of focus in the background. Courtesy of Adam Monkowski, DTU Nanotech 2008.

$h_0 \sim 100\,\mu\text{m}$, and that the remaining geometrical parameters of Table 7.2 are set.

From the topology optimized reactor structures presented above in Figs. 7.6 and 7.7, a new photolithography mask was established and used in the fabrication of the actual microreactors. Fig. 7.9 show a SEM picture of the raw, etched silicon surface in the reactor chamber. The picture is a top/side view from an edge cleaved through the reactor chamber. The bulk silicon wafer is seen in the bottom of the picture, while the edged, topology optimized channel is running through the densely packed pillars from the cleaved edge and into the picture. In the background of the picture a second channel through the pillars is glimpsed.

The platinum was deposited in the etched reactor chamber by placing an exact amount of platinum particle solution and letting it distribute throughout the chamber while heating it up. The control with this deposition technique is limited, but however yielded a good

coverage of most of the silicon surface in the chamber. Care was taken so especially the areas with high reaction rate became covered with platinum. After the platinum deposition, a pyrex glass lid was bonded on top of the processed silicon chips.

Preliminary CO-oxidation tests has been performed by Jacob L. Olsen, and the results are promising. Graphs of the detected outlet products as function of the applied pressure difference across the chambers lead to clearly different curves for the various reactor types. Thus, it is possible to discriminate between the performance of the reactors experimentally. However, tests are still being performed, and more work is needed to reach conclusions for the applicability of the topology optimization method for design of actual microreactors.

Chapter 8

Conclusion and outlook

Conclusion

The present thesis has been devoted to the investigation of microfluidic devices relying on an interplay between convection, diffusion and reaction. Within the induced-charge electro-osmotic field an ACEO microfluidic pump has been experimentally investigated and numerical calculations on an ICEO model system has been carried out. The numerical topology optimization method has been applied both to the ICEO system, and to a cleanroom fabricated chemical microreactor.

The ACEO asymmetric electrode micropump mentioned above has been experimentally investigated with particular focus on low voltages and low frequencies compared to the parameter ranges considered in previous experiments. Due to an increased sensitivity of the device, a flow reversal in this parameter range was detected, which up until that point had never been observed before. A thorough impedance characterization of the pumping device over eight frequency decades was performed, and the impedance spectra were fitted to Bode plots using realistic parameter values. The observed trends of the flow velocity curves fit with existing theories, however, the quantitative agreement with previously published theoretical models is lacking. Especially, the strong concentration dependence of the measured flow has only very recently been accounted for theoretically.

Concerning the topic of induced-charge elecro-osmosis, a full nonlinear numerical model of an ICEO system with fully resolved double layers has been implemented and solved in 2D for an infinite cylinder in an electrolyte confined by a parallel plate capacitor. The flows have been validated against two analytical results; the slip velocity for a cylinder in an infinite domain, and the slip velocity for a perturbed cylinder in a confined domain. Both analytical models have been calculated in the Debye–Hückel regime and with the assumption of an infinitely thin Debye layer. Complete agreement between the analytical and numerical models has not been achieved, mainly due to computational limitations. It turned out that the slip-velocities predicted by the infinitely-thin-Debye layer models are generally overestimated. To find a deviation less than 5% between the two models, the full Debye layer resolving model must have a Debye length less than 10^{-3} of the flow-generating electrode size. Since the infinitely thin Debye layer approximation is often applied as reference for experimentally observed flows, these findings could provide a

partial explanation for the quantitative discrepancies between observed and calculated ICEO velocities.

In extension of the numerical ICEO studies described above, topology optimization has successfully been established for a linearized AC-driven ICEO system with fully resolved Debye layers. An artificial design field ensuring a continuous transition from liquid to solid has been implemented in the conventional governing equations to allow for an efficient gradient-based optimization of the problem. This extended model has been validated against the conventional ICEO model without the design field. In contrast to previous applications of the topology optimization method, which all have been relying on bulk properties of the system with a static, externally applied energy source, the ICEO effect is relying exclusively on a boundary layer effect, which at the same time induces the flow. The structure of the ICEO flow-inducing dielectric solid between the externally biased capacitor plates, has been optimized to generate the largest possible flow-rate parallel to the capacitor plates. The optimization has been carried out for varying driving frequencies and sizes of the design domain, and the self-consistency of the topology optimization method has been checked. The optimal dielectric geometries have been transferred to the conventional electrokinetic model without the artificial design field, and the optimized flow rate has been validated within a deviation of 37%, which is satisfactory given that the ICEO effect is very sensitive to small changes of the boundary. It has been shown that the topology optimized structures perform better than single geometric shapes of the same size. Furthermore, by application of shape-optimization it has been shown that structures with the same topology performs equally well. Conclusively, there seems to be a great potential for improving actual ICEO-based devices by changing simple geometrical shapes of the dielectric solids into more complex topologies.

Finally, an existing microfabricated reactor for CO oxidation supported by a platinum catalyst has been topology optimized and prepared for experimental testing. An existing implementation of topology optimization of a simplified liquid-phase catalytic reaction, has been improved to include a realistic reaction kinetics model for a gas-phase CO oxidation on platinum. The distribution of catalyst in the reactor chamber has been topology optimized in order to maximize the overall production rate in the chamber. Optimizations have been performed for varying combinations of the pressure difference driving the flow through the chamber, and the temperature controlling the local reaction rate. Four different designs have been chosen for cleanroom fabrication of actual microreactor chips, and a photolithographic mask for the DRIE process has been prepared. The preliminary reports from the testing of these devices have been promising.

Outlook

After initial tests of first generation reactor designs, a calibration of the numerical reactor simulations would make it possible to establish a more accurate model. Especially a measurement of the actual reaction rate for the areas with a homogenous pillar distribution would be extremely useful as direct input for the reaction rate in the model. Also, measurements of the hydraulic resistance and the degree of conversion for the reactants at the outlet could increase the accuracy of the numerical simulations. The hope is to

experimentally point out two different parameter ranges that correspond to two different optimal reactor designs, i.e. to experimentally verify the graph in Fig. 7.5.

Returning to the topology optimization of the ICEO systems, an investigation of the whole parameter space could lead to interesting results. Especially a gradual increase of the design-area size could possibly lead to interesting optimal geometries for the large domains between the capacitor plates. Inspired by the symmetry-breaking properties of semi-screened micro-spheres, partially covered by insulating material, and suspended in an electrolyte [29], it would be interesting to introduce a second material in the topology optimization model. In this way, an additional symmetry breaking degree of freedom would be available. With the general establishment of the topology optimization of ICEO systems, other applications could also be possible. For instance, it would be natural to optimize the degree of mixing in a microfluidic system, e.g. see Ref. [7]. The suggested model relies on an AC-driven system, where the electrodes may be incorporated directly along the sidewalls of the channel, making it suitable for experimental purposes. Thus, an experimental testing of the topology optimized structures could be realized using systems resembling Ref. [7] or Ref. [76].

Regarding the modeling of the double layer dynamics in ICEO systems, two problems have been pointed out in this thesis. The experimentally observed flows in ACEO systems are not fully understood, and the classical modeling approach based on the assumption of infinitely thin double layers breaks down even for electrodes in the micrometer range in contact with the typically used electrolyte concentrations of 0.1 mM. Thus, there is need for a better theoretical understanding of the basic ICEO phenomenon. A closer analysis of the effects coming into play for finite Debye layers would be useful both as a better reference for the experimental work, but also for a possible improvement of the slip-velocity models. To support improvement of the theoretical model, experiments on systems much simpler than the complex ACEO pump are needed, thereby making it possible to study the involved effects separately. Steps towards this kind of experimental analysis have already been taken, see Refs. [53, 76], and correlation with the theoretical models are to be expected.

Conclusively, many open questions and possibilities for improvement remain, both theoretically and experimentally within the fields of ICEO and applied topology optimization. Hopefully, this will be addressed in the future.

Appendix A

Comsol code

The code included below has been used for topology optimization of the ICEO system described in Chap. 6 and for the optimization of the chemical microreactors described in Chap. 7, respectively. The implementation follows Ref. [41], and here only the Main-file, Setup-file, and GammaOn-file for each of the implementations are shown. The subroutines mmasub and subsolv are unchanged from Ref. [41].

A.1 Optmization of ICEO system

Main file for ICEO optimization:

```
% TOPOLOGY OPTIMIZATION OF ICEO FLOW AROUND DIELECTRICUM IN CAPACITOR

clear all
close all
flclear fem

% Setup constants
% Physical constants
e = 1.602e-19;
kB = 1.38e-23;
epsilon0 = 8.85e-12;

% Parameters for bulk electrolyte
Z = 1;
T = 293;
D0 = 2e-9; % Diffusion constant of ions in the bulk
rho_bulk = 1e3;
eta_bulk = 1e-3;
epsilon_bulk = 78*epsilon0;

```

```
% Characteristic numbers
charL0 = 0.25e-6; % Characteristic lengthscale - dielectric mat. diameter
lambdaDbulk = 2e-8; % Wanted Debye length in bulk electrolyte
c0 = (kB*T*epsilon_bulk)/(2*(Z*e)^2*lambdaDbulk^2); % Bulk electrolyte conc.
phi0 = kB*T/(Z*e); % Thermal voltage
u0 = epsilon_bulk*phi0^2/(eta_bulk*charL0); % Char. EO velocity
p0 = eta_bulk*u0/charL0; % Char. microfluidic pressure
alpha0 = eta_bulk/charL0^2; % Char. Darcy friction coefficient

Pe = u0*charL0/D0; % Peclet number
Re = rho_bulk*u0*charL0/eta_bulk; % Reynolds number

% Parameter values
phi1 = 1; % Potential boundary conditions
phi2 = -1;
epsilon1 = 78*epsilon0/epsilon_bulk; % Permitivity of bulk
epsilon2 = 1e6*epsilon0/epsilon_bulk; % Permitivity of material
Da = 1e-5; % Darcy number (1e-6 - 1e-2)
omega = 6.25;
gamma0 = 1; % Maximum value of gamma
gammast = 0.99; % Initial value of gamma
kappa = 3; % Energy preventing ions from entering the solid (2-7).
L0 = 2.0; % Domain height, e.g. distance between capacitor plates.

% Position and size of optimization area
h0 = 0.8;
w0 = 0.6;
x0 = 0.0;
y0 = h0/2;

% TOPOPT Constants
charL = 0.125; % Char. dimensionless value for normalization of obj.fct.
q = 1.0;

% Constant-string
fem.const = {'phi1',phi1,'phi2',phi2,'q',q, ...
  'epsilon1', epsilon1, 'epsilon2', epsilon2, ...
  'kappa',kappa,'omega',omega ...
  'epss',lambdaDbulk/charL0, 'Pe',Pe, 'Re',Re, ...
  'alphamin',0/alpha0,'alphamax',eta_bulk/(Da*charL0^2)/alpha0, ...
  'gamma0',gamma0,'gammast',gammast};
siq = 6;   %Constant-string index of q-value

% Get Geometry
```

```
Setup_EHD_AverageFlow_sym_OF_ubulk_cutoff;

% Include gamma
GammaOn_EHD_AverageFlow_box_strip;

% DESIGN LOOP FOR THE ACTUAL TOPOLOGY OPTIMIZATION
plotiter = 1;
preiter = 0;
for iter = 1:500

    % Solve electric problem
    fem.sol=femstatic(fem, ...
                'init',fem.sol, ...
                'solcomp',{'phir','phii','rhor','rhoi'}, ...
                'outcomp',{'phir','phii','rhor','rhoi','gamma'}, ...
                'LinSolver','Pardiso');

    % Solve flow problem
    fem.sol=femstatic(fem, ...
                'init',fem.sol, ...
                'solcomp',{'v','u','p'}, ...
                'outcomp',{'v','u','p','phir','phii','rhor','rhoi','gamma'}, ...
                'LinSolver','Pardiso','nonlin','on');

    % SOLVE ADJOINT PROBLEM FOR LAGRANGE MULTIPLIERS
    [K N] = assemble(fem,'Out',{'K' 'N'},'U',fem.sol.u);
    [L M] = assemble(femadj,'Out',{'L' 'M'},'U',fem.sol.u);
    femadj.sol = femlin('In',{'K' K(ivar,ivar)' 'L' L(ivar) ...
            'M' zeros(size(M)) 'N' N(:,ivar)});

    % SENSITIVITY ANALYSIS
    gamma = fem.sol.u(igamma);
    Phi = real(postint(fem,'A') + postint(fem,'B','Edim',1));
    dPhidgamma = L(igamma) - K(ivar,igamma)'*femadj.sol.u;
    Phi0 = charL^2;

    % PERFORM MMA STEP TO UPDATE DESIGN FIELD
    mmax = gamma;
    f = Phi/Phi0;
    g = gamma'*Vgamma/Vdomain - gamma0;
    dfdx = dPhidgamma/Phi0;
    dgdx = Vgamma'/Vdomain;
    d2fdx2 = zeros(size(gamma));
    d2gdx2 = zeros(size(gamma'));
```

```
    [mmaxnew,y,z,lambda,ksi,eta,mu,zeta,s,mmalow,mmaupp] = ...
        mmasub(1,size(gamma,1),iter,mmax,mmaxmin,mmaxmax,mmaxold,mmaxolder, ...
        f,dfdx,d2fdx2,g,dgdx,d2gdx2,mmalow,mmaupp,mmaa0,mmaa,mmac,mmad);
    mmaxolder = mmaxold;
    mmaxold = mmax;
    gamma = mmaxnew;

    % TEST CONVERGENCE
    preiter = preiter + 1;
    if max(abs(gamma-mmaxold)) < 0.01 & preiter > 3
        break
    end

    % UPDATE DESIGN VARIABLE
    u0 = fem.sol.u;
    u0(igamma) = gamma;
    fem.sol = femsol(u0);

    % DISPLAY RESULTS FOR EACH ITERATION STEP
    disp(sprintf('Iter.:%3d Obj.: %8.4f Vol.: %6.3f Change: %6.3f q: %5.3f', ...
    iter,f,g,max(abs(mmaxnew-mmaxold)),fem.const{siq}))
end
```

Setup file for ICEO optimization:

```
% SETUP FILE FOR TOPOPT ON ICEO SYSTEM

% Geometry
height = L0/2;
width = L0;
boxheight = h0;
boxwidth = w0;
g1=rect2(width,height,'base','center','pos',[0,L0/4]);
g2=rect2(boxwidth,boxheight,'base','center','pos',[x0,y0]);

% Analyzed geometry
clear s
s.objs={g1,g2};
s.name={'R1','R2'};
s.tags={'g1','g2'};

fem.draw=struct('s',s);
fem.geom=geomcsg(fem);
```

```
19  geomplot(fem,'edgelabels','on','pointmode','off')
20
21  % Initialize mesh
22  fem.mesh=meshinit(fem, ...
23      'hmaxedg',[3,0.024],'hmaxsub',[1,0.4,2,0.024], ...
24      'hgradedg',[1,1.09,9,1.09]);
25
26  % Space dimension
27  fem.sdim = {'x' 'y'};
28
29  % Shape functions
30  fem.shape = {'shlag(2,''u'')','shlag(2,''v'')','shlag(1,''p'')', ...
31      'shlag(2,''phir'')', 'shlag(2,''phii'')', ...
32      'shlag(2,''rhor'')','shlag(2,''rhoi'')','shlag(1,''gamma'')'};
33  fem.border = 1;
34
35  % Equation form
36  fem.form = 'general';
37
38  % Subdomain settings
39  clear equ
40  equ.f = {{'F_x-px';'F_y-py';'-(ux+vy)'; ...
41      '-rhor/(epss^2)';'-rhoi/(epss^2)'; ...
42      '-omega*rhoi/epss';'omega*rhor/epss';0}, ...
43      {'F_x-px';'F_y-py';'-(ux+vy)'; ...
44      '-rhor/(epss^2)';'-rhoi/(epss^2)'; ...
45      '-omega*rhoi/epss';'omega*rhor/epss';1}};
46  equ.da = 0;
47  equ.init = {{0;0;0;0;0;0;0;1},{0;0;0;0;0;0;0;'gammast'}};
48  equ.ga = {{ ...
49      {'-2*ux';'-(uy+vx)'}; ...
50      {'-(vx+uy)';'-2*vy'};{0;0};
51      {'epsilon*phirx';'epsilon*phiry'}; ...
52      {'epsilon*phiix';'epsilon*phiiy'}; ...
53      {'phirx+rhorx'; ...
54      'phiry+rhory'}; ...
55      {'phiix+rhoix'; ...
56      'phiiy+rhoiy'}; ...
57      {0;0}}, ...
58      {{'-2*ux';'-(uy+vx)'}; ...
59      {'-(vx+uy)';'-2*vy'};{0;0};
60      {'epsilon*phirx';'epsilon*phiry'}; ...
61      {'epsilon*phiix';'epsilon*phiiy'}; ...
62      {'phirx+rhorx-rhor*kappa*gammax'; ...
```

```
    'phiry+rhory-rhor*kappa*gammay'}; ...
    {'phiix+rhoix-rhoi*kappa*gammax'; ...
    'phiiy+rhoiy-rhoi*kappa*gammay'}; ...
    {0;0}}};
equ.ind = [1,2];
equ.dim = {'u','v','p','phir','phii','rhor','rhoi','gamma'};
equ.var = { ...
  'F_x',{'-(rhor*phirx+rhoi*phiix)/(2*epss^2)', ...
  '-(rhor*phirx+rhoi*phiix)/(2*epss^2)-alpha*u'}, ...
  'F_y',{'-(rhor*phiry+rhoi*phiiy)/(2*epss^2)', ...
  '-(rhor*phiry+rhoi*phiiy)/(2*epss^2)-alpha*v'}, ...
  'U_ns','sqrt(u^2+v^2)'};

% Subdomain expressions
equ.expr.epsilon = ...
    {'epsilon1', ...
    'epsilon2+(epsilon1-epsilon2)*(1-((1-gamma)/2*(tanh(((1-gamma)-0.03)/0.002)+1)))'};
equ.expr.alpha = {'','alphamax+(alphamin-alphamax)*gamma'};
equ.expr.A = {'u'};
fem.equ = equ;

% Boundary settings
clear bnd
bnd.shape = 1;
bnd.g = 0;
bnd.r = ...
    {{'u-u_cpl','v-v_cpl','p-p_cpl', ...
    'phir-phir_cpl','phii-phii_cpl', ...
    'rhor-rhor_cpl','rhoi-rhoi_cpl',0}, ...
    {'nx*u+ny*v',0,0,'-phir','-phii','-rhor','-rhoi',0}, ...
    {'-u','-v',0,'-phir+phi1','-phii',0,0,0}, 0, 0};
bnd.ind = {[1] [2 5 8] [3] [9] [4 6 7]};

% Boundary expressions
bnd.expr.B = 0;
fem.bnd = bnd;

% COUPLING ELEMENT FOR PERIODIC B.C.
% rightmost boundary is source and leftmost is destination
clear cpl src dst map
% extrusion coupling variables acting in geometry one with names {xx_cpl}
cpl.elem = 'elcplextr';
cpl.g = {'1'};
cpl.var = {'u_cpl' 'v_cpl' 'p_cpl' 'phir_cpl' 'phii_cpl' 'rhor_cpl' 'rhoi_cpl'};
```

```
% source expressions and trivial map {0 0 0} *FROM* source *TO*
% intermediate mesh
src.expr = {{'u'} {'v'} {'p'} {'phir'} {'phii'} {'rhor'} {'rhoi'}};
src.map = {'0' '0' '0' '0' '0' '0' '0'};
src.ind = {{'9'}};
cpl.src = {{{} src {}}};
% define linear transformation *FROM* destination *TO*
% intermediate mesh - on source boundary
map.type = 'linear';
map.sg = '1';
map.sv = {'1','2'};
map.dg = '1';
map.dv = {'7','8'}; % symmetric destination
cpl.map = {map};
% declare map *FROM* destination *TO* intermediate mesh
% - {1 1 1} are indices in cpl.map
dst.map = {{'1'} {'1'} {'1'} {'1'} {'1'} {'1'} {'1'}};
dst.ind = {{'1'}};
cpl.geomdim = {{{} dst {}}};
% finally add cpl to fem.elem
fem.elem = {cpl};

% Point settings
% Clamp pressure at a single point
clear pnt
pnt.ind = {[1] [2:8]};
pnt.constr = {'p',0};
fem.pnt = pnt;
```

GammaOn file for ICEO optimization:

```
% GAMMAON FILE FOR TOPOPT ON ICEO SYSTEM
% GammaOn file for Topology Optimization of a dielectric material shape
% in a parallel plate capacitor. The design domain is a rectangular area
% with dimensions and position specified in the Setup file/Main file.

fem=femdiff(fem);

% Extend mesh
fem.xmesh=meshextend(fem);

% Assemble Initial-condition
fem.sol = asseminit(fem);
```

```
13
14 % DEFINE STRUCTURE FOR COMPUTING RIGHT-HAND-SIDE IN ADJOINT PROBLEM
15 femadj = fem;
16 femadj.equ.ga = {{ ...
17     {'diff(A,ux)'; 'diff(A,uy)'}; {'diff(A,vx)'; 'diff(A,vy)'}; ...
18     {'diff(A,px)'; 'diff(A,py)'};{'diff(A,phirx)'; 'diff(A,phiry)'}; ...
19     {'diff(A,phiix)'; 'diff(A,phiiy)'};{'diff(A,rhorx)'; 'diff(A,rhory)'}; ...
20     {'diff(A,rhoix)'; 'diff(A,rhoiy)'};{'diff(A,gammax)'; 'diff(A,gammay)'}}};
21 femadj.equ.f = {{'diff(A,u)'; 'diff(A,v)'; 'diff(A,p)'; ...
22     'diff(A,phir)'; 'diff(A,phii)'; 'diff(A,rhor)'; 'diff(A,rhoi)'; ...
23     'diff(A,gamma)'}};
24 femadj.bnd.g = {{'diff(B,u)'; 'diff(B,v)'; 'diff(B,p)'; ...
25     'diff(B,phir)'; 'diff(B,phii)'; 'diff(B,rhor)'; 'diff(B,rhoi)'; ...
26     'diff(B,gamma)'}};
27
28 femadj.xmesh = meshextend(femadj);
29
30 % GET INDICES OF DESIGN VARIABLE IN THE GLOBAL SOLUTION VECTOR (fem.sol.u)
31 gxp = asseminit(fem,'Init',{'gamma' 'x+10'},'Out','U');
32 gyp = asseminit(fem,'Init',{'gamma' 'y+10'},'Out','U');
33 igamma = find([gxp > (10-boxwidth/2+x0) & gxp < (10+boxwidth/2+x0) & ...
34              gyp > (10-boxheight/2+y0) & gyp < (10+boxheight/2+y0)]);
35
36 % COMPUTE VOLUME BELOW DESIGN VARIABLE BASIS FUNCTIONS
37 L = assemble(fem,'Out',{'L'});
38 Vgamma = L(igamma);
39 Vdomain = sum(Vgamma);
40
41 % GET INDICES OF VELOCITY-PRESSURE VARIABLES
42 ivar = find(asseminit(fem,'Init', ...
43     {'u' 1 'v' 1 'p' 1 'phir' 1 'phii' 1 'rhor' 1 'rhoi' 1},'Out','U'));
44
45 % DEFINE VARIABLES PARAMETERS FOR MMA OPTIMIZATION ALGORITHM
46 mmaa0 = 1;
47 mmaa = 0;
48 mmac = 1000;
49 mmad = 0;
50 mmaxmin = 0;
51 mmaxmax = 1;
52 mmaxold = fem.sol.u(ivar);
53 mmaxolder = mmaxold;
54 mmalow = 0;
55 mmaupp = 1;
```

A.2 Optmization of chemical microreactor

Main file for reactor optimization:

```
% MAIN FILE FOR REACTOR OPTIMIZATION

clear all
close all
flclear fem

% Setup Constants
Da = 1.7e-5; % Darcy number (1e-6 - 1e-2)
gamma0 = 1; % Maximum value of gamma
gammast = 0.99; % Initial value of gamma
dp = 1000; % Inlet pressure
k3p = 33; % Reaction constant in pillar area
kch = 1.78; % Reaction constant in channel area
o20 = 0.025;
co0 = 0.050;
h0 = 100e-6; % Channel height
phirho = 0.30; % Dielectric porosity

% Pluid properties
TK = 600; % Between 300K and 700K (mu(T) & rho(T) 300-1000, D(T) 200-700)
fluid_eta = 6.3e-6+4.82e-8*TK-8.4e-12*TK^2; %Poly. fit to temp. dependence
rho_fluid = 0.62*exp(-TK/268)+0.069; %Exp. decay fit to temp. dep. of fluid mix.
D0 = 9.5e-8*TK+5.0e-10*TK^2; % Diffusivity

% Characteristic numbers
charl0 = 1e-4; % Characteristic lengthscale
U0 = 4; % Characteristic convection velocity
Pe = U0*charl0/D0; % Péclet number
Re = rho_fluid*U0*charl0/fluid_eta; % Reynolds number
Dmp = k3p*charl0^2/D0; % Damköhler number in pillar area
Dmch = kch*charl0^2/D0; % Damköhler number in channel area

% TOPOPT Constants
qarr = [0.03 0.1 0.3 1];
maxnrq = size(qarr,2);
nrq = 1;
charL = 5e-3/sqrt(o20*k3p*charl0^2);

% Constant-string
fem.const = {'gamma0',gamma0,'dp',dp,'alphamin',12*charl0^2/h0^2, ...
```

```
    'alphamax',1/Da+12*charl0^2/h0^2,'q',qarr(nrq),'gammast',gammast, ...
    'o20',o20,'co0',co0,'k3p',k3p,'kch',kch,'Pe',Pe,'Re',Re, ...
    'Dmp',Dmp,'Dmch',Dmch,'TK',TK,'phirho',phirho};
siq = 10;   %Constant-string index of q-value

% Get Geometry
Setup_CO_O2_gas_asym_fnew;

% Include gamma
GammaOn_CO_O2_gas;

% DESIGN LOOP FOR THE ACTUAL TOPOLOGY OPTIMIZATION
preiter = 0;
plotiter = 1;
for iter = 1:500

    % Solve problem
    fem.sol=femstatic(fem, ...
                'init',fem.sol, ...
                'solcomp',{'v','u','p'}, ...
                'outcomp',{'v','u','p','gamma'}, ...
                'Linsolver','pardiso');

    % Solve CC problem
    fem.sol=femstatic(fem, ...
                'init',fem.sol, ...
                'solcomp',{'o2','co'}, ...
                'outcomp',{'u','v','p','o2','co','gamma'}, ...
                'nonlin','on','Linsolver','pardiso');

    % SOLVE ADJOINT PROBLEM FOR LAGRANGE MULTIPLIERS
    [K N] = assemble(fem,'Out',{'K' 'N'},'U',fem.sol.u);
    [L M] = assemble(femadj,'Out',{'L' 'M'},'U',fem.sol.u);
    femadj.sol = femlin('In',{'K' K(ivar,ivar)' 'L' L(ivar) ...
            'M' zeros(size(M)) 'N' N(:,ivar)});

    % SENSITIVITY ANALYSIS
    gamma = fem.sol.u(igamma);
    Phi = real(postint(fem,'A') + postint(fem,'B','Edim',1));
    dPhidgamma = L(igamma) - K(ivar,igamma)'*femadj.sol.u;
    Phi0 = charL^2;

    % PERFORM MMA STEP TO UPDATE DESIGN FIELD
    mmax = gamma;
```

```
    f = Phi/Phi0;
    g = gamma'*Vgamma/Vdomain - gamma0;
    dfdx = dPhidgamma/Phi0;
    dgdx = Vgamma'/Vdomain;
    d2fdx2 = zeros(size(gamma));
    d2gdx2 = zeros(size(gamma'));
    [mmaxnew,y,z,lambda,ksi,eta,mu,zeta,s,mmalow,mmaupp] = ...
        mmasub(1,size(gamma,1),iter,mmax,mmaxmin,mmaxmax,mmaxold,mmaxolder, ...
        f,dfdx,d2fdx2,g,dgdx,d2gdx2,mmalow,mmaupp,mmaa0,mmaa,mmac,mmad);
    mmaxolder = mmaxold;
    mmaxold = mmax;
    gamma = mmaxnew;

    % TEST CONVERGENCE / q-STEP
    preiter = preiter + 1;
    if max(abs(gamma-mmaxold)) < 0.01 & preiter > 3
        if nrq < maxnrq % CHANGE q & RESET MMA-HISTORY
            nrq = nrq+1;
            fem.const{siq}= qarr(nrq);
            femadj.const{siq} = qarr(nrq);
            mmaxold = gamma;
            mmaolder = gamma;
            preiter = 0;
            disp(sprintf(' #### CHANGE q to: %6.4f ####',qarr(nrq)))
        else
            break
        end
    end

    % UPDATE DESIGN VARIABLE
    u0 = fem.sol.u;
    u0(igamma) = gamma;
    fem.sol = femsol(u0);

    % DISPLAY RESULTS FOR EACH ITERATION STEP
    disp(sprintf('Iter.:%3d Obj.: %8.4f Vol.: %6.3f Change: %6.3f q: %5.3f', ...
    iter,f,g,max(abs(mmaxnew-mmaxold)),fem.const{siq}))
end
```

Setup file for reactor optimization:

```
% SETUP FILE FOR REACTOR OPTIMIZATION

```

```
% Geometry
height = 100;
g1=rect2(height,height,'base','center','pos',[0,0]);
g2=rect2(height/5,3,'base','corner','pos',[-0.7*height,47]);
g3=rect2(height/5,3,'base','corner','pos',[0.5*height,-0.5*height]);

% Analyzed geometry
clear s
s.objs={g1,g2,g3};
s.name={'R1','R2','R3'};
s.tags={'g1','g2','g3'};

fem.draw=struct('s',s);
fem.geom=geomcsg(fem);

% Initialize mesh
fem.mesh=meshinit(fem, ...
                'hmaxsub',[1:3;ones(1,3)*2]);

% Space dimension
fem.sdim = {'x' 'y'};

% Shape functions
fem.shape = {'shlag(2,''u'')','shlag(2,''v'')','shlag(1,''p'')', ...
    'shlag(2,''o2'')','shlag(2,''co'')','shlag(1,''gamma'')'};

% Integration order
fem.gporder = {4,2};

% Constraint order
fem.cporder = {2,1};
fem.border = 1;

% Equation form
fem.form = 'general';

% Subdomain settings
clear equ
equ.f = { ...
    {'-alphamin*u-Re*(u*ux+v*uy)';'-alphamin*v-Re*(u*vx+v*vy)'; ...
    '-(ux+vy)';'-Pe*(u*o2x+v*o2y)';'-Pe*(u*cox+v*coy)';0}, ...
    {'-alpha*u-Re*(u*ux+v*uy)';'-alpha*v-Re*(u*vx+v*vy)'; ...
    '-(ux+vy)';'-Peeff*(u*o2x+v*o2y)+Dm*fR/2'; ...
    '-Peeff*(u*cox+v*coy)+Dm*fR';1}};
```

```
equ.init = {{0;0;0;0;0;'1'},{0;0;0;0;0;'gammast'}};
equ.ga = {{{'-2*ux+p';'-(uy+vx)'}; ...
    {'-(vx+uy)';'-2*vy+p'};{0;0}; ...
    {'-o2x';'-o2y'};{'-cox';'-coy'};{0;0}}};
equ.ind = [1,2,1];
% Dependent variables
equ.dim = {'u','v','p','o2','co','gamma'};
equ.var = {'U_ns','sqrt(u^2+v^2)', ...
  'V_ns','vx-uy', ...
  'divU_ns','ux+vy'};

% Subdomain expressions
% Bug in sqrt-function!
equ.expr.tfree = {0,'1/(1+co+realsqrt(abs(o2)))'};
equ.expr.fR = {0,'-184.6*co*realsqrt(abs(o2))*tfree^2'};
equ.expr.A = {0,'fR*(k3p+(kch-k3p)*gamma)'};
equ.expr.alpha = {'','alphamax+(alphamin-alphamax)*gamma*(1+q)/(q+gamma)'};
equ.expr.Peeff = {0,'Pe*(1/phirho+(1-1/phirho)*gamma)'};
equ.expr.Dm = {0,'Dmp+(Dmch-Dmp)*gamma'};

% Interior mesh boundary settings
equ.bnd.ind = [1,1,1];
fem.equ = equ;

% Boundary settings
clear bnd
bnd.g = {{'-nx*dp';'-ny*dp';0;0;0;0}, ...
    {0;0;0;'-(-nx*u-ny*v)*o2';'-(-nx*u-ny*v)*co';0},0,0};
bnd.shape = [1;2;3;4;5];
bnd.r = {{'nx*v-ny*u';0;0;'-o2+o20';'-co+co0';0}, ...
    {'-u';'-v';0;0;0;0},0, ...
    {'nx*v-ny*u';0;0;0;0;0}};
bnd.ind = [1,2,2,2,2,3,2,3,2,2,2,4];

% Boundary expressions
bnd.expr.B = 0;
fem.bnd = bnd;
```

GammaOn file for reactor optimization:

```
% GAMMAON FILE FOR REACTOR OPTIMIZATION

fem=femdiff(fem);
```

```
4
5  % Extend mesh
6  fem.xmesh=meshextend(fem);
7
8  % Assemble Initial-condition
9  fem.sol = asseminit(fem);
10
11 % DEFINE STRUCTURE FOR COMPUTING RIGHT-HAND-SIDE IN ADJOINT PROBLEM
12 femadj = fem;
13 femadj.equ.ga = {{ ...
14     {'diff(A,ux)'; 'diff(A,uy)'}; {'diff(A,vx)'; 'diff(A,vy)'}; ...
15     {'diff(A,px)'; 'diff(A,py)'}; {'diff(A,o2x)'; 'diff(A,o2y)'}; ...
16     {'diff(A,cox)'; 'diff(A,coy)'}; {'diff(A,gammax)'; 'diff(A,gammay)'}}};
17 femadj.equ.f = {{'diff(A,u)'; 'diff(A,v)'; 'diff(A,p)'; ...
18     'diff(A,o2)'; 'diff(A,co)'; 'diff(A,gamma)'}};
19 femadj.bnd.g = {{'diff(B,u)' 'diff(B,v)' 'diff(B,p)' ...
20     'diff(B,o2)' 'diff(B,co)' 'diff(B,gamma)'}};
21
22 femadj.xmesh = meshextend(femadj);
23
24 % GET INDICES OF DESIGN VARIABLE IN THE GLOBAL SOLUTION VECTOR (fem.sol.u)
25 igamma = find(asseminit(fem,'Init',fem.sol,'Out','U'));
26
27 % COMPUTE VOLUME BELOW DESIGN VARIABLE BASIS FUNCTIONS
28 L = assemble(fem,'Out',{'L'});
29 Vgamma = L(igamma);
30 Vdomain = sum(Vgamma);
31
32 % GET INDICES OF VELOCITY-PRESSURE VARIABLES ###### UPDATE THIS ######
33 ivar = find(asseminit(fem,'Init', ...
34     {'u' 1 'v' 1 'p' 1 'o2' 1 'co' 1},'Out','U'));
35
36 % DEFINE VARIABLES PARAMETERS FOR MMA OPTIMIZATION ALGORITHM
37 mmaa0 = 1;
38 mmaa = 0;
39 mmac = 1000;
40 mmad = 0;
41 mmaxmin = 0;
42 mmaxmax = 1;
43 mmaxold = fem.sol.u(ivar);
44 mmaxolder = mmaxold;
45 mmalow = 0;
46 mmaupp = 1;
```

Appendix B

Paper published in Phys. Rev. E

Title: Flow reversal at low voltage and low frequency in a microfabricated ac electrokinetic pump

Authors: Misha Marie Gregersen, Laurits Højgaard Olesen, Anders Brask, Mikkel Fought Hansen, and Henrik Bruus.

Reference: Published in Phys. Rev. E **76**, 056305 (2007) (9 pages)

Flow reversal at low voltage and low frequency in a microfabricated ac electrokinetic pump

Misha Marie Gregersen, Laurits Højgaard Olesen, Anders Brask, Mikkel Fougt Hansen, and Henrik Bruus
MIC–Department of Micro and Nanotechnology, Technical University of Denmark, DTU Building 345 East, DK-2800 Kongens Lyngby, Denmark
(Received 30 March 2007; published 9 November 2007)

Microfluidic chips have been fabricated in Pyrex glass to study electrokinetic pumping generated by a low-voltage ac bias applied to an in-channel asymmetric metallic electrode array. A measurement procedure has been established and followed carefully resulting in a high degree of reproducibility of the measurements over several days. A large coverage fraction of the electrode array in the microfluidic channels has led to an increased sensitivity allowing for pumping measurements at low bias voltages. Depending on the ionic concentration a hitherto unobserved reversal of the pumping direction has been measured in a regime, where both the applied voltage and the frequency are low, $V_{\mathrm{rms}}<1.5$ V and $f<20$ kHz, compared to previously investigated parameter ranges. The impedance spectrum has been thoroughly measured and analyzed in terms of an equivalent circuit diagram to rule out trivial circuit explanations of our findings. Our observations agree qualitatively, but not quantitatively, with theoretical electrokinetic models published in the literature.

DOI: 10.1103/PhysRevE.76.056305 PACS number(s): 47.57.jd, 47.61.Fg, 47.15.Rq

I. INTRODUCTION

The recent interest in ac electrokinetic micropumps was initiated by experimental observations by Green, Gonzales *et al.* of fluid motion induced by ac electroosmosis over pairs of microelectrodes [1–3] and by a theoretical prediction by Ajdari that the same mechanism would generate flow above an electrode array [4]. Brown *et al.* [5] demonstrated experimental pumping of an electrolyte with a low voltage, ac-biased electrode array, and soon after the same effect was reported by a number of other groups observing flow velocities on the order of mm/s [6–13]. Several theoretical models have been proposed parallel to the experimental observations [14–16]. However, so far not all aspects of the flow-generating mechanisms have been explained.

Studer *et al.* [10] made a thorough investigation of flow dependence on electrolyte concentration, driving voltage, and frequency for a characteristic system. In that work a reversal of the pumping direction for frequencies above 10 kHz and rms voltages above 2 V was reported. For a traveling wave device Ramos *et al.* [12] observed reversal of the pumping direction at 1 kHz and voltages above 2 V. The reason for this reversal is not yet fully understood and the goal of this work is to contribute with further experimental observations of reversing flow for other parameters than those reported previously.

We have fabricated and studied an integrated electrokinetic ac-driven micropump. The design follows Studer *et al.* [10], where an effective electrokinetic slip velocity is generated just above an asymmetric array of electrodes that covers the channel bottom in one section of a closed pumping loop. Pumping velocities are measured in another section of the channel without electrodes. In this way electrophoretic interaction between the beads used as flow markers and the electrodes is avoided. In contrast to the soft lithography utilized by Studer *et al.*, we use more well-defined MEMS fabrication techniques in Pyrex glass. This results in a very robust system, which exhibits stable properties and remains functional over time periods extending up to a year. Furthermore, we have a larger electrode coverage of the total channel length allowing for the detection of a given pumping velocity generated by a smaller electrokinetic slip velocity at a lower voltage. Our improved design has led to the observation of a phenomenon, namely, reversal of the flow at low voltages ($V_{\mathrm{rms}}<1.5$ V) and low frequencies ($f<20$ kHz). The electrical properties of the fabricated microfluidic chip have been investigated to clarify whether these affect the reversal of the flow direction. We propose an equivalent circuit diagram, evaluate it based on the electrical measurements, and conclude that we can rule out trivial circuit explanations of our findings. Supplementary details related to the present work can be found in Ref. [17].

II. EXPERIMENT

A. System design

The microchip was fabricated for studies of the basic electrokinetic properties of the system. Hence, a simple microfluidic circuit was designed to eliminate potential side effects due to complex device issues. The microfluidic chip has a size of approximately 16 mm × 28 mm and is shown in Fig. 1, while the device parameters are listed in Table I. It consists of two 500-μm-thick Pyrex glass wafers anodically bonded together. Metal electrodes are defined on the bottom wafer and channels are contained in the top wafer, as illustrated schematically in Fig. 1(a). This construction ensures an electrical insulated chip with fully transparent channels.

An electrode geometry akin to the one utilized by Brown *et al.* [5] and Studer *et al.* [10] was chosen. The translation period of the electrode array is 50 μm with electrode widths of $W_1=4.2$ μm and $W_2=25.7$ μm, and corresponding electrode spacings of $G_1=4.5$ μm and $G_2=15.6$ μm [see Fig. 1(d)]. Further theoretical investigations have shown that this geometry results in a nearly optimal flow velocity [16]. The total electrode array consists of eight subarrays each having their own connection to the shared contact pad, Fig. 1(b). This construction makes it possible to disconnect a malfunctioning subarray. The entire electrode array has a width of 1.3 mm ensuring that the alignment of the electrodes and the 1.0-mm-wide fluidic channels is not critical.

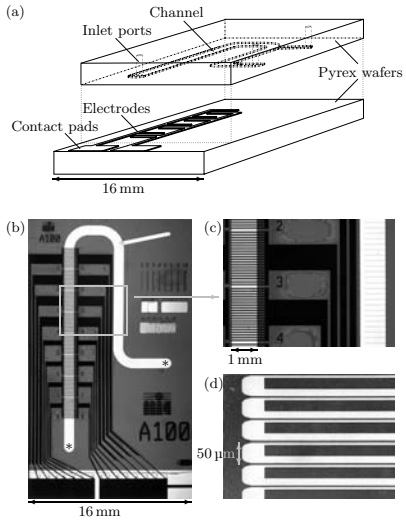

FIG. 1. (a) Sketch of the fabricated chip consisting of two Pyrex glass wafers bonded together. The channels are etched into the top wafer, which also contains the fluid access ports. Flow-generating electrodes are defined on the bottom wafer. (b) Micrograph of the full chip containing a channel (white) with flow-generating electrodes (black) and a narrow side channel for bead injection (upper right corner). During flow measurements the channel ends, marked with asterisks, are connected by an outer tube. The electrode array is divided into eight subarrays, each having its own connection to the electrical contact pad. (c) Magnification of the framed area in panel (b) showing the flow-generating electrodes to the left and the measurement channel with ruler lines to the right. (d) Closeup of an electrode array section with an electrode translation period of 50 μm.

A narrow side channel, Fig. 1(b), allows beads to be introduced into the part of the channel without electrodes, where a number of ruler lines with a spacing of 200 μm enable flow measurements by particle tracing, Fig. 1(c).

An outer circuit of valves and tubes is utilized to control and direct electrolytes and bead solutions through the channels. During flow-velocity measurements, the inlet to the narrow side channel is blocked and to eliminate hydrostatic pressure differences the two ends of the main channel are connected by an outer teflon tube with an inner diameter of 0.5 mm. The hydraulic resistance of this outer part of the pump loop is three orders of magnitude smaller than the on-chip channel resistance and is thus negligible.

In our design the channel has a rectangular cross section of width $w=967$ μm and height $H=33.6$ μm, while the total length is $L_{\mathrm{tot}}=40.8$ mm. The subsection containing electrodes has the length $L_{\mathrm{el}}=16.0$ mm and the hydraulic resistance R_1, and here an average slip velocity v_{slip} is generated by electroosmosis just above the electrodes. The subsection containing the measurement channel section has length $L_{\mathrm{tot}}-L_{\mathrm{el}}=24.2$ mm and hydraulic resistance R_2, and there a Poiseuille flow profile is established with a maximal center-point velocity denoted v_{Pois}. In the electrode subsection of the channel the flow rate Q is the sum of a forward Couette flow [14] and a backward Poiseuille flow, $Q=\frac{1}{2}wHv_{\mathrm{slip}}-\Delta p/R_1$, while in the measurement subsection it is a forward Poiseuille flow, $Q=\Delta p/R_2$. By combining these two expressions, the unknown overpressure Δp can be eliminated, and we find $(1+R_2/R_1)Q=\frac{1}{2}wHv_{\mathrm{slip}}$ or

$$v_{\mathrm{Pois}}=\frac{3}{4}\frac{1}{\left(1-0.63\frac{H}{w}\right)}\frac{L_{\mathrm{el}}}{L_{\mathrm{tot}}}v_{\mathrm{slip}}\approx 0.30v_{\mathrm{slip}}, \qquad (1)$$

where we have used that for Poiseuille flow in a rectangular channel $Q\approx\frac{2}{3}\left(1-0.63\frac{H}{w}\right)wHv_{\mathrm{Pois}}$ and $1+R_2/R_1=(R_1+R_2)/R_1=L_{\mathrm{tot}}/L_{\mathrm{el}}$. So to obtain a given pumping velocity v_{Pois} for as low an electrokinetic slip velocity v_{slip} as possible, the electrode coverage ratio $L_{\mathrm{el}}/L_{\mathrm{tot}}$ should be as large as possible. In our system $L_{\mathrm{el}}/L_{\mathrm{tot}}=0.39$, which almost doubles the sensitivity compared to Studer *et al.* [10], where $L_{\mathrm{el}}/L_{\mathrm{tot}}=0.21$.

TABLE I. Dimensions and parameters of the fabricated microfluidic system.

Channel height	H	33.6 μm
Channel width	w	967 μm
Channel length, total	L_{tot}	40.8 mm
Channel length with electrodes	L_{el}	16.0 mm
Width of electrode array	w_{el}	1300 μm
Narrow electrode gap	G_1	4.5 μm
Wide electrode gap	G_2	15.6 μm
Narrow electrode width	W_1	4.2 μm
Wide electrode width	W_2	25.7 μm
Electrode thickness	h	0.40 μm
Electrode surface area ($[W_1+2h]w$)	A_1	4.84×10^{-9} m^2
Electrode surface area ($[W_2+2h]w$)	A_2	25.63×10^{-9} m^2
Number of electrode pairs	p	312
Electrode resistivity (Pt)	ρ	10.6×10^{-8} Ωm
Electrolyte conductivity (0.1 mM)	σ	1.43 mS/m
Electrolyte conductivity (1.0 mM)	σ	13.5 mS/m
Electrolyte permittivity	ϵ	$80\epsilon_0$
Pyrex permittivity	ϵ_p	$4.6\epsilon_0$

B. Chip fabrication

The flow-generating electrodes of *e*-beam evaporated Ti(10 nm)/Pt(400 nm) were defined by lift-off in 1.5-μm-thick photoresist AZ 5214-E (Hoechst) using a negative process. Platinum is electrochemically stable and has a low resistivity, which makes it suitable for the application.

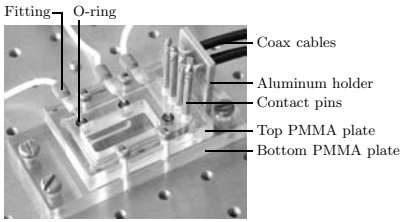

FIG. 2. Chip holder constructed to connect external tubing and electrical wiring with the microfluidic chip.

The thin Ti layer ensures good adhesion of the Pt layer to the Pyrex substrate. By choosing an electrode thickness of $h=400$ nm, the metallic resistance between the contact pads and the channel electrolyte is at least one order of magnitude smaller than the resistance of the bulk electrolyte covering the electrode array.

In the top Pyrex wafer the channel of width $w=967$ μm and height $H=33.6$ μm was etched into the surface using a solution of 40% hydrofluoric acid. A 100-nm-thick amorphous silicon layer was sputtered onto the wafer surface and used as etch mask in combination with a 2.2-μm-thick photoresist layer. The channel pattern was defined by a photolithography process akin to the process used for electrode definition, and the wafer backside and edges were protected with a 70-μm-thick etch resistant PVC foil. The silicon layer was then etched away in the channel pattern using a mixture of nitric acid and buffered hydrofluoric acid, $HNO_3:BHF:H_2O=20:1:20$. The wafer was subsequently baked at 120 °C to harden the photoresist prior to the HF etching of the channels. Since the glass etching is isotropic, the channel edges were left with a rounded shape. However, this has only a minor impact on the flow profile, given that the channel aspect ratio is $w/H\approx 30$. The finished wafer was first cleaned in acetone, which removes both the photoresist and the PVC foil, and then in a piranha solution.

After alignment of the channel and the electrode array, the two chip layers were anodically bonded together by heating the ensemble to 400 °C and applying a voltage difference of 700 V across the two wafers for 10 min. During this bonding process, the previously deposited amorphous Si layer served as a diffusion barrier against the sodium ions in the Pyrex glass. Finally, immersing the chip in de-ionized water holes were drilled for the inlet and outlet ports using a cylindrical diamond drill with a diameter of 0.8 mm.

C. Measurement setup and procedures

Liquid injection and electrical contact to the microchip was established through a specially constructed PMMA chip holder, shown in Fig. 2. Teflon tubing was fitted into the holder in which drilled channels provided a connection to the on-chip channel inlets. The interface from the chip holder to the chip inlets was sealed by O-rings. Electrical contact was obtained with spring loaded contact pins fastened in the chip holder and pressed against the electrode pads. The inner wires of thin coax cables were soldered onto the pins and likewise fastened to the holder.

The pumping was induced by electrolytic solutions of KCl in concentrations ranging from $c=0.1-1.0$ mM. The chip was prepared for an experiment by careful injection of this electrolyte into the channel and tubing system, after which the three valves to inlets and outlets were closed. The electrical impedance spectrum of the microchip was measured before and after each series of flow measurements to verify that no electrode damaging had occurred during the experiments. If the impedance spectrum had changed, the chip and the series of performed measurements were discarded. Velocity measurements were only carried out when the tracer beads were completely at rest before biasing the chip, and it was always verified that the beads stopped moving immediately after switching off the bias. The steady flow was measured for 10–60 s depending on the velocity (see Sec. II E). After a series of measurements was completed, the system was flushed thoroughly with milli-Q water. When stored in milli-Q water between experiments the chips remained functional for at least one year.

D. ac-biasing and impedance measurements

Using an impedance analyzer (HP 4194 A), electrical impedance spectra of the microfluidic chip were obtained by four-point measurements, where each contact pad was probed with two contact pins. Data were acquired from 100 Hz to 15 MHz. To avoid electrode damaging by application of a too high voltage at low frequencies, all impedance spectra were measured at $V_{\mathrm{rms}}=10$ mV.

The internal sinusoidal output signal of a lock-in amplifier (Stanford Research Systems SR830) was used for ac biasing of the electrode array during flow-velocity measurements. The applied rms voltages were in the range from 0.3 to 1.5 V and the frequencies between 1.0 and 100 kHz. A current amplification was necessary to maintain the correct potential difference across the electrode array, since the overall chip resistance could be small ($\sim 0.1-1$ kΩ) when frequencies in the given interval were applied. The current through the microfluidic chip was measured by feeding the output signal across a small series resistor back into the lock-in amplifier. The lock-in amplifier was also used for measuring impedance spectra for frequencies below 100 Hz, which were beyond the span of the impedance analyzer.

E. Flow-velocity measurements

After filling the channel with an electrolyte and actuating the electrodes, the flow measurements were performed by optical tracing of fluorescent beads suspended in the electrolyte. Instead of the previously employed micro-PIV method [10,18], we used a simpler, less accurate, but adequate optical particle tracing method for the velocity determination to be described below. We have demonstrated that our method is accurate within 10% for velocities between 10 and 100 μm/s by the following calibration measurements. A reservoir containing beads suspended in milli-Q water was placed at an adjustable height and connected by teflon tubing to the measurement channel through a partially closed valve.

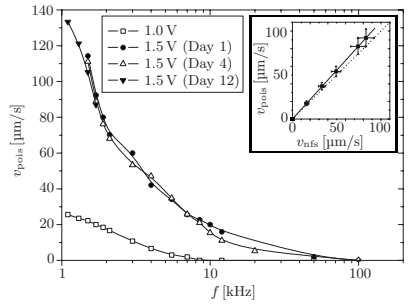

FIG. 3. Reproducible flow velocities induced in a 0.1 mM KCl solution and observed at different days as a function of frequency at a fixed rms voltage of 1.5 V. A corresponding series was measured at $V_{\mathrm{rms}}=1.0$ V. The frequencies are distributed on a $\log_{10}$ scale, and lines have been added to guide the eye. The inset shows the flow velocity v_{Pois}, measured using our optical tracing method, versus v_{nfs}, deduced from flow rates measured directly with a nanoflow sensor. The linear fit, $v_{\mathrm{Pois}}=1.1$ v_{nfs} (full line), is within 10% of perfect agreement, $v_{\mathrm{Pois}}=v_{\mathrm{nfs}}$ (dotted line).

For each setting of the height the resulting hydrostatic pressure generated a Poiseuille flow in the microchannel. After waiting for half an hour to allow for compliant relaxation of the system, the flow velocity v_{Pois} was measured using our optical tracing method and compared to the velocity $v_{\mathrm{nfs}}=\frac{1}{2}Q/\left[(1-0.63\frac{H}{w})wH\right]$ for a rectangular channel deduced from the flow rate Q measured directly by an Upchurch scientific N-565 nanoflow sensor connected to the outlet. The two sets of velocity determinations agree within 10% (see the inset of Fig. 3).

For our optical tracing method we introduced fluorescent tracer beads (molecular probes, FluoSpheres F-8765) with a diameter $d=1$ μm into the measurement section of the channel. The diffusivity of the beads are estimated by using the Stokes-Einstein relation, $D=k_BT/(3\pi\eta d)=4.4\times 10^{-13}$ m^2/s. The concentration of beads was kept low enough to allow the individual beads to be distinguished, when our Leica MZ-FLIII fluorescence microscope was focused on a section of length 700 μm of the measurement channel using a focal depth in the vertical z direction slightly larger than the channel depth of 34 μm. With an attached Sony DFW-X710 digital camera, we recorded a series of pictures of the beads at preset time intervals. We utilize the fact that for a Poiseuille flow in a wide, flat channel all particles in the middle third of the channel, $H/3<z<2H/3$ (except those within a distance H of the side walls), move with nearly the same horizontal velocity, namely, between 0.9 and 1.0 times the maximal center-point velocity v_{Pois}. Due to the size and density of the beads their vertical sedimentation speed and Brownian motion are negligible; it takes 420 s for a bead to fall from $z=2H/3$ to $z=H/3$ under the influence of gravity and 275 s to diffuse out of that region; no single bead was followed for more than 20 s during our measurements.

The preset time intervals for acquiring pictures of the bead flows were adjusted to the velocity determined by the voltage setting on the electrode array. It ranged from 1.00 s for very low velocities below 15 μm/s to 0.125 s for high velocities around 100 μm/s. The measurement series for a given voltage setting contained between 80 and 600 frames, and for each series the displacements of the fastest moving particles in the 700-μm-long field of view were traced over at least 20 frames. The displacement distances Δx we traced, using the in-channel ruler lines, were between 50 μm for the slowest and 200 μm for the fastest beads, while the corresponding measurement times Δt were between 20 and 2 s. The diffusion length for these times is 1 and 3 μm, respectively, leading to relative uncertainties in displacement of 3 μm/50 μm=6% and 1 μm/200 μm=0.5% for slowest and fastest particles, respectively. By averaging over ensembles of ten particles these uncertainties are lowered to 2% and 0.2%, respectively. For a given series it was checked that the selected fastest moving particles (typically ten) all moved with (nearly) the same, constant velocity, and the velocity v_{Pois} was determined as the average over the individually determined velocities $\Delta x/\Delta t$. The total statistical uncertainty, mainly due to the vertical bead position and the horizontal Brownian motion, was estimated to be on the order of 10%. This estimate is in good agreement with the calibration measurements described above.

Flow reversal appearing as a result of a change in the bias voltage setting between two measurements (see Sec. III) was thoroughly verified. It was checked that the beads were completely at rest before biasing the chip, and then the forward flow was measured. Subsequently, it was again controlled that the beads were completely at rest when turning off the bias. The bias value was then changed and turned on, and the reverse flow was measured. Finally, the bias was turned off and the beads were once more confirmed to be completely at rest.

III. RESULTS

In the parameter ranges corresponding to those published in the literature, our flow velocity measurements are in agreement with previously reported results. Using a $c=0.1$ mM KCl solution and driving voltages of $V_{\mathrm{rms}}=1.0-1.5$ V over a frequency range of $f=1.1-100$ kHz, we observed among other measurement series the pumping velocities shown in Fig. 3. The general tendencies were an increase of velocity toward lower frequencies and higher voltages, and absence of flow above $f\sim 100$ kHz. The measured velocities corresponded to slightly more than twice those measured by Studer *et al.* [10] due to our larger electrode coverage of the total channel. We observed damaging of the electrodes if more than 1 V was applied to the chip at a driving frequency below 1 kHz, for which reason there are no measurements at these frequencies. It is, however, plausible that the flow velocity for our chip peaked just below $f\sim 1$ kHz.

A. Reproducibility of measurements

Our measured flow velocities were very reproducible due to the employed MEMS chip fabrication techniques and the

careful measurement procedures described in Sec. II. This is illustrated in Fig. 3, which shows three velocity series recorded several days apart. The measurements were performed on the same chip and for the same parameter values. Between each series of measurements, the chip was dismounted and other experiments performed. However, it should be noted that a very slow electrode degradation was observed when a dozen of measurement series were performed on the same chip over a couple of weeks.

B. Flow reversal at low voltage and low frequency

Devoting special attention to the low-voltage ($V_{\rm rms}<1.5$ V), low-frequency ($f<20$ kHz) regime, not studied in detail previously, we observed an unanticipated flow reversal for certain parameter combinations. This observation was made possible by the large electrode coverage ratio $L_{\rm el}/L_{\rm tot}$ appearing in the expression Eq. (1) for $v_{\rm Pois}$ in terms of $v_{\rm slip}$.

Figure 4(a) shows flow velocities measured for a frequency of 1.0 kHz as a function of applied voltage for various electrolyte concentrations. It is clearly seen that the velocity series of $c=0.1$ mM exhibits the known exclusively forward and increasing pumping velocity as a function of voltage, whereas for slightly increased electrolyte concentrations an unambiguous reversal of the flow direction is observed for rms voltages below approximately 1 V.

This reversed flow direction was observed for all frequencies in the investigated spectrum when the electrolyte concentration and the rms voltage were kept constant. This is shown in the inset of Fig. 4(a), where a velocity series was obtained over the frequency spectrum for an electrolyte concentration of 0.4 mM at a constant rms voltage of 0.8 V. It is noted that the velocity is nearly constant over the entire frequency range and tends to zero above $f\sim 20$ kHz.

C. Electrical characterization

To investigate whether the flow reversal was connected to unusual properties of the electrical circuit, we carefully measured the impedance spectrum $Z(f)$ of the microfluidic system. Spectra were obtained for the chip containing KCl electrolytes with the different concentrations $c=0.1$, 0.4, and 1.0 mM.

Figure 5 shows the Bode plots of the impedance spectrum obtained for $c=1.0$ mM. For frequencies between $f\sim 1$ and $f\sim 10^3$ Hz the curve shape of the impedance amplitude $|Z|$ is linear with slope -1, after which a horizontal curve section follows, and finally, the slope again becomes -1 for frequencies above $f\sim 10^6$ Hz. Correspondingly, the phase θ changes between 0° and 90°. From the decrease in phase toward low frequencies it is apparent that $|Z|$ must have another horizontal curve section below $f\sim 1$ Hz. When the curve is horizontal and the phase is 0°, the system behaves resistively, while it is capacitively dominated when the phase is 90° and the curve has a slope of -1.

IV. DISCUSSION

As we shall see in the following, our observation of a reproducible and stable flow reversal cannot be explained by the existing theories of induced-charge (ac) electroosmosis, even when faradaic current injection is taken into account as in the most developed theoretical model, the weakly nonlinear electrohydrodynamic model presented in Ref. [16] and extended in Ref. [19] (see Sec. IV B). This is not surprising, as this model and other similar models are limited to the weakly nonlinear regime $V\lesssim 0.2$ V. We nevertheless do find some qualitative agreement and discuss the experimentally observed trends of the flow velocities, in particular, the flow reversal. The following discussion is included to relate our experimental results to a state-of-the-art theoretical model, and to indicate possible directions for future work in the field.

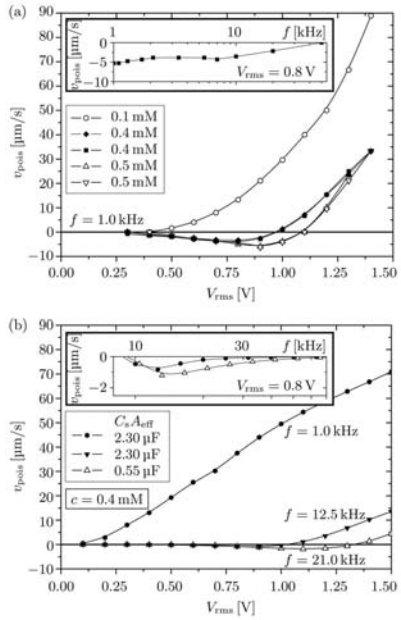

FIG. 4. (a) Experimentally observed flow reversal for repeated measurements of two concentrations of KCl at 1.0 kHz. The inset shows that for a 0.4 mM KCl solution at a fixed rms voltage of 0.8 V the flow direction remains negative, but slowly approaches zero on a $\log_{10}$ scale for frequencies up to 50 kHz. (b) The theoretical model presented in Ref. [19] predicts the trends of the experimentally observed velocity curves. The depicted graphs are calculated for a $c=0.4$ mM solution and parameters corresponding to the experiments (Table II) with $\zeta_{\rm eq}=160$ mV. Additional curves have been plotted for slightly different parameter values in order to obtain a closer resemblance to the experimental graphs (see Sec. IV).

A. Equivalent circuit impedance analysis

In electrochemistry the standard way of analyzing impedance measurements is in terms of an equivalent circuit diagram [20]. Based on the Gouy-Chapman-Stern model for the electric double layer, the component values extracted from this analysis are used to estimate three important electrokinetic parameters: the Stern layer capacitance C_s, the intrinsic zeta potential $\zeta_{\rm eq}$ on the electrodes, and the charge transfer resistance $R_{\rm ct}$.

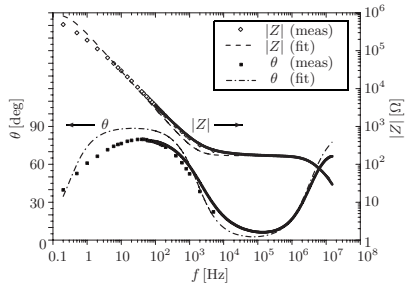

FIG. 5. Bode plot showing the measured amplitude $|Z|$ on a $\log_{10}$ scale (right ordinate axis) and phase θ (left ordinate axis) of the impedance as a function of frequency over eight decades distributed on a $\log_{10}$ scale from 0.2 Hz to 15 MHz. The voltage was $V_{\rm rms}=10$ mV and the electrolyte concentration $c=1.0$ mM KCl. The measurements are shown with symbols while the curves of the fitted equivalent diagram (see Fig. 6) are represented by dashed lines. The measurement series obtained with the impedance analyzer consist of 400 very dense points while the series measured using the lock-in amplifier contains fewer points with a clear spacing.

Following [3,16,21] the basic unit in the diagram Fig. 6(a) is a double-layer electrode capacitor in series with a bulk electrolyte resistor and a double-layer counterelectrode capacitor. The order of the series components is unimportant, so in the diagram the electrode pair can be placed next to each other. In our system all electrodes are identical except for their widths W_1 and W_2 and thus their respective surface areas A_1 and A_2. However, the important physical parameter, the RC time due to the charge transfer resistance R and the capacitance C, is independent of the area since $R\propto 1/A$ and $C\propto A$. Consequently, only one RC time is present in the system due to the electric double layers. As seen in Fig. 6(a) this can be represented by one single parallel coupling of $C_{\rm dl}$ (the total capacitance due to accumulation of charge in the double layers at all the electrodes) and $R_{\rm ct}$ (the total resistance due to faradaic current injection from electrochemical reactions at all the electrodes) in series with the bulk electrolyte resistor R_b. Moreover, we include the ohmic resistance of the metal electrodes $R_{\rm el}$, a shunt resistance $R_{x'}=10$ MΩ to represent the internal resistance of the lock-in amplifier, and the mutual capacitance between the narrow and wide electrodes $C_{\rm el}$. The latter contains contributions from both the electrolyte and the surrounding glass. However, since it is three orders of magnitude smaller than $C_{\rm dl}$ its precise placement relative to $C_{\rm dl}$ is not important. Finally, since the separation between the electrodes is small and the charge transfer resistance is large, the diffusion-related Warburg impedance [20] can be neglected.

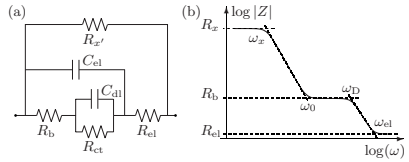

FIG. 6. (a) Equivalent circuit diagram showing the total electrode resistance $R_{\rm el}$, the total bulk electrolyte resistance R_b, the total faradaic (charge transfer) resistance $R_{\rm ct}$, the internal resistance of the lock-in amplifier $R_{x'}$, the total electrode capacitance $C_{\rm el}$, and the total double-layer capacitance $C_{\rm dl}$. (b) Sketch of the impedance amplitude response of the equivalent diagram. It consists of three plateaus, $R_{\rm el}$, R_b, and the dc-limit R_x of the total resistance. These are delimited by four characteristic frequencies: the inverse faradaic charge transfer time ω_x, the inverse ohmic relaxation time ω_0, the Debye frequency ω_D, and the electrode circuit frequency $\omega_{\rm el}$.

By fitting the circuit model Fig. 6(a) to the impedance measurements [see Figs. 5 and 6(b)], we extract the component values listed in Table II including the four characteristic angular frequencies $\omega=2\pi f$. The inverse frequency $\omega_x^{-1}=R_x C_{\rm dl}$ primarily expresses the characteristic time for the faradaic charge transfer into the Debye layer. The characteristic time for charging the Debye layer through the electrolyte is given by $\omega_0^{-1}=R_b C_{\rm dl}$. The Debye frequency is $\omega_D=1/(R_b C_{\rm el})$, and $\omega_{\rm el}=1/(R_{\rm el}C_{\rm el})$ states the characteristic frequency for the on-chip electrode circuit in the absence of electrolyte.

These fitted values can be compared with the modeled values, which are found as explained in Table II, with the following additional remarks regarding the parameters of the electric double layers. Although the impedance measurements were performed at a low voltage of $V_{\rm rms}=10$ mV the presence of an intrinsic zeta potential $\zeta_{\rm eq}$ of the order of typically 100 mV nevertheless forces us to use the nonlinear Gouy-Chapman-Stern theory, where $C_{\rm dl}$ can be expressed as a series coupling of the compact Stern layer capacitance C_s and the differential Debye layer capacitance C_D (see Table II). For simplicity C_s is often assumed constant and independent of potential and concentration, while C_D is given by $C_D=(\epsilon/\lambda_D)\cosh[\zeta_{\rm eq}ze/(2k_BT)]$. Indeed, the measured $C_{\rm dl}$ is roughly 10 times larger than predicted by the Debye-Hückel theory, which indicates that the intrinsic zeta potential is at least ±125 mV. Unfortunately, it is not possible to estimate the exact values of both C_s and $\zeta_{\rm eq}$ from a measurement of $C_{\rm dl}$, because a range of parameters led to the same $C_{\rm dl}$. We can, nevertheless, state lower limits as $C_s\geqslant 0.39$ F/m^2 and $|\zeta_{\rm eq}|\geqslant 175$ mV for $c=0.1$ mM or $C_s\geqslant 0.43$ F/m^2 and $|\zeta_{\rm eq}|\geqslant 125$ mV at $c=1.0$ mM. For the model values in Table II we used $C_s=1.8$ F/m^2 and $\zeta_{\rm eq}=190$, 160, and 140 mV at 0.1, 0.4, and 1.0 mM KCl, respectively, in accordance with the trend often observed that $\zeta_{\rm eq}$ decreases with increasing concentration [22].

At frequencies above 100 kHz the impedance is dominated by R_b, $C_{\rm el}$, and $R_{\rm el}$, and the Bode plot closely resembles a circuit with ideal components (see Fig. 5). Around 1 kHz we observe some frequency dispersion, which could be due to the change in the electric field line pattern around the

TABLE II. Comparison of measured (meas.) and modeled (mod.) values of the components in the equivalent diagram, Fig. 6. The measured values are given by curve fits of Bode plots (Fig. 5), obtained on two similar chips labeled *A* and *B*, respectively. Due to a minor error on the chip introduced during the bonding process, we were unable to measure R_{ct} for chip *B*. The modeled values are estimated on the basis of Table I and a particular choice of the parameters ζ_{eq} and C_s as follows: The inverse of the total double-layer capacitance is $1/C_{dl}=(1/C_s+1/C_D)(1/A_1+1/A_2)/p$, while the bulk electrolyte resistance is $R_b=0.85/(\sigma wp)$ and the mutual capacitance between the electrodes is $C_{el}=(p/0.85)[\epsilon w+\epsilon_p(2w_{el}-w)]$, where 0.85 is a numerical factor computed for our particular electrode layout using the finite-element-based program COMSOL MULTIPHYSICS.

Concentration (chip)	R_b mod. (kΩ)	R_b meas. (kΩ)	R_{el} mod. (Ω)	R_{el} meas. (Ω)	R_{ct} meas. (MΩ)	C_{dl} mod. (μF)	C_{dl} meas. (μF)	C_{el} mod. (nF)	C_{el} meas. (nF)	ω_D mod. (M rad s^{-1})	ω_D meas. (M rad s^{-1})	ω_0 mod. (k rad s^{-1})	ω_0 meas. (k rad s^{-1})
0.1 mM (*A*)	2.0	1.0	7.6	5	1.0	0.50	0.50	0.28	0.30	2.0	3.3	1.0	2.0
1.0 mM (*A*)	0.21	0.17	7.6	6	1.0	0.56	0.55	0.28	0.29	19.1	20.6	8.5	10.7
0.1 mM (*B*)	2.0	1.4	7.6	6		0.50	0.51	0.28	0.29	2.0	3.0	1.0	1.4
0.4 mM (*B*)	0.52	0.41	7.6	7		0.54	0.53	0.28	0.28	7.7	9.3	3.6	4.6
1.0 mM (*B*)	0.21	0.17	7.6	8		0.56	0.55	0.28	0.26	19.1	22.6	8.5	10.5

inverse *RC* time $\omega_0=1/(R_bC_{dl})$ [19]. Finally, below 1 kHz where the impedance is dominated by C_{dl}, the phase never reaches 90° indicating that the double layer capacitance does not behave as an ideal capacitor but more like a constant phase element (CPE). This behavior is well known experimentally, but not fully understood theoretically [23].

Overall, we have a fair agreement between the measurements and the equivalent diagram analysis, so we conclude that the observation of flow reversal is not related to any unusual electrical properties of the chip, but must be due to the intrinsic electrokinetic properties of the electrolyte.

B. Weakly nonlinear flow analysis

We analyze our experimental results in terms of the weakly nonlinear model [16,19] based on the following classical approximations [15,20,21]: (i) The bulk electrolyte is an ohmic resistor assumed to be charge neutral with uniform salt concentration. (ii) The Debye layer is assumed to be in local equilibrium with the electrolyte immediately outside the layer. (iii) The thickness of the Debye layer is much smaller than the size of the electrodes, and surface diffusion and migration of charge is neglected. (iv) The bulk fluid motion is described by Stokes flow with a slip condition on the electrodes set by the electroosmotic flow induced in the Debye layer. (v) Finally, following the extended model in [19], Butler-Volmer reaction kinetics models a generic faradaic electrode reaction [20] and small perturbative variations in the concentration in the diffusive layer of the reactants in the faradaic electrode reaction are allowed.

The forward flow velocities measured at $c=0.1$ mM as a function of frequency (Fig. 3) qualitatively exhibit the trends predicted by standard theory, namely, the pumping increases with voltage and falls off at high frequency [4,14].

More specifically, the theory predicts that the pumping velocity should peak at a frequency around the inverse *RC* time ω_0, corresponding to $f\approx 0.3$ kHz, and decay as the inverse of the frequency for our applied driving voltages (see Fig. 11 in Ref. [16]). Furthermore, the velocity is predicted to grow like the square of the driving voltage at low voltages, changing to $V\ln V$ at large voltages [16,19].

Experimentally, the velocity is indeed proportional to ω^{-1} and the peak is not observed within the range 1.1–100 kHz, but it is likely to be just below 1 kHz. However, the increase in velocity between 1.0 and 1.5 V displayed in Fig. 3 is much faster than V^2. That is also the result in Fig. 4(a) for $c=0.1$ mM where no flow is observed below $V_{rms}=0.5$ V, while above that voltage the velocity increases rapidly. For $c=0.4$ mM and $c=0.5$ mM the velocity even becomes negative at voltages $V_{rms}\leqslant 1$ V. This cannot be explained by the standard theory and is also rather different from the flow reversal that has been observed by other groups at larger voltages $V_{rms}>2$ V and at frequencies above the inverse *RC* time [10,12,13].

The velocity shown in the inset of Fig. 4(a) is remarkable because it is almost constant between 1 and 10 kHz. This is unlike the usual behavior for ac electroosmosis that always peaks around the inverse *RC* time, because it depends on partial screening at the electrodes to simultaneously get charge and tangential field in the Debye layer. At lower frequency the screening is almost complete so there is no electric field in the electrolyte to drive the electroosmotic fluid motion, while at higher frequency the screening is negligible so there is no charge in the Debye layer and again no electroosmosis.

One possible explanation for the almost constant velocity as a function of frequency could be that the amount of charge in the Debye layer is controlled by a faradaic electrode reaction rather than by the ohmic current running through the bulk electrolyte. Our impedance measurement clearly shows that the electrode reaction is negligible at $f=1$ kHz and $V_{rms}=10$ mV bias, but since the reaction rate grows exponentially with voltage in an Arrhenius-type dependence, it may still play a role at $V_{rms}=0.8$ V. However, previous theoretical investigations have shown that faradaic electrode reactions do not lead to the reversal of the ac electroosmotic flow or pumping direction [16].

Due to the strong nonlinearity of the electrode reaction and the asymmetry of the electrode array, there may also be a dc faradaic current running although we drive the system with a harmonic ac voltage. In the presence of an intrinsic

zeta potential ζ_{eq} on the electrodes and/or the glass substrate this would give rise to an ordinary dc electroosmotic flow. This process does not necessarily generate bubbles because the net reaction products from one electrode can diffuse rapidly across the narrow electrode gap to the opposite electrode and be consumed by the reverse reaction.

To investigate to which extent this proposition applies, we used the extended weakly nonlinear theoretical model presented in Ref. [19]. The concentration of the oxidized and reduced species in the diffusion layer near the electrodes is modeled by a generalization of the Warburg impedance, while the bulk concentration is assumed uniform. The model parameters are chosen in accordance with the result of the impedance analysis, i.e., $C_s=1.8$ F/m^2, $R_{ct}=1$ MΩ, and $\zeta_{eq}=160$ mV, as discussed in Sec. IV A. Further, we assume an intrinsic zeta potential of $\zeta_{eq}=-100$ mV on the borosilicate glass walls [22], and choose (arbitrarily) an equilibrium bulk concentration of 0.02 mM for both the oxidized and the reduced species in the electrode reaction, which is much less than the KCl electrolyte concentration of $c=0.4$ mM.

The result of the model calculation is shown in Fig. 4(b). At 1 kHz the fluid motion is dominated by ac electroosmosis, which is solely in the forward direction. However, at 12.5 kHz the ac electroosmosis is much weaker and the model predicts a (small) reverse flow due to the dc electroosmosis for $V_{rms}<1$ V. Figure 4(b) shows that the frequency interval with reverse flow is only from 30 kHz down to 10 kHz, while the measured velocities remain negative down to at least 1 kHz. The figure also shows results obtained with a lower Stern layer capacitance $C_s=0.43$ F/m^2 in the model, which turns out to enhance the reverse flow.

In both cases, the reverse flow predicted by the theoretical model is weaker than that observed experimentally and does not show the almost constant reverse flow profile below 10 kHz. Moreover, the model is unable to account for the strong concentration dependence displayed in Fig. 4(a).

According to Ref. [24], steric effects give rise to a significantly lowered Debye layer capacitance and a potentially stronger concentration dependence when ζ exceeds $10k_BT/e\sim 250$ mV, which roughly corresponds to a driving voltage of $V_{rms}\sim 0.5$ V. Thus, by disregarding these effects we overestimate the double-layer capacitance slightly in the calculations of the theoretical flow velocity for $V_{rms}=0.8$ V. This seems to fit with the observed tendencies, where theoretical velocity curves calculated on the basis of a lowered C_{dl} better resemble the measured curves.

Finally, it should be noted that several electrode reactions are possible for the present system. As an example we mention $2H_2O_{(l)}+O_{2(aq)}+4e^-\rightleftharpoons 4OH^-_{(aq)}$. This reaction is limited by the amount of oxygen present in the solution, which in our experiment is not controlled. If this reaction were dominating the faradaic charge transfer, the value of R_{ct} could change from one measurement series to another.

V. CONCLUSION

We have produced an integrated ac electrokinetic micropump using MEMS fabrication techniques. The resulting systems are very robust and may preserve their functionality over years. Due to careful measurement procedures it has been possible over weeks to reproduce flow velocities within the inherent uncertainties of the velocity determination.

An increased electrode coverage fraction of the channel has led to an increased sensitivity as reflected in the velocity ratio $v_{Pois}/v_{slip}=0.30$. Based on this, a hitherto unobserved reversal of the pumping direction has been measured in a regime, where the frequency and the applied voltage are low ($f<20$ kHz and $V_{rms}<1.5$ V) compared to earlier investigated parameter ranges. This reversal depends on the exact electrolytic concentration and the applied voltage. The measured velocities are of the order -5 μm/s to -10 μm/s. Previously reported studies of flow measured at the same parameter combinations show zero velocity with the given resolution in this regime [10].

Finally, we have performed an impedance characterization of the pumping devices over eight frequency decades. By fitting Bode plots of the data, the measured impedance spectra compared favorably with our model using reasonable parameter values.

The trends of our flow-velocity measurements are accounted for by a previously published theoretical model, but the quantitative agreement is lacking. Most important, the predicted velocities do not depend on electrolyte concentration, yet the concentration seems to be one of the causes of our measured low-voltage, low-frequency flow reversal, Fig. 4(a). This shows that there is a need for further theoretical work on the electrohydrodynamics of these systems and, in particular, on the effects of electrolyte concentration variations.

ACKNOWLEDGMENT

We would like to thank Torben Jacobsen, Department of Chemistry, DTU, for enlightening discussions about electrokinetics and the interpretation of impedance measurements on electrokinetic systems.

[1] N. G. Green, A. Ramos, A. Gonzalez, H. Morgan, and A. Castellanos, Phys. Rev. E **61**, 4011 (2000).
[2] A. Gonzalez, A. Ramos, N. G. Green, A. Castellanos, and H. Morgan, Phys. Rev. E **61**, 4019 (2000).
[3] N. G. Green, A. Ramos, A. Gonzalez, H. Morgan, and A. Castellanos, Phys. Rev. E **66**, 026305 (2002).
[4] A. Ajdari, Phys. Rev. E **61**, R45 (2000).
[5] A. B. D. Brown, C. G. Smith, and A. R. Rennie, Phys. Rev. E **63**, 016305 (2000).
[6] V. Studer, A. Pépin, Y. Chen, and A. Ajdari, Microelectron. Eng. **61-62**, 915 (2002).
[7] M. Mpholo, C. G. Smith, and A. B. D. Brown, Sens. Actuators

B **92**, 262 (2003).
[8] D. Lastochkin, R. Zhou, P. Whang, Y. Ben, and H.-C. Chang, J. Appl. Phys. **96**, 1730 (2004).
[9] S. Debesset, C. J. Hayden, C. Dalton, J. C. T. Eijkel, and A. Manz, Lab Chip **4**, 396 (2004).
[10] V. Studer, A. Pépin, Y. Chen, and A. Ajdari, Analyst (Cambridge, U.K.) **129**, 944 (2004).
[11] B. P. Cahill, L. J. Heyderman, J. Gobrecht, and A. Stemmer, Phys. Rev. E **70**, 036305 (2004).
[12] A. Ramos, H. Morgan, N. G. Green, A. Gonzalez, and A. Castellanos, J. Appl. Phys. **97**, 084906 (2005).
[13] P. García-Sánchez, A. Ramos, N. G. Green, and H. Morgan, IEEE Trans. Dielectr. Electr. Insul. **13**, 670 (2006).
[14] A. Ramos, A. Gonzalez, A. Castellanos, N. G. Green, and H. Morgan, Phys. Rev. E **67**, 056302 (2003).
[15] N. A. Mortensen, L. H. Olesen, L. Belmon, and H. Bruus, Phys. Rev. E **71**, 056306 (2005).
[16] L. H. Olesen, H. Bruus, and A. Ajdari, Phys. Rev. E **73**, 056313 (2006).
[17] M. M. Gregersen, M.Sc. thesis, Technical University of Denmark, 2005, www.mic.dtu.dk/microfluidics
[18] J. G. Santiago, S. T. Wereley, C. D. Meinhart, D. J. Beebe, and R. J. Adrian, Exp. Fluids **25**, 316 (1998).
[19] L. H. Olesen, Ph.D. thesis, Technical University of Denmark, 2006, www.mic.dtu.dk/microfluidics
[20] A. J. Bard and L. R. Faulkner, *Electrochemical Methods*, 2nd ed. (Wiley, New York, 2001).
[21] M. Z. Bazant, K. Thornton, and A. Ajdari, Phys. Rev. E **70**, 021506 (2004).
[22] B. J. Kirby and E. F. Hasselbrink, Electrophoresis **25**, 187 (2004).
[23] Z. Kerner and T. Pajkossy, Electrochim. Acta **46**, 207 (2000).
[24] M. S. Kilic, M. Z. Bazant, and A. Ajdari, Phys. Rev. E **75**, 021502 (2007); **75**, 021503 (2007).

Appendix C

Paper in press in New J. Phys.

Title: Topology and shape optimization of induced-charge electro-osmotic micropumps

Authors: Misha Marie Gregersen, Fridolin Okkels, Martin Z. Bazant, and Henrik Bruus.

Reference: New. J. Phys. (in press, 2009) (20 pages)

Topology and shape optimization of induced-charge electro-osmotic micropumps

M M Gregersen[1], F Okkels[1], M Z Bazant[2,3], and H Bruus[1]

[1]Department of Micro- and Nanotechnology, Technical University of Denmark, DTU Nanotech, Building 345 East, DK-2800 Kongens Lyngby, Denmark
[2]Departments of Chemical Engineering and Mathematics, MIT, Cambridge, MA 02139 USA
[3]Physico-Chimie Théorique, UMR 7083 Gulliver-CNRS, ESPCI, 10 rue Vauquelin, Paris 75005, France

E-mail: Henrik.Bruus@nanotech.dtu.dk

8 March 2009

Abstract. For a dielectric solid surrounded by an electrolyte and positioned inside an externally biased parallel-plate capacitor, we study numerically how the resulting induced-charge electro-osmotic (ICEO) flow depends on the topology and shape of the dielectric solid. In particular, we extend existing conventional electrokinetic models with an artificial design field to describe the transition from the liquid electrolyte to the solid dielectric. Using this design field, we have succeeded in applying the method of topology optimization to find system geometries with non-trivial topologies that maximize the net induced electro-osmotic flow rate through the electrolytic capacitor in the direction parallel to the capacitor plates. Once found, the performance of the topology optimized geometries has been validated by transferring them to conventional electrokinetic models not relying on the artificial design field. Our results show the importance of the topology and shape of the dielectric solid in ICEO systems and point to new designs of ICEO micropumps with significantly improved performance.

Submitted to: *New J. Phys.*

1. Introduction

Induced-charge electro-osmotic (ICEO) flow is generated when an external electric field polarizes a solid object placed in an electrolytic solution [1, 2]. Initially, the object acquires a position-dependent potential difference ζ relative to the bulk electrolyte. However, this potential is screened out by the counter ions in the electrolyte by the formation of an electric double layer of width λ_D at the surface of the object. The ions in the diffusive part of the double layer are then electromigrating in the resulting external electric field, and by viscous forces they drag the fluid along. At the outer surface of the double layer a resulting effective slip velocity is thus established. For a review of ICEO see Squires and Bazant [3].

The ICEO effect may be utilized in microfluidic devices for fluid manipulation, as proposed in 2004 by Bazant and Squires [1]. Theoretically, various simple dielectric shapes have been analyzed for their ability to pump and mix liquids [3, 4]. Experimentally ICEO was observed and the basic model validated against particle

image velocimetry in 2005 [2], and later it has been used in a microfluidic mixer, where a number of triangular shapes act as passive mixers [5]. However, no studies have been carried out concerning the impact of topology changes of the dielectric shapes on the mixing or pumping efficiency. In this work we focus on the application of topology optimization to ICEO systems. With this method it is possible to optimize the dielectric shapes for many purposes, such as mixing and pumping efficiency.

Our model system consists of two externally biased, parallel capacitor plates confining an electrolyte. A dielectric solid is shaped and positioned in the electrolyte, and the external bias induces ICEO flow at the dielectric surfaces. In this work we focus on optimizing the topology and shape of the dielectric solid to generate the maximal flow perpendicular to the external applied electric field. This example of establishing an optimized ICEO micropump serves as demonstration of the implemented topology optimization method.

Following the method of Borrvall and Petersson [6] and the implementation by Olesen, Okkels and Bruus [7] of topology optimization in microfluidic systems, we introduce an artificial design field $\gamma(\boldsymbol{r})$ in the governing equations. The design field varies continuously from zero to unity, and it defines to which degree a point in the design domain is occupied by dielectric solid or electrolytic fluid. Here, $\gamma = 0$ is the limit of pure solid and $\gamma = 1$ is the limit of pure fluid, while intermediate values of γ represent a mixture of solid and fluid. In this way, the discrete problem of placing and shaping the dielectric solid in the electrolytic fluid is converted into a continuous problem, where the sharp borders between solid and electrolyte are replaced by continuous transitions throughout the design domain. In some sense one can think of the solid/fluid mixture as a sort of ion-exchange membrane in the form of a sponge with varying permeability. This continuum formulation allows for an efficient gradient-based optimization of the problem.

In one important aspect our system differs from other systems previously studied by topology optimization: induced-charge electro-osmosis is a boundary effect relying on the polarization and screening charges in a nanometer-sized region around the solid/fluid interface. Previously studied systems have all been relying on bulk properties such as the distribution of solids in mechanical stress analysis [8], photonic band gap structures in optical wave guides [9], and acoustic noise reduction [10], or on the distribution of solids and liquids in viscous channel networks [6, 7, 11] and chemical microreactors [12]. In our case, as for most other applications of topology optimization, no mathematical proof exists that the topology optimization routine indeed will result in an optimized structure. Moreover, since the boundary effects of our problem result in a numerical analysis which is very sensitive on the initial conditions, on the meshing, and on the specific form of the design field, we take the more pragmatic approach of finding non-trivial geometries by use of topology optimization, and then validate the optimality by transferring the geometries to conventional electrokinetic models not relying on the artificial design field.

2. Model system

We consider a parallel-plate capacitor externally biased with a harmonic oscillating voltage difference $\Delta\phi = 2V_0\cos(\omega t)$ and enclosing an electrolyte and a dielectric solid. The two capacitor plates are positioned at $z = \pm H$ and periodic boundary conditions are applied at the open ends at $x = \pm L/2$. The resulting bound domain of size $L \times 2H$ in the xz-plane is shown in Fig. 1. The system is assumed to be unbounded

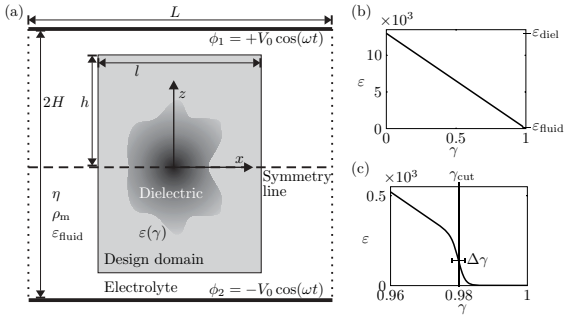

Figure 1. (a) A sketch of the rectangular $L \times 2H$ cross-section of the electrolytic capacitor in the xz-plane. The external voltages ϕ_1 and ϕ_2 are applied to the two infinite parallel-plate electrodes (thick black lines) at $z = \pm H$. The voltage difference $\phi_1 - \phi_2$ induces an ICEO flow around the un-biased dielectric solid (dark gray) shaped by the topology optimization routine limited to the rectangular $l \times 2h$ design domain (light gray). The dielectric solid is surrounded by pure electrolyte (light gray and white). Periodic boundary conditions are applied ar the vertical edges (dotted lines). (b) The dimensionless electric permittivity ε as a function of the design variable γ. (c) Zoom-in on the rapid convergence of $\varepsilon(\gamma)$ towards $\varepsilon_{\text{fluid}} = 1$ for γ approaching unity after passing the value $\gamma_{\text{cut}} - \Delta\gamma \simeq 0.98$.

and translational invariant in the perpendicular y-direction. The topology and shape of the dielectric solid is determined by the numerical optimization routine acting only within a smaller rectangular, central design domain of size $l \times 2h$. The remaining domain outside this area is filled with pure electrolyte. Double layers, or Debye screening layers, are formed in the electrolyte around each piece of dielectric solid to screen out the induced polarization charges. The pull from the external electric field on these screening layers in the design domain drives an ICEO flow in the entire domain.

The magnitude of the ICEO effect increases as the permittivity $\varepsilon_{\text{diel}}$ of the dielectric solid increases relative to that of the electrolyte, $\varepsilon_{\text{fluid}} = 78\varepsilon_0$. For maximum effect we therefore employ $\varepsilon_{\text{diel}} = 10^6\varepsilon_0$ throughout this work. For such a large value of the permittivity the potential inside the dielectric solid is nearly constant as for a metal. Placed in an external electric field E, the largest potential difference, denoted the zeta potential ζ, between the dielectric solid and the surrounding electrolyte just outside the screening double layer can thus be estimated as $\zeta = Ea$ [3].

If the dielectric solid is symmetric around the x-axis, the anti-symmetry of the applied external bias voltage ensures that the resulting electric potential is anti-symmetric and the velocity and pressure fields symmetric around the center plane $z = 0$. This symmetry appears in most of the cases studied in this paper, and when present it is exploited to obtain a significant decrease in memory requirements of the numerical calculations.

The specific goal of our analysis is to determine the topology and shape of the dielectric solid such that a maximal flow rate Q is obtained parallel to the x-axis, i.e. perpendicular to the direction of external potential field gradient.

3. Governing equations

We follow the conventional continuum approach to the electrokinetic modeling of the electrolytic capacitor [3]. For simplicity we consider a symmetric, binary electrolyte, where the positive and negative ions with concentrations c_+ and c_-, respectively, have the same diffusivity D and valence charge number Z.

3.1. Bulk equations in the conventional ICEO model

Neglecting chemical reactions in the bulk of the electrolyte, the ionic transport is governed by particle conservation through the continuity equation,

$$\frac{\partial c_\pm}{\partial t} = -\boldsymbol{\nabla}\cdot\boldsymbol{J}_\pm, \tag{1}$$

where $\boldsymbol{J}_\pm$ is the flux density of the two ionic species, respectively. Assuming a dilute electrolytic solution, the ion flux densities are governed by the Nernst–Planck equation,

$$\boldsymbol{J}_\pm = -D\left(\boldsymbol{\nabla}c_\pm + \frac{\pm Ze}{k_{\text{B}}T}c_\pm\boldsymbol{\nabla}\phi\right), \tag{2}$$

where the first term expresses ionic diffusion and the second term ionic electromigration due to the electrostatic potential ϕ. Here e is the elementary charge, T the absolute temperature and k_{B} the Boltzmann constant. We note that due to the low fluid velocity $\boldsymbol{v}$ obtained in the ICEO systems under consideration, we can safely neglect the convective ion fluxes $c_\pm\boldsymbol{v}$ throughout this paper, see Table 2.

The electrostatic potential ϕ is determined by the charge density $\rho_{\text{el}} = Ze(c_+ - c_-)$ through Poisson's equation,

$$\boldsymbol{\nabla}\cdot(\varepsilon_{\text{fluid}}\boldsymbol{\nabla}\phi) = -\rho_{\text{el}}, \tag{3}$$

where $\varepsilon_{\text{fluid}}$ is the fluid permittivity, which is assumed constant. The fluid velocity field $\boldsymbol{v}$ and pressure field p are governed the the continuity equation and the Navier–Stokes equation for incompressible fluids,

$$\boldsymbol{\nabla}\cdot\boldsymbol{v} = 0, \tag{4a}$$

$$\rho_{\text{m}}\left[\frac{\partial\boldsymbol{v}}{\partial t} + (\boldsymbol{v}\cdot\boldsymbol{\nabla})\boldsymbol{v}\right] = -\boldsymbol{\nabla}p + \eta\nabla^2\boldsymbol{v} - \rho_{\text{el}}\boldsymbol{\nabla}\phi, \tag{4b}$$

where ρ_{m} and η are the fluid mass density and viscosity, respectively, both assumed constant.

3.2. The artificial design field γ used in the topology optimization model of ICEO

To be able to apply the method of topology optimization, it is necessary to extend the conventional ICEO model with three additional terms, all functions of a position-dependent artificial design field $\gamma(\boldsymbol{r})$. The design field varies continuously from zero to unity, where $\gamma = 0$ is the limit of a pure dielectric solid and $\gamma = 1$ is the limit of a pure electrolytic fluid. The intermediate values of γ represent a mixture of solid and fluid.

The first additional term concerns the purely fluid dynamic part of our problem. Here, we follow Borrvall and Petersson [6] and model the dielectric solid as a porous medium giving rise to a Darcy friction force density $-\alpha(\gamma)\boldsymbol{v}$, where $\alpha(\gamma)$ may be regarded as a local inverse permeability, which we denote the Darcy friction. We let $\alpha(\gamma)$ be a linear function of γ of the form $\alpha(\gamma) = \alpha_{\text{max}}(1-\gamma)$, where $\alpha_{\text{max}} = \eta/\ell^2_{\text{pore}}$ is

the Darcy friction of the porous dielectric material assuming a characteristic pore size ℓ_{pore}. In the limit of a completely impenetrable solid the value of $\alpha_{\max}$ approaches infinity, which leads to a vanishing fluid velocity $\boldsymbol{v}$. The modified Navier–Stokes equation extending to the entire domain, including the dielectric material, becomes

$$\rho_{\text{m}}\left[\frac{\partial \boldsymbol{v}}{\partial t} + (\boldsymbol{v}\cdot\boldsymbol{\nabla})\boldsymbol{v}\right] = -\boldsymbol{\nabla}p + \eta\nabla^2\boldsymbol{v} - \rho_{\text{el}}\boldsymbol{\nabla}\phi - \alpha(\gamma)\boldsymbol{v}. \tag{5}$$

The second additional term is specific to our problem. Since the Navier–Stokes equation is now extended to include also the porous dielectric medium, our model must prevent the unphysical penetration of the electrolytic ions into the solid. Following the approach of Kilic *et al.* [13], where current densities are expressed as gradients of chemical potentials, $\boldsymbol{J} \propto -\boldsymbol{\nabla}\mu$, we model the ion expulsion by adding an extra free energy term $\kappa(\gamma)$ to the chemical potential $\mu_\pm = \pm Ze\phi + k_{\text{B}}T\ln(c_\pm/c_0) + \kappa(\gamma)$ of the ions, where c_0 is the bulk ionic concentration for both ionic species. As above we let $\kappa(\gamma)$ be a linear function of γ of the form $\kappa(\gamma) = \kappa_{\max}(1-\gamma)$, where $\kappa_{\max}$ is the extra energy cost for an ion to enter a point containing a pure dielectric solid as compared to a pure electrolytic fluid. The value of $\kappa_{\max}$ is set to an appropriately high value to expel the ions efficiently from the porous material while still ensuring a smooth transition from dielectric solid to electrolytic fluid. The modified ion flux density becomes

$$\boldsymbol{J}_\pm = -D\left(\boldsymbol{\nabla}c_\pm + \frac{\pm Ze}{k_{\text{B}}T}c_\pm\boldsymbol{\nabla}\phi + \frac{1}{k_{\text{B}}T}c_\pm\boldsymbol{\nabla}\kappa(\gamma)\right). \tag{6}$$

The third and final additional term is also specific to our problem. Electrostatically, the transition from the dielectric solid to the electrolytic fluid is described through the Poisson equation by a γ-dependent permittivity $\varepsilon(\gamma)$. This modified permittivity varies continuously between the value $\varepsilon_{\text{diel}}$ of the dielectric solid and $\varepsilon_{\text{fluid}}$ of the electrolytic fluid. As above, we would like to choose $\varepsilon(\gamma)$ to be a linear function of γ. However, during our analysis using the aforementioned large value $\varepsilon_{\text{diel}} = 10^6\varepsilon_0$ for the solid in an aqueous electrolyte with $\varepsilon_{\text{fluid}} = 78\,\varepsilon_0$, we found unphysical polarization phenomena in the electrolyte due to numerical rounding-off errors for γ near, but not equal to, unity. To overcome this problem we ensured a more rapid convergence towards the value $\varepsilon_{\text{fluid}}$ by introducing a cut-off value $\gamma_{\text{cut}} \simeq 0.98$, a transition width $\Delta\gamma \simeq 0.002$, and the following expression for $\varepsilon(\gamma)$,

$$\varepsilon(\gamma) = \varepsilon_{\text{diel}} + (\varepsilon_{\text{fluid}} - \varepsilon_{\text{diel}})\left\{1 - \frac{(1-\gamma)}{2}\left[\tanh\left(\frac{\gamma_{\text{cut}}-\gamma}{\Delta\gamma}\right) + 1\right]\right\}. \tag{7}$$

For $\gamma \lesssim \gamma_{\text{cut}}$ we obtain the linear relation $\varepsilon(\gamma) = \varepsilon_{\text{diel}} + (\varepsilon_{\text{fluid}} - \varepsilon_{\text{diel}})\gamma$, while for $\gamma \gtrsim \gamma_{\text{cut}}$ we have $\varepsilon(\gamma) = \varepsilon_{\text{fluid}}$, see Fig. 1(b)-(c). For γ sufficiently close to unity (and not only when γ equals unity with numerical precision), this cut-off procedure ensures that the calculated topological break up of the dielectric solid indeed leads to several correctly polarized solids separated by pure electrolyte. The modified Poisson equation becomes

$$\boldsymbol{\nabla}\cdot\left[\varepsilon(\gamma)\boldsymbol{\nabla}\phi\right] = -\rho_{\text{el}}. \tag{8}$$

Finally, we introduce the γ-dependent quantity, the so-called objective function $\Psi[\gamma]$, to be optimized by the topology optimization routine: the flow rate in the x-direction perpendicular to the applied potential gradient. Due to incompressibility, the flow rate $Q(x)$ is the same through cross-sections parallel to the yz-plane at any

position x. Hence we can use the numerically more stable integrated flow rate as the objective function,

$$\Psi[\gamma(\boldsymbol{r})] = \int_0^L Q(x)\,\mathrm{d}x = \int_\Omega \boldsymbol{v}\cdot\hat{\boldsymbol{n}}_x\,\mathrm{d}x\,\mathrm{d}z, \tag{9}$$

where Ω is the entire geometric domain (including the design domain), and $\hat{\boldsymbol{n}}_x$ the unit vector in the x direction.

3.3. Dimensionless form

To prepare the numerical implementation, the governing equations are rewritten in dimensionless form, using the characteristic parameters of the system. In conventional ICEO systems the size a of the dielectric solid is the natural choice for the characteristic length scale ℓ_0, since the generated slip velocity at the solid surface is proportional to a. However, when employing topology optimization we have no prior knowledge of this length scale, and thus we choose it to be the fixed geometric half-length $\ell_0 = H$ between the capacitor plates. Further characteristic parameters are the ionic concentration c_0 of the bulk electrolyte, and the thermal voltage $\phi_0 = k_{\text{B}}T/(Ze)$. The characteristic velocity u_0 is chosen as the Helmholtz–Smoluchowski slip velocity u_0, which for the induced zeta potential $\zeta = E\ell_0$ in a local electric field $E = \phi_0/\ell_0$ is [3]

$$u_0 = \frac{\varepsilon_{\text{fluid}}\zeta}{\eta}\,E = \frac{\varepsilon_{\text{fluid}}\phi_0^2}{\eta\ell_0}. \tag{10}$$

The pressure scale is set by the characteristic microfluidic pressure scale $p_0 = \eta u_0/\ell_0$. Although strictly applicable only to parallel-plate capacitors, the characteristic time τ_0 of the general system in chosen as the RC time of the double layer in terms of the Debye length λ_{D} of the electrolyte [14],

$$\tau_0 = \frac{\ell_0}{D}\,\lambda_{\text{D}} = \frac{\ell_0}{D}\sqrt{\frac{k_{\text{B}}T\varepsilon_{\text{fluid}}}{2(Ze)^2c_0}}. \tag{11}$$

Moreover, three characteristic numbers are connected to the γ-dependent terms in the governing equations: The characteristic free energy κ_0, the characteristic permittivity chosen as the bulk permittivity $\varepsilon_{\text{fluid}}$, and the characteristic Darcy friction coefficient α_0. In summary,

$$\ell_0 = H, \qquad \phi_0 = \frac{k_{\text{B}}T}{Ze}, \quad u_0 = \frac{\varepsilon_{\text{fluid}}\phi_0^2}{\eta\,\ell_0}, \quad p_0 = \frac{\eta\,u_0}{\ell_0}, \tag{12a}$$

$$\tau_0 = \frac{\ell_0\lambda_{\text{D}}}{D}, \quad \omega_0 = \frac{1}{\tau_0}, \qquad \kappa_0 = k_{\text{B}}T, \qquad \alpha_0 = \frac{\eta}{\ell_0^2}. \tag{12b}$$

The new dimensionless variables (denoted by a tilde) thus become

$$\tilde{\boldsymbol{r}} = \frac{\boldsymbol{r}}{\ell_0}, \quad \tilde{\boldsymbol{v}} = \frac{\boldsymbol{v}}{u_0}, \quad \tilde{p} = \frac{p}{p_0}, \quad \tilde{\phi} = \frac{\phi}{\phi_0}, \quad \tilde{c}_\pm = \frac{c_\pm}{c_0}, \tag{13a}$$

$$\tilde{t} = \frac{t}{\tau_0}, \quad \tilde{\kappa} = \frac{\kappa}{\kappa_0}, \quad \tilde{\alpha} = \frac{\alpha}{\alpha_0}, \quad \tilde{\varepsilon} = \frac{\varepsilon}{\varepsilon_{\text{fluid}}}. \tag{13b}$$

In the following all variables and parameters are made dimensionless using these characteristic numbers and for convenience the tilde is henceforth omitted.

3.4. Linearized and reformulated equations

To reduce the otherwise very time- and memory- consuming numerical simulations, we choose to linearize the equations. There are several nonlinearities to consider.

By virtue of a low Reynolds number $Re \approx 10^{-6}$, see Table 2, the nonlinear Navier–Stokes equation is replaced by the linear Stokes equation. Likewise, as mentioned in Sec. 3.1, the low Péclet number $Pé \approx 10^{-3}$ allows us to neglect the nonlinear ionic convection flux density $c_\pm \boldsymbol{v}$. This approximation implies the additional simplification that the electrodynamic problem is independent of the hydrodynamics.

Finally, we employ the linear Debye–Hückel approximation, which is valid when the electric energy $Ze\zeta$ of an ion traversing the double layer is smaller than the thermal energy $k_\mathrm{B}T$. For our system we find $Ze\zeta/k_\mathrm{B}T \lesssim 0.5$, so the linear Debye–Hückel approximation is valid, and we can utilize that the ionic concentrations only deviate slightly from the bulk equilibrium ionic concentration. The governing equations are reformulated in terms of the average ion concentration $c \equiv (c_+ + c_-)/2$ and half the charge density $\rho \equiv (c_+ - c_-)/2$. Thus, by expanding the fields to first order as $c = 1 + \delta c$ and $\rho = 0 + \delta\rho$, the resulting differential equation for ρ is decoupled from that of c. Introducing complex field notation, the applied external bias voltage is $\Delta\phi(t) = 2V_0\cos(\omega t) = \mathrm{Re}[2V_0\exp(\mathrm{i}\omega t)]$, yielding a corresponding response for the potential ϕ and charge density ρ, with the complex amplitudes $\Phi(\boldsymbol{r}) = \Phi_R(\boldsymbol{r}) + \mathrm{i}\Phi_I(\boldsymbol{r})$ and $P(\boldsymbol{r}) = P_R(\boldsymbol{r}) + \mathrm{i}P_I(\boldsymbol{r})$, respectively. The resulting governing equations for the electrodynamic problem is then

$$\boldsymbol{\nabla}\cdot\big[\varepsilon(\gamma)\boldsymbol{\nabla}\Phi_R\big] = -\frac{1}{\lambda^2}P_R, \tag{14a}$$

$$\boldsymbol{\nabla}\cdot\big[\varepsilon(\gamma)\boldsymbol{\nabla}\Phi_I\big] = -\frac{1}{\lambda^2}P_I, \tag{14b}$$

$$\boldsymbol{\nabla}\cdot\big[\boldsymbol{\nabla}\Phi_R + \boldsymbol{\nabla}P_R + P_R\boldsymbol{\nabla}\kappa(\gamma)\big] = -\frac{\omega}{\lambda}P_I, \tag{14c}$$

$$\boldsymbol{\nabla}\cdot\big[\boldsymbol{\nabla}\Phi_I + \boldsymbol{\nabla}P_I + P_I\boldsymbol{\nabla}\kappa(\gamma)\big] = +\frac{\omega}{\lambda}P_R, \tag{14d}$$

where we have introduced the dimensionless thickness of the linear Debye layer $\lambda = \lambda_\mathrm{D}/\ell_0$. Given the electric potential Φ and the charge density P, we solve for the time-averaged hydrodynamic fields $\langle\boldsymbol{v}\rangle$ and $\langle p\rangle$,

$$\boldsymbol{\nabla}\cdot\langle\boldsymbol{v}\rangle = 0, \tag{15a}$$

$$0 = -\boldsymbol{\nabla}\langle p\rangle + \nabla^2\langle\boldsymbol{v}\rangle + \langle\boldsymbol{f}_\mathrm{el}\rangle - \alpha(\gamma)\langle\boldsymbol{v}\rangle, \tag{15b}$$

where the time-averaged electric body force density $\langle\boldsymbol{f}_\mathrm{el}\rangle$ is given by

$$\langle\boldsymbol{f}_\mathrm{el}\rangle = -\frac{1}{2\lambda^2}\big[P_R\boldsymbol{\nabla}\Phi_R + P_I\boldsymbol{\nabla}\Phi_I\big]. \tag{15c}$$

3.5. Boundary conditions

For symmetric dielectric solids we exploit the symmetry around $z = 0$ and consider only the upper half ($0 < z < 1$) of the domain. As boundary condition on the driving electrode we set the spatially constant amplitude V_0 of the applied potential. Neglecting any electrode reactions taking place at the surface there is no net ion flux in the normal direction to the boundary with unit vector $\hat{\boldsymbol{n}}$. Finally, for the fluid velocity we set a no-slip condition, and thus at $z = 1$ we have

$$\Phi_R = V_0, \quad \Phi_I = 0, \tag{16a}$$

$$\hat{\boldsymbol{n}}\cdot\big[\boldsymbol{\nabla}\Phi_R + \boldsymbol{\nabla}P_R + P_R\boldsymbol{\nabla}\kappa(\gamma)\big] = 0, \tag{16b}$$

$$\hat{\boldsymbol{n}}\cdot\big[\boldsymbol{\nabla}\Phi_I + \boldsymbol{\nabla}P_I + P_I\boldsymbol{\nabla}\kappa(\gamma)\big] = 0, \tag{16c}$$

$$\langle\boldsymbol{v}\rangle = \boldsymbol{0}. \tag{16d}$$

On the symmetry axis ($z = 0$) the potential and the charge density must be zero due to the anti-symmetry of the applied potential. Furthermore, there is no fluid flux in the normal direction and the shear stresses vanish. So at $z = 0$ we have

$$\Phi_R = \Phi_I = 0, \quad P_R = P_I = 0, \tag{17a}$$

$$\hat{\boldsymbol{n}}\cdot\langle\boldsymbol{v}\rangle = 0, \qquad \hat{\boldsymbol{t}}\cdot\langle\boldsymbol{\sigma}\rangle\cdot\hat{\boldsymbol{n}} = 0, \tag{17b}$$

where the dimensionless stress tensor is $\langle\sigma_{ik}\rangle = -\langle p\rangle\delta_{ik} + \big(\partial_i\langle v_k\rangle + \partial_k\langle v_i\rangle\big)$, and $\hat{\boldsymbol{n}}$ and $\hat{\boldsymbol{t}}$ are the normal and tangential unit vectors, respectively, where the latter in 2D, contrary to 3D, is uniquely defined. On the remaining vertical boundaries ($x = \pm L/2\ell_0$) periodic boundary conditions are applied to all the fields.

Corresponding boundary conditions apply to the conventional ICEO model Eqs. (1)-(4*b*), without the artificial design field but with a hard-wall dielectric solid. For the boundary between a dielectric solid and electrolytic fluid the standard electrostatic conditions apply, moreover, there is no ion flux normal to the surface, and a no-slip condition is applied to the fluid velocity.

4. Implementation and validation of numerical code

4.1. Implementation and parameter values

For our numerical analysis we use the commercial numerical finite-element modeling tool Comsol [16] controlled by scripts written in Matlab [15]. The mathematical method of topology optimization in microfluidic systems is based on the seminal paper by Borrvall and Petersson [6], while the implementation (containing the method of moving asymptotes by Svanberg [17, 18]) is taken from Olesen, Okkels and Bruus [7].

In Comsol all equations are entered in the divergence form $\boldsymbol{\nabla}\cdot\boldsymbol{\Gamma} = \boldsymbol{F}$. The tensor $\boldsymbol{\Gamma}$ contains all the generalized fluxes in the governing equations, one per row, eg. $\boldsymbol{J}_\pm$ from Eq. (1), $\varepsilon_\mathrm{fluid}\boldsymbol{\nabla}\phi$ from Eq. (3), 0 from Eq. (4*a*), and $\boldsymbol{\nabla}\boldsymbol{v} + (\boldsymbol{\nabla}\boldsymbol{v})^\mathrm{T}$ from Eq. (4*b*). The source-term vector $\boldsymbol{F}$ contains all other terms in the governing equations that cannot be written as the divergence of a vector. Note that the continuity equation (4*a*) is not interpreted as an equation for $\boldsymbol{v}$ but rather as a divergence of a pressure-related flux (which is always zero), with the term $\boldsymbol{\nabla}\cdot\boldsymbol{v}$ acting as the corresponding source-term, thus appearing in the vector $\boldsymbol{F}$. As in Ref. [7] we have used second-order Lagrange elements for all fields except the pressure and the design field, for which first-order elements suffices. The resulting algebraic FEM-equations are solved using the sparse direct linear solvers UMFPACK or PARDISO. More details concerning the numerical implementation in Comsol can be found in Ref. [7].

Due to the challenges discussed in Sec. 4.2 of resolving all length scales in the electrokinetic model, we have chosen to study small systems, $2H = 500$ nm, with a relatively large Debye length, $\lambda_\mathrm{D} = 20$ nm. Our main goal is to provide a proof of concept for the use of topology optimization in electro-hydrodynamic systems, so the difficulties in fabricating actual devices on this sub-micrometric scale is not a major concern for us in the present work. A list of the parameter values chosen for our simulations is given in Table 1.

Table 1. Parameters used in the simulations of the topology optimization ICEO model and the conventional ICEO model.

Parameter	Symbol	Dimensionless value	Physical value
Characteristic length	ℓ_0	1.0	250 nm
Channel half-height	H	1.0	250 nm
Channel length	L	2.0	500 nm
Design domain half-height	h	0.8	200 nm
Design domain length	l	0.6	150 nm
Linear Debye length	$\lambda_{\rm D}$	0.08	20 nm
Characteristic velocity	u_0	1.0	1.7×10^{-3} m/s
Characteristic potential	ϕ_0	1.0	25 mV
External potential amplitude	V_0	1.0	25 mV
External potential frequency	ω	6.25	4×10^5 rad/s
Bulk fluid permittivity	$\varepsilon_{\rm fluid}$	1.0	$78\,\varepsilon_0$
Dielectric permittivity	$\varepsilon_{\rm diel}$	1.3×10^4	$10^6\,\varepsilon_0$
Bulk ionic concentration	c_0	1.0	0.23 mM
Fluid viscosity	η	1.0	10^{-3} Pa s
Ionic diffusion constant	D	1.0	2×10^{-9}m^2/s
Ionic free energy in solid	κ	3.0	75 mV
Maximum Darcy friction	$\alpha_{\rm max}$	10^5	2×10^{16} Pa s/m^2

For a typical topology optimization, as the one shown in Fig. 4(a), approximately 5400 FEM elements are involved. In each iteration loop of the topology optimization routine three problems are solved: the electric problem, the hydrodynamic problem, and the so-called adjunct problem for the sensitivity analysis $\partial\Psi/\partial\gamma$ (used to update the design field γ, see Ref. [7] for details), involving 4×10^4, 2×10^4, and 7×10^4 degrees of freedom, respectively. On an Intel Core 2 Duo 2 GHz processer with 2 GB RAM the typical CPU time is several hours.

4.2. Analytical and numerical validation by the conventional ICEO model

We have validated our simulations in two steps. First, the conventional ICEO model not involving the design field $\gamma(\boldsymbol{r})$ is validated against the analytical result for the slip velocity at a simple dielectric cylinder in an infinite AC electric field given by Squires and Bazant [3]. Second, the design field model is compared to the conventional model. This two-step validation procedure is necessary because of the limited computer capacity. The involved length scales in the problem make a large number of mesh elements necessary for the numerical solution by the finite element method. Four different length scales appear in the gamma-dependent model for the problem of a cylinder placed mid between the parallel capacitor plates: The distance H from the center of the dielectric cylinder to the biased plates, the radius a of the cylinder, the Debye length $\lambda_{\rm D}$, and the length d over which the design field γ changes from zero to unity. This last and smallest length-scale d in the problem is controlled directly be the numerical mesh size set up in the finite element method. It has to be significantly smaller than $\lambda_{\rm D}$ to model the double layer dynamics correctly, so here a maximum value of the numerical mesh size is defined. Examples of meshing are shown in Fig. 2.

The analytical solution of Squires and Bazant [3] is only strictly valid in the

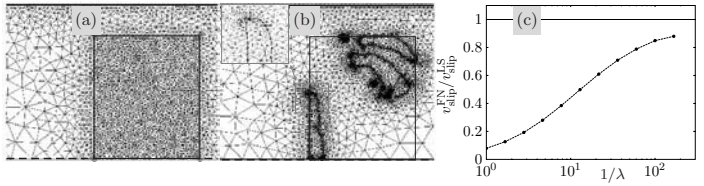

Figure 2. (a) Meshing for the design-field model of Fig. 4(a) with a uniformly fine mesh inside the design domain and a coarser mesh outside. (b) Meshing for the hard-wall model of Fig. 4(b) with a mesh refinement in the double layer surrounding the dielectric solids. (c) A Debye-length convergence analysis for a cylinder with radius a. The maximum ICEO slip velocity $v_{\rm slip}^{\rm FN}$ in units of the maximum analytical linear slip velocity $v_{\rm slip}^{\rm LS}$ is plotted as a function of the inverse dimensionless Debye length $1/\lambda = a/\lambda_D$. Unity is approached as λ tends to zero.

case of an infinitely thin Debye layer in an infinite electric field. So, to compare this model with the bounded numerical model the plate distance must be increased to minimize the influence on the effective slip velocity. Furthermore, it has been shown in a numerical study by Gregersen *et al.* [19] that the Debye length $\lambda_{\rm D}$ should be about a factor of 10^3 smaller than the cylinder radius a to approximate the solution for the infinitely thin Debye layer model. Including the demand of d being significantly smaller than $\lambda_{\rm D}$ we end up with a length scale difference of at least 10^5, which is difficult to resolve by the finite element mesh, even when mesh adaption is used. Consequently, we have checked that the slip velocity for the conventional model converges towards the analytical value when the ratio $a/\lambda_{\rm D}$ increases, see Fig. 2(c). Afterwards, we have compared the solutions for the conventional and gamma-dependent models in a smaller system with a ratio of $a/\lambda_{\rm D} \sim 10$ and found good agreement.

4.3. Validation of the self-consistency of the topology optimization

As an example of our validation of the self-consistency of the topology optimization, we study the dependence of the objective function $Q = \Psi[\omega, \gamma(\omega, \boldsymbol{r})]$ on the external driving frequency ω. As shown in Fig. 3(a)-(c) we have calculated the topology optimized dielectric structures $\gamma_j = \gamma(\omega_j, \boldsymbol{r})$, $j = a, b, c$, for three increasing frequencies $\omega = \omega_a = 1.25$, $\omega = \omega_b = 12.5$, and $\omega = \omega_c = 62.5$. In the following we let $Q_j(\omega)$ denote the flow rate calculated at the frequency ω for a structure optimized at the frequency ω_j.

First, we note that $Q_j(\omega_j)$ decreases as the frequency increases above the characteristic frequency $\omega_0 = 1$; $Q_a(\omega_a) = 2.95 \times 10^{-3}$, $Q_b(\omega_b) = 1.82 \times 10^{-3}$, and $Q_c(\omega_c) = 0.55 \times 10^{-3}$. This phenomenon is a general aspect of ICEO systems, where the largest effect is expected to happen at $\omega \approx 1$ (in units of $1/\tau_0$).

Second, and most significant, we see in Fig. 3(d) that structure γ_a is indeed the optimal structure for $\omega = \omega_a$ since $Q_a(\omega_a) > Q_b(\omega_a), Q_c(\omega_a)$. Likewise, γ_b is optimal for $\omega = \omega_b$, and γ_c is optimal for $\omega = \omega_c$.

We have gained confidence in the self-consistency of our topology optimization routine by carrying out a number of tests like the one in the example above.

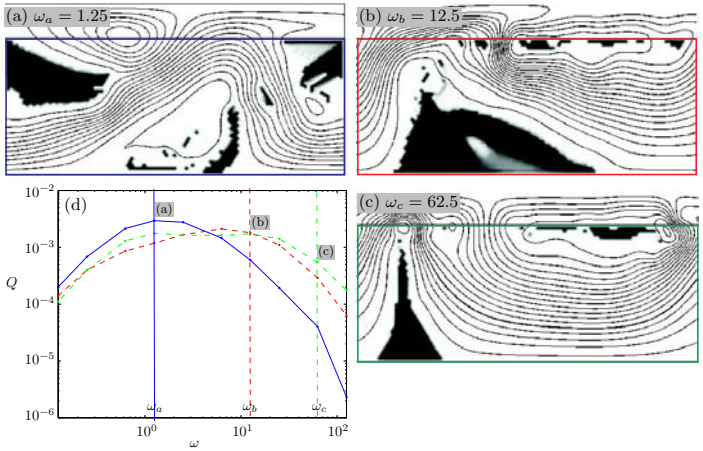

Figure 3. Validation of the self-consistency of the topology optimization for different driving frequencies ω (in units of $1/\tau_0$). (a) The streamline pattern (thick lines) for $\omega = \omega_a = 1.25$ calculated using the design-field ICEO model with a porous dielectric medium represented by the design field γ in gray scale from $\gamma = 0$ (black, solid) to $\gamma = 1$ (white, fluid), and the corresponding structure γ_a, which has been found by topology optimization within the indicated rectangular design domain (straight lines). The flow rate for this converged solution structure is $Q = 2.95\times10^{-3}$. (b) As panel (a) but with $\omega = \omega_b = 12.5$ and $Q = 1.82\times10^{-3}$. (c) As panel (a) but with $\omega = \omega_c = 62.5$ and $Q = 0.55\times10^{-3}$. (d) Flow rate Q versus frequency ω for each of the three structures in panel (a), (b), and (c). Note that structure γ_a indeed yields the highest flow rate Q for $\omega = \omega_a$, structure γ_b maximizes Q for $\omega = \omega_b$, and structure γ_c maximizes Q for $\omega = \omega_c$.

5. Results

5.1. Topology optimization

For each choice of parameters the topology optimization routine converges to a specific distribution of dielectric solid given by $\gamma(\boldsymbol{r})$. As a starting point for the investigation of the optimization results we used the parameters listed in Table 1. As discussed above, the geometric dimensions are chosen as large as possible within the computational limitations: the Debye length is set to $\lambda_D = 20$ nm and the distance between the capacitor plates to $2H = 500$ nm. The external bias voltage V_0 is of the order of the thermal voltage $V_0 = \phi_0 = 25$ mV to ensure the validity of the linear Debye–Hückel approximation. We let the bulk fluid consist of water containing small ions, such as dissolved KCl, with a concentration $c_0 = 0.23$ mM set by the chosen Debye length. As mentioned above, the permittivity of the dielectric solid is set to $\varepsilon_{\text{diel}} = 10^6\,\varepsilon_0$ for maximum ICEO effect. The artificial parameters κ and $\alpha_{\max}$ are chosen on a pure computational basis, where they have to mimic the real physics in the limits of fluid and solid, but also support the optimization routine when the phases are mixed.

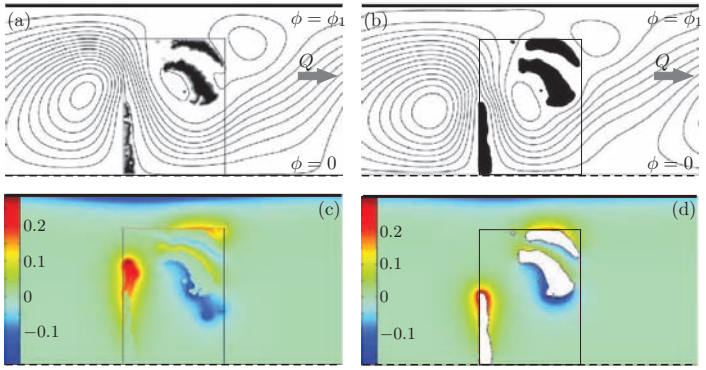

Figure 4. (a) The streamline pattern (thick lines) calculated for $\omega = 6.25$ using the design-field ICEO model with a porous dielectric solid (black and gray), the structure of which has been found by topology optimization within the rectangular design domain (thin lines). The flow rate for this converged solution structure is $Q = 2.99\times10^{-3}$. (b) The streamline pattern (full lines) calculated using the conventional ICEO model with a hard-walled dielectric solid (black). The shape of the dielectric solid is the 0.95-contour of the γ-field taken from the topology-optimized structure shown in panel (a). The flow rate is $Q = Q^* = 1.88\times10^{-3}$. (c) and (d) Color plots of the charge density $\rho(\boldsymbol{r})$ corresponding to panel (a) and (b), respectively. See Table 1 for parameter values.

Throughout our simulations we have primarily varied the applied frequency ω and the size $l\times 2h$ of the design domain. In Fig. 3 we have shown examples of large design domains with $l\times h = 2.0\times0.8$ covering 80% of the entire domain and frequency sweeps over three orders of magnitude. However, in the following we fix the frequency to be $\omega = 6.25$, where the ICEO response is close to maximum. Moreover we focus on a smaller design domain $l\times h = 0.6\times0.8$ to obtain better spatial resolution for the given amount of computer memory and to avoid getting stuck in local optima. It should be stressed that the size of the design domain has a large effect on the specific form and size of the dielectric islands produced by the topology optimization. Also, it is important if the design domain is allowed to connect to the capacitor plates or

Table 2. The value of characteristic physical quantities calculated in the topology optimization ICEO model corresponding to Fig. 4.

Quantity	Symbol	Dimensionless value	Physical value
Gap between dielectric pieces	ℓ_{gap}	0.4	100 nm
Velocity in the gap	u_{gap}	$0.016\,u_0$	28 μm/s
Largest zeta potential	$\zeta_{\max}$	$0.5\,\phi_0$	12.5 mV
Reynolds number *Re*	$\rho_m u_{\text{gap}}\ell_{\text{gap}}/\eta$	2.8×10^{-6}	–
Péclet number *Pé*	$u_{\text{gap}}\ell_{\text{gap}}/D$	1.4×10^{-3}	–
Debye–Hückel number *Hü*	$e\zeta_{\max}/(4k_BT)$	0.13	–

not, see the remarks in Sec. 6.

The converged solution found by topology optimization under these conditions is shown in Fig. 4(a). The shape of the porous dielectric material is shown together with a streamline plot of equidistant contours of the flow rate. We notice that many stream lines extend all the way through the domain from left to right indicating that a horizontal flow parallel to the x-axis is indeed established. The resulting flow rate is $Q = 2.99 \times 10^{-3}$. The ICEO flow of this solution, based on the design-field model, is validated by transferring the geometrical shape of the porous dielectric medium into a conventional ICEO model with a hard-walled dielectric not depending on the design field. In the latter model the sharp interface between the dielectric solid and the electrolyte is defined by the 0.95-contour of the topology optimized design field $\gamma(\boldsymbol{r})$. The resulting geometry and streamline pattern of the conventional ICEO model is shown in Fig. 4(b). The flow rate is now found to be $Q = Q^* = 1.88 \times 10^{-3}$. There is a close resemblance between the results of two models both qualitatively and quantitatively. It is noticed how the number and positions of the induced flow rolls match well, and also the absolute values of the induced horizontal flow rates differs only by 37%, which is a small deviation as discussed in Sec. 6.

Based on the simulation we can now justify the linearization of our model. The largest velocity u_{gap} is found in the gap of width ℓ_{gap} between the two satellite pieces and the central piece. As listed in Table 2 the resulting Reynolds number is $Re = 2.8 \times 10^{-7}$, the Péclet number is $Pé = 1.4 \times 10^{-3}$, while the Debye–Hückel number is $Hü = 0.13$.

5.2. Comparison to simple shapes

We evaluate our result for the optimized flow rate by comparing it to those obtained for more basic, simply connected, dielectric shapes, such as triangles and perturbed circles previously studied in the literature as flow inducing objects both analytically and experimentally [3, 4, 5]. For comparison, such simpler shapes have been fitted into the same design domain as used in the topology optimization Fig. 4(a), and the conventional ICEO model without the design field was solved for the same parameter set. In Fig. 5(a) the resulting flow for a triangle with straight faces and rounded corners is shown. The height b of the face perpendicular to the symmetry line was

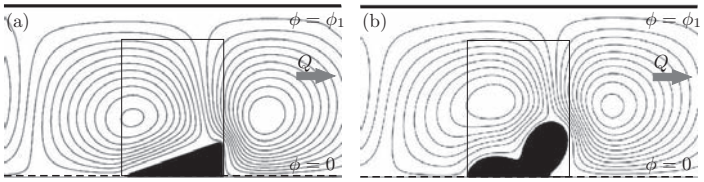

Figure 5. (a) The streamline pattern (thick lines) for a simple triangular reference structure calculated for $\omega = 6.25$ using the conventional ICEO model with a hard-walled dielectric solid (black). The height $b = 0.32$ of the triangle is chosen to give the largest flow rate for a fixed base line given by the rectangular design domain of Fig. 4(a). The flow rate is $Q = 0.22 \times 10^{-3}$. (b) The same as panel (a) except the geometry of the dielectric solid is given by the perturbed circle $r(\theta) = 0.24[1 + 0.5\cos(3\theta)]$. The flow rate is $Q = 0.46 \times 10^{-3}$.

varied within the height of the design domain $0 < b < 0.8$, and the height $b = 0.32$ generating the largest flow in the x-direction results in a flow rate of $Q = 0.22 \times 10^{-3}$, which is eight times smaller than the topology optimized result. In Fig. 5(b) the induced flow around a perturbed cylinder with radius $r(\theta) = 0.24\big[1 + 0.5\cos(3\theta)\big]$ is depicted. Again the shape has been fitted within the allowed design domain. The resulting flow rate $Q = 0.46 \times 10^{-3}$ is higher than for the triangle but still a factor of four slower than the optimized result. It is clearly advantageous to change the topology of the dielectric solid from simply to multiply connected.

For the topology optimized shape in Fig. 4(a) it is noticed that only a small amount of flow is passing between the two closely placed dielectric islands in the upper left corner of the design domain. To investigate the importance of this separation, the gap between the islands was filled out with dielectric material and the flow calculated. It turns out that this topological change only lowered the flow rate slightly (15%) to a value of $Q = 1.59 \times 10^{-3}$. Thus, the important topology of the dielectric solid in the top-half domain is the appearance of one center island crossing the antisymmetry line and one satellite island near the tip of the center island.

5.3. Shape optimization

The topology optimized solutions are found based on the extended ICEO model involving the artificial design field $\gamma(\boldsymbol{r})$. To avoid the artificial design field it is desirable to validate and further investigate the obtained topology optimized results by the physically more correct conventional ICEO model involving hard-walled dielectric solids. We therefore extend the reasoning behind the comparison of the two models shown in Fig. 4 and apply a more stringent shape optimization to the various topologies presented above. With this approach we are gaining further understanding of the specific shapes comprising the overall topology of the dielectric solid. Moreover, it is possible to point out simpler shapes, which are easier to fabricate, but still perform well.

In shape optimization the goal is to optimize the objective function Ψ, which depends on the position and shape of the boundary between the dielectric solid and the electrolytic fluid. This boundary is given by a line interpolation through a small number of points on the boundary. These control points are in turn given by N design variables $\boldsymbol{g} = (g_1, g_2, \ldots, g_N)$, so the objective function of Eq. (9) depending on the design field $\gamma(\boldsymbol{r})$ is now written as $\Psi[\boldsymbol{g}]$ depending on the design variables $\boldsymbol{g}$,

$$\Psi[\boldsymbol{g}] = \int_\Omega \boldsymbol{v} \cdot \hat{\boldsymbol{n}}_x \, \mathrm{d}x \, \mathrm{d}z. \tag{18}$$

To carry out the shape optimization we use a direct bounded Nelder–Mead simplex method [20] implemented in MATLAB [21, 22]. This robust method finds the optimal point $\boldsymbol{g}_{\text{opt}}$ in the N-dimensional design variable space by initially creating a simplex in this space, e.g. a N-dimensional polyhedron spanned by $N+1$ points, one of which is the initial guess. The simplex then iteratively moves towards the optimal point by updating one of the $N + 1$ points at the time. During the iteration, the simplex can expand along favorable directions, shrink towards the best point, or have its worst point replaced with the point obtained by reflecting the worst point through the centroid of the remaining N points. The iteration terminates once the extension of the simplex is below a given tolerance. We note that unlike topology optimization, the simplex method relies only on values of the objective function $\Psi[\boldsymbol{g}]$ and not on the sensitivity $\partial\Psi/\partial\boldsymbol{g}$ [23].

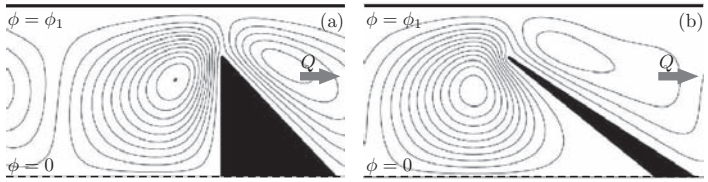

Figure 6. (a) The streamline pattern (thick lines) for the shape-optimized right-angled triangle fixed at the symmetry line $z = 0$ calculated for $\omega = 6.25$ using the conventional ICEO model with a hard-walled dielectric solid (black). In the full domain this is a triangle symmetric around $z = 0$. The flow rate is $Q = 0.32 \times 10^{-3}$. (b) As in panel (a) but without constraining the triangle to be right-angled. In the full domain the shape is foursided polygon symmetric around $z = 0$. The flow rate is $Q = 0.76 \times 10^{-3}$. Note that all sharp corners of the polygons have been rounded by circular arcs of radius 0.01.

First, we perform shape optimization on a right-angled triangle corresponding to the one shown in Fig. 5(a). Due to the translation invariance in the x-direction, we can without loss of generality fix one base point of the triangle $(x_1, 0)$ to the right end of the simulation domain, while the other $(x_2, 0)$ can move freely along the baseline, in contrast to the original rectangular design. To ensure a right-angled triangle only the z-coordinate of the top point (x_2, z_2) may move freely. In this case the design variable becomes the two-component vector $\boldsymbol{g} = (x_2, z_2)$. The optimal right-angled triangle is shown in Fig. 6(a). The flow rate is $Q = 0.32 \times 10^{-3}$ or 1.5 times larger than that of the original right-angled triangle confined to the design domain.

If we do not constrain the triangle to be right-angled, we instead optimize a polygon shape spanned by three corner points in the upper half of the electrolytic capacitor. So, due to the symmetry of the problem, we are in fact searching for the most optimal, symmetric foursided polygon. The three corner points are now given as $(x_1, 0)$, $(x_2, 0)$,and (x_3, z_3), and again due to translation invariance, it results in a three-component design variable $\boldsymbol{g} = (x_2, x_3, z_3)$. The resulting shape-optimized polygon is shown in Fig. 6(b). The flow rate is $Q = 0.76 \times 10^{-3}$, which is 3.5 times larger than that of the original right-angled triangle confined to the design domain and 2.4 times better than that of the best right-angled triangle. However, this flow rate is still a factor of 0.4 lower than the topology optimized results.

To be able to shape optimize the more complex shapes of Fig. 4 we have employed two methods to obtain a suitable set of design variables. The first method, the radial method, is illustrated in Fig. 7. The boundary of a given dielectric solid is defined through a cubic interpolation line through N control points $(x_i, z_i), i = 1, 2, \ldots, N$, which are parameterized in terms of two co-ordinates (x_c, z_c) of a center point, two global scale factors A and B, N lengths r_i, and N fixed angles θ_i distributed in the interval from 0 to 2π,

$$(x_i, z_i) = (x_c, z_c) + r_i\,(A\cos\theta_i,\ B\sin\theta_i). \tag{19}$$

In this case the design variable becomes $\boldsymbol{g} = (x_c, z_c, r_1, r_2, \ldots, r_N, A, B)$.

The second parametrization method involves a decomposition into harmonic components. As before we define a central point (x_c, z_c) surrounded by N control points. However now, the distances r_i are decomposed into M harmonic components

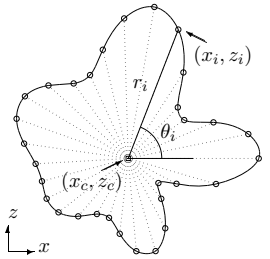

Figure 7. Illustration of the polar-coordinate parametrization Eq. (19) of the boundary of a dielectric solid with a complex shape. The polar representation (r_i, θ_i) is shown for the ith point (x_i, z_i). The shape consists of five harmonic components represented by Eq. (20) with the design-variables $x_c = -0.1312$, $z_c = 0.7176$, $r_0 = 0.1403$, $A_i = \{0.2501,\ 0.0151,\ 0.0062,\ 0.2103,\ 0.2313\}$, and $\varphi_i = \{-1.7508,\ -2.2526,\ 0.4173,\ 0.1172,\ -0.2419\}$.

given by

$$r_i = r_0\left(1 + \sum_{n=1}^{M} A_n \cos(n\theta_i + \varphi_n)\right), \tag{20}$$

where r_0 is an overall scale parameter and φ_n is a phase shift. In this case the design variable becomes $\boldsymbol{g} = (x_c, z_c, r_0, A_1, A_2, \ldots, A_M, \varphi_1, \varphi_2, \ldots, \varphi_M)$.

5.4. Comparing topology optimization and shape optimization

When shape-optimizing a geometry similar to the one found by topology optimization, we let the geometry consist of two pieces: (*i*) an elliptic island centered on the symmetry-axis and fixed to the right side of the design domain, and (*ii*) an island with a complex shape to be placed anywhere inside the design domain, but not overlapping with the elliptic island. For the ellipse we only need to specify the major axis A and the minor axis B, so these two design parameters add to the design variable listed above for either the radial model or the harmonic decomposition model. To be able to compare with the topology optimized solution the dielectric solid is restricted to the design domain.

The result of this two-piece shape optimization is shown in Fig. 8. Compared to the simply connected topologies, the two-piece shape-optimized systems yields much improved flow rates. For the shape optimization involving the radial method with 16 directional angles and $A = B$ for the complex piece, the flow rate is $Q = 1.92 \times 10^{-3}$, Fig. 8(a), which is 2.5 times larger than that of the shape-optimized foursided symmetric polygon. The harmonic decomposition method, Fig. 8(b), yields a flow rate of $Q = 1.52 \times 10^{-3}$ or 2.0 times larger than that of the polygon.

All the results for the obtained flow rates are summarized in Table 3. It is seen that two-piece shape optimized systems performs as good as the topology optimized system, when analyzed using the conventional ICEO model without the artificial design field. We also note by comparing Figs. 4 and 8 that the resulting geometry found using either topology optimization or shape optimization is essentially the same. The

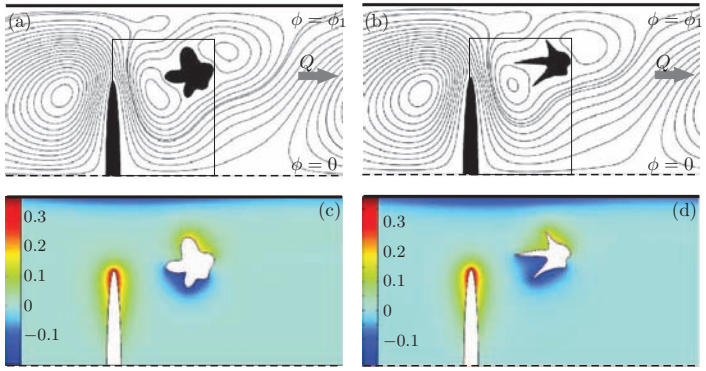

Figure 8. Shape-optimized dielectric solids with a topology corresponding to the topology-optimized shapes of Fig. 4. (a) The streamline pattern (thick lines) for a two-piece geometry calculated using the conventional ICEO model. The shape of the hard-walled dielectric solid (black) is found by shape optimization using the radial method Eq. (19) with $N = 16$ directional angles. The flow rate is $Q = 1.92 \times 10^{-3}$. (b) The same as panel (a) except the geometry of the dielectric solid is by shape optimization using the harmonic decomposition method Eq. (20) with $M = 5$ modes. The flow rate is $Q = 1.52 \times 10^{-3}$. (c) and (d) Color plot of the charge density $\rho(\boldsymbol{r})$ corresponding to panel (a) and (b), respectively.

central island of the dielectric solid is a thin structure perpendicular to the symmetry axis and covering approximately 60% of the channel width. The satellite island of complex shape is situated near the tip of the central island. It has two peaks pointing towards the central island that seem to suspend a flow roll which guides the ICEO flow through the gap between the two islands.

Table 3. Overview of the resulting flow rates Q relative to the topology optimized value $Q^* = 1.88 \times 10^3$, see Fig. 4(b), for the various geometries analyzed in the conventional ICEO model. The methods by which the geometries have been determined are listed.

Shape	Method	Flow rate Q/Q^*
Triangle with optimal height, Fig. 5(a)	Shape optimization	0.12
Perturbed cylinder, Fig. 5(b)	Fixed shape	0.24
Optimized triangle, Fig. 6(a)	Shape optimization	0.17
Optimized foursided polygon, Fig. 6(b)	Shape optimization	0.40
Topology optimized result, Fig. 4(b)	Topology optimization	1.00
Harmonic decomposition and ellipse, Fig. 8(a)	Shape optimization	0.81
Radial varying points and ellipse, Fig. 8(b)	Shape optimization	1.02

6. Concluding remarks

The main result of this work is the establishment of the topology optimization method for ICEO models extended with the design field $\gamma(\boldsymbol{r})$. In contrast to the conventional ICEO model with its sharply defined, impenetrable dielectric solids, the design field ensures a continuous transition between the porous dielectric solid and the electrolytic fluid, which allows for an efficient gradient-based optimization of the problem. By concrete examples we have shown how the use of topology optimization has led to non-trivial system geometries with a flow rate increase of nearly one order of magnitude, from $Q = 0.22 \times 10^{-3}$ in Fig. 5(a) to $Q = 1.92 \times 10^{-3}$ in Fig. 8(a).

When applied to ICEO, the design field method is qualitatively but not quantitatively correct. We have found deviations of 37% when comparing design field simulations with hard-wall simulations. The magnitude of the ICEO effect is sensitive to the exact configuration of the charge density and the electric field within the only 20 nm thick double layer. Even for the relatively simple hard-wall model, we have shown in another numerical analysis [19], how the magnitude of the ICEO depends on the width of the double layer. By introducing the design field γ and the associated artificial smoothing of the transition between the dielectric solid and the liquid, the electric properties within the double layer is changed by γ in several ways: The electric field is directly affected by the permittivity $\varepsilon[\gamma(\boldsymbol{r})]$, while the charge density is directly affected by the chemical potential term $\kappa[\gamma(\boldsymbol{r})]$ pushing ions away from the solid, and (to a lesser degree) by the viscous drag from the velocity field of the electrolyte, which is affected by the Darcy term $-\alpha[\gamma(\boldsymbol{r})]\boldsymbol{v}$. Quantitative agreement between the design field model and the hard-wall model can therefore only be achieved by an extremely fine (and in practice un-reachable) resolution of the transition zone, the position of which is not even known a priori. Given this insight, the discrepancy of 37% may be regarded as relatively small. Moreover, in spite of the quantitative discrepancy, the design field method nevertheless produces qualitatively correct solutions with topologically non-trivial geometries, which, as we have shown, easily can be transferred to quantitatively correct hard-wall models and further improved by shape optimization.

The topology optimization algorithm of ICEO systems leads to many local optima, and we cannot be sure that the converged solution is the global optimum. The resulting shapes and the generated flow rates depend on the initial condition for the artificial γ-field. Generally, the initial condition used throughout this paper, $\gamma = 0.99$ in the entire design domain, leads to the most optimal results compared to other initial conditions. This initial value corresponds to a very weak change from the electrolytic capacitor completely void of dielectric solid. In contrast, if we let $\gamma = 0.01$ corresponding to almost pure dielectric material in the entire design region, the resulting shapes are less optimal, i.e. the topology optimization routine is more likely to be caught caught in a local optimum. Furthermore, the resulting shapes turns out to be mesh-dependent as well. So, we cannot conclude much about global optima. Instead, we can use the topology optimized shapes as inspiration to improve existing designs. For this purpose shape optimization turns out to be a powerful tool. We have shown in this work how shape optimization can be used efficiently to refine the shape of the individual pieces of the dielectric solid once its topology has been identified by topology optimization.

For all three additional γ-dependent fields $\alpha(\gamma)$, $\kappa(\gamma)$, and $\varepsilon(\gamma)$ we have used (nearly) linear functions. In many previous applications of topology optimization

non-linear functions have successfully been used to find global optima by gradually changing the non-linearity into strict linearity during the iterative procedure [6, 7, 8, 12]. However, we did not improve our search for a global optimum by employing such schemes, and simply applied the (nearly) linear functions during the entire iteration process.

The limited size of the design domain is in some cases restricting the free formation of the optimized structures. This may be avoided by enlarging the design domain. However, starting a topology optimization in a very large domain gives a huge amount of degrees of freedoms, and the routine is easily caught in local minima. These local minima often yield results not as optimal as those obtained for the smaller design boxes. A solution could be to increase the design domain during the optimization iteration procedure. It should be noted that increasing the box all the way up to the capacitor plates results in solution shapes, where some of the dielectric material is attached to the electrode in order to extend the electrode into the capacitor and thereby maximize the electric field locally. This may be a desirable feature for some purposes. In this work we have deliberately avoided such solutions by keeping the edges of the design domain from the capacitor plates.

Throughout the paper we have only presented results obtained for dielectric solids shapes forced to be symmetric around the center plane $z = 0$. However, we have performed both topology optimization and shape optimization of systems not restricted to this symmetry. In general we find that the symmetric shapes always are good candidates for the optimal design. It cannot be excluded, though, that in some cases a spontaneous symmetry breaking occurs similar to the asymmetric S-turn channel studied in Ref. [7].

By studying the optimized shapes of the dielectric solids, we have noted that pointed features often occurs, such as those clearly seen on the dielectric satellite island in Fig. 8(b). The reason for these to appear seems to be that the pointed regions of the dielectric surfaces can support large gradients in the electric potential and, associated with this, also large charge densities [24, 25]. As a result large electric body forces act on the electrolyte in these regions. At the same time the surface between the pointed features curve inward which lowers the viscous flow resistance due to the no-slip boundary condition. This effect is similar to that obtained by creating electrode arrays of different heights in AC electro-osmosis [26, 27].

Another noteworthy aspect of the topology optimized structures is that the appearance of dielectric satellite islands seem to break up flow rolls that would otherwise be present and not contribute to the flow rate. This leads to a larger net flow rate, as can be seen by comparing Figs. 5 and 8.

Throughout the paper we have treated the design field γ as an artificial field. However, the design-field model could perhaps achieve physical applications to systems containing ion exchange membranes, as briefly mentioned in Sec. 1. Such membranes are indeed porous structures permeated by an electrolyte.

In conclusion, our analysis points out the great potential for improving actual ICEO-based devices by changing simply connected topologies and simple shapes of the dielectric solids, into multiply connected topologies of complex shapes.

Acknowledgement

We would like to thank Elie Raphaël and Patrick Tabeling at ESPCI for their hospitality and support during our collaboration.

References

[1] M.Z. Bazant and T. M. Squires, Phys. Rev. Lett. **92** 066101 (2004).
[2] J. A. Levitan, S. Devasenathipathy, V. Studer, Y. Ben, T. Thorsen, T. M. Squires, M. Z. Bazant, Coll. Surf. A **267**, 122 (2005).
[3] T.M. Squires, and M.Z. Bazant, J. Fluid Mech. **509**, 217 (2004).
[4] T.M. Squires, and M.Z. Bazant, J. Fluid Mech. **560**, 65 (2006).
[5] C.K. Harnett, J. Templeton, K. Dunphy-Guzman, Y.M. Senousy, and M.P. Kanouff, Lab Chip **8**, 565 (2008).
[6] T. Borrvall and J. Petersson, Int. J. Numer. Methods Fluids **41**, 77 (2003).
[7] L. H. Olesen, F. Okkels, and H. Bruus, Int. J. Numer. Methods Eng. **65**, 975 (2006).
[8] M.P. Bendsøe and O. Sigmund, *Topology Optimization-Theory, Methods and Applications*, Springer (Berlin, 2003).
[9] J.S. Jensen and O. Sigmund, Appl. Phys. Lett. **84**, 2022 (2004).
[10] M.B. Düring, J.S. Jensen, and O. Sigmund, J. Sound Vib. **317**, 557 (2008).
[11] A. Gersborg-Hansen, O. Sigmund, and R.B. Haber, Struct. Multidiscip. Optim. **30**, 181 (2005).
[12] F. Okkels and H. Bruus, Phys. Rev. E **75**, 016301 1–4 (2007).
[13] M. S. Kilic, M. Z. Bazant, and A. Ajdari, Phys. Rev. E **75**, 034702 (2007).
[14] M. Z. Bazant, K. Thornton, and A. Ajdari, Phys. Rev. E **70**, 021506 (2004).
[15] MATLAB, The MathWorks, Inc. (`www.mathworks.com`).
[16] COMSOL MULTIPHYSICS, COMSOL AB (`www.comsol.com`).
[17] K. Svanberg, Int. J. Numer. Methods Eng. **24**, 359 (1987).
[18] A MATLAB implementation, mmasub, of the MMAoptimization algorithm [17] can be obtained from Krister Svanberg, KTH, Sweden. E-mail address: krille@math.kth.se.
[19] M.M. Gregersen, M.B. Andersen, G. Soni, C. Meinhart, and H. Bruus, Phys. Rev. E (submitted, 2009), http://arxiv.org/abs/0901.1788.
[20] J.A. Nelder and R. Mead, Computer Journal, **7**, 308 (1965).
[21] J.C. Lagarias, J.A. Reeds, M.H. Wright, and P.E. Wright, SIAM Journal of Optimization, Vol. **9** No. 1, 112 (1998)
[22] The routine `fminsearch` in MATLAB version 7 (R14).
[23] The MATLAB function `fminsearch` is actually unbounded. Therefore the arcus tangent function is used to map the unbounded real axis to the bounded interval of the design variables.
[24] S.K. Thamida and Hseue-Chia Chang, Phys. Fluids **14**, 4315 (2002).
[25] G. Yossifon, T. Miloh, and I. Frankel, Phys. Fluids **18**, 117108 (2006).
[26] M.Z. Bazant and Y. Ben, Lab Chip **6**, 1455 (2006).
[27] J. Urbanski, T. Thorsen, J. Levitan, and M. Bazant Appl. Phys. Lett. **89**, 143508 (2006).

Appendix D

Paper submitted to Phys. Rev. E

Title: A numerical analysis of finite Debye-length effects in induced-charge electro-osmosis

Authors: Misha Marie Gregersen, Mathias Bækbo Andersen, Gaurav Soni, Carl Meinhart, and Henrik Bruus.

Reference: Submitted to Phys Rev. E February 2009 (11 pages)

A numerical analysis of finite Debye-length effects in induced-charge electro-osmosis

Misha Marie Gregersen[1], Mathias Bækbo Andersen[1], Gaurav Soni[2], Carl Meinhart[2], and Henrik Bruus[1]
[1]*Department of Micro- and Nanotechnology, Technical University of Denmark*
DTU Nanotech Building 345 East, DK-2800 Kongens Lyngby, Denmark
[2]*Department of Mechanical Engineering, University of California*
Engineering II Building, Santa Barbara, CA 93106, USA
(Dated: 23 February 2008)

For a microchamber filled with a binary electrolyte and containing a flat un-biased center electrode at one wall, we employ three numerical models to study the strength of the resulting induced-charge electro-osmotic (ICEO) flow rolls: (*i*) a full nonlinear continuum model resolving the double layer, (*ii*) a linear slip-velocity model not resolving the double layer and without tangential charge transport inside this layer, and (*iii*) a nonlinear slip-velocity model extending the linear model by including the tangential charge transport inside the double layer. We show that compared to the full model, the slip-velocity models significantly overestimate the ICEO flow. This provides a partial explanation of the quantitative discrepancy between observed and calculated ICEO velocities reported in the literature. The discrepancy increases significantly for increasing Debye length relative to the electrode size, i.e. for nanofluidic systems. However, even for electrode dimensions in the micrometer range, the discrepancies in velocity due to the finite Debye length can be more than 10% for an electrode of zero height and more than 100% for electrode heights comparable to the Debye length.

PACS numbers: 47.57.jd, 47.61.-k, 47.11.Fg

I. INTRODUCTION

Within the last decade the interest in electrokinetic phenomena in general and induced-charge electro-osmosis (ICEO) in particular has increased significantly as the field of lab-on-a-chip technology has developed. Previously, the research in ICEO has primarily been conducted in the context of colloids, where experimental and theoretical studies have been carried out on the electric double layer and induced dipole moments around spheres in electric fields, as reviewed by Dukhin [1] and Murtsovkin [2]. In microfluidic systems, electrokinetically driven fluid motion has been used for fluid manipulation, e.g. mixing and pumping. From a microfabrication perspective planar electrodes are easy to fabricate and relatively easy to integrate in existing systems. For this reason much research has been focused on the motion of fluids above planar electrodes. AC electrokinetic micropumps based on AC electroosmosis (ACEO) have been thoroughly investigated as a possible pumping and mixing device. Experimental observations and theoretical models were initially reported around year 2000 [3, 4, 5, 6], and further investigations and theoretical extensions of the models have been published by numerous groups since [7, 8, 9, 10, 11, 12]. Recently, ICEO flows around inert, polarizable objects have been observed and investigated theoretically [13, 14, 15, 16, 17, 18]. For a thorough historical review of research leading up to these results, we refer the reader to Squires *et al.* [13] and references therein.

In spite of the growing interest in the literature not all aspects of the flow-generating mechanisms have been explained so far. While qualitative agreement is seen between theory and experiment, quantitative agreement is often lacking as reported by Gregersen *et al.* [11], Harnett *et al.* [16], and Soni *et al.* [19]. In the present work we seek to illuminate some of the possible reasons underlying these observed discrepancies.

ICEO flow is generated when an external electric field polarizes an object in an electrolytic solution. Counter ions in the electrolyte screen out the induced dipole, having a potential difference ζ relative to the bulk electrolyte, by forming an electric double layer of width λ_{D} at the surface of the object. The ions in the diffuse part of the double layer then electromigrate in the external electric field and drag the entire liquid by viscous forces. At the outer surface of the double layer a resulting effective slip velocity $\boldsymbol{v}_{\mathrm{slip}}$ is thus established. Many numerical models of ICEO problems exploit this characteristic by applying the so-called Helmholtz–Smoluchowski slip condition on the velocity field at the electrode surface [20, 21]. Generally, the slip-condition based model remains valid as long as

$$\frac{\lambda_{\mathrm{D}}}{a_c}\exp\left(\frac{Ze\zeta}{2k_{\mathrm{B}}T}\right)\ll 1, \tag{1}$$

where $k_{\mathrm{B}}T/(Ze)$ is the thermal voltage and a_c denotes the radius of curvature of the surface [13]. The slip-velocity condition may be applied when the double layer is infinitely thin compared to the geometrical length scale of the object, however, for planar electrodes, condition (1) is not well defined. In the present work we investigate to what extent the slip condition remains valid.

Squires *et al.* [13] have presented an analytical solution to the ICEO flow problem around a metallic cylinder with radius a_c using a linear slip-velocity model in the two dimensional plane perpendicular to the cylinder axis. In this model with its infinitely thin double layer, the surrounding electrolyte is charge neutral, and hence the strength of the ICEO flow can be defined solely in terms of the hydrodynamic stress tensor $\boldsymbol{\sigma}$, as the mechanical power $P_{\mathrm{mech}}=\oint_{|\boldsymbol{r}|=a_c}\hat{\boldsymbol{n}}\cdot\boldsymbol{\sigma}\cdot\boldsymbol{v}_{\mathrm{slip}}\mathrm{d}a$ exerted on the electrolyte by the tangential slip-velocity $\boldsymbol{v}_{\mathrm{slip}}=u_{\mathrm{eo}}\hat{\boldsymbol{t}}$, where $\hat{\boldsymbol{n}}$ and $\hat{\boldsymbol{t}}$ is the normal and tangential vector to the cylinder surface, respectively. In steady flow, this power is equal to the total kinetic energy dissipation $P_{\mathrm{kin}}=\frac{1}{2}\eta\int_{a_c<|\boldsymbol{r}|}(\partial_i v_j+\partial_j v_i)^2\mathrm{d}\boldsymbol{r}$ of the resulting quadrupolar velocity field in the electrolyte.

When comparing the results for the strength of the ICEO flow around the cylinder obtained by the analytical model with those obtained by a numerical solution of the full equation system, where the double layer is fully resolved, we have noted significant discrepancies. These discrepancies, which are described in the following, have become the primary motivation for the study presented in this paper.

First, in the full double-layer resolving simulation we determined the value $P^*_{\mathrm{mech}}(R_0)=\oint_{|\boldsymbol{r}|=R_0}\hat{\boldsymbol{n}}\cdot\boldsymbol{\sigma}\cdot\boldsymbol{v}\,\mathrm{d}a$ of the mechanical input power, where R_0 is the radius of a cylinder surface placed co-axially with the metallic cylinder. Then, as expected due to the electrical forces acting on the net charge in the double layer, we found that $P^*_{\mathrm{mech}}(R_0)$ varied substantially as long as the integration cylinder surface was inside the double layer. For $R_0\approx a_c+6\lambda_{\mathrm{D}}$ the mechanical input power stabilized at a certain value. However, this value is significantly lower than the analytical value, but the discrepancy decreased for decreasing values of λ_{D}. Remarkably, even for a quite thin Debye layer, $\lambda_{\mathrm{D}}=0.01\,a_c$, the value of the full numerical simulation was about 40% lower than the analytical value. Clearly, the analytical model overestimates the ICEO effect, and the double-layer width must be extremely thin before the simple analytical model agrees well with the full model.

A partial explanation of the quantitative failure of the analytical slip velocity model is the radial dependence of the tangential field $E_{\parallel}$ combined with the spatial extent of the charge density ρ_{el} of the double layer. In the Debye–Hückel approximation $E_{\parallel}$ and ρ_{el} around the metallic cylinder of radius a_c become

$$E_{\parallel}(r,\theta)=E_0\left[1+\frac{a_c^2}{r^2}-2\frac{a_c}{r}\frac{K_1\left(\frac{r}{\lambda_{\mathrm{D}}}\right)}{K_1\left(\frac{a_c}{\lambda_{\mathrm{D}}}\right)}\right]\sin\theta, \tag{2a}$$

$$\rho_{\mathrm{el}}(r,\theta)=2\,\frac{\epsilon E_0 a_c}{\lambda_{\mathrm{D}}^2}\,\frac{K_1\left(\frac{r}{\lambda_{\mathrm{D}}}\right)}{K_1\left(\frac{a_c}{\lambda_{\mathrm{D}}}\right)}\cos\theta, \tag{2b}$$

where K_1 is the decaying modified Bessel function of order 1. The slowly varying part of $E_{\parallel}$ is given by $E_0\left[1+(a_c/r)^2\right]\sin\theta$. For very thin double layers it is well approximated by the r-independent expression $2E_0\sin\theta$, while for wider double layers, the screening charges sample the decrease of $E_{\parallel}$ as a function of the distance from the cylinder. Also tangential hydrodynamic and osmotic pressure gradients developing in the double layer may contribute to the lower ICEO strength when taking the finite width of the double layer into account.

In this work we analyze quantitatively the impact of a finite Debye length on the kinetic energy of the flow rolls generated by ICEO for three different models: (*i*) The full nonlinear electrokinetic model (FN) with a fully resolved double layer, (*ii*) the linear slip-velocity model (LS), where electrostatics and hydrodynamics are completely decoupled, and (*iii*) a nonlinear slip-velocity model (NSL) including the double layer charging through ohmic currents from the bulk electrolyte and the surface conduction in the Debye layer. The latter two models are only strictly valid for infinitely thin double layers, and we emphasize that the aim of our analysis is to determine the errors introduced by these models neglecting the finite width of the double layers compared to the full nonlinear model resolving the double layer. We do not seek to provide a more accurate description of the physics in terms of extending the modeling by adding, say, the Stern layer (not present in the model) or the steric effects of finite-sized ions (not taken into account).

II. MODEL SYSTEM

To keep our analysis simple, we consider a single unbiased metallic electrode in a uniform, external electric field. The electrode of width $2a$ and height h is placed at the bottom center, $-a<x<a$ and $z=0$, of a square $2L\times 2L$ domain in the xz-plane filled with an electrolyte, see Fig. 1. The system is unbounded and translational invariant in the perpendicular y-direction. The uniform electric field, parallel to the surface of the center electrode, is provided by biasing the driving electrodes placed at the edges $x=\pm L$ with the DC voltages $\pm V_0$, respectively. This anti-symmetry in the bias voltage ensures that the constant potential of the center electrode is zero. A double layer, or a Debye screening layer, is induced above the center electrode, and an ICEO flow is generated consisting of two counter-rotating flow rolls. Electric insulating walls at $z=0$ (for $|x|>a$) and at $z=2L$ confine the domain in the z-direction. The symmetry of the system around $x=0$ is exploited in the numerical calculations.

III. FULL NONLINEAR MODEL (FN)

We follow the usual continuum approach to the electrokinetic modeling of the electrolytic microchamber and treat only steady-state problems. For simplicity we consider a symmetric, binary electrolyte, where the positive and negative ions with concentrations c_+ and c_-, respectively, have the same diffusivity D and charge number Z. Using the ideal gas model for the ions, an ion is affected by the sum of an electrical and an osmotic force given by $\boldsymbol{F}_{\pm}=\mp Ze\boldsymbol{\nabla}\phi-(k_{\mathrm{B}}T/c_{\pm})\,\boldsymbol{\nabla}c_{\pm}$. Here e is the elementary charge, T is the absolute temperature and k_{B} is

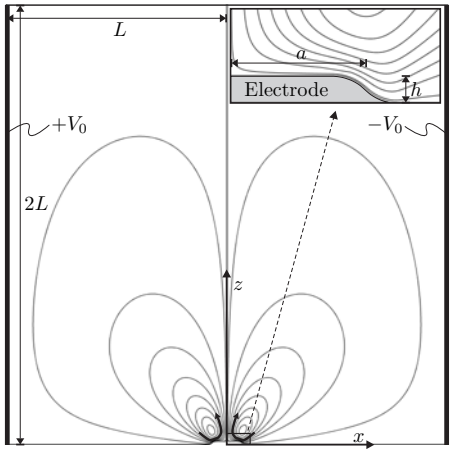

FIG. 1: A sketch of the square $2L\times 2L$ electrolytic microchamber in the xz-plane. The external voltage $\pm V_0$ is applied to the two electrodes (thick black lines) at $x=\pm L$, respectively. It induces two counter-rotating flow rolls (curved black arrows) by electro-osmosis over the un-biased metallic center electrode of length $2a$ and height h placed at the bottom wall around $(x,z)=(0,0)$. The spatial extent of the flow rolls is represented by the streamline plot (thin black curves) drawn as equidistant contours of the flow rate. The inset is a zoom-in on the right half, $0<x<a$, of the un-biased center electrode and the nearby streamlines.

Boltzmann's constant. Assuming a complete force balance between each ion and the surrounding electrolyte, the resulting body force density $\boldsymbol{f}_{\rm ion}=\sum_{i=\pm}c_i\boldsymbol{F}_i$, appearing in the Navier–Stokes for the electrolyte due to the forces acting on the ions, is

$$\boldsymbol{f}_{\rm ion}=-Ze\big(c_+-c_-\big)\boldsymbol{\nabla}\phi-k_{\rm B}T\boldsymbol{\nabla}\big(c_++c_-\big). \tag{3}$$

As the second term is a gradient, namely the gradient of the osmotic pressure of the ions, it can in the Navier–Stokes equation be absorbed into the pressure gradient $\boldsymbol{\nabla}p=\boldsymbol{\nabla}p_{\rm dyn}+\boldsymbol{\nabla}p_{\rm os}$, which is the gradient of the sum of hydrodynamic pressure and the osmotic pressure. Only the electric force is then kept as an explicit body force.

A. Bulk equations

Neglecting bulk reactions in the electrolyte, the ionic transport is governed by the particle conservation

$$\boldsymbol{\nabla}\cdot\boldsymbol{J}_\pm=0, \tag{4}$$

where $\boldsymbol{J}_\pm$ is the flux density of the two ionic species. Assuming the electrolytic solution to be dilute, the ion flux densities are governed by the Nernst–Planck equation

$$\boldsymbol{J}_\pm=-D\Big(\boldsymbol{\nabla}c_\pm+\frac{\pm Ze}{k_{\rm B}T}c_\pm\boldsymbol{\nabla}\phi\Big)+c_\pm\boldsymbol{v}, \tag{5}$$

where the first term expresses ionic diffusion and the second term ionic electromigration due to the electrostatic potential ϕ. The last term expresses the convective transport of ions by the fluid velocity field $\boldsymbol{v}$.

The electrostatic potential is determined by the charge density $\rho_{\rm el}=Ze(c_+-c_-)$ through Poisson's equation

$$\boldsymbol{\nabla}\cdot(\varepsilon\boldsymbol{\nabla}\phi)=-\rho_{\rm el}, \tag{6}$$

where ε is the fluid permittivity, which is assumed constant. The fluid velocity field $\boldsymbol{v}$ and pressure field p are governed the the continuity equation and the Navier–Stokes equation for incompressible fluids,

$$\boldsymbol{\nabla}\cdot\boldsymbol{v}=0, \tag{7a}$$

$$\rho_{\rm m}(\boldsymbol{v}\cdot\boldsymbol{\nabla})\boldsymbol{v}=-\boldsymbol{\nabla}p+\eta\nabla^2\boldsymbol{v}-\rho_{\rm el}\boldsymbol{\nabla}\phi, \tag{7b}$$

where $\rho_{\rm m}$ and η are the fluid mass density and viscosity, respectively, both assumed constant.

B. Dimensionless form

To simplify the numerical implementation, the governing equations are rewritten in dimensionless form, as summarized in Fig. 2, using the characteristic parameters of the system: The geometric half-length a of the electrode, the ionic concentration c_0 of the bulk electrolyte, and the thermal voltage $\phi_0=k_{\rm B}T/(Ze)$. The characteristic zeta-potential ζ of the center electrode, i.e. its induced voltage, is given as the voltage drop along half of the electrode, $\zeta=(a/L)V_0$, and we introduce the dimensionless zeta-potential α as $\zeta\equiv\alpha\phi_0$, or $\alpha=(aV_0)/(L\phi_0)$. The characteristic velocity u_0 is chosen as the Helmholtz–Smoluchowski slip velocity induced by the local electric field $E=\zeta/a$, and finally the pressure scale is set by the characteristic microfluidic pressure scale $p_0=\eta u_0/a$. In summary,

$$\phi_0=\frac{k_{\rm B}T}{Ze},\quad u_0=\frac{\varepsilon\zeta}{\eta}\frac{\zeta}{a}=\frac{\varepsilon\phi_0^2}{\eta a}\alpha^2,\quad p_0=\frac{\eta u_0}{a}. \tag{8}$$

The new dimensionless variables (denoted by a tilde) thus become

$$\tilde{\boldsymbol{r}}=\frac{\boldsymbol{r}}{a},\quad \tilde{c}_i=\frac{c_i}{c_0},\quad \tilde{\phi}=\frac{\phi}{\phi_0},\quad \tilde{\boldsymbol{v}}=\frac{\boldsymbol{v}}{u_0},\quad \tilde{p}=\frac{p}{p_0}. \tag{9}$$

To exploit the symmetry of the system and the binary electrolyte, the governing equations are reformulated in terms of the average ion concentration $c\equiv(c_++c_-)/2$ and half the charge density $\rho\equiv(c_+-c_-)/2$. Correspondingly, the average ion flux density $\boldsymbol{J}_c=(\boldsymbol{J}_++\boldsymbol{J}_-)/2$ and half the current density $\boldsymbol{J}_\rho=(\boldsymbol{J}_+-\boldsymbol{J}_-)/2$ are introduced.

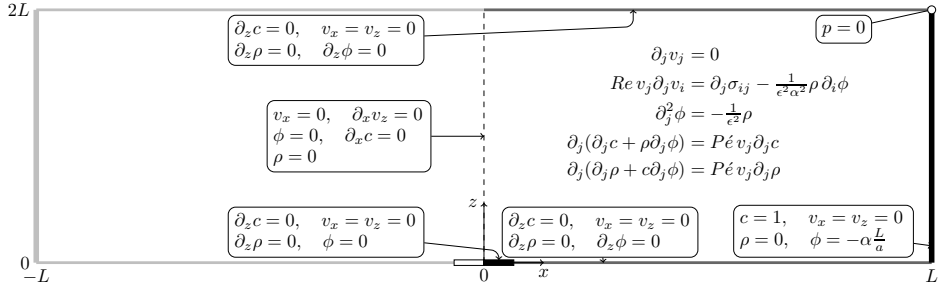

FIG. 2: The governing equations (without box) and boundary conditions (with boxes, arrows points to specific boundaries) in dimensionless form (the tilde is omitted for clarity) for the entire quadratic $2L\times 2L$ domain (not shown in correct aspect ratio) bisected into two symmetric halves. Only the right half ($x>0$) of the domain is included in the simulations. The boundaries are the surface of the un-biased center electrode (black rectangle), the solid insulating walls (dark gray lines), the external electrode (black line), and the symmetry line (dashed black line).

Thus, the resulting full system of coupled nonlinear equations takes the following form for the ionic fields

$$\tilde{\boldsymbol{\nabla}}\cdot\tilde{\boldsymbol{J}}_c=\tilde{\boldsymbol{\nabla}}\cdot\tilde{\boldsymbol{J}}_\rho=0, \tag{10a}$$

$$\tilde{\boldsymbol{J}}_c=-\tilde{\rho}\tilde{\boldsymbol{\nabla}}\tilde{\phi}-\tilde{\boldsymbol{\nabla}}\tilde{c}+Pé\,\tilde{c}\tilde{\boldsymbol{v}}, \tag{10b}$$

$$\tilde{\boldsymbol{J}}_\rho=-\tilde{c}\tilde{\boldsymbol{\nabla}}\tilde{\phi}-\tilde{\boldsymbol{\nabla}}\tilde{\rho}+Pé\,\tilde{\rho}\tilde{\boldsymbol{v}}, \tag{10c}$$

$$Pé=\frac{u_0a}{D}, \tag{10d}$$

while the electric potential obeys

$$\tilde{\boldsymbol{\nabla}}^2\tilde{\phi}=-\frac{1}{\epsilon^2}\tilde{\rho}, \tag{11}$$

and finally the fluid fields satisfy

$$\tilde{\boldsymbol{\nabla}}\cdot\tilde{\boldsymbol{v}}=0, \tag{12a}$$

$$Re\big(\tilde{\boldsymbol{v}}\cdot\tilde{\boldsymbol{\nabla}}\big)\tilde{\boldsymbol{v}}=-\tilde{\boldsymbol{\nabla}}\tilde{p}+\tilde{\boldsymbol{\nabla}}^2\tilde{\boldsymbol{v}}-\frac{\tilde{\rho}}{\epsilon^2\,\alpha^2}\tilde{\boldsymbol{\nabla}}\tilde{\phi}, \tag{12b}$$

$$Re=\frac{\rho u_0a}{\eta}. \tag{12c}$$

Here the small dimensionless parameter $\epsilon=\lambda_{\rm D}/a$ has been introduced, where $\lambda_{\rm D}$ is the Debye length,

$$\epsilon=\frac{\lambda_{\rm D}}{a}=\frac{1}{a}\sqrt{\frac{\varepsilon k_{\rm B}T}{2(Ze)^2c_0}}. \tag{13}$$

We note that the dimensionless form of the osmotic force, the second term in Eq. (3), is $\tilde{\boldsymbol{f}}_{\rm ion}^{\rm os}=-(1/\epsilon^2\alpha^2)\boldsymbol{\nabla}\tilde{c}$.

C. Boundary conditions

We exploit the symmetry around $x=0$ and consider only the right half ($0<x<L$) of the domain, see Fig. 2. As boundary conditions on the driving electrode we take both ion concentrations to be constant and equal to the bulk charge neutral concentration. Correspondingly, the charge density is set to zero. Consequently, we ignore all dynamics taking place on the driving electrode and simply treat it as an equipotential surface with the value V_0. We set a no-slip condition for the fluid velocity, and thus at $x=L$ we have

$$\tilde{c}=1,\quad \tilde{\rho}=0,\quad \tilde{\phi}=\frac{V_0}{\phi_0}=\alpha\frac{L}{a},\quad \tilde{\boldsymbol{v}}=\boldsymbol{0}. \tag{14}$$

On the symmetry axis ($x=0$) the potential and the charge density must be zero due to the anti-symmetry of the applied potential. Moreover, there is neither a fluid flux nor a net ion flux in the normal direction and the shear stresses vanish. So at $x=0$ we have

$$\tilde{\phi}=0,\quad \hat{\boldsymbol{n}}\cdot\tilde{\boldsymbol{J}}_c=0,\quad \tilde{\rho}=0, \tag{15a}$$

$$\hat{\boldsymbol{t}}\cdot\tilde{\boldsymbol{\sigma}}\cdot\hat{\boldsymbol{n}}=0,\quad \hat{\boldsymbol{n}}\cdot\tilde{\boldsymbol{v}}=0, \tag{15b}$$

where the stress tensor is $(\boldsymbol{\sigma})_{ik}=-p\delta_{ik}+\eta(\partial_iu_k+\partial_ku_i)$, and $\hat{\boldsymbol{n}}$ and $\hat{\boldsymbol{t}}$ are the normal and tangential unit vectors, respectively, which in 2D, contrary to 3D, are uniquely defined. The constant potential on the un-biased metallic electrode is zero due to symmetry, and on the electrode surface we apply a no-slip condition on the fluid velocity and no-current condition in the normal direction. So on the electrode surface we have

$$\hat{\boldsymbol{n}}\cdot\tilde{\boldsymbol{J}}_c=0,\quad \hat{\boldsymbol{n}}\cdot\tilde{\boldsymbol{J}}_\rho=0,\quad \tilde{\phi}=0,\quad \tilde{\boldsymbol{v}}=\boldsymbol{0}. \tag{16}$$

On the solid, insulating walls there are no fluxes in the normal direction, the normal component of the electric field vanishes and there are no-slip on the fluid velocity.

$$\hat{\boldsymbol{n}}\cdot\tilde{\boldsymbol{J}}_c=0,\quad \hat{\boldsymbol{n}}\cdot\tilde{\boldsymbol{J}}_\rho=0,\quad \hat{\boldsymbol{n}}\cdot\tilde{\boldsymbol{\nabla}}\tilde{\phi}=0,\quad \tilde{\boldsymbol{v}}=\boldsymbol{0}. \tag{17}$$

A complete overview of the governing equations and boundary conditions is given in Fig. 2.

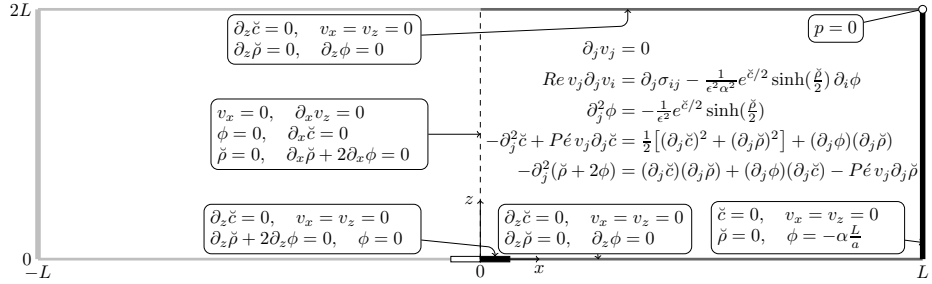

FIG. 3: The governing equations (without box) and boundary conditions (with boxes) in dimensionless form (the tilde is omitted) using the logarithmic concentrations (denoted by a breve) of Eq. (18). Otherwise the figure is identical to Fig. 2.

D. The strongly nonlinear regime

At high values of the induced ζ-potential, the concentrations of counter- and co-ions acquire very large and very small values, respectively, near the center electrode. Numerically this is problematic. The concentration ratio becomes extremely large and the vanishingly small concentration of co-ions is comparable to the round-off error and may even become negative. However, this numerical problem can be circumvented by working with the logarithms (marked by a breve accent) of the concentration fields, $\check{c}_\pm = \log(c_\pm/c_0)$. By inserting

$$c_\pm = c_0\, \exp\left(\check{c}_\pm\right) \tag{18}$$

in the governing equations (5), (6), and (7b), a new equivalent set of governing equations is derived. The symmetry is exploited by defining the symmetric $\check{c} = \check{c}_+ + \check{c}_-$ and antisymmetric $\check{\rho} = \check{c}_+ - \check{c}_-$ combination of the logarithmic fields and the corresponding formulation of the governing equations is

$$\tilde{\nabla}^2\check{c} = Pé\,\tilde{\boldsymbol{v}}\cdot\tilde{\boldsymbol{\nabla}}\check{c} - \frac{(\tilde{\boldsymbol{\nabla}}\check{c})^2+(\tilde{\boldsymbol{\nabla}}\check{\rho})^2}{2} - \tilde{\boldsymbol{\nabla}}\tilde{\phi}\cdot\tilde{\boldsymbol{\nabla}}\check{\rho}, \tag{19a}$$

$$\tilde{\nabla}^2\big(\check{\rho}+2\tilde{\phi}\big) = Pé\,\tilde{\boldsymbol{v}}\cdot\tilde{\boldsymbol{\nabla}}\check{\rho} - \tilde{\boldsymbol{\nabla}}\check{c}\cdot\tilde{\boldsymbol{\nabla}}\check{\rho} - \tilde{\boldsymbol{\nabla}}\tilde{\phi}\cdot\tilde{\boldsymbol{\nabla}}\check{\rho}, \tag{19b}$$

$$\tilde{\nabla}^2\tilde{\phi} = -\frac{1}{\epsilon^2}\,e^{\check{c}/2}\sinh\left(\frac{\check{\rho}}{2}\right), \tag{19c}$$

$$Re\big(\tilde{\boldsymbol{v}}\cdot\tilde{\boldsymbol{\nabla}}\big)\tilde{\boldsymbol{v}} = -\tilde{\boldsymbol{\nabla}}\tilde{p} + \tilde{\nabla}^2\tilde{\boldsymbol{v}} - \frac{1}{\epsilon^2\alpha^2}\,e^{\check{c}/2}\sinh\left(\frac{\check{\rho}}{2}\right)\tilde{\boldsymbol{\nabla}}\tilde{\phi}, \tag{19d}$$

while the continuity equation remains the same as in Eq. (12a). The governing equations and boundary conditions for the logarithmic fields (breve-notation) is summarized in Fig. 3. This transformation serves to help linearize solutions of the dependent variables, $\check{c}$ and $\check{\rho}$, at the expense of introducing more nonlinearity into the governing equations.

IV. SLIP-VELOCITY MODELS

The numerical calculation of ICEO flows in microfluidic systems is generally connected with computational limitations due to the large difference of the inherent length scales. Typically, the Debye length is much smaller than the geometric length scale, $\lambda_D \ll a$, making it difficult to resolve both the dynamics of the Debye layer and the entire microscale geometry with the available computer capacity. Therefore, it is customary to use slip-velocity models, where it is assumed that the electrodes are screened completely by the Debye layer leaving the bulk electrolyte charge neutral. The dynamics of the Debye layer is modeled separately and applied to the bulk fluid velocity through an effective, so-called Helmholtz–Smoluchowski slip velocity condition at the electrode surface,

$$\boldsymbol{v}_{\rm HS} = -\frac{\varepsilon}{\eta}\,\zeta\,\boldsymbol{E}_\parallel. \tag{20}$$

where ζ is the zeta potential at the electrode surface, and $\boldsymbol{E}_\parallel$ is the electric field parallel to the surface. Regardless of the modeled dynamics in the double layer the slip-velocity models are only strictly valid in the limit of infinitely thin double layers $\lambda_D \ll a$.

A. The linear slip-velocity model (LS)

The double-layer screening of the electrodes leaves the bulk electrolyte charge neutral, and hence the governing equations only include the potential ϕ, the pressure field p and the flow velocity field $\boldsymbol{v}$. In dimensionless form they become,

$$\tilde{\boldsymbol{\nabla}}^2\tilde{\phi} = 0, \tag{21a}$$

$$Re\big(\tilde{\boldsymbol{v}}\cdot\tilde{\boldsymbol{\nabla}}\big)\tilde{\boldsymbol{v}} = -\tilde{\boldsymbol{\nabla}}\tilde{p} + \tilde{\boldsymbol{\nabla}}^2\tilde{\boldsymbol{v}}, \tag{21b}$$

$$\tilde{\boldsymbol{\nabla}}\cdot\tilde{\boldsymbol{v}} = 0. \tag{21c}$$

The electrostatic problem is solved independently of the hydrodynamics, and the potential is used to calculate the effective slip velocity applied to the fluid at the unbiased electrode surface. The boundary conditions of the potential and fluid velocity are equivalent to the conditions applied to the full non-linear system, except at the surface of the un-biased electrode. Here, the normal component of the electric field vanishes, and the effective slip velocity of the fluid is calculated from the electrostatic potential using $\zeta = -\phi$ and $\boldsymbol{E}_\parallel = -\big[(\hat{\boldsymbol{t}}\cdot\tilde{\boldsymbol{\nabla}})\tilde{\phi}\big]\,\hat{\boldsymbol{t}}$,

$$\hat{\boldsymbol{n}}\cdot\tilde{\boldsymbol{\nabla}}\tilde{\phi} = 0, \tag{22a}$$

$$\tilde{\boldsymbol{v}}_{\rm HS} = \frac{1}{\alpha^2}\,\tilde{\phi}\left[(\hat{\boldsymbol{t}}\cdot\tilde{\boldsymbol{\nabla}})\tilde{\phi}\right]\hat{\boldsymbol{t}}. \tag{22b}$$

This represents the simplest possible, so-called linear slip-velocity model; a model which is widely applied as a starting point for numerical simulations of actual microfluidic systems [20, 21]. In this simple model all the dynamics of the double layer has been neglected, an assumption known to be problematic when the voltage across the electrode exceeds the thermal voltage.

B. The nonlinear slip-velocity model (NLS)

The linear slip-velocity model can be improved by taking into account the nonlinear charge dynamics of the double layer. This is done in the so-called nonlinear slip-velocity model, where, although still treated as being infinitely thin, the double layer has a non-trivial charge dynamics with currents from the bulk in the normal direction and currents flowing tangential to the electrode inside the double layer. For simplicity we assume in the present nonlinear model that the neutral salt concentration c_0 is uniform. This assumption breaks down at high zeta potentials, where surface transport of ionic species can set up gradients in the salt concentrations leading to chemi-osmotic flow. In future more complete studies of double layer charge dynamics these effects should be included.

The charging of the double layer by the ohmic bulk current is assumed to happen in quasi-equilibrium characterized by a nonlinear differential capacitance $C_{\rm dl}$ given by the Gouy–Chapmann model, $C_{\rm dl} = \varepsilon\cosh[ze\zeta/(2k_BT)]/\lambda_D$, which in the the low-voltage, linear Debye–Hückel regime reduces to $C_{\rm dl} = \varepsilon/\lambda_D$. Ignoring the Stern layer, the zeta-potential is directly proportional to the bulk potential right outside the double layer, $\zeta = -\phi$.

The current along the electrode inside the Debye layer is described by a 2D surface conductance σ_s, which for a binary, symmetric electrolyte is given by [1]

$$\sigma_s = 4\lambda_D\sigma(1+m)\sinh^2\left(\frac{Ze\zeta}{4k_BT}\right), \tag{23}$$

where σ is the bulk 3D conductivity and

$$m = 2\frac{\varepsilon}{\eta D}\left(\frac{k_BT}{Ze}\right)^2 \tag{24}$$

is a dimensionless parameter indicating the relative contribution of electroosmosis to surface conduction. In steady state the conservation of charge then yields [25]

$$0 = \hat{\boldsymbol{n}}\cdot(\sigma\boldsymbol{\nabla}\phi) + \boldsymbol{\nabla}_s\cdot\big[\sigma_s\boldsymbol{\nabla}_s\phi\big], \tag{25}$$

where the operator $\boldsymbol{\nabla}_s = \hat{\boldsymbol{t}}(\hat{\boldsymbol{t}}\cdot\boldsymbol{\nabla})$ is the gradient in the tangential direction of the surface.

Given the length scale a of the electrode, the strength of the surface conductance can by characterized by the dimensionless Dukhin number Du defined by

$$Du = \frac{\sigma_s}{a\sigma} = \frac{4\lambda_D}{a}(1+m)\sinh^2\left(\frac{Ze\zeta}{k_BT}\right). \tag{26}$$

Conservation of charge then takes the dimensionless form

$$0 = \hat{\boldsymbol{n}}\cdot(\tilde{\boldsymbol{\nabla}}\tilde{\phi}) + \tilde{\boldsymbol{\nabla}}_s\cdot\big[Du\tilde{\boldsymbol{\nabla}}_s\cdot\tilde{\phi}\big], \tag{27}$$

and this effective boundary condition for the potential on the flat electrode constitutes a 1D partial differential equation and as such needs accompanying boundary conditions. As a boundary condition the surface flux is assumed to be zero at the edges of the electrode,

$$\sigma_s(\hat{\boldsymbol{t}}\cdot\boldsymbol{\nabla})\phi\big|_{x=\pm a} = 0, \tag{28}$$

which is well suited for the weak formulation we employ in our numerical simulation as seen in Eq. (34).

V. NUMERICS IN COMSOL

The numerical calculations are performed using the commercial finite-element-method software COMSOL with second-order Lagrange elements for all the fields except the pressure, for which first-order elements suffices. We have applied the so-called weak formulation mainly to be able to control the coupling between the bulk equations and the boundary constraints, such as Eqs. (22b) and (25), in the implementation of the slip-velocity models in script form.

The Helmholtz–Smoluchowski slip condition poses a numerical challenge because it is a Dirichlet condition including not one, but up to three variables, for which we want a one-directional coupling from the electrostatic field ϕ to the hydrodynamic fields $\boldsymbol{v}$ and p. We use the weak formulation to unambiguously enforce the boundary condition with the explicit introduction of the required hydrodynamic reaction force $\boldsymbol{f}$ on the un-biased electrode

$$\boldsymbol{f} = \boldsymbol{\sigma}\cdot\hat{\boldsymbol{n}}. \tag{29}$$

The x and z components of Navier–Stokes equation are multiplied with test functions u_x and u_z, respectively,

and subsequently integrated over the whole domain Ω. Partial integration is then used to move the stress tensor contribution to the boundaries $\partial\Omega$,

$$0 = \int_{\partial\Omega} u_i \sigma_{ij} n_j \mathrm{d}s - \int_{\Omega} \left[(\partial_j u_i)\sigma_{ij} + u_i B_i \right] \mathrm{d}a, \quad (30)$$

where $B_i = Re\,(v_j \partial_j)\, v_i + \rho(\partial_i \phi)/(\epsilon^2 \alpha^2)$. The boundary integral on the un-biased electrode $\partial\Omega_{\mathrm{ue}}$ is rewritten as

$$\int_{\partial\Omega_{\mathrm{ue}}} u_i \sigma_{ij} n_j \mathrm{d}s = \int_{\partial\Omega_{\mathrm{ue}}} \left[u_i f_i + F_i (v_i - v_{\mathrm{HS},i}) \right] \mathrm{d}s, \quad (31)$$

where F_i are the test functions belonging to the components f_i of the reaction force $\boldsymbol{f}$. These test functions are used to enforce the Helmholtz–Smoluchowski slip boundary condition consistently. This formulation is used for both slip-velocity models.

In the nonlinear slip-velocity model the Laplace equation (21a) is multiplied with the electrostatic test function Φ and partially integrated to get a boundary term and a bulk term

$$0 = \int_{\partial\Omega} \Phi\, (\partial_i \phi)\, n_i \mathrm{d}s - \int_{\Omega} (\partial_i \Phi)\, (\partial_i \phi)\, \mathrm{d}a. \quad (32)$$

The boundary integration term on the electrode is simplified by substitution of Eq. (25) which results in

$$\int_{\partial\Omega_{\mathrm{ue}}} \Phi\, (\partial_i \phi)\, n_i \mathrm{d}s = -\int_{\partial\Omega_{\mathrm{ue}}} \Phi \left[\hat{t}_i \partial_i \left(Du\, \hat{t}_j \partial_j \phi \right) \right] \mathrm{d}s. \quad (33)$$

Again, the resulting boundary integral is partially integrated, which gives us explicit access to the end-points of the un-biased electrode. This is necessary for applying the boundary conditions on this 1D electrode,

$$\begin{aligned} &\int_{\partial\Omega_{\mathrm{ue}}} \Phi \Big[\hat{t}_i \partial_i (Du\, \hat{t}_j \partial_j \phi) \Big] \mathrm{d}s \\ &\quad = \Big[\Phi\, Du\, (\hat{t}_i \partial_i \phi) \Big]_{x=-a}^{x=+a} - \int_{\partial\Omega_{\mathrm{ue}}} (\hat{t}_i \partial_i \Phi)\, Du\, (\hat{t}_j \partial_j \phi)\, \mathrm{d}s, \end{aligned} \quad (34)$$

The no-flux boundary condition can be explicitly included with this formulation. Note that in both slip-velocity models the zeta-potential is given by the potential just outside the Debye layer, $\zeta = -\phi$, and it is therefore not necessary to include it as a separate variable.

The accuracy and the mesh dependence of the simulation as been investigated as follows. The comparison between the three models quantifies relative differences of orders down to 10^{-3}, and the convergence of the numerical results is ensured in the following way. COMSOL has a build-in adaptive mesh generation technique that is able to refine a given mesh so as to minimize the error in the solution. The adaptive mesh generator increases the mesh density in the immediate region around the electrode to capture the dynamics of the ICEO in the most optimal way under the constraint of a maximum number of degrees of freedom (DOFs). For a given set of physical parameters, the problem is solved each time increasing the number of DOFs and comparing consecutive solutions. As a convergence criterium we demand that the standard deviation of the kinetic energy relative to the mean value should be less than a given threshold value typically chosen to be around 10^{-5}. All of the simulations ended with more than 10^6 DOFs, and the ICEO flow is therefore sufficiently resolved even for the thinnest double layers in our study for which $\epsilon = 10^{-4}$.

VI. RESULTS

Our comparison of the three numerical models is primarily focused on variations of the three dimensionless parameters ϵ, α, and β relating to the Debye length λ_{D}, the applied voltage V_0, and the height h of the electrode, respectively,

$$\epsilon = \frac{\lambda_{\mathrm{D}}}{a}, \quad \alpha = \frac{aV_0}{L\phi_0}, \quad \beta = \frac{h}{a}. \quad (35)$$

As mentioned in Sec. I, the strength of the generated ICEO flow can be measured as the mechanical power input P_{mech} exerted on the electrolyte by the slip-velocity just outside the Debye layer or equivalently by the kinetic energy dissipation P_{kin} in the bulk of the electrolyte. However, both these methods suffers from numerical inaccuracies due to the dependence of both the position of the integration path and of the less accurately determined velocity gradients in the stress tensor $\boldsymbol{\sigma}$. To obtain a numerically more stable and accurate measure, we have chosen in the following analysis to characterize the strength of the ICEO flow by the kinetic energy E_{kin} of the induced flow field $\boldsymbol{v}$,

$$E_{\mathrm{kin}} = \tfrac{1}{2}\rho_{\mathrm{m}} \int_{\Omega} v^2 \,\mathrm{d}x\,\mathrm{d}z, \quad (36)$$

which depends on the velocity field and not its gradients, and which furthermore is a bulk integral of good numerical stability.

A. Zero height of the un-biased center electrode

We assume the height h of the un-biased center electrode to be zero, i.e. $\beta = 0$, while varying the Debye length and the applied voltage through the parameters ϵ and α. We note that the linear slip-velocity model Eqs. (21) and (22) is independent of the dimensionless Debye length ϵ. It is therefore natural to use the kinetic energy $E_{\mathrm{kin}}^{\mathrm{LS}}$ of this model as a normalization factor.

In the lin-log plot of Fig. 4 we show the kinetic energy $E_{\mathrm{kin}}^{\mathrm{NLS}}$ and $E_{\mathrm{kin}}^{\mathrm{FN}}$ normalized by $E_{\mathrm{kin}}^{\mathrm{LS}}$ as a function of the inverse Debye length $1/\epsilon$ for three different values of the applied voltage, $\alpha = 0.05, 0.5$ and 5, ranging from the linear to the strongly nonlinear voltage regime.

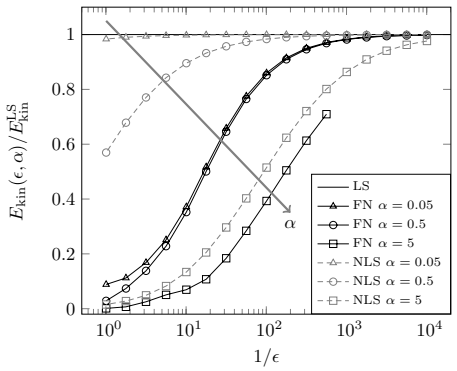

FIG. 4: The total induced kinetic energy $E_{\mathrm{kin}}^{\mathrm{NLS}}$ (gray dashed) and $E_{\mathrm{kin}}^{\mathrm{FN}}$ (black) for the nonlinear slip-velocity model and the full model, respectively, relative to $E_{\mathrm{kin}}^{\mathrm{LS}}$ (horizontal black line) of the linear slip-velocity model as a function of dimensionless inverse Debye length $1/\epsilon$. Each are shown for three values of the dimensionless applied voltage $\alpha = 0.05, 0.5$ and 5. The value of ϵ decreases from 1 to 10^{-4} going from left to right.

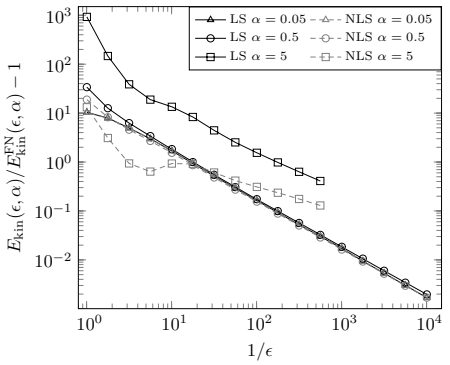

FIG. 5: The difference between the induced kinetic energies $E_{\mathrm{kin}}^{\mathrm{LS}}$ and $E_{\mathrm{kin}}^{\mathrm{NLS}}$ of the linear and nonlinear slip-velocity models, respectively, relative to the full model $E_{\mathrm{kin}}^{\mathrm{FN}}$ as a function of the inverse Debye length $1/\epsilon$. for three different applied voltages $\alpha = 0.05, 0.5, 5$.

We first note that in the limit of vanishing Debye length (to the right in the graph) all models converge towards the same value for all values of the applied voltage α. For small values of α the advanced slip-velocity model $E_{\mathrm{kin}}^{\mathrm{NLS}}$ is fairly close to the linear slip-velocity model $E_{\mathrm{kin}}^{\mathrm{LS}}$, but as α increases, it requires smaller and smaller values of ϵ to obtain the same results in the two models. In the linear regime $\alpha = 0.05$ a deviation less than 5% is obtained already for $\epsilon < 1$. In the nonlinear regime $\alpha = 0.5$ the same deviation requires $\epsilon < 10^{-2}$, while in the strongly nonlinear regime $\epsilon < 10^{-4}$ is needed to obtain a deviation lower than 5%.

In contrast, it is noted how the more realistic full model $E_{\mathrm{kin}}^{\mathrm{FN}}$ deviates strongly from $E_{\mathrm{kin}}^{\mathrm{LS}}$ for most of the displayed values of ϵ and α. To obtain a relative deviation less than 5% in the linear ($\alpha = 0.05$) and nonlinear ($\alpha = 0.5$) regimes, a minute Debye length of $\epsilon < 10^{-3}$ is required, and in the strongly nonlinear regime the 5% level it not reached at all.

The deviations are surprisingly large. The Debye length in typical electrokinetic experiments is $\lambda_{\mathrm{D}} = 30$ nm. For a value of $\epsilon = 0.01$ this corresponds to an electrode of width 2×3 µm $= 6$ µm, comparable to those used in Refs. [7, 10, 11]. In Fig. 4 we see that for $\alpha = 5$, corresponding to a moderate voltage drop of 0.26 V across the electrode, the linear slip-velocity model overestimates the ICEO strength by a factor $1/0.4 = 2.5$. The nonlinear slip-model does a better job. For the same parameters it only overestimates the ICEO strength by a factor $0.5/0.4 = 1.2$.

For more detailed comparisons between the three models the data of Fig. 4 are plotted in a different way in Fig. 5. Here the overestimates $(E_{\mathrm{kin}}^{\mathrm{LS}}/E_{\mathrm{kin}}^{\mathrm{FN}}) - 1$ and $(E_{\mathrm{kin}}^{\mathrm{NLS}}/E_{\mathrm{kin}}^{\mathrm{FN}}) - 1$ of the two slip-velocity models relative to the more correct full model are plotted in a log-log plot as a function of the inverse Debye length $1/\epsilon$ for three different values of the applied voltage. It is clearly seen how the relative deviation decreases proportional to ϵ as ϵ approaches zero.

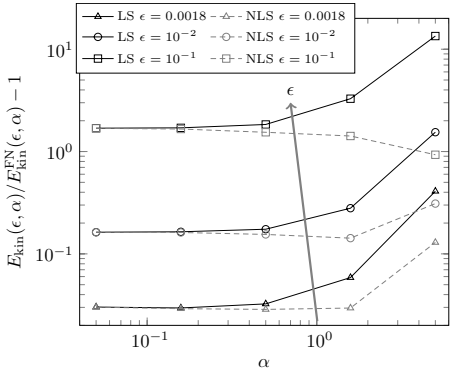

FIG. 6: The difference between the induced kinetic energies $E_{\mathrm{kin}}^{\mathrm{LS}}$ and $E_{\mathrm{kin}}^{\mathrm{NLS}}$ of the linear and nonlinear slip-velocity models, respectively, relative to the full model $E_{\mathrm{kin}}^{\mathrm{FN}}$ as a function of the voltage bias α for three different Debye layer thicknesses $\epsilon = 1.8 \times 10^{-3}, 10^{-2}, 10^{-1}$.

Finally, in Fig. 6 the relative deviations $(E_{\mathrm{kin}}^{\mathrm{LS}}/E_{\mathrm{kin}}^{\mathrm{FN}}) - 1$

and $(E_{\rm kin}^{\rm NLS}/E_{\rm kin}^{\rm FN})-1$ are plotted versus the voltage α in a log-log plot. For any value of the applied voltage α, both slip-velocity models overestimates by more than 100% for large Debye lengths $\epsilon = 10^{-1}$ and by more than 10% for $\epsilon = 10^{-2}$. For the minute Debye length $\lambda_{\rm D} = 1.8 \times 10^{-3}$ the overestimates are about 3% in the linear and weakly nonlinear regime $\alpha < 1$, however, as we enter the strongly nonlinear regime with $\alpha = 5$ the overestimation increases to a level above 10%.

B. Finite height of the un-biased electrode

Compared to the full numerical model, the slip-velocity models are convenient to use, but even for small Debye lengths, say $\lambda_{\rm D} = 0.01a$, they are prone to significant quantitative errors as shown above. Similarly, it is of relevance to study how the height of the un-biased electrode influences the strength of the ICEO flow rolls. In experiments the thinnest electrodes are made by evaporation techniques. The resulting electrode heights are of the order 50 nm − 200 nm, which relative to the typical electrode widths $a \approx 5$ µm results in dimensionless heights $10^{-3} < \beta < 10^{-1}$.

In Fig. 7 is shown the results for the numerical calculation of the kinetic energy $E_{\rm kin}^{\rm FN}(\epsilon,\beta)$ using the full numerical model. The dependence on the kinetic energy of the dimensionless Debye length $\epsilon = \lambda_{\rm D}/a$ and the dimensionless electrode height $\beta = h/a$ is measured relative to the value $E_{\rm kin}^{\rm FN}(\epsilon,\beta)$ of the infinitely small Debye length for an electrode of zero height. For small values of the height no major deviations are seen. The curve for $\beta = 0$ and $\beta = 0.001$ are close. As the height is increased to $\beta = 10^{-2}$ we note that the strength of the ICEO is increased by 20%−25% as $\beta > \epsilon$. This tendency is even stronger pronounced for the higher electrode $\beta = 10^{-1}$. Here the ICEO strength is increased by approximately 400% for a large range of Debye lengths.

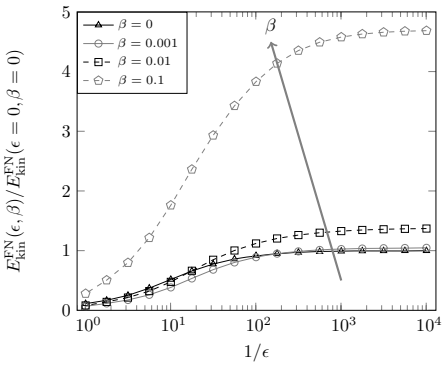

FIG. 7: The difference between the induced kinetic energies $E_{\rm kin}^{\rm FN}(\epsilon,\beta)$ of the full model at finite Debye length and electrode height relative to the full model $E_{\rm kin}^{\rm FN}(0,0)$ at zero Debye length and zero electrode height as a function of the inverse Debye length $1/\epsilon$ for four electrode heights $\beta = 0, 10^{-3}, 10^{-2}, 10^{-1}$.

C. Thermodynamic efficiency of the ICEO system

Conventional electro-osmosis is known to have a low thermodynamic efficiency defined as the delivered mechanical pumping power relative to the total power delivered by the driving voltage. Typical efficiencies are of the order of 1% [26], while in special cases an efficiency of 5.6% have been reported [27]. In the following we provide estimates and numerical calculations of the corresponding thermodynamic efficiency of the ICEO system.

The applied voltage drop $2V_0 = 2E_0L$ across the system in the x-direction is written as the average electrical field E_0 times the length $2L$, while the electrical current is given by $I = WH\sigma E_0$, where W and H is the width and height in the y- and z-direction, respectively, and $\sigma = D\varepsilon/\lambda_{\rm D}^2 = \varepsilon/\tau_D$ is the conductivity written in terms of the Debye time $\tau_D = \lambda_{\rm D}^2/D$. The total power consumption to run the ICEO system is thus

$$P_{\rm tot} = 2V_0 \times I = \frac{4}{\tau_{\rm D}} \left(\frac{1}{2}\varepsilon E_0^2\right) LWH. \qquad (37)$$

This expression can be interpreted as the total energy, $\frac{1}{2}\varepsilon E_0^2 \times LWH$, stored in the average electrical field of the system with volume LWH multiplied by the characteristic electrokinetic rate $4/\tau_{\rm D}$.

The velocity-gradient part of the hydrodynamic stress tensor is denoted $\tilde{\boldsymbol{\sigma}}$, i.e. $(\tilde{\boldsymbol{\sigma}})_{ij} = \eta(\partial_i v_j + \partial_j v_i)$. In terms of $\tilde{\boldsymbol{\sigma}}$, the kinetic energy dissipation $P_{\rm kin}$ necessary to sustain the steady-state flow rolls is given by $P_{\rm kin} = \frac{W}{2\eta}\int_0^L {\rm d}x \int_0^H {\rm d}z\, {\rm Tr}(\tilde{\boldsymbol{\sigma}}^2)$. In the following estimate we work in the Debye–Hückel limit for an electrode of length $2a$, where the induced zeta potential is given by $\zeta_{\rm ind} = aE_0$ and the radius of each flow roll is approximately a. In this limit the electro-osmotic slip velocity $u_{\rm eo}$ and the typical size of the velocity gradient $|\partial_i v_j|$ are

$$u_{\rm eo} = \frac{\varepsilon\zeta_{\rm ind}}{\eta} E_0 = \frac{\varepsilon a}{\eta} E_0^2, \qquad (38a)$$

$$|\partial_i v_j| \approx \frac{u_{\rm eo}}{a} = \frac{\varepsilon}{\eta} E_0^2. \qquad (38b)$$

Thus, since the typical area covered by each flow roll is πa^2 , we obtain the following estimate of $P_{\rm kin}$,

$$P_{\rm kin} \approx 2\frac{W}{2\eta}\pi a^2 4\left[\eta\frac{u_{\rm eo}}{a}\right]^2 = 8\frac{\varepsilon E_0^2}{\eta}\left(\frac{1}{2}\varepsilon E_0\right)^2 \pi a^2 W. \qquad (39)$$

Here the power dissipation can be interpreted as the energy of the electrical field in the volume $\pi a^2 W$ occupied by each flow roll multiplied by an ICEO rate given by the electric energy density εE_0^2 divided by the rate of viscous energy dissipation per volume given by η.

The thermodynamic efficiency can now be calculated as the ratio $P_{\rm kin}/P_{\rm tot}$ using Eqs. (37) and (39),

$$\frac{P_{\rm kin}}{P_{\rm tot}} \approx \frac{2\pi a^2}{LH}\,\frac{\varepsilon E_0^2}{\eta/\tau_{\rm D}} \approx 2.4 \times 10^{-8}. \qquad (40)$$

This efficiency is the product of the ratio between the volumes of the flow rolls and the entire volume multiplied and the ratio of the electric energy density in the viscous energy density $\eta/\tau_{\rm D}$. The value is found using $L = H = 15a = 0.15$ mm, $E_0 = 2.5$ kV/m, and $\lambda_{\rm D} = 20$ nm, which is in agreement with the conventional efficiencies for conventional electro-osmotic systems quoted above.

VII. CONCLUSION

We have shown that the ICEO velocities calculated using the simple zero-width models significantly overestimates those calculated in more realistic models taking the finite size of the Debye screening length into account. This may provide a partial explanation of the observed quantitative discrepancy between observed and calculated ICEO velocities. The discrepancy increases substantially for increasing ϵ, i.e. in nanofluidic systems.

Even larger deviations of the ICEO strength is calculated in the full numerical model when a small, but finite height of the un-biased electrode is taken into account.

A partial explanation of the quantitative failure of the analytical slip velocity model is the decrease of the tangential electric field as a function of the distance to the surface of the polarized ICEO object combined with the spatial extent of the charge density of the double layer. Also tangential hydrodynamic and osmotic pressure gradients developing inside the double layer may contribute to the lowering ICEO strength when taking the finite width of the double layer into account. The latter may be related to the modification of the classical Helmholtz–Smoluchowski expression of the slip-velocity obtained by adding a term proportional to the gradient of the salt concentration c [28].

Our work shows that for systems with a small, but non-zero Debye length of 0.001 to 0.01 times the size of the electrode, and even when the Debye-Hückel approximation is valid, a poor quantitative agreement between experiments and model calculations must be expected when applying the linear slip-velocity model based on a zero Debye-length. It is advised to employ the full numerical model of ICEO, when comparing simulations with experiments.

VIII. ACKNOWLEDGEMENTS

We thank Sumita Pennathur and Martin Bazant for illuminating discussions, and we are particularly grateful to Todd Squires for a number of valuable comments and suggestions. This work is supported in part by the Institute for Collaborative Biotechnologies through contract no. W911NF-09-D-0001 from the U.S. Army Research Office. The content of the information herein does not necessarily reflect the position or policy of the Government and no official endorsement should be inferred.

[1] S.S. Dukhin, Adv. Colloid Interface Sci. **44**, 1 (1993).
[2] V.A. Murtsovkin, Colloid J. **58**, 341 (1996).
[3] A. Gonzalez, A. Ramos, N.G. Green, A. Castellanos and H. Morgan, Phys. Rev. E **61**(4), 4019 (2000).
[4] N.G. Green, A. Ramos, A. Gonzalez, H. Morgan and A. Castellanos, Phys. Rev. E **66**, 026305 (2002).
[5] A. Ajdari, Phys. Rev. E **61**, R45 (2000).
[6] A.B.D. Brown, C.G. Smith and A.R. Rennie, Phys. Rev. E **63**, 016305 (2000).
[7] V. Studer, A. Pépin, Y. Chen and A. Ajdari, The Analyst **129**, 944 (2004).
[8] D. Lastochkin, R. Zhou, P. Whang, Y. Ben and H.-C. Chang, J. Appl. Phys. **96**, 1730 (2004).
[9] S. Debesset, C.J. Hayden, C. Dalton, J.C.T. Eijkel and A. Manz, Lab Chip **4**, 396 (2004).
[10] B.P. Cahill, L.J. Heyderman, J. Gobrecht and A. Stemmer, Phys. Rev. E **70**, 036305 (2004).
[11] M.M. Gregersen, L.H. Olesen, A. Brask, M.F. Hansen, and H. Bruus, Phys. Rev. E **76** 056305 (2007).
[12] L.H. Olesen, H. Bruus and A. Ajdari, Phys. Rev. E **73**, 056313 (2006).
[13] T.M. Squires, and M.Z. Bazant, J. Fluid Mech. **509**, 217 (2004).
[14] J.A. Levitan, S. Devasenathipathy, V. Studer, Y. Ben, T. Thorsen, T.M. Squires, and M.Z. Bazant, Coll. Surf. A **267**, 122 (2005).
[15] T.M. Squires, and M.Z. Bazant, J. Fluid Mech. **560**, 65 (2006).
[16] C.K. Harnett, J. Templeton, K. Dunphy-Guzman, Y.M. Senousy, and M.P. Kanouff, Lab Chip **8**, 565 (2008).
[17] A.S. Khair and T.M. Squires, J. Fluid Mech. **615**, 323 (2008).
[18] M.M. Gregersen, F. Okkels, M.Z. Bazant, and H. Bruus, New J. Phys. (submitted, 2008), http://arxiv.org/abs/0901.1788
[19] G. Soni, T.M. Squires, and C.D. Meinhart, in *Proceedings of 2007 ASME International Mechanical Engineering Congress and Exposition*, 2007.
[20] R.F. Probstein, *Physicochemical hydrodynamics*, (John Wiley & Sons, New York, 1994).
[21] H. Bruus, *Theoretical Microfluidics*, (Oxford University Press, Oxford, 2008).
[22] S.S. Dukhin, R. Zimmermann, and C. Werner, Coll. Surf.

A **195**, 103 (2001).
[23] J. Lyklema, J. Phys.: Condens. Matter **13**, 5027 (2001).
[24] K.T. Chu, and M.Z. Bazant, J. Colloid. Interf. Sci. **315**, 319 (2007).
[25] G. Soni, M.B. Andersen, H. Bruus, T. Squires, C. Meinhart, Phys. Rev. E (in preparation, 2009)
[26] D.J. Laser and J.G. Santiago J. Micromech. Microeng. **14**, R1 (2004).
[27] D.S. Reichmuth, G.S. Chirica, and B.J. Kirby Sens. Actuators B **92**, 37 (2003).
[28] A.S. Khair and T.M. Squires, Phys. Fluids **20**, 087102 (2008)

Bibliography

[1] A. B. D. Brown, C. G. Smith, and A. R. Rennie
Pumping of water with ac electric fields applied to asymmetric pairs of microelectrodes
Physical Review E **63**, 016305 (2000)

[2] M. Mpholo, C. G. Smith, A. B. D. Brown
Low voltage plug flow pumping using anisotropic electrode arrays
Sensors and Actuators B **92**, 262-268 (2003)

[3] V. Studer, A. Pépin, Y. Chen, and A. Ajdari
An integrated AC electrokinetic pump in a microfluidic loop for fast and tunable flow control
Analyst **129**, 944-949 (2004)

[4] S. Debesset, C. J. Hayden, C. Dalton, J. C. T. Eijkel, and A. Manz
An AC electroosmotic micropump for circular chromatographic applications
Lab Chip **4**, 396-400 (2004)

[5] A. Ramos, H. Morgan, N. G. Green, A. Gonzalez and A. Castellanos, J. Appl. Phys. **97**, 084906 (2005).

[6] A. Brask, D. Snakenborg, J. P. Kutter, and H. Bruus
AC electroosmotic pump with bubble-free palladium electrodes and rectifying polymer membrane valves
Lab. Chip. **6**, 280 (2006)

[7] C.K. Harnett, J. Templeton, K. Dunphy-Guzman, Y.M. Senousy, and M.P. Kanouff, Lab Chip **8**, 565 (2008).

[8] A. Brask, J. P. Kutter, and H. Bruus
Long-term stable electroosmotic pump with ion exchange membranes
Lab. Chip. **5**, 730 (2005)

[9] H. Bruus
Theoretical microfluidics
Oxford University Press, Oxford (2008)

[10] R. F. Probstein
Physicochemical Hydrodynamics, 2. ed.
Wiley Interscience (2003)

[11] S. S. Dukhin
Non-equilibrium electric surface phenomena
Adv. Colloid Interface Sci. **44**, 1 (1993)

[12] V. A. Murtsovkin
Colloid J. **58**, 341 (1996)

[13] A. Ramos, H. Morgan, N. G. Green, and A. Castellanos
AC electrokinetics: a review of forces in microelectrode structures
J. Phys. D **31**, 2338 (1998)

[14] N. G. Green, A. Ramos, A. Gonzáles, H. Morgan, and A. Castellanos
Fluid flow induced by nonuniform ac electric fields in electrolytes on microelectrodes. I. Experimental measurements
Physical Review E **61**, 4011 (2000)

[15] A. Gonzalez, A. Ramos, N. G. Green, A. Castellanos and H. Morgan, Phys. Rev. E **61**(4), 4019 (2000).

[16] N. G. Green, A. Ramos, A. Gonzáles, H. Morgan, and A. Castellanos
Fluid flow induced by nonuniform ac electric fields in electrolytes on microelectrodes. III. Observation of streamlines and numerical simulation
Physical Review E **66**, 026305 (2002)

[17] A. Ajdari
Pumping liquids using asymmetric electrode arrays
Physical Review E **61**, R45-R48 (2000)

[18] V. Studer, A. Pépin, Y. Chen and A. Ajdari, Microelectron. Eng. **61-62**, 915 (2002).

[19] A. Ramos, A. Gonzalez, A. Castellanos, N. G. Green and H. Morgan, Phys. Rev. E **67**, 056302 (2003).

[20] D. Lastochkin, R. Zhou, P. Whang, Y. Ben and H.-C. Chang, J. Appl. Phys. **96**, 1730 (2004).

[21] B. P. Cahill, L. J. Heyderman, J. Gobrecht and A. Stemmer, Phys. Rev. E **70**, 036305 (2004).

[22] N. A. Mortensen, L. H. Olesen, L. Belmon and H. Bruus,
Electro-hydrodynamics of binary electrolytes driven by modulated surface potentials
Phys. Rev. E **71**, 056306 (2005).

[23] P. García–Sánchez, A. Ramos, N. G. Green and H. Morgan, IEEE Trans. Dielect. El. In. **13**, 670 (2006).

[24] L. H. Olesen, H. Bruus, and A. Ajdari
AC electrokinetic micropumps: the effect of geometrical confinement, Faradaic current injection, and nonlinear surface capacitance
Physical Review E **73**, 056313 (2006)

[25] M.M. Gregersen, L.H. Olesen, A. Brask, M.F. Hansen, and H. Bruus, Phys. Rev. E **76** 056305 (2007).

[26] M.Z. Bazant and T. M. Squires, Phys. Rev. Lett. **92** 066101 (2004).

[27] T.M. Squires, and M.Z. Bazant
Induced-charge electro-osmosis
J. Fluid Mech. **509**, 217 (2004).

[28] J. A. Levitan, S. Devasenathipathy, V. Studer, Y. Ben, T. Thorsen, T. M. Squires, M. Z. Bazant, a metal wire in a microchannel, Coll. Surf. A **267**, 122 (2005).

[29] T.M. Squires, and M.Z. Bazant
Breaking symmetries in induced-charge electro-osmosis and electrophoresis
J. Fluid Mech. **560**, 65 (2006).

[30] M.M. Gregersen, M.B. Andersen, G. Soni, C. Meinhart, T. Squires, H. Bruus, Phys. Rev. E (submitted, 2009), http://arxiv.org/abs/0901.1788..

[31] G. Soni, T.M. Squires, and C.D. Meinhart
Proceedings of 2007 ASME International Mechanical Engineering Congress and Exposition, 2007.

[32] T. Borrvall and J. Petersson, Int. J. Numer. Methods Fluids **41**, 77 (2003).

[33] M. P. Bendsøe, and N. Kikuchi
Generating optimal topologies in structural design using a homogenization method
Comp. Meth. App. Mech. Eng. **71**, 197 (1988)

[34] J.S. Jensen and O. Sigmund
Systematic design of photonic crystal structures using topology optimization: low-loss waveguide bends
Appl. Phys. Lett. **84**, 2022 (2004)

[35] M.B. Dühring, J.S. Jensen, and O. Sigmund
Acoustic design by tooplogy optimization
J. Sound Vib. **317**, 557 (2008)

[36] F. Okkels and H. Bruus
Scaling behavior of optimally structured catalytic microfluidic reactors
Phys. Rev. E **75**, 016301 (2007).

[37] R. J. Hunter
Foundations of Colloid Science, 2. ed.
Oxford University Press, Oxford (2001).

[38] A. J. Bard and L. R. Faulkner,
Electrochemical Methods, 2.ed.
John Wiley and Sons, Inc. (2001).

[39] Anders Brask
Electroosmotic micropumps
Department of Micro and Nanotecnology, DTU, PhD Thesis (2005),
www.nanotech.dtu.dk/microfluidics

[40] L. H. Olesen,
AC Electrokinetic micropumps,
Dept. of Micro and Nanotechnology, DTU, PhD Thesis (2006),
www.nanotech.dtu.dk/microfluidics

[41] L. H. Olesen, F. Okkels, and H. Bruus, Int. J. Numer. Methods Eng. **65**, 975 (2006).

[42] Comsol Multiphysics, COMSOL AB (`www.comsol.com`).

[43] Matlab, The MathWorks, Inc. (`www.mathworks.com`).

[44] M. Heller,
Numerical study of free surfaces and particle sorting in microfluidic systems
Dept. of Micro and Nanotechnology, DTU, PhD Thesis (2008),
www.nanotech.dtu.dk/microfluidics

[45] K. Svanberg, Int. J. Numer. Methods Eng. **24**, 359 (1987).

[46] A MATLAB implementation, mmasub, of the MMAoptimization algorithm [45] can be obtained (free of charge for academic purposes) from Krister Svanberg, KTH, Sweden. E-mail address: krille@math.kth.se.

[47] M. M. Gregersen, *AC Asymmetric Electrode Micropumps*, MSc Thesis, MIC - Dept. of Micro and Nanotechnology, DTU (2005), www.nanotech.dtu.dk/microfluidics

[48] J. G. Santiago, S. T. Wereley, C. D. Meinhart, D. J. Beebe, and R. J. Adrian, Exp. Fluids **25**, 316 (1998).

[49] M. Z. Bazant, K. Thornton, and A. Ajdari, Phys. Rev. E **70**, 021506 (2004).

[50] B. J. Kirby and E. F. Hasselbrink, Electrophoresis **25**, 187 (2004).

[51] Z. Kerner and T. Pajkossy, Electrochim. Acta **46**, 207 (2000).

[52] M. S. Kilic, M. Z. Bazant and A. Ajdari, Phys. Rev. E **75**, 021502 (2007) and Phys. Rev. E **75**, 021503 (2007).

[53] P. García-Sánchez
Travelling-wave electrokinetic micropumps
Electronics and electromagnetism department, University of Seville (2008).

[54] L. D. Landau, and E. M. Lifshitz
Fluid Mechanics, 2. ed., Vol. 6 of Course of Theoretical Physics
Elsevier (2004)

[55] G. Soni, M.B. Andersen, H. Bruus, T. Squires, C. Meinhart, Phys. Rev. E (in preparation, 2009)

[56] S.S. Dukhin, R. Zimmermann, and C. Werner, Coll. Surf. A **195**, 103 (2001)

[57] M.P. Bendsøe and O. Sigmund, *Topology Optimization-Theory, Methods and Applications*, Springer (Berlin, 2003).

[58] A. Gersborg-Hansen, O. Sigmund, and R.B. Haber, Struct. Multidiscip. Optim. **30**, 181 (2005)

[59] M. S. Kilic, M. Z. Bazant, and A. Ajdari, Phys. Rev. E **75**, 034702 (2007).

[60] J.A. Nelder and R. Mead, Computer Journal, **7**, 308 (1965).

[61] J.C. Lagarias, J.A. Reeds, M.H. Wright, and P.E. Wright, SIAM Journal of Optimization, Vol. **9** No. 1, 112 (1998)

[62] The routine `fminsearch` in MATLAB version 7 (R14).

[63] The MATLAB function `fminsearch` is actually unbounded, i.e. the design variables tuned by the function must give rise to a well-defined boundary regardless of their value. This is circumvented by using the arcus tangent function to map an unbounded interval into an open bounded interval.

[64] M.Z. Bazant and Y. Ben, Lab Chip **6**, 1455 (2006).

[65] J. Urbanski, T. Thorsen, J. Levitan, and M. Bazant Appl. Phys. Lett. **89**, 143508 (2006).

[66] F. Okkels, and H. Bruus
Design of microfluidic bioreactors using topology optimization
Journal of Computational and Theoretical Nanosceince **4**, 814-816 (2007)

[67] S. Jensen, S. Thorsteinsson, O. Hansen, and U. J. Quaade
Parametric investigation of rate enhancement during fast temperature cycling of co oxidation in microreactors
Chem. Eng. J. **135**, 237 (2007).

[68] M. Rinnemo, D. Kulginov, S. Johansson, K. L. Wong, V. Pv Zhdanov, and B. Kasemo
Catalytic ignition in the CO-O_2 reaction on platinum: experiment and simulations
Surface Sceince **376**, 297-309 (1997)

[69] V. P. Zhdanov, and B. Kasemo
Steady-state kinetics of CO oxidation on Pt: extrapolation from 10^{-10} *to* 1 bar
Applied Surface Science **74**, 147-164 (1994)

[70] I. Chorkendorff, J. W. Niemantsverdriet
Concepts of Modern Catalysis and kinetics
WILEY-VCH Verlag GmbH & Co. KGaA (2003)

[71] U. J. Quaade, S. Jensen, and O. Hansen
Microsystem with integrated capillary leak to mass spectrometer for high sensitivity temperature programmed desorption
Rev. Sci. Instrum. **75**, 3345 (2004).

[72] H. A. Hansen, J. L. Olsen, S. Jensen, O. Hansen, and U. J. Quaade
Rate enhancement in microfabricated chemical reactors under fast forced temperature oscillations
Catal. Com. **7**, 272 (2006).

[73] S. Jensen, J. L. Olsen, S. Thorsteinsson, O. Hansen, and U. J. Quaade
Forced thermal cycling of catalytic reactions: Experiments and modelling Catal. Com. **8**, 1985 (2007).

[74] D. R. Lide
CRC Handbook of Chemistry and Physics, 75. ed.
CRC Press (1994)

[75] J. Bear
Dynamics of Fluids in Porous Media
American Elsevier Publishing Company Inc. (1972)

[76] M. B. Andersen, T. Wolfcale, M. M. Gregersen, S. Pannathur, and H. Bruus
Microchannel electrokinetics of charged analytes in buffered solutions near floating electrodes
GAMM-2009, Gdansk, Poland, February 2009.

[77] E. A. Mason, A.P. Malinauskas
Gas Transport in Porous Media: The Dusty-Gas Model
Elsevier Science Publishers B.V. (1983)

[78] Pernille Voss Larsen
Fabrication Methods and Reactivity Measurements for Catalytic Nanoparticles in Microreactors

Department of Micro and Nanotecnology, Technical University of Denmark, MSc Thesis (2008)

[79] S. Jensen, J. M. Jensen, U. J. Quaade, and O. Hansen
Uniformity-improving dummy structures for deep reactive ion etching (DRIE) processes
SPIE-2005, Bellingham (WA) USA, proc. vol. 5715, pp. 39 (2005)